Modelling of Gas-Condensate Flow around Complex Well Geometries and Cleanup Efficiency in Heterogeneous Systems

By

Saad Ebrahim Alajmi

Submitted for the degree of **Doctor of Philosophy** in

Petroleum Engineering

Heriot-Watt University

Institute of Petroleum Engineering

July 2012

The copyright in this thesis is owned by the author. Any quotation from the thesis or use of any of the information contained in it must acknowledge this thesis as the source of the quotation or information.

ABSTRACT

Two phase flow of gas and condensate fluids in porous media is different from that of conventional Gas-Oil fluid systems. Such reservoirs are characterized by their complex phase and flow behaviors that significantly affect the well performance. The presence of retrograde fluid, when the pressure drops below dew point, and the dependency of the gas and condensate relative permeability (k_r) on the velocity and interfacial tension (*IFT*) makes numerical modeling and performance prediction of gas condensate systems a real challenge, especially for complex well geometries such as hydraulically fractured wells (HFWs).

The current research work is divided into three elements. The first one is devoted to study the flow behaviour around Single and Multi-layer hydraulically fractured wells (HFWs) in gas condensate reservoirs. Here, several in-house simulators have been developed for single-phase and two-phase gas condensate flow. The two phase in-house simulators correctly account for the phase change and the dependency of relative permeability to velocity and interfacial tension, due to inertia (reduction in k_r as velocity increases) and coupling (improvement in k_r as velocity increases and/or *IFT* decrease). The integrity of the in-house simulators have been verified by comparing some of their results with those obtained using the fine grid option of the ECLIPSE (E300) commercial reservoir simulator under the same prevailing flow conditions. Benefiting from, the 2 and 3-D in-house simulators a large data bank has been generated covering a wide range of variations of pertinent geometrical and flow parameters. Then, a new formula is proposed for estimation of an effective wellbore radius of an equivalent open-hole (EOH) radial 1-D system replicating flow around the 2 and 3-D HFW systems. The proposed formulation is general, in the sense that if the total gas fractional flow (GTR) is unity, then it correctly converts to that suitable for single phase gas system under Non-Darcy flow conditions and when Reynolds number is small to that under Darcy flow conditions.

The second part of this thesis is devoted to study the optimization of hydraulic fracture geometry in gas condensate reservoirs. In this part of the study, a general optimum fracture design formulation is proposed based on the effective proppant number concept. In this new formula the maximum productivity index and optimum penetration ratio can be calculated for a certain proppant number, both accounted for the coupling and inertia effects.

Here an effective proppant number formula is proposed (i.e. correcting the absolute proppant number for the effect of coupling and inertia). The proposed formula is general as it correctly converts to that suitable for single-phase Darcy and Non-Darcy flow. Furthermore, using the effective proppant number formula proposed here, the well-known Unified Fracture Design (UFD, Economides and Valko formula) has been modified to account for gas condensate flow conditions, i.e. coupling and inertia effects.

The third part of this research work presents a thorough and extensive evaluation of the impact of the pertinent parameters on the clean-up efficiency process, which is often considered as one of the main reasons for the under-performance of hydraulic fracturing treatments, in gas reservoirs.

In fact, most available clean up efficiency literature studies are concentrated on evaluating the impact of a single pertinent parameter at a time. That is, none of these studies have investigated the variation of all pertinent parameters simultaneously over a wide practical range of their variations, which may help in better understanding of the clean-up process and may provide practical guidelines to successful hydraulic fracturing jobs. Accordingly, this work embarked on a much more expanded study following statistical approaches. First, the key parameters which have significant impact on the gas production loss (GPL) are identified and then a 2-level full factorial statistical experimental design method has been used to sample a reasonably wide range of variation of pertinent parameters covering many practical cases for a total of 12 parameters. Since over 36,000 simulation runs were required, to cover the range of variation of all parameters, the simulation process has been simplified using a computer code, which was developed to automatically link different stages of these simulations. The analysis of the simulation runs using two response surface models (with and without interaction of parameters) demonstrates the relative importance of the pertinent parameters after different production time periods and provide a practical guidelines to a successful hydraulic fracturing job.

In conclusion, this research cover the following main elements of HFW research, 1) – To propose simple numerical modelling methods for gas and gas condensate flow around single and multi-Layer HFWs, 2) – To propose a general Optimum Fracture Design method for gas and gas condensate reservoirs, which correctly account for the effects of coupling and inertia. 3) – To provide a thorough and extensive evaluation of the impact of pertinent parameters on clean-up efficiency of hydraulically fractured gas well.

Dedication1

To My Father

Ebrahim

It has been 20 years since your departure, and if you think those 20 years are enough times to forget about you. Then Honest to God, even 200 years will not be enough to take you out of mind. I love you more than you think; I miss you every day; every day.

I did this PhD because of you, because you have told one day, that you will be happy if I do PhD.

For those who read this thesis, if your Father and/or Mother are still alive then you are very lucky, take care of them, be close to them, be kind to them. Life is nothing without them.

Dedication 2

To my Friend and brother

Mohammed Nasser
1976- 2011

Who lost his fight with Cancer last December, he is a big loss.

Mohammed, I just want to tell you that I really miss you, and your Departure was a big shock for me.

Acknowledgment

I would like to express my deepest gratitude and respect to my supervisor, Dr. Panteha Ghahri. Indeed, her contributions to the production of this thesis were maximal. I have always benefited from her expertise supervision, brilliant ideas, valuable advices, productive discussions and extensive knowledge. She cares more about me before the work; she is always there whenever I need her. One thing I learnt from her and she always says it to me “if you cannot explain it simply, then you do not understand it well enough”. Therefore, a “Big Thank you” is due for her.

I would like to thank my other supervisor, Dr. Mahmoud Jamiolahmady, for his technical review of the work and editing of this thesis.

I am also very grateful to my examiners, Dr Jim Somerville and Prof. Chris E Brown for giving their time to read my thesis and sharing their valuable comments and suggestions, their role were very constructive. I did really enjoy my time during the viva, although it was one of the most difficult meetings I have ever had. However, it gave me the chance to look differently to my research, and improve the way I think about research problems and the way I do search for solutions.

My special thanks go to my mother; my words will not do justice to how I feel about her. She is the light of my life. I feel speechless when it comes to her because nothing better than her satisfaction on me. My sincere thanks also go to my brothers and sisters for their continuous help and support.

Finally, special thanks to my wife and lovely little daughter who got the entire headache from my sleepless nights and stressful times. Indeed, they helped me to pass these difficulties and gave me some energy to carry on my PhD journey. It was a very difficult 5 years but at the end it worth it. I love you both more than you think.

Table of Contents

List of Symbols

Nomenclature

GCR-HW	Gas Condensate Research Group in Heriot-Watt University
J_D	Dimensionless productivity index
k	Absolute Reservoir Permeability
K_{max}	End Point Of The Corey Relative Permeability Curve
$\dot{m}$	Mass Flow Rate
$\mathbf{n_g}$	Exponent Of The Gas Corey Relative Permeability Curve
$\mathbf{n_w}$	Exponent Of The Water Corey Relative Permeability Curve
P	Pressure
P_c	Capillary Pressure
P_d	Threshold Pressure
$\bar{p}$	Volumetric Average Pressure
q	Flow Rate
r	Radius
ε	Reciprocal Effective Wellbore Radius of Infinite Conductivity Fracture
r_w'	Effective Wellbore Radius
R_e	Reynolds Number
R^2	The Coefficient of Multiple Regression Determination
S	Skin Factor
S_d	Damage Skin Factor
S_f	Flow Skin Factor
S_g	Geometric Skin Factor
V	Velocity
w_f	Fracture Width
x_j	Mass Fraction Of Component J In Liquid Phase
x_f	Half Length Of The Fracture
X_e	Length Of The Reservoir
y_j	Mass Fraction Of Component J In Vapour Phase
Y_e	Width Of The Reservoir
z_j	Mass Fraction Of Component J In The Mixture Of Liquid And Vapour

Greek Letters:

ϕ	undamaged porosity
μ	viscosity
M	mobility
ρ	density
β	inertia factor
Ψ	pseudo pressure
θ	Angle between two successive fractures
λ	pore size distribution index
∇	Laplace operator
σ	interfacial tension
v	velocity

Subscript

ave	average
bhp	bottom hole pressure
c	condensat
d	damage
dew	Dew point
Darcy	Darcy flow
e	External as in r_e.
eqphase	Equivalent phase
f	fracture
g	gas
h	thickness
HFW	Hydraulically fractured well
i	an index
j	an index
m	matrix
c	condensate
EOH	Equivalent open-hole system
x	x-direction
y	y-direction
well	refers to well-bore

Abbreviations

AD%	Absolute deviation (percentage)
AAD%	Average absolute deviation (percentage)
C1	Methane
n-C4	Normal butane
1-D	One dimensional
2-D	Two dimensional
3-D	Three dimensional
EOH	Equivalent open-hole
FVR	The ratio of injected fracture fluid to fracture volume
GTR	Gas total flo ratio
IFT	Interfacial tension
HFW	Hydraulically fractured well
IFT	Interfacial tension
ILRM	Linear with interaction response surface model
k_{rgtr}	Relative permeability ratio
LRM	Linear response surface model
OH	Open-hole
UFD	Unified Fracture Design
HWU	Heriot watt university
GPL	Gas production loss
IFT	Interfacial tension
λ_r	Relative mass mobility ratio
PDE	Partial differential equation
RSM	Response surface model
MLDO	Maximum liquid drop out
VW	Vertical well
CI	Coupling and Inertia effects

INTRODUCTION

Gas condensate reservoirs gained a wide interest and intensive research in the petroleum industry due to the challenges it poses in term of understanding their flow and phase behaviour. The negative impact of near-wellbore condensate banking, when the pressure drops below dew point, and the dependency of the gas and condensate relative permeability (k_r) on interfacial tension (IFT) (Bardon and Longeron 1980) and velocity (Danesh *et. al*, 1994, Henderson *et. al* 1995) are the main source of complexity in development, monitoring, and performance modelling of such reservoirs.

Condensate banking or blockage has a negative impact on well productivity due to the fact that it decreases fluid mobility in the near wellbore region and it causes a loss of valuable high quality liquid retrograde, which may not be recovered under natural depletion. In general, the severity of condensate blockage is a function of fluid and rock properties as well as the phase behaviour. Therefore, any attempt to mitigate the negative impact of condensate banking and improve well productivity in gas condensate systems should come through a full understanding of their complex phase and flow behaviours.

Hydraulic fracturing is a well proven technique to stimulate well productivity, especially in tight reservoirs. An accurate estimation of productivity of HFWs for gas condensate systems using a numerical simulator is a challenging task. This is mainly due to the fact that simulation of flow, in such geometry, requires fine grid to capture the abrupt variations of fluid and flow parameters around the wellbore. This can be cumbersome and impractical for field applications. The main body of this research work is devoted to present a fully integrated study about hydraulically fractured wells. That is, the following aspects were considered in this research, 1) - to review the available techniques for the estimation of the well productivity of single and multi-layer (HFWs) and to propose a practical methodology for flow calculations of such complex geometries in gas condensate reservoirs, 2) – to review the available techniques of fracture geometry optimization and to propose a general formula for gas condensate fracture optimization, 3) – to evaluate the impact of the pertinent parameters on HFWs clean-up efficiency, which is often considered as one of the main reasons for poor post-fracture performance.

Chapter 2 of this thesis, a brief description of the key elements of gas condensate reservoirs will be presented and linked to main body of author's research. The condensate blockage which is one of the main characteristics of such reservoirs will be discussed. Also, the dependency of the gas and condensate relative permeability (k_r) on IFT (Interfacial tension) and velocity will be discussed. Finally, the generalized k_r correlation (Jamiolahmady *et al.* 2009) used in this study to predict the combined impact of coupling (increase in k_r by an increase in velocity and/or decrease in IFT) and inertia (a decrease in k_r by an increase in velocity) will be also described in section 3.

Chapter 3 focuses on the single phase and two-phase (gas condensate) flow behaviour around single layer hydraulically fractured wells (HFWs). This chapter starts with the problem statement. Then, the single phase 2-D HFW in-house simulators which have been developed to simulate the flow of a single-phase (under Steady State and Pseudo-Steady State) around a HFW will be described next, a Finite element based Comsol mathematical package was used in this exercise. The details of governing equations and mathematical solution techniques will be presented in section 2. In section 3, the equivalent open-hole 1-D modelling concept (EOH) is presented. The required geometric skin for (EOH) under Darcy flow will be proposed in section 3.3.2. Also, an extension of the proposed geometric skin formulation to a more complex case (where two perpendicular fractures are intersecting a vertical well) will be presented in section 3.3.4. Finally, a verification of the proposed geometric skin will be given in this section.

The negative impact of inertia on well flow performance around HFWs is discussed in section 3.4. Here it will be shown that the concept of equivalent 1-D open-hole radial model can be applied for Non-Darcy flow, using a total skin factor which accounts for the combined impact of pertinent geometrical and flow parameters. Then, the total skin formulation based on effective dimensionless fracture conductivity, will be proposed. A newly developed 1-D in-house simulator will be presented here for efficient implementation of the proposed formulation which depends on velocity. Finally, the 1-D simulator will be verified for a large data bank of (Non-Darcy flow simulations) covering a wide range of flow and geometrical parameters.

In gas condensate reservoirs, the flow behaviour around HFWs is more complex due to the combined effects of coupling and inertia. Therefore, section 4 of this chapter is devoted to study two-phase flow of gas condensate around the HFWs under Steady State and Pseudo-Steady State conditions. A 2-D mathematical in-house simulator and

(EOH) 1-D two-phase compositional in-house simulators have been developed for this purpose. Here the proposed formulation for calculation of the effective wellbore radius for single phase non-Darcy flow is extended to two-phase flow of gas condensate. The validation of the proposed procedure and formulation will then be demonstrated over a wide range of variation of the pertinent parameters, which will highlight the added value of using the developed 1-D in house compositional simulator.

In Chapter 4, which is devoted to the study of flow behaviour around a multi-layer HFWs, starts with the problem statement. Similarly to the single layer HFWs study, first the structure of an in-house simulator developed to simulate the flow behaviour of single phase around a multi-layer HFW is presented. The results of the in-house simulator with those of a similar model constructed using ECLIPSE will be compared to demonstrate the integrity of the in-house model. Next, the proposed formulations for calculation of single phase Darcy flow geometric skin and single-phase non-Darcy flow total skin for such well geometries are presented. Also, an effective single phase inertial factor formulation for multi-layer system is presented, which is required in the total skin formula for Non-Darcy flow, to the best of author knowledge such formula is not available in the literature. Similarly to the approach proposed for HFWs in the previous chapter, the skin is converted into an effective wellbore radius, before being applied in the pseudo-pressure calculation of the equivalent open-hole system EOH.

Finally, the single-phase mathematical modelling approach has been extended to two-phase flow of gas and condensate by developing a 3-D two phase compositional in-house simulator as described in section 4 of this chapter. Here the governing equations, structure and solution method will be discussed. The results of two phase multi-layer HFW in-house simulator with those of the same multi-layer HFW model constructed using ECLIPSE-300 will be compared next. A 1-D in-house simulator for modelling two-phase flow of gas and condensate around multi-layer HFWs has also been proposed using an equivalent open-hole approach. A verification of this 1-D simulator results have been presented for a wide range of geometric and flow parameters.

In chapter 5 of this thesis, the subject of hydraulic fracture geometry optimization in gas condensate reservoir is discussed. In this chapter the Unified Fracture Design method is reviewed, and the limitation of such method is highlighted. Here, the author proposes a new and general optimum fracture design formulation, since the current UFD formula (Economides and Valko 2002) is only applicable for single phase Darcy flow under pseudo-steady state condition.

The newly developed formula is based on the effective proppant number concept, which properly accounts for the combined effect of coupling and inertia. Full derivation and governing equations of such formula is presented in sections 2 and 3 of this chapter for single phase gas and two phase gas condensate, respectively. Finally, the accuracy of the proposed formulae was verified, where different illustrations confirm their applicability.

Chapter 6 focuses on the study of the clean-up efficiency of hydraulically fractured wells in gas reservoirs. Here, the author embarked on a much needed extensive study, which evaluates the impact of pertinent parameters on HFWs clean-up efficiency, over a wide range of their variations using statistical tools.

First, the author identified the key pertinent parameters. Then, a two-level full factorial statistical experimental design method was used to sample a reasonably wide range of variation of pertinent parameters, covering many practical cases. The variation of a total of 12 parameters describing the matrix and fracture relative permeability of gas and fracture fluid, and matrix capillary pressure curve were studied for two separate fracture fluid volume values. More than (36,000) simulations were required for this purpose. Therefore, a computer code was developed using MATLAB mathematical package, to simplify the numerical process and automatically link different stages of the simulations conducted using (ECLIPSE, E-100). The structure of the computer code is explained in this chapter.

In these simulations, the gas production loss (GPL %), defined as a measure of un-clean fracture productivity deviation from the productivity of a fully (100%) clean fracture job, was also calculated automatically as an output data for each run, at different production periods. Then, two linear response surface methods, with and without interaction terms, were used to map the GPL variations with pertinent parameters.

The results of over 36,000 simulations were presented using Tornado Charts for the main linear terms. Also, Histogram Figures and FF Saturation Maps have been used to support the presented discussions and verify the drawn conclusions.

The results highlighted the scenarios where GPL can be significant or minimal at different production time intervals. Such results help in better understanding of the clean-up process and provide practical guidelines to successful hydraulic fracturing jobs.

Finally, the main conclusions of this thesis will be found in chapter 7. This chapter also includes some recommendations for further investigations of the research areas discussed in this work.

References

Bardon C. and Longeron D.G., Oct 1980: Influence of Very Low Interfacial Tension on Relative Permeability, SPEJ 20(3), 391-401.

Danesh A., Khazem M., Henderson G.D., Tehrani D.H. and Peden J.M., June 1994: As Condensate Recovery Studies, Proc. of DTI Oil Recovery and Research Dissemination Seminar London.

Henderson G.D., Danesh A., Tehrani D.H., Al-Shaidi, S. and Peden J.M., Oct 22-25 1995: Measurement and Correlation of Gas Condensate Relative Permeability by the Steady State Method, SPE paper presented at the 1995 SPE annual Technical Conference and Exhibition, Dallas, Texas, USA.

Jamiolahmady M., Sohrabi M., Ireland S., and Ghahri P., 2009: A Generalized Correlation for Predicting Gas-Condensate Relative Permeability at near the Wellbore Conditions, Journal of Petroleum Science and Engineering.

Economides, M., Oligney, R., and Valko, P.: Unified Fracture Design, Orsa Press, Alvin, Texas, USA, 2002.

CHAPTER 2
GAS CONDENSATE RESERVOIRS

Two phase flow of gas and condensate fluids in porous media is different from that of conventional Gas-Oil fluid systems. Such reservoirs are characterized by their complex phase and flow behaviours that significantly affect the well performance. The presence of retrograde fluid, when the pressure drops below dew point, and the dependency of the gas and condensate relative permeability (k_r) on the velocity and interfacial tension (IFT) makes gas condensate reservoir management a real challenge.

In this chapter the author will present a brief description of the key characteristics or elements of gas condensate reservoirs. Particularly, the author will address the following elements, 1) - Definition of a gas condensate fluid, 2) - Impact of condensate blockage, 3) - Gas condensate relative permeability dependency on velocity and interfacial tension (i.e. coupling and inertia), 4) - quantification of coupling and inertia effects. These elements, which are available in the work of Gas Condensate Research Group at Heriot Watt University (GCR-HW) and in the literature, will be discussed and related to the main body of the author's research.

2.1 Introduction

In general, gas condensate fluids are single phase at discovery time, where reservoir pressure is above the fluid dew-point pressure. However, in the case of isothermal reservoir depletion and once the pressure falls below the fluid dew-point pressure, a gas condensation process will take place in the reservoir where retrograde liquid (condensate) will appear in the system. This gas condensation process will continue, with decreasing pressure, and therefore condensate saturation will increase until it reaches a maximum value, called maximum liquid dropout MLDO, after which condensate saturation will decrease and a vaporization process may take place if depletion continues to a certain pressure in the fluid phase envelope.

Gas retrograde condensation (in reservoir conditions) is undesirable process due to two main reasons: (i) the condensate is a valuable heavy but high quality hydrocarbon components which may be lost in the reservoir during liquid dropout, or it may not be recovered under natural depletion. (ii) Its deposition in the reservoir causes a severe loss in well productivity due to the liquid accumulation around the wellbore region which significantly reduces gas mobility, this phenomenon is called condensate

blockage. The severity of condensate blockage is a function of both fluid and rock physical properties. That is, the amount of retrograde fluid depends on the reservoir pressure, temperature and the fluid composition (i.e. fluid richness). The reduction in productivity due to condensate blockage is also governed by the relative permeability dependency on interfacial tension and velocity as well as the formation flow capacity (*kh*). Furthermore, condensate blockage remediation techniques (e.g. hydraulic fracturing, chemical treatments, or gas cycling) add more unwanted operational costs which may reduce the profit margin if not well planned.

Therefore, controlling gas retrograde condensation is one of the most important operational issues in developing gas condensate reservoirs. That is, a good reservoir management and fields development of such systems certainly requires a comprehensive understanding of gas condensate phase and flow behaviors.

2.2 Gas Condensate Blockage

In a gas condensate producing well, when the bottom-hole pressure drops below dew-point, a condensate liquid phase will accumulate around the well. Next, the condensate bank will propagate away from the well bore as pressure drops below dew-point across the reservoir. This process will create two fluid regions. The first is a two-phase region, in the wellbore vicinity, where both gas and condensate coexist and flow toward the wellbore. While in the reservoir body, away from the wellbore, a second region contains a single-phase gas only. Many literature studies claimed that the condensate fluid in the near wellbore two-phase region will remain immobile in the rock pores unless its saturation is higher than the critical condensate saturation, at which it can flow. Very high critical condensate saturation was also reported, i.e. some of these studies claimed that condensate saturation as high as 50% is required for the condensate to become mobile (e.g. Gravier *et al.*1983). However, many experimental investigations performed by GCR-HW group, through performing different depletion tests on horizontally and vertically oriented cores as well as pore scale micro-models, demonstrated that the critical condensate saturation is close to zero; i.e. in most practical cases much smaller than the unrealistic high values that are usually assumed (e.g. Danesh *et. al* 1991 and Gas Condensate Recovery Final Report 1999-2002). These experimental studies (i.e. flow visualization micro-model experiments) also showed that condensate flow with gas through the pores as soon as it forms. However the condensate relative permeability is very small compared to that of the gas and therefore a major part of the formed condensate reside in the pores and keep accumulating until a steady state

condition is reached where the inflow toward any specific pore is equal to the outflow from it. Technically, in a reservoir scale, this means that the condensate will accumulate in the wellbore vicinity for a certain period of time until the moment where the two-phase region inflow equal to the well outflow. It should be noted that at this moment of time the near-wellbore condensate saturation is not a function of time and the total fluid composition across the drainage area will be constant and equal to that at the well-stream. Indeed, this is a very important piece of information as it helps in simplifying the numerical modeling of the well flow performance in gas condensate reservoirs. For instance, Whitson *et al.* (2003) introduced the concept of generalized pseudo-pressure calculations based on the fact that the thermodynamic flow equations are steady-state in nature around a producing gas condensate well. Actually, the time needed to reach steady state conditions mainly depends on the rock pore structure as well as the fluid characteristics.

2.3 GAS CONDENSATE RELATIVE PERMEABILITY

In the last twenty five years, many experiments on two phase flow of gas and condensate have been conducted both in micro-model pore and core scales within the GCR-HW Group. These Lab studies have been used to develop a large data bank of relative permeability measurements for a wide range of velocity and IFT values. These experiments were conducted under steady state conditions to mimic the flow environments in the near-wellbore region. The results clearly demonstrated the negative inertia and positive coupling effects on k_r measurements for different rock types and fluid characteristics.

The negative inertial effect within porous media, which refers to the reduction of relative permeability as velocity increases, is primarily a "result of the subsequent acceleration and deceleration of fluid through the tortuous pores, with variable cross section, which provides an extra energy loss" (Mahdiyar 2009). The positive coupling effect, which refers to the improvement of relative permeability as velocity increases and/or IFT decreases, has been proven mechanistically (using micro-model flow visualization) to be due to "the simultaneous coupled flow of the gas and condensate phases with the intermittent opening and closure of the gas passage by the condensate at the pore level" (Jamiolahmady *et al.* 2000, 2003).

Experimental work of GCR-HW (Gas Condensate Recovery Final Report 1999-2002) showed that for gas condensate relative permeability there is base values of velocity and interfacial tension, at which the relative permeability is independent of both. That is, the base velocity ($\boldsymbol{v}_{\mathbf{base}}$) is the minimum velocity value below which k_r is not a function of velocity and the base interfacial tension (IFT_{base}) is the IFT value above which k_r is not a function of interfacial tension. Relative permeability curve measured at the base conditions is called the base relative permeability curve. This curve is usually used to predict the improvement or reduction in k_r due to coupling or inertia. It was also shown that for cores with high condensate saturation increasing the velocity improves the gas relative permeability (coupling effect) while for low condensate saturation an increase in velocity will decrease the gas relative permeability (inertial effect). Figure 2.1 shows an example of some relative permeability measurements of a typical gas condensate system conducted at different velocities and a fixed value of IFT (IFT = 0.15 mN/m) (measured in GCR-HW Laboratory). In this figure gas relative permeability is presented as a function of velocity and condensate saturation. It can be seen from this figure that at low condensate saturation (e.g. Sc < 10%), gas relative permeability decrease as velocity increases (i.e. Inertia is dominant at such low condensate saturations). It can also be noticed that Inertia has its maximum effect when the flow is single phase, i.e. at zero condensate saturation. In the opposite direction, it can be noticed that as condensate saturation increase inertia become less effective and gas relative permeability start increasing as velocity increase (i.e. coupling is dominant at such high condensate saturation).

In fact, positive coupling and negative inertia are two interrelated forces which are always in competition to control well productivity. The resultant impact of this competition is a complex function of many parameters such as rock properties, fluid properties (e.g. density, viscosity, fluid richness, interfacial tension) and pore velocity. Generally speaking, it can be said that the coupling effect is more pronounced at low to moderate velocities, especially at higher condensate saturations, whilst inertial effect is dominant at high velocities and its effect is more intensive at lower condensate saturations.

Many empirical correlations have been developed to predict the dependency of relative permeability on velocity and IFT (positive coupling and negative inertia). Comprehensive details and comparisons of these empirical correlations are available elsewhere (Jamiolahmady et al. 2009). However, it should be mentioned that most of

the available k_r correlations in the literature are based on saturation. These saturation based correlations account for coupling and inertia effects separately. That is, the relative permeability of both gas and condensate are interpolated between a base curve (k_{rb}) and a miscible curve (k_{rm}) to account for coupling effects. Then, the interpolated gas and condensate relative permeability are corrected for the negative impact of inertia at high velocities using a separate formula which requires the measurement of two-phase inertial factor ($\beta_{two\text{-}phase}$), a rock property which is cumbersome and difficult to measure in the Lab. Furthermore, core specific constants, which are a function of rock pore structure, need to be measured in order to use saturation-based correlations, making their use a cumbersome and practically less attractive process, especially if someone wants to study the impact of coupling and inertia for a wide range of fluid and rock properties.

Accordingly, in this thesis the author used a generalized correlation developed by Jamiolahmady *et al.* (2009), which has been developed based on a large data bank of steady-state relative permeability measurements. The main advantages of this correlation compared to the aforementioned ones (i.e. saturation-based correlations) are as follow, 1) - it uses either universal parameters or those parameters that can be estimated from readily available petrophysical data, 2) - it accounts for the combined effect of coupling and inertia in one calculation step, i.e. it uses one formula to predict k_r that is affected by both coupling and inertial effects, 3) – it uses the single phase inertial factor, and therefore no need to measure two-phase inertial factor, 4) – it is based on relative permeability ratio rather than saturation, which is closely related to fluid fractional flow, (Jamiolahmady *et al.* 2009) stated that "in gas-condensate systems fractional flow is directly related to fluid composition and pressure at the steady-state conditions generally prevailing near the wellbore, hence, making it much more attractive practically compared to saturation, which depends on core characteristics".

References

Gravier, J.F., Lemouzy, P., Barroux, C. and Abed A.F., 1983: "Determination of Gas Condensate Relative Permeability on Whole Cores under Reservoir Conditions", SPE 11493-PA.

Danesh, A., Henderson, G.D. and Peden J.M., Aug. 1991: "Experimental investigation of critical condensate saturation and its dependence on connate saturation in water wet rocks", SPE 19695, SPE Journal of Reservoir Engineering, pp.336-342.

Whitson, C., Fevang, O., Aud, S.: "Gas Condensate Relative Permeability for Well Calculations", Transport in Porous Media **52**; 279-311, 2003.Jamiolahmady M., Danesh A., Tehrani D.H., Duncan D.B., 2000: "A Mechanistic Model of Gas Condensate Flow in Pores", Trans Porous Media 41(1), 17-46.

Jamiolahmady M., Danesh A, Henderson G.D. and Tehrani D.H., September 2003: "Variations of Gas Condensate Relative Permeability with Production Rate at Near Wellbore Conditions: A general Correlation", SPE 83960, presented at SPE offshore Europe Conference, Aberdeen, UK.

Gas Condensate Recovery Project (1999-2002) Final Report, 2002, IPE, Heriot Watt University, UK.

Jamiolahmady M., Sohrabi M., Ireland S. and Ghahri P., 2009: "A Generalized Correlation for Predicting Gas-Condensate Relative Permeability at near the Wellbore Conditions", Journal of Petroleum Science and Engineering.

Panteha Ghahri: "Modelling of Gas-Condensate Flow around Horizontal and Deviated wells and Cleanup Efficiency of Hydraulically Fractured Wells", PhD 2010, Heriot-Watt University.

Hojjat Mahdiyar: "Gas Condensate Flow aroundHydraulically Fractured / Perforated Wells", PhD 2009, Heriot-Watt University.

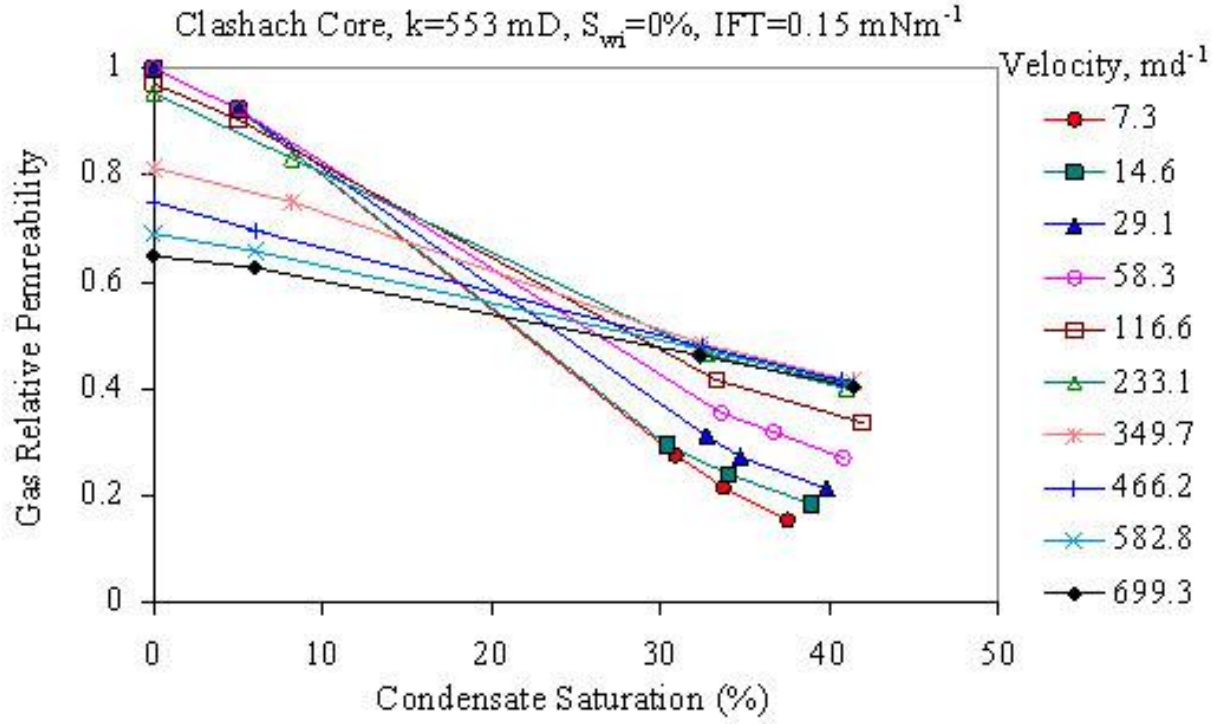

Figure 2.1: The velocity effect on the gas relative permeability, for Demonstration Purposes. (*From Final Report of Gas Condensate Research Group 1999-2002*).

CHAPTER 3
GAS CONDENSATE FLOW AROUND SINGLE LAYER HYDRAULICALLY FRACTURED WELLS

3.1 PROBLEM STATEMENT AND OBJECTIVES

Hydraulic fracturing is a well proven technique to stimulate wells and improve productivity. The main challenge on modelling hydraulically fractured wells is the fact it requires very fine gridding around the fracture due to the big contrast in rock properties between the fracture and matrix domains. Although, many guidelines on how to properly grid and model HFWs are available in the literature; yet it is not practical, if not technically infeasible, to apply these guidelines in full field simulation or to use them for large number of sensitivity studies.

Two phase flow of gas and condensate fluids in a porous medium is different from that of conventional Gas-Oil fluid system. Such reservoirs are characterized by their complex phase and flow behaviors that significantly affect the well performance. The presence of retrograde fluid, when the pressure drops below dew point, and the dependency of the gas and condensate relative permeability (k_r) on the velocity and interfacial tension (*IFT*) makes numerical modeling and performance prediction of gas condensate systems a real challenge. Having a complex wellbore geometry such as hydraulically fractured wells (HWF), add another level of complexity to modelling such reservoirs.

Therefore, there is a need to propose simple numerical methods for modelling gas condensate flow around hydraulically fracture wells.

Here the author proposes a new formula for estimation of an effective wellbore radius of an equivalent open-hole (EOH) radial 1-D system replicating flow around the 2-D HFW system. The proposed formulation is general, in the sense that if the total gas fractional flow (GTR) is unity, then it correctly converts to that suitable for single phase gas system under Non-Darcy flow conditions and when Reynolds number is small to that under Darcy flow conditions.

On the other hand, many published experimental studies and field observations argued that fracture propagation is a complex process, which should not always yield a single planer fracture. That is, these studies argued that vertical well might be intercepted by a finite number of induced vertical fractures rather than a single fracture, as a result of fracturing job.

Therefore, the author also considers extending the developed formula for the case of a vertical well intersected by two perpendicular vertical fractures, which accounts for more complex fracture configurations in both gas and gas condensate reservoirs.

3.1.1 Literature Review

In recent years, hydraulic fracture treatment has become a key element of field development and reservoir management protocols, especially for tight reservoirs. Indeed, it has gained a high interest in term of real field applications and research activities. Most of these research studies were primarily aimed at the prediction of improvement in well performance due to hydraulic fracture treatment. The results of these studies are in the form of either charts or correlations to calculate the effective wellbore radius based on a 1-D equivalent open hole system (EOH) that replicate the flow performance of the actual 2-D system.

McGuire and Sikora (1960) studied the effect of finite-conductivity vertical fractures on the productivity of vertical wells. They presented different sets of charts which demonstrate the productivity increase gained from hydraulic fracturing as a function of fracture penetration ratio and fracture conductivity.

Prats (1961) presented an analytical model for the pseudo-steady state behaviour of finite-conductivity vertical fractures. Prats introduced, for the first time, the concept of effective wellbore radius and the fact that there is an optimum fracture design, length-to-width ratio, for a given fracture volume that maximizes productivity. He also showed that for infinite conductivity fractures, the effective wellbore radius is equal to a quarter of the whole fracture length.

Raghavan *et al.* (1978) illustrated the effect of fracture penetration ratio on the effective wellbore radius. In this paper he presented a mathematical model based on constant pressure external boundary conditions for uniform flux and infinite conductivity fractures. The main outcome of this study is the fact that the performance of HFWs with infinite conductivity depends on the boundary conditions, if the fracture penetration ratio is greater than 0.2.

Meyer and Jacot (2005) presented a new semi-analytical solution for a finite conductivity vertical fracture under pseudo-steady state condition based on resistivity domains concept. They presented a new Darcy flow fracture pseudo-skin formulation and validated it with those available in the literature. They also improved Gringarten's (1974) dimensionless productivity index for infinite conductivity vertical fractures in rectangular closed reservoirs.

Up to this point, all aforementioned studies were for Darcy flow. However, the importance of the inertial effect (Non-Darcy Flow) on HFW productivity has also been the subject of some literature studies.

Holditch and Morse (1976) were among the first to numerically analyse the effect of Non-Darcy flow on the behaviour of hydraulically fractured gas wells. They showed that inertial effects inside the fracture could exist for a wide range of formation properties and it could significantly reduce the fracture conductivity. Therefore, it should be considered in the analysis of well- testing and history matching of HFWs in gas reservoirs.

Guppy *et al.* (1982) provided a method to analyse the pressure response of constant rate HFWs with finite conductivity, under Non-Darcy flow conditions. They showed how inertial effect can reduce the absolute fracture conductivity and they also developed a correlation to correct the dimensionless fracture conductivity for the effect of inertia.

Gidley (1991) proposed an approximation to correct the dimensionless fracture conductivity for non-Darcy flow effects, similar to that presented by Guppy (1982).

Settari *et al.* (2002) presented different simulations of a hydraulically fractured well at pseudo-steady state conditions, in order to propose a correlation to estimate Non-Darcy flow skin. They compared the results of their simulations with Guppy's correlation, demonstrating that Guppy's equation overestimates the non-Darcy effect.

Gas condensate flow around HFWs has also been the focus of some recent studies.

Actually, well productivity assessment and numerical modeling of gas condensate reservoir, when the pressure fall below due point, has been considered as a real challenge by reservoir engineers due to the complex phase and flow behavior that a gas condensate well exhibit during its life cycle. Furthermore, the dependency of gas condensate relative permeability (k_r) on the velocity and interfacial tension (IFT) complicates the well performance modeling of such reservoirs. Having a complex wellbore geometry such as hydraulically fractured wells (HWF), add another level of complexity to modeling such reservoirs.

Several studies on productivity estimation or fracture optimization of gas condensate reservoirs, such as Wang *et al.* (2000), Indriati *et al.* (2002), Mohan *et al.* (2006), have considered gas condensate flow around the fracture to behave like single-phase flow with a damaged matrix zone, which has a reduced permeability of (kk_{rg}) and a thickness equal to that of the two-phase region around the fracture. However such unrealistic assumption can lead to erroneous results in term of HFW productivity as well as fracture design optimization, which will be shown later in this thesis.

Carajaval et al. (2005) numerically simulated a HFW in a square closed boundary gas condensate reservoir using ECLIPSE simulator. He showed that a Cartesian grid system better captures the impact of velocity in both single-phase flow of gas affected by inertia and two phase flow of gas and condensate affected by coupling and inertia. He also concluded that coupling affects are dominant within the matrix whilst inertial affects are dominant inside the fracture. Later, Mahdiyar et al. (2008) developed an effective wellbore radius formulation for gas condensate systems by extending the Guppy's single phase correlation to two-phase using effective, instead of absolute, fracture conductivity which includes coupling and inertia effects.

All existing correlations cited above assume that vertical fracture is a single planner, which is uniform in conductivity. Although, the author agrees that this simplification is valid for many practical cases. However, it is not representative of all hydraulic fracture propagation scenarios. As a matter of fact, many published experimental studies and field observations confirm that fracture propagation is a complex process, which should not always yield a single planner fracture.

Germanovich *et al.* (1997) presented observations on fractured cores, experimental analysis, and geological evidences, which suggested that hydraulic fractures are not single and symmetric planar in the rock. Instead they are irregular in shape and multiple in number either in the near-wellbore or in the far field region.

Choo *et al.* (1987), Freddy *et al.* (2001), and Restrepo *et al.* (2009) studied the transient pressure behaviour around a multiple vertical fractured well (MHFW) with different number of fractures. The main conclusions of these studies were that for infinite dimensionless fracture conductivity the pressure response of MHFW is similar to that of single hydraulically fractured well having the same conductivity. Also, for finite dimensionless fracture conductivity the pressure response of MHFW behaves like that of a well with equivalent single fracture of an average or equivalent conductivity ($CF_{D\text{-}eq}$). However, they have not presented any specific criteria on how to calculate this average or equivalent fracture conductivity.

As mentioned earlier, here the author proposes a new formula for estimation of an effective wellbore radius of an equivalent open-hole (EOH) radial 1-D system replicating flow around the 2-D HFW which is intercepted by single or multiple fractures. In order to achieve these objectives and cover reasonable variation range of pertinent parameters and their impact on both single fracture and multiple fracture wells and verify the integrity of the proposed approaches, a large bank of data is needed.

Accordingly, the author has developed in-house simulators for single and two-phase gas condensate flow, which are also described in this chapter.

3.2 In-House Mathematical Single Phase Simulators

3.2.1 In-House Mathematical Single Phase Steady-State HFW Model, Darcy and Non-Darcy Flow

The main aim of the present study is to develop a 2-D simulator that can be used to create a large bank of data for HFWs with different fracture geometries (i.e. different fracture lengths and widths) in a reservoir with different dimensions.

The 2-D system considered in here consists of a HFW with fracture width w_f and length of x_f, as shown in Figure 3.1. This homogenous isotropic porous medium has an absolute permeability k_m and formation thickness of h_m.

Because of the existing symmetry only a quarter of the HFW model has been considered in this study. This saves the computation time and reduces the meshing requirments as well as the required CPU memory.

The main assumptions used in this in-house simulator are as follow:

1. The fracture and matrix are two different porous media but each one is a uniform and homogenous porous medium.
2. The width of the fracture is constant.
3. The fracture has penetrated the well symmetrically in both directions along the X-axis.
4. Wellbore flow directly from the matrix is negligible, compared to that from the fracture to the well.
5. The fracture has penetrated vertically through the whole height of matrix.
6. Gravity force is neglected in this 2-D system.

2-D simulator Governing Equations

The mathematical derivations and equations employed in this part of the study, are the same as those described for gas condensate flow in a perforated region and around deviated wells (Jamiolahmady et al. 2006 and Ghahri 2010, both studies conducted in GCR-HWU group, Gas Condensate Recovery Final Report 2005-2008 and 2008-2011). These equations and their derivations are as follow:

1) The continuity equation for a compressible fluid at steady-state conditions

$$\nabla.(\rho v) = 0. \tag{3.1}$$

2) The 2-D form of the Forchheimer equation is:

$$\nabla P = \frac{\mu}{k} V + \beta\rho|V|V \,. \tag{3.2}$$

$$\nabla P = \left(\frac{\mu}{k} + \beta\rho|V|\right) \times V$$

$$\frac{k}{\mu}\nabla P = \left(1 + \frac{k\beta\rho|V|}{\mu}\right) \times V \tag{3.2a}$$

$$V = \frac{k}{\mu}\left(\frac{\nabla P}{1 + \frac{k\beta\rho|V|}{\mu}}\right) \tag{3.3}$$

Where |V| is the absolute value of the velocity vector, which can be related to pressure gradient by solving the second-order polynomial Equation 3.2 for |V| as

$$|V| = \left[\frac{-1 + \sqrt{1 + 4\beta\rho\left(\frac{k}{\mu}\right)^2 |\nabla P|}}{2\left[\frac{\beta\rho k}{\mu}\right]}\right] \tag{3.4}$$

The negative root for the second-order polynomial is discarded because |V| cannot be negative. Substituting Equation 3.4 into Equation 3.1 gives the final form of continuity equation which includes Non-Darcy effects:

$$\nabla.\left[2\left[\frac{k}{\mu}\right].\frac{\rho\nabla P}{1 + \sqrt{1 + 4\beta\rho\left(\frac{k}{\mu}\right)^2 |\nabla P|}}\right] = 0 \,. \tag{3.5}$$

It should be noted that in the case of Darcy flow and at low velocities, the second term in the square root term of the denominator is minimal. In the model, a flag can deactivate this term ensuring a pure Darcy flow calculations when needed.

Also, to avoid dimensional inconsistency, all the parameters in the equations presented here and implemented in the in-house simulator are in consistent (SI) units.

Mathematical Solution Technique

The governing non-linear partial differential equation (PDE), Equation 3.5, is solved using Comsol multi-physic software (version 3.4a, 2007), which uses the finite element method. The main dependent variable in this equation is P (pressure).

The boundary conditions applied are:

1) The pressure at outer boundary (external radius, P_{ext}) is known,
2) The pressure at the inner boundary (wellbore radius, P_{well}) is known.

Mesh Quality

The mesh quality plays a very important rule in the numerical accuracy of finite element simulators (such as Comsol Multi-physics). Generally speaking, it is expected that numerical models with mesh quality higher than 0.3, should relatively yield accurate results (Ghahri 2010). Therefore, the author made considerable attempts to generate consistent and high quality mesh files for different 2-D HFW geometries. That is, in order to capture the complexity of flow behaviour around the HFW accurately, the 2-D system was divided into two regions, 1) the inner region, which starts from wellbore and expands inside the fracture until it reaches the fracture tip, 2) the second region starts from the outer boundary of the first region and ends at the outer dimension of the reservoir model.

Figure 3.1 displays the mesh quality for one of the geometries defined in this study. As can be seen, the majority of the elements have a mesh quality of more than 0.8. Also, the minimum mesh quality is higher than 0.6, which ensures the accuracy of the results under different conditions. Finally, it should be stated that the acceptable mesh quality criteria (i.e. mesh quality > 0.6) were honoured for all constructed geometries in this study.

3.2.2 ECLIPSE Single Phase Steady-State HFW Model

In order to confirm the integrity of the in-house single phase mathematical simulator, a single HFW model was constructed using the fine grid option of ECLIPSE E100.

The core properties of Texas Cream (Table 3.1) with porosity 0.21 and permeability 9.1 mD were used to describe the reservoir in this model. The single phase gas properties are those listed in Table 3.1a. The reservoir was 200 m in the X and 200 m in Y directions and 10 m in the Z direction. The fracture has a length of 40 m and a width

of 5mm. the fracture has a permeability of 146 D. The reservoir pressure was 1100 Psi and the HFW was producing under a controlled bottom-hole pressure of 1000 Psi. Fine grids were used to capture the flow complexity near the wellbore.

Sixty injection wells were located in the boundary of the reservoir to make the reservoir pressure at the drainage boundary constant (P_{ext} = 1100 Psi). The results of the in-house mathematical simulator were compared with those of similar simulations conducted using ECLIPSE simulator E100. Figure 3.2 shows the good agreement between the two results. The arithmetic average absolute percentage of deviations (AAD%) of the predicted mass flow rates values by the ECLIPSE simulator compared to those estimated by the HFW in-house simulator was 0.73 % for the simulation with a constant pressure drop (ΔP) of 100 psi maintained over the drainage area. Also, the same exercise was repeated using different fracture permeability (14.6 and 1.46D), and the same level of accuracy has been achieved (AAD < 1.25%).

3.2.3 Mathematical Single Phase Pseudo Steady State HFW Model, Darcy and Non-Darcy Flow

When a new or existing well start production following a new completion or shut-in period, the reservoir goes through a transient flow period where the pressure derivative is changing with time. However for a closed boundary reservoir, i.e. there is no flow across the exterior boundaries, a transient flow is transformed to pseudo steady state (PSS) flow after a certain time of production. At PSS conditions, the derivate of pressure with time throughout the whole drainage area remains constant, i.e. $\frac{\partial P}{\partial t} = cons.$

Here the 2-D HFW geometries, which were developed to study the flow behaviour at steady state conditions, were used for this section. However, the governing equations are those for pseudo-steady state conditions, as described below.

2-D Simulator Governing Equations

The mathematical derivations and equations employed in this part of the study, are the same as those presented by GCR-HWU group to study gas condensate flow around deviated wells (Ghahri 2010 and Gas Condensate Recovery Final Report 2008-2011), these equations and their mathematical derivations are as follow:

1) The continuity equation for a compressible fluid:

$$\nabla.(\rho v) = \frac{\partial(\rho\varphi)}{\partial t}. \qquad (3.6)$$

in which ρ and φ are fluid density and rock porosity.

2) The flow equation is the Forchheimer equation:

$$\nabla P = \frac{\mu}{k} v + \beta \rho |v| v . \tag{3.7}$$

Combining the continuity and 2-D form of the Forchheimer equation, after some mathematical manipulation, gives:

$$\nabla . \left[2 \left[\frac{k}{\mu} \right] . \frac{\rho \nabla P}{1 + \sqrt{1 + 4\beta \left(\frac{k}{\mu} \right)^2 |\nabla P|}} \right] = \frac{\partial (\rho \varphi)}{\partial t}, \tag{3.8}$$

Rearranging the right hand side of Equation 3.8, using the chain rule of differentiation gives:

$$\frac{\partial (\rho \phi)}{\partial t} = \frac{\partial (\rho \phi)}{\partial p} \times \frac{\partial p}{\partial t}, \tag{3.9}$$

Substituting Equation 3.9 back into Equation 3.8 gives:

$$\nabla . \left[2 \left[\frac{k}{\mu} \right] . \frac{\rho \nabla P}{1 + \sqrt{1 + 4\beta \left(\frac{k}{\mu} \right)^2 |\nabla P|}} \right] = \frac{\partial (\rho \phi)}{\partial p} \times \frac{\partial p}{\partial t}, \tag{3.10}$$

Where, the term $\frac{\partial (\rho \phi)}{\partial p}$ can be expanded to:

$$\frac{\partial (\rho \phi)}{\partial p} = \rho \times \frac{\partial \phi}{\partial p} + \phi \times \frac{\partial \rho}{\partial p} = \rho \phi \left(\frac{1}{\phi} \frac{\partial \phi}{\partial p} + \frac{1}{\rho} \frac{\partial \rho}{\partial p} \right), \tag{3.11}$$

The term $\left(\frac{1}{\phi} \frac{\partial \phi}{\partial p} + \frac{1}{\rho} \frac{\partial \rho}{\partial p} \right)$ on the right hand side of Equation 3.11 can be considered as a total compressibility, c_t , hence Equation 3.11 becomes as follows:

$$\frac{\partial (\rho \phi)}{\partial p} = \rho \times \phi \times c_t , \tag{3.12}$$

Substituting Equation 3.12 into Equation 3.10 gives:

$$\nabla . \left[2 \left[\frac{k}{\mu} \right] . \frac{\rho \nabla P}{1 + \sqrt{1 + 4\beta \left(\frac{k}{\mu} \right)^2 |\nabla P|}} \right] = \rho \times \phi \times c_t \times \frac{\partial p}{\partial t} \tag{3.13}$$

As pointed out earlier, for PSS conditions, the pressure derivative with time across the reservoir is constant. As shown below:

$$\frac{\partial P}{\partial t} = \frac{\partial \overline{P}}{\partial t} = cons. \tag{3.14}$$

$\overline{p}$ is the volumetric average pressure defined by:

$$\overline{p} = \frac{\int p dV}{V} \tag{3.15}$$

Where, V and p are the pore volume and pressure, respectively.

The compressibility, c_t , is defined in term of volume by Equation 3.16 .

$$c_t = \frac{-1}{V}\frac{\partial V}{\partial p} \tag{3.16}$$

For PSS conditions, producing with a total constant flow rate, one can write:

$$c_t \times V \times \partial p = \partial V \tag{3.17}$$

Differentiating the above Equation to time results in the following equation:

$$c_t \times V \times \frac{\partial p}{\partial t} = \frac{\partial V}{\partial t} \tag{3.18}$$

One can also write:

$$\frac{\partial V}{\partial t} = q_{well} . \tag{3.19}$$

Substituting Equation 3.19 into Equation 3.18, the pressure derivative to time can be related to q_{well} as follows:

$$\frac{\partial p}{\partial t} = \frac{q_{well}}{c_t V} \tag{3.20}$$

Note that V is the pore volume defined by Equation 3.21.

$$V = \phi \times V_t \tag{3.21}$$

Combining Equation 3.21 and 3.20 and substituting this in Equation 3.13 results in the following equation:

$$\nabla . \left[2\left[\frac{k}{\mu}\right] . \frac{\rho \nabla P}{1 + \sqrt{1 + 4\beta\left(\frac{k}{\mu}\right)^2 |\nabla P|}} \right] = \frac{\rho_{well} q_{well}}{V_t} . \tag{3.22}$$

Mathematical Solution Technique

The governing non-linear partial differential equation (PDE), Equation 3.22, is solved using Comsol multi-physic software (Version 3.4a, 2007), where the main dependent variable in this equation is P (pressure).

The boundary conditions applied to this system are:

1) At the outer boundary (external radius) there are no flow:

$$\frac{\partial P}{\partial x} = 0 , \qquad (3.23)$$

$$\frac{\partial P}{\partial y} = 0 ,$$

2) The flow rate at the inner boundary (wellbore radius, q_{well}) is known.

3.2.4 ECLIPSE Single-Phase Pseudo Steady State HFW Model

The accuracy of the pseudo steady state HFW in-house simulator was confirmed by comparing its results with those of a similar model constructed using ECLIPSE. The core properties of Texas Cream, with porosity 0.21 and permeability 9.1 mD, were used to describe the reservoir in this model. The reservoir is 200 m in the X and 200 m in Y directions and 10 m in the Z direction. The fracture has a length of 40 m and a width of 5 mm. the fracture has a permeability of 146 D. The initial reservoir pressure is 1100 Psi.

In ECLIPSE simulations, to simulate pseudo steady state condition, the inflow at the outer boundary of the steady state model described in Section 3.2.2 was set to zero. The flow rate at the wellbore was kept constant during production time. The volumetric average pressure derivative with time was monitored and when it stabilised, Equation 3.14, it was concluded that the pseudo steady state conditions had been achieved; then the wellbore pressure and the volumetric average reservoir pressure are recorded.

Using the in-house simulator, for each time step, the same wellbore pressure as that of Eclipse simulator was used, and then the volumetric average reservoir pressure, Equation 3.15, was calculated.

The average pressures calculated by the in-house mathematical simulator were compared with those of similar simulations conducted using the ECLIPSE simulator. Figure 3.3 shows the good agreement between the two results. The arithmetic average absolute percentage deviation (AAD %) of the predicted P_{avg} values by the ECLIPSE simulator compared to those estimated by the HW simulator was 1.8 %.

3.3 Single Phase Darcy Flow

3.3.1 Equivalent Open-Hole 1-D Modelling Concept

Complex wellbore geometries such as HFWs are usually difficult and cumbersome to model in the sense that they require fine grid simulation around the wellbore in order to capture any abrupt changes in flow. Furthermore, in gas condensate flow the problem gets more complicated due to the fact that compositional simulations should be used, which are usually associated with numerical stability issues. Therefore, there is a need to propose and develop simple but reliable ways of modelling such complicated problem. One of these simple ways of modelling is the equivalent open-hole concept (EOH).

(EOH) modelling is a concept in which complex wellbore geometries (e.g. HFWs) are transferred to an equivalent open-hole vertical well using a skin factor or effective wellbore radius. In case of Darcy flow (Non-Damaged well), this skin should represents the difference in geometries between (2-D or even 3-D) complex wellbore geometry and its equivalent open hole vertical well. This skin is called "geometric skin" since it represents wellbore geometry effects. Therefore, using this skin we can define an equivalent open hole vertical well with an effective wellbore radius that should give the same performance as that of a complex wellbore geometry.

Nonetheless, it should be mentioned that in the case of single phase Non-Darcy flow or two phase gas condensate flow, the previous mentioned skin will not be a function of geometry only, instead, it is a function of both geometry and flow parameters. Both types of skin will be discussed in details for different (HFW geometries) throughout this thesis.

In summary, the main aim of the forthcoming sections is to propose a skin or effective wellbore radius formulations for different HFW geometries under single phase (Darcy and Non-Darcy) and two phase (gas condensate) flow.

3.3.2 Geometric Skin of Single Fracture Intercepting Vertical Well

For steady state single phase flow the productivity of vertical well (VW) can be expressed as follows.

$$q_{VW} = \frac{2\pi kh(P_e - P_{well})}{\mu\left(\ln\left(\frac{r_e}{r_w}\right) + S_t\right)} \tag{3.24}$$

Where, P_e and P_{well} are the external and wellbore pressure, respectively.

S_t is the total skin, which includes the damage skin (S_d), geometry skin (S_g), and flow skin (S_f). as shown below,

$$S_t = S_d + S_g + S_f \tag{3.25}$$

For a vertical well under Darcy flow, both geometry and flow skins are zero. Also, throughout this thesis damage skin is always considered as zero, unless otherwise stated.

Based on that, the Darcy flow productivity of HFW can be expressed in term of the productivity of vertical well with a fracture geometric skin factor (S_{gf}), as shown below.

$$q_{HFW} = \frac{2\pi kh\Delta P}{\mu\left(\ln\left(\frac{r_e}{r_w + x_f}\right) + S_{gf}\right)} \tag{3.26}$$

Because the wellbore radius r_w can be neglected compared to the fracture length x_f, then Equation 3.26 can be written as:

$$q_{HFW} = \frac{2\pi kh\Delta P}{\mu\left(\ln\left(\frac{r_e}{x_f}\right) + S_{gf}\right)} \tag{3.27}$$

r_e is the exterior radius of the reservoir model, which for a square drainage area can be calculated as follows:

$$r_e = \frac{X_{res}}{\sqrt{\pi}}. \tag{3.28}$$

In Equation 3.27 S_{gf} is the fracture geometric skin (also known in some of the literature studies as Pseudo-Fracture skin, ***f***).

The final form of Equation 3.27 can be written in term of EOH with effective wellbore radius ($r_w^{'}$) as follow,

$$q_{HFW} = \frac{2\pi kh\Delta P}{\mu\left(\ln\left(\frac{r_e}{r_w^{'}}\right)\right)} \tag{3.29}$$

$$r_w^{'} = x_f \times e^{-S_{gf}} \tag{3.30}$$

In order to solve this EOH productivity equation, a geometric skin formulation (S_{gf}) is needed.

Accordingly, the important pertinent parameters which influence the pressure behaviour and productivity performance of vertical well intercepted by a single fracture will be discussed. Then formulation geometrical skin will be proposed and its verification for single phase Darcy flow under both Steady and Pseudo-Steady state conditions will be presented.

Dimensionless fracture conductivity (C_{FD}) is one of the most important parameters which have significant impact on HFW performance. (C_{FD}) is the product of (fracture to matrix) permeability ratio and fracture width to fracture length ratio. For a fracture which penetrating the whole height of matrix (C_{FD}) can be defined as below,

$$C_{FD} = \left(\frac{k_f}{k_m}\right) \cdot \left(\frac{w_f}{x_f}\right). \tag{3.31}$$

Where, (k_f, k_m, w_f, x_f) are the fracture permeability, fracture width, and fracture half-length respectively. It should be noted that if the fracture is not completely penetrating the matrix height then the previous form of (C_{FD}) should be multiplied by the ratio of fracture to matrix height (h_f /h_t).

Technically speaking, (C_{FD}) is a combination of flow and geometrical parameters, which makes it a general and useful tool to analyze the performance of HFWs under different conditions (single phase Darcy/Non-Darcy and two phase flow), as will be shown throughout this thesis. Actually, C_{FD} is a measure of the ability of fracture to pass on the fluid to the wellbore to that of the matrix to pass on the fluid to the fracture. In a qualitative nature, it can be said that the higher the dimensionless fracture conductivity the better is the HFW performance.

However, having (C_{FD}) alone will not be helpful in quantifying how good is the HFW performance, unless it is combined with the relative size of the fracture to that of the drainage area under consideration. Accordingly, many studies in the literature used the term called penetration ratio (I_x) in order to present the relative size of the fracture, (I_x) is defined as the ratio of fracture length to reservoir drainage length, as shown below.

$$I_x = \left(\frac{x_f}{x_e}\right). \tag{3.32}$$

The impact of these two dimensionless parameters on HFW performance will be discussed next.

Figures 3.4 to 3.7 shows the pressure profile around a HFW with different dimensionless fracture conductivity (C_{FD} = 240, 24, 2.4, and 0.24, respectively). Detailed description of this example dimensions and rock properties can be found in

Table 3.2, HFW-1 data set. It can be seen that for the highest fracture conductivity case (Figure 3.4), the pressure streamlines around the fracture are elliptical in shape; however they tend to become circular as their position (away) from the fracture increase. Also, as the fracture conductivity decrease (Figures 3.5, 3.6, and 3.7) the pressure streamlines around the fracture tend to change shape from elliptical to radial. That is, in Figure 3.5 where the fracture conductivity equal to 24 (C_{FD} = 24), the pressure line were almost elliptical. However, in Figure 3.7 where the fracture conductivity has been reduced to 0.24 (C_{FD} = 0.24), the pressure lines around the fracture were completely radial. This means that as fracture conductivity decrease then the flow around HFW become similar to that of vertical well (i.e. radial flow).

In this study three new dimensionless parameters have been introduced in order to have a better understanding of the dimensionless fracture conductivity impact on HFW performance. These three parameters are the dimensionless pressure drop inside the fracture (P_{dp}), the dimensionless velocity inside the fracture (v_d), and the dimensionless fracture length (x_{fd}). The definitions of these parameters are as follow,

a. The dimensionless pressure drop inside the fracture is the ratio of the local pressure drop (pressure at the external radius minus local pressure value) at any point inside the fracture to the total pressure drop of the system (pressure at the external radius minus wellbore pressure).
b. The dimensionless velocity inside the fracture is the ratio of local velocity at any point inside the fracture to the wellbore velocity.
c. The dimensionless fracture length is the ratio of the length at any point inside the fracture to the total fracture length.

The mathematical expressions of these parameters are shown as below,

$$P_{dp} = \left(\frac{P_{res} - P_x}{P_{res} - P_{well}} \right). \tag{3.33a}$$

$$v_d = \left(\frac{v_x}{v_{well}} \right). \tag{3.33b}$$

$$x_{fd} = \left(\frac{x}{x_f} \right). \tag{3.33c}$$

Figure 3.8 shows the dimensionless pressure drop inside the fracture (P_{dp}) versus the dimensionless fracture length (x_{fd}) for different fracture conductivity, HFW-1 data set. It can be seen from this figure that for high fracture conductivity, the dimensionless

pressure drop curve across the fracture is a straight line which has a constant value of 1 (P_{dp} =1). That is, the difference between (P_{dp}) at wellbore and that at any point inside the fracture is almost negligible, which means that the pressure at the fracture tip is almost the same as that at the wellbore. Or in other words, the pressure drop inside the fracture is negligible (this case refers to what is called infinite conductivity fracture). Also, it can be seen from Figure 3.8 that as fracture conductivity decrease the difference between (P_{dp}) at wellbore and that at any point inside the fracture increase. For instance, in case of (C_{FD} =24) the difference between (P_{dp}) at the wellbore and that at the fracture tip is (0.1), that is the pressure drop at the fracture tip is (90%) of that at the wellbore (i.e. low pressure drop inside the fracture). While, in case of (C_{FD} = 0.24) the difference between (P_{dp}) at the wellbore and that at the fracture tip is (0.75), that is the pressure drop at the fracture tip is (25%) of that at the wellbore (i.e. high pressure drop inside the fracture). It should be mentioned that fractures with high (C_{FD}) and low (but not negligible) pressure drop are called (uniform flux fractures). Therefore, fractures with high (C_{FD}) are preferable because they have less resistance to flow and thus more benefit in term of well productivity. However, in reality there is a limit to the maximum possible achievable productivity and as a result there is a limit to maximum or optimum fracture conductivity, this subject will be discussed in details in chapter 5 of this thesis.

Figure 3.9 shows the dimensionless velocity profile inside the fracture versus dimensionless fracture length, for the same model shown in Figure 3.8.

It can be seen from this figure that the shape of velocity profile inside the fracture is a function of fracture conductivity. That is, for high fracture conductivity (C_{FD} = 240 and 24 curves in this figure), the dimensionless velocity is almost uniform across fracture length, albeit increasing toward the wellbore where it reaches its maximum. In other words, for high fracture conductivities the dimensionless velocity is almost directly proportional to (1-x_d).

As fracture conductivity decrease (C_{FD} = 2.4 and 0.24 curves), it can be noticed that the dimensionless velocity value is low and the profile corresponding to the farthest portion of the fracture is almost straight line (minimal variation), especially in the case of C_{FD} = 0.24. However, the dimensionless velocity profile in these two low C_{FD}'s increase steeply in the portion near to the wellbore. Therefore, it can be said that for low fracture conductivities most of the flow inside the fracture comes from the area near to the wellbore and the contribution from the farthest portion of the fracture is minimal. These observations are consistent with the work of Cinco-Ley (1987).

In conclusion, it can be said that the flow around the fracture is elliptical for high fracture conductivities, however, it turns to radial (similar to that around boundary dominated vertical well) as fracture conductivity decrease. The pressure drop inside the fracture decrease as fracture conductivity increase. Flow velocity across the fracture is uniform and directly proportional to dimensionless distance for high C_{FD} while as fracture conductivity decreases its value decrease significantly in the farthest part of the fracture, however, it increases steeply in the area near to the wellbore.

Figure 3.10 shows the geometric skin as a function of dimensionless fracture conductivity (C_{FD}) and penetration ratio (I_x) for the HFW-2 data set listed in Table 3.2. In this figure three C_{FD} values have been used (C_{FD} = 1, 10, 1000), at each C_{FD} value the geometric skin S_{gf} has been obtained (using the developed steady-state in house simulator) for different I_x ($0.05<I_x<0.98$). It can be seen from this figure that for the infinite conductivity fracture (C_{FD} =1000) S_{gf} is decreasing as penetration ratio increase, however the change in S_{gf} is minimal for penetration ratio less than 0.2 ($I_x < 0.2$) compared to that of higher I_x. The same trend has been observed for (C_{FD} =10) albeit to a lesser extent. However, for low fracture conductivity (C_{FD} =1), it can be noticed that the change in S_{gf} with respect to I_x is almost minimal.

In Figure 3.11 the same exercise has been repeated using the developed pseudo-steady state in house simulator. It can be seen from this figure that the behaviour is the same as that seen in steady state conditions but the direction of trend is different. That is, for high dimensionless fracture conductivity C_{FD} 1000 and 10, S_{gf} is increasing as penetration ratio increase, however the change in S_{gf} is minimal for penetration ratio less than 0.2 ($I_x < 0.2$) compared to that of higher I_x. For low fracture conductivity (C_{FD} =1), it can be noticed that the change in S_{gf} with respect to I_x is minimal.

In summary, it can be concluded from these two Figures that (for Both SS and PSS) S_{gf} increase as fracture conductivity decrease for a fixed penetration ratio value. Furthermore, for fixed fracture conductivity value, at SS conditions S_{gf} decrease as penetration ratio increase, while at PSS conditions S_{gf} increase as penetration ratio increase.

Figure 3.12 shows the geometric skin of (SS and PSS) for (C_{FD} = 1 and 1000). From this figure it can be stated that, when penetration ratio is less than 0.2 the geometric skin of both boundary condition (SS and PSS) is almost the same, and therefore the effective wellbore radius for both systems should be the same.

However, for (I_X > 0.2) the results are different. It is also noticed that with decreasing fracture conductivity the difference in geometric skin between SS and PSS is decreased. These results are consistent with those found in the literature (Ravaghan et al. 1978) Accordingly, it can be concluded that C_{FD} and I_x are the dominant pertinent parameters, which controls pressure behaviour and productivity performance of HFWs. In coming sections it will be shown how C_{FD} and I_x can be used to propose a simple and reliable HFW numerical modelling approach.

Many studies have focused on development of a formulation to calculate fracture geometry skin. All available (S_{gf}) formulae have used the dimensionless fracture conductivity (C_{FD}) as the main parameter. This is not surprising, as the significant impact that C_{FD} has on HFW performance has been shown earlier. Here, some of the most widely known fracture geometric skin formulations available in the literature are summarized.

Reliy et. al. (1991) developed a formula for calculating geometric fracture skin as a function of fracture conductivity. as shown below,

$$S_{gf} = \ln(2 + \frac{2e^{\gamma}}{C_{FD}}) . \tag{3.34}$$

Where, γ is Euler's constant (γ = 0.577216).

It should be mentioned that Equation 3.34 is only valid for penetration ratio less than 0.2 (I_x < 0.2).

Economides et al. (2002) studied a large number of numerical HFW simulations for different fracture geometrical parameters. Then, they curve fitted their data using the following correlation for fracture geometric skin. Their correlation is shown below,

$$S_{gf} = \frac{1.65 - 0.328u + 0.116u^2}{1 + 0.18u + 0.064u^2 + 0.005u^3} . \tag{3.35}$$

Where, u is the natural logarithm of dimensionless fracture conductivity, u = Ln (C_{FD}). They stated that Equation 3.35 is only valid for C_{FD} range of 0.1 to 1000 ($0.1<C_{FD}>1000$) and a penetration ratio less than 0.2 (I_x < 0.2).

Later, Mayer and Jacot (2005) presented a general formulation to calculate (S_{gf}) for rectangular reservoir with different aspect ratios ($\lambda = \boldsymbol{X_e}/\boldsymbol{Y_e}$) including (square reservoir). Their formulation is shown below,

$$S_{gf} = \ln(\varepsilon + \frac{\pi}{g_\lambda \cdot C_{FD}}) . \tag{3.36}$$

Where, g_λ is a geometrical parameter related to the drainage area shape and it is a function of dimensionless fracture conductivity (C_{FD}), penetration ratio (I_x), and reservoir aspect ratio (λ).

The formula to calculate g_λ is given as,

$$g_\lambda = \frac{2e^{-2\cdot C_{FD}\cdot I_x^2}}{1+\frac{1}{\lambda}} + \frac{2\cdot\lambda\cdot(1-e^{-2\cdot C_{FD}\cdot I_x^2})}{1+\frac{1}{\lambda}} . \tag{3.37}$$

It can be noticed that for $\lambda = 1$ (i.e. square reservoir), the parameter g_λ has a value of one (g_λ=1 at $\lambda = 1$). Thus, for a square reservoir Equation 3.36 can be written as,

$$S_{gf} = \ln(\varepsilon + \frac{\pi}{C_{FD}}) . \tag{3.38}$$

Since Equation 3.38 is general compared to the previous two formulations, it will be considered for more discussion and analysis.

In Equation 3.38 the term (ε) is the ratio of fracture length to effective wellbore radius for infinite conductivity fracture. Because of its importance in determining (S_{gf}), more explanation of the parameter (ε) will be given next.

First, the mathematical expression of ε is given as,

$$\varepsilon = \frac{x_f}{r_w'\big|_{C_{FD}\to\infty}} . \tag{3.39}$$

$r_w'\big|_{C_{FD}\to\infty}$ is the effective wellbore radius of an infinite fracture conductivity. Prat (1960) has shown that for a penetration ratio of less than or equal 0.2 ($I_x \le 0.2$), the effective wellbore radius of infinite conductivity fracture ($r_w'\big|_{C_{FD}\to\infty}$) is equal to half of the fracture half length (x_f), i.e. $r_w'\big|_{C_{FD}\to\infty} = 0.5x_f \Rightarrow I_x \le 0.2$.

As a result, ε has a value of 2 when penetration ratio is less than or equal 0.2 ($\varepsilon = 2 \Rightarrow I_x \le 0.2$). However, it should be mentioned that Prat's study was based on Steady state boundary conditions. Later, Ravaghan *et al.* (1978) confirmed this conclusion and added that it is valid for both steady state (SS) and pseudo-steady state (PSS) boundary conditions. Furthermore, they pointed out that if the HFW penetration ratio is higher than 0.2 ($I_x > 0.2$), then the boundary conditions will affect the flow

performance. That is, they have shown that the effective wellbore radius of infinite conductivity fracture ($r_w'\big|_{C_{FD}\to\infty}$) for (SS and PSS) are different when ($I_x > 0.2$).

Accordingly, it can be said that the parameter (ε) is a function of penetration ratio and a mathematical expression of this relationship is needed to be used in the geometric skin formula, Equation 3.38.

Although, Mayer and Jacot (2005) presented a mathematical expression to calculate the parameter ε, yet from the author experience it is a complicated expression to use. As a result, it is recommended to numerically calculate ε and then find a more convenient or simpler expression by curve fitting the results with respect to I_x or any other parameter, as will be shown next.

From Equation 3.38 it can be stated that, if the fracture has infinite conductivity, then the term ($\frac{\pi}{C_{FD}}$) can be ignored. Therefore, the geometric skin of infinite conductivity fracture will be as follow,

$$S_{gf} = \ln(\varepsilon)\,. \tag{3.40}$$

Knowing that, the Darcy flow dimensionless productivity index J_D of a Non-Damaged HFW in a square reservoir can be written as,

$$J_D = \frac{1}{\left(\ln\left(\frac{r_e}{x_f}\right) + S_{gf} - c\right)} \tag{3.41}$$

Here c is a constant, which is 0.5 for SS and 0.75 for PSS.

Then, the Darcy flow dimensionless productivity index J_D of a Non-damaged HFW with infinite fracture conductivity in a square reservoir can be written by combining Equations 3.40 and 3.41, as follows,

$$J_D = \frac{1}{\left(\ln\left(\frac{r_e}{x_f}\right) + \ln(\varepsilon) - c\right)} \tag{3.42}$$

$$r_e = \frac{2X_e}{\sqrt{\pi}}\,. \tag{3.43}$$

Combining Equations 3.42 and 3.43 we can solve for (ε) using the following equation,

$$J_D = \frac{1}{\left(\ln\left(\frac{2}{\sqrt{\pi} I_x}\right) + \ln(\varepsilon) - c\right)} \tag{3.42}$$

Accordingly, ε can be calculated numerically for different I_x under SS and PSS condition. The procedure to calculate (ε) can be summarized as follow,

1. Simulate the flow around infinite conductivity HFW (i.e. $C_{FD} > 200$, at least) for different I_x values covering the whole range of I_x. A minimum of 10 data points is desirable.
2. Obtain J_D (using Numerical Simulator) for different penetration ratio.
3. Calculate ε at each I_x.
4. Curve fit ε. In this study ε has been curve fitted as a function of I_x.
5. Finally, it should be mentioned that the same procedure can be followed for rectangular reservoirs with any aspect ratio provided that the (c) factor is known for the aspect ratio under consideration.

Using these procedures, the author was able to numerically obtain the parameter ε for different penetration ratio in a square reservoir under both steady-state and pseudo-steady state conditions. Then, it was curve fitted with respect to penetration ratio (I_x) giving the following simple formula,

For SS conditions:
$$\varepsilon_{SS} = 2 - \left(\frac{0.112 I_x}{1 - 0.796 I_x} \right) \tag{3.44}$$

For PSS conditions:
$$\varepsilon_{PSS} = 2 + \left(\frac{0.355 I_x}{1 - 0.704 I_x} \right) \tag{3.45}$$

Figure 3.13 shows the variation of parameters ε_{ss} and ε_{pss} versus penetration ratio. From this figure it can be noticed that for penetration ratio less than 0.2 (Ix < 0.2) the parameter ε is the same regardless of boundary condition applied. Furthermore, for penetration ratio higher than 0.2 (Ix > 0.2), it can be clearly seen (from the same figure) that ε_{ss}, under SS conditions, decreases as penetration ratio increases. However, under PSS conditions, ε_{pss} increases as penetration ratio increases. Therefore, The difference between the geometric skin of HFW at SS and that at PSS depends on the absolute value of ε and also its relative magnitude compared to ($\frac{\pi}{C_{FD}}$), refer to Equation 3.38.That is, for high C_{FD} the difference between SS and PSS geometric skin is controlled by the magnitude of the parameter (ε) because ($\frac{\pi}{C_{FD}}$) is almost negligible. However, as C_{FD} decrease then the value of (ε) becomes negligible compared to the

term ($\frac{\pi}{C_{FD}}$) especially when C_{FD} is very low, and therefore the difference between SS and PSS geometric skin reduces.

Based on that, the final form of HFW geometric skin in a square reservoir (Equation 3.38) can be re-written as follow,

For SS conditions:

$$S_{gf} = \ln(\varepsilon_{SS} + \frac{\pi}{C_{FD}}) \tag{3.46}$$

For PSS conditions:

$$S_{gf} = \ln(\varepsilon_{PSS} + \frac{\pi}{C_{FD}}) \tag{3.47}$$

Where, ($\varepsilon_{SS}, \varepsilon_{PSS}$) can be calculated using Equations 3.44 and 3.45, respectively.

3.3.3 Verification of Single Fracture Geometric Skin

In this section, a verification of the geometric skin of HFW will be given by comparing the in-house simulator results with those from Equations 3.46 and 3.47 for a wide range of HFW geometrical parameters.

Figure 3.14 confirms the accuracy of the developed steady state geometric skin (S_{gf}) equation (Equation 3.46 and 3.47) by comparing the calculated S_{gf}, with those of the HFW steady sate and pseud-steady state in-house simulator. In this figure a wide range of variation of pertinent geometrical parameters has been used. The range of parameters covered are shown below,

Fracture width (w_f): 5, 10, 15 mm

Fracture half length (x_f): 20, 40, 80, 100, and 200 m

Fracture permeability (k_f): 5, 10, 50, 100, 150, 200 D

Reservoir permeability (k_m): 0.1, 1, 10, 100 mD

Penetration Ratio (I_x): 0.05-0.98

The AAD% (average absolute deviation error) is only 1.6% for 470 data points confirming the integrity of the proposed geometric skin formula.

3.3.4 Geometric Skin of Multiple-hydraulic Fractures Intercepting Vertical Well

As discussed earlier, many studies in the literature suggested that hydraulic fracture propagation is a complex process and should not always yield single planner geometry.

In this study, Multiple hydraulic vertical fractures well (MHFW), is defined as a vertical well intercepted by finite number (n) of vertical fractures. It is assumed that these fractures are uniform and equally spaced. The number of fractures in the system (n) can be mathematically expressed as follow,

$$n = \left(\frac{\pi}{\theta} \right). \tag{3.48}$$

Where, (θ) is the angle between two successive fracture wings and is measured in radians.

For instance, if the angle between each two successive wings in a multiple fracture system equal to $\pi/4$ ($\theta = \pi/4$), then the well is intercepted by four fractures. Also, if the well is intercepted by two fracture wings where the angle between them is ($\theta = \pi$), then the number of fractures in the system will be equal to one and this indeed represents the well-known single planner fracture model (discussed in the previous section).

Based on that, the aim of this section is to study the behaviour of multiple vertical fractures well (MHFW) with (n=2), (i.e. a vertical well intercepted by two perpendicular fractures, $\theta = \pi/2$), as shown in Figure 3.15. Also, the aim is to extend the geometric skin formulation proposed in the previous section to this case of multiple HFW.

Choo et al., Freddy et al., and Restrepo et al. (1987, 2001, and 2009) studied the transient pressure behaviour around multiple vertical fractured well with different number of fractures. The main conclusions of these studies were that for the infinite dimensionless fracture conductivity case, the pressure response of MHFW is similar to that of a single hydraulically fractured well if all fractures have the same conductivity as that of a single-fracture model. For the finite dimensionless fracture conductivity case, the pressure response of MHFW behaves like that of a well with equivalent single fracture of an average or equivalent conductivity ($C_{FD\text{-}eq}$). However, they have not presented any specific criteria on how to calculate this average or equivalent fracture conductivity.

With this in mind, the author goal in this part of the study is to extend the single hydraulic fracture (SHFW) geometric skin formulation to the case of multiple hydraulic fractured well (MHFW). Considering that the existing geometrical skin formulation of SHFW is a function of fracture conductivity, then it is expected that any extension of the SHFW formulation to be applicable for MHFW should come through the dimensionless fracture conductivity. That is, the aim is to propose an equivalent single fracture model, which has ($C_{FD\text{-}eq}$) that should give the same performance as that of MHFW.

Here, first, the pressure distribution around MHFW is discussed. Then, a generated large bank of data for different MHFW with different geometrical parameters combination (i.e. w_f, x_f, k_f, k_m, x_e) is used to propose an equivalent single fracture model with equivalent fracture conductivity (C_{FD-eq}) which should replicate the same flow performance as that of multiple fractures well.

Figure 3.16 shows the pressure distribution around MHFW (C_{FD1} = C_{FD2} =240), HFW-3 data set in Table 3.2. It can be seen from this figure that (similar to the single fracture case, Figure 3.5) the pressure distribution around MHFW is elliptical for high fracture conductivity fracture. In Figure 3.17 the same exercise has been repeated but with lower fractured conductivity (C_{FD1} = C_{FD2} =0.24), it can be seen that when fractured conductivity has decreased the pressure distribution around the fracture has been change to radial in a trend similar to that observed for the single fracture model (Figure 3.8).

In order to propose a geometrical skin for MHFW, more than 8,000 simulations of MHFW have been done, covering a wide range of variation of pertinent geometrical parameters. The range of parameters covered are shown below,

Fracture width (w_f): 5, 10, 15 mm

Fracture half length (x_f): 20, 40, 80, 100, and 200 m

Fracture permeability (k_f): 5, 10, 50, 100, 150, 200 D

Reservoir permeability (k_m): 0.1, 1, 10, 100 mD

Fracture half-length ratio (x_{f1}/ x_{f2}): 0.05 to 1

Fracture permeability ratio (k_{f1}/ k_{f2}): 0.05 to 1

After a careful examination of these runs, it was concluded that the flow rate of the two fractures model can be matched with the flow rate of an equivalent single fracture model with equivalent fracture length ($x_{f\text{-}eq}$) and equivalent fracture permeability ($k_{f\text{-}eq}$), as will be shown in the verification section.

The equivalent fracture length ($x_{f\text{-}eq}$) and equivalent fracture permeability ($k_{f\text{-}eq}$) formulae are shown below,

$$x_{f-eq} = x_f \cdot \sqrt{1+\left(\frac{y_f}{x_f}\right)^2}, \Rightarrow y_f \le x_f \tag{3.49}$$

Where, x_f and y_f are the fracture half length in x and y-directions.

$$k_{feq} = k_{f-high}(1+k_{ratio}) \tag{3.50a}$$

$$k_{ratio} = \frac{k_{f-low}}{k_{f-high}} \tag{3.50b}$$

Where, $k_{f\,ratio}$ is the ratio of low to high fracture permeability in the system. Accordingly, the two multiple vertical fractures can be replaced by an equivalent single fracture with an equivalent fracture conductivity ($C_{FD\text{-}eq}$), as follow,

$$C_{FD-eq} = \frac{k_{f-eq} \cdot w_f}{k_m \cdot x_{f-eq}} \tag{3.51}$$

Also, it can be said that if the two fractures are identical (i.e. $C_{FD1} = C_{FD2} = C_{FD}$), then ($k_{f\text{-}eq} = 2k_f$) and ($x_{f\text{-}eq} = \sqrt{2}\, x_f$). Thus, the equivalent dimensionless fracture conductivity $C_{FD\text{-}eq}$ equal to,

$$C_{FD-eq} = \sqrt{2} \cdot C_{FD} \tag{3.52}$$

Therefore, equations 3.51 or 52 can be used in Equations 3.46 or 3.47, depending on the outer boundary condition applied, to calculate the equivalent geometric skin ($S_{gf\text{-}eq}$) for MHFW with two perpendicular fractures as follows,

For SS conditions: $$S_{gf-eq} = \ln(\varepsilon_{SS} + \frac{\pi}{C_{FD-eq}}) \tag{3.53}$$

For PSS conditions: $$S_{gf-eq} = \ln(\varepsilon_{PSS} + \frac{\pi}{C_{FD-eq}}) \tag{3.54}$$

Where, ($\varepsilon_{SS}, \varepsilon_{PSS}$) can be calculated using Equations 3.44 and 3.45, respectively.

3.3.5 Verification of Multiple Fractures Geometric Skin

Figure 3.18 confirms the accuracy of the developed steady state multiple fracture geometric skin formulae (Equations 3.53 and 3.54) by comparing its results, with those of the MHFW in-house simulator. In this figure a wide range of variation of pertinent geometrical parameters has been used. The range of parameters covered are shown below,

Fracture width (w_f): 5, 10, 15 mm

Fracture half length (x_f): 20, 40, 80, 100, and 200 m

Fracture permeability (k_f): 5, 10, 50, 100, 150, 200 D

Reservoir permeability (k_m): 0.1, 1, 10, 100 mD

Fracture half length ratio (x_{f1}/ x_{f2}): 1

Fracture permeability ratio (k_{f1}/ k_{f2}): 1

It should be noted that in this example the two fractures were identical. Here the AAD% (average absolute deviation error) 2% for more than 6,000 data points confirming the integrity of the proposed multiple fractures geometric skin.

Figure 3.19 confirms the accuracy of the developed steady state multiple fracture geometric skin formula (Equations 3.53 and 3.54) by comparing it results, with those of the MHFW in-house simulator. In this figure the range of variation of pertinent geometrical parameters is similar to that presented earlier but with Un-equal fracture lengths and permeability (i.e. Non-identical two perpendicular fractures).

Fracture half length ratio (x_{f1}/ x_{f2}): 0.05 to 0.95

Fracture permeability ratio (k_{f1}/ k_{f2}): 0.05 to 0.95

Here the AAD% (average absolute deviation error) 3.5% for 2000 data points confirming the integrity of the steady state multiple fractures geometric skin.

Figure 3.20 shows the difference in geometric skin S_{gf} between single vertical fracture intersecting a vertical well (SHFW) and two identical vertical fractures intersecting a vertical well (MHFW). The dimensionless fracture conductivity for both type of wells were 1000 (i.e. for SHFW C_{FD} = 1000 and for MHFW C_{FD1} = C_{FD2} =1000). It can be clearly seen from this figure that for this high C_{FD} value there is no difference in S_{gf} between SHFW and MHFW. This is consistent with literature studies (Choo et al. 1987, Freddy et al. 2001, and Restrepo et al. 2009) which suggest that for infinite conductivity the pressure response of MHFW is similar to that of SHFW.

Furthermore, in Figure 3.21 the same exercise was repeated but with low dimensionless fracture conductivity of 1 (i.e. for SHFW C_{FD} = 1 and for MHFW C_{FD1} = C_{FD2} =1). It can be clearly seen from this figure that the geometric skin of MHFW is lower than that of the SHFW. This due to the fact that the MHFW equivalent single fracture conductivity is higher than that of SHFW (i.e. for SHFW C_{FD} = 1 and for MHFW $C_{FD\text{-}eq}$ $=1\times\sqrt{2}$). This is also consistent with the aforementioned literature studies conclusions, where they stated that for finite dimensionless fracture conductivity the pressure response of MHFW behaves like that of a well with equivalent single fracture of an average or equivalent conductivity ($CF_{D\text{-}eq}$). However as it was mentioned before prior to this study no formula had been proposed for calculation of the equivalent conductivity.

Up to this point, the single phase Darcy flow geometric skin of vertical hydraulically fractured well has been proposed. The applicability of this formula has been verified for single fracture and multiple (two perpendicular) fractures system.

In coming sections, the aim will be to extend the proposed skin formulae for the case of single phase Non-Darcy flow and two phase gas condensate flow.

3.4 SINGLE PHASE NON-DARCY FLOW

Darcy law states that the pressure drop inside a porous media is a linear function of velocity, as shown below,

$$V = -\frac{k}{\mu}\nabla P . \tag{3.55}$$

However, this linear function is not valid for high fluid velocities. Accordingly, Forchheimer (1914) added a quadratic term to the Darcy flow equation to express nonlinear flow nature at higher fluid velocities, given by:

$$-\nabla P = \frac{\mu}{k}V + \rho\beta|v|v , \tag{3.56}$$

After some re-arrangements Equation 3.56 can be written as follow,

$$V = -\frac{k}{\mu}\left(\frac{\nabla P}{1+\frac{k\beta\rho|V|}{\mu}}\right) \tag{3.57}$$

Comparing Equations 3.57 and 3.55, the inertial effect could be expressed as a relative permeability term, in the Darcy flow equation, which depends on the Reynolds number as follows (Ghahri 2010):

$$k_r = \frac{1}{1+R_e} \Rightarrow V = -\frac{kk_r}{\mu}\nabla P , \tag{3.58}$$

$$R_e = \frac{k\beta\rho|V|}{\mu} . \tag{3.59}$$

It should be noted that the term ($k\beta$) in Equation 3.59 is the formation permeability and single phase inertial factor product.

As mentioned earlier the flow of a HFW can be defined using the flow equation of a VW with a geometric skin, Equation 3.32. In the case of non-Darcy flow, Equation 3.32 can be replaced by Equation 3.60 (Jamiolahmady et al. 2005):

$$m = \frac{2\pi kh\Delta\psi}{Ln\left(\frac{r_e}{x_f}\right)+S_t} , \tag{3.60}$$

Where, ψ is the pseudo pressure and S_t is the total skin, which can be mathematically expressed as follows:

$$\psi = \int \frac{k_r}{\mu} dp \tag{3.61}$$

$$S_t = S_{gf} + S_f \, . \tag{3.62}$$

In the total skin equation, S_{gf} and S_f are the geometrical and flow skins, respectively. For Darcy flow, the velocity is low and the effect of inertia is ignored, therefore the flow skin is zero. S_f is a function of the fluid properties, velocity, as well as the geometrical parameters.

In next section the impact of inertia inside the fracture and matrix will be discussed. Then, a formulation of total skin will be proposed.

3.4.1 Impact of inertia in Hydraulically Fractured Wells

In vertical well, inertia has a significant negative impact on well productivity as it increases the pressure drop in the near wellbore area.

In HFW the same thing happens however it is believed that inertia will mainly take place inside the fracture as the velocity inside the matrix (V_{Matrix}) is much lower than that in the fracture ($V_{Fracture}$) due to the significant contrast between their flow areas. That is, the flow area inside the fracture is equal to ($2w_f.h_f$) while the flow area inside the matrix equal to ($4x_f.h_f$, this is the surface area around the fracture). For any arbitrary fracture geometry the fracture length is much higher than the fracture width ($x_f >> w_f$), and therefore it is expected that ($V_{Fracture} >> V_{Matrix}$). Also, it is well understood that flow from the matrix directly to the wellbore is very minimal compared to that from the fracture, and therefore, it should be expected that the main part of the inertial effect occurs inside the fracture.

Figure 3.22 shows the total skin factor for a HFW under (Darcy and Non-Darcy flow) for different fracture conductivity values under the same pressure drop. Details of this well are given in Table 3.2, HWF-4 data set. It can be seen from this figure that the total fracture skin has increased for all (C_{FD}) values when (Non-Darcy) flow was activated, albeit to a lesser extent for higher conductivity values. That is, the impact of inertia increases as fracture conductivity decreases.

Figure 3.23a and b show the dimensionless velocity profile inside the fracture versus dimensionless fracture length for the same example (HFW-4) under Darcy and Non-Darcy flow respectively. It can be clearly seen that the shape of velocity profile is different for case of Non-Darcy flow compared to that under Darcy flow for all fracture

conductivity values studied. It is noted that for the highest fracture conductivity the variation in dimensionless velocity profile shape is minimal, however, for all other (C_{FD}) values it is significant. For instance, for the fracture with (C_{FD} =24), the Darcy dimensionless velocity at x_{fd} of 0.6 is equal to almost 0.6 (i.e. v_d = 0.6 at x_{fd} =0.6), however this value has been reduced to 0.4 under Non-Darcy flow (i.e. for Non-Darcy flow v_d = 0.4 at x_{fd} =0.6). It can be noticed that for the fracture with C_{FD} =2.4, the Darcy dimensionless velocity (Figure 3.23a) at x_{fd} of 0.6 is equal to around 0.4 (i.e. Darcy flow for C_{FD} =2.4, v_d = 0.4 at x_{fd} =0.6). Based on this observation, it can be said that under Non-Darcy flow the fracture with (C_{FD} =24) act behave like it has an effective dimensionless fracture conductivity of 2.4 (C_{FD} =2.4).

This leads to a very important conclusion that the Non-Darcy effects inside the fracture manifest itself as a change (certainly reduction) in dimensionless fracture conductivity.

Accordingly, it can be said that flow effects can be included in the geometric skin formula as a correction to fracture conductivity (i.e. replace C_{FD} by $C_{FD\text{-}eff}$), and therefore, there is no need to propose a separate formula to calculate flow skin. Therefore, the total skin can be given as effective geometric skin. This can be mathematically expressed as

$$S_t = S_{gf} + S_f = S_{gf-eff}\,. \tag{3.63}$$

In Equation 3.63 $S_{gf\text{-}eff}$ is the effective geometric skin, which should be calculated, based on an effective dimensionless fracture conductivity (i.e. corrected for the inertial effect) rather than the absolute one. The mathematical expression of $S_{gf\text{-}eff}$ or S_t is as follows,

$$S_t = S_{gf-eff} = \ln\left(\varepsilon_{ss} + \frac{\pi}{C_{FD-eff}}\right). \tag{3.64}$$

Accordingly, a proper formulation to calculate effective fracture conductivity ($C_{FD\text{-}eff}$) is presented next.

Physically, the inertia or high velocity effect does not change the geometric parameters of the fracture (i.e. w_f and x_f); however it affects the flow parameter (k_f, fracture permeability). That is, because inertia is defined as the continuous acceleration and deceleration of fluid molecules due to high velocity, thus for these molecules it will feel as if they are moving in a lower permeability fracture rather than a shorter or narrower fracture. Therefore, it can be said that in HFW $C_{FD\text{-}eff}$ can be obtained by

correcting the fracture permeability for the effect of inertia using a relative permeability term (k_{rf}) similar to that (for vertical well) presented in Equation 3.58, as given below.

$$C_{FD-eff} = \frac{k_f w_f}{k_m x_f} \cdot (k_{rf}) = \frac{k_f w_f}{k_m x_f} \cdot \left(\frac{1}{1+R_{e-f}} \right) = \left(\frac{C_{FD}}{1+R_{e-f}} \right). \quad (3.65a)$$

$$R_{e-f} = \frac{k_f \beta_f \rho |V|}{\mu}. \quad (3.65b)$$

Where, R_{e-f} is the Reynolds number inside the fracture and ($k_f \beta_f$) is the fracture permeability and single-phase inertial factor product.

Equation 3.65a is the exact form of dimensionless fracture conductivity accounting for the impact of inertia. However, it is not practical to use as it is, because it requires the knowledge of local velocity at each point inside the fracture, which is not readily available piece of information. Therefore, an approximation is required or in other words an average Reynolds number should be defined to express inertia inside the fracture. This simple idea was the centre of many research studies in the literature where some correlation has been proposed (as will be shown later). Indeed, the most readily available point for evaluating Reynolds number will be "the wellbore condition". That is, Reynolds number at the wellbore is more readily available and can be used to correct fracture conductivity.

Recalling Figure 3.23a and 3.23b which shows the dimensionless velocity profile inside the fracture for a wide range of dimensionless fracture conductivity ($240<C_{FD}>0.24$), it can be noticed that the dimensionless velocity is increasing toward the wellbore and reaches its maximum at the wellbore. This means that the fluid velocity inside the fracture reaches its maximum at the wellbore or in other words, the Reynolds number reaches its maximum at the wellbore. Based on that, it is expected that the average Reynolds number ($R_{\mathbf{e\text{-}avg}}$) inside the fracture should be always less than that at the wellbore ($R_{\mathbf{ew}}$), (i.e. $R_{\mathbf{e\text{-}avg}} < R_{\mathbf{ew}}$). This can be expressed as,

$$R_{avg-f} = c \cdot R_{ew}. \quad (3.66a)$$

$$R_{ew} = \frac{k_f \cdot \beta_f \cdot \rho \cdot v_{well}}{\mu} = \frac{k_f \cdot \beta_f \cdot \rho \cdot q_{well}}{w_f h_f \mu}. \quad (3.66b)$$

Where, $R_{avg\text{-}f}$ is the average Reynolds number inside the fracture, R_{ew} is the Reynolds number at wellbore condition and ***c*** is a constant, which is always less than one.

Again, from Figure 3.23a and 3.23b (discussed above) it can be seen that for high fracture conductivity the dimensionless velocity profile is almost linear with respect to dimensionless fracture distance. Accordingly, the average velocity inside the fracture

can be approximated by half of that at the wellbore. Therefore, the average Reynolds number for high fracture conductivity will be 50% of that at the wellbore ($R_{avg\text{-}f}$ $=0.5R_{ew}$). However, for lower fracture conductivity (Also shown in the same figure), the average Reynolds number will be different because (v_d) shape is changing as fracture conductivity decrease. Thus, the area under the curve of (v_d) needed to be known in order to determine ($R_{avg\text{-}f}$), although this is mathematically possible but it is not a practical and easy approximation to use, because the constant *c* will change as fracture conductivity changes and thus it will not be a readily available approximation.

Accordingly, the author decided to use ($R_{avg\text{-}f}$ $=0.5R_{ew}$) and examine its limits and if it can be used as a good approximation for a wide range of dimensionless fracture conductivity. That is the effective dimensionless fracture conductivity proposed here is shown as below,

$$C_{FD-eff} = \left(\frac{C_{FD}}{1+0.5R_{ew}} \right). \tag{3.67}$$

Based on that, a large bank of (Non-Darcy flow) simulation runs has been conducted in order to propose an appropriate approximation of effective fracture conductivity, more than 1400 data points, including both single HFW (one fracture) and Multiple HFW (two fractures). The range of geometric and flow parameters used are shown below,

Fracture width (w_f): 5, 10, 15 mm

Fracture half length (x_f): 20, 40, 80, 100, and 200 m

Fracture permeability (k_f): 146, 15 D

Fracture inertia factor (β_f): 3.5E+5, 1E+6 m^{-1}

Reservoir permeability (k_m): 0.1, 11, 110mD

Reservoir inertia factor (β_m): 1E+12, 3.9E+9, 1.85E+8 m^{-1}

Absolute Dimensionless fracture conductivity range: ($0.2<C_{FD}>500$)

Reynolds number at wellbore condition range: ($1<R_{ew}>80$)

For all cases studied, the average AAD% of the in-house simulator results and those calculated using the total skin formula, which includes the proposed effective dimensionless fracture conductivity (i.e. Equation 3.67), was less than 3.5%. More details of the validity of this approximation will be presented in the verification section. But first the author would like to compare the proposed correlation with those available in the literature.

Many investigators have studied the impact of inertia in HFW. Although all investigators are in agreement on the significant negative impact of inertial effect on the

HFW performance, however there is not such agreement on the introduced formulae expressing this effect.

Guppy et al. (1982) studied inertial effect in hydraulically fractured wells. They simulated a series of draw down tests and developed the following correlation:

$$C_{fD-eff} = \frac{C_{fD}}{1+0.31\times q_D}. \tag{3.68}$$

Here, q_D is the dimensionless flow constant defined as:

$$q_D = \frac{k_f \rho \beta q_w}{w_f h \mu} = 2R_{e_w}, \tag{3.69}$$

Where, q_w is the total flow rate from both wings of the fracture.

Equation 3.68 can be re-written in terms of R_{ew} as follows:

$$C_{fD-eff} = \frac{C_{fD}}{1+0.62\times R_{e_w}}. \tag{3.70}$$

In another paper, Guppy et al. (1982) simulated a fractured well for a build-up test and introduced this correlation:

$$C_{fD-eff} = \frac{C_{fD}}{1+0.55\times q_D} = \frac{C_{fD}}{1+1.1\times R_{e_w}}. \tag{3.71}$$

Gidely (1991) proposed that inertial effect reduces effective fracture conductivity as follows:

$$C_{fD-eff} = \frac{C_{fD}}{1+R_{e_w}}, \tag{3.72}$$

From the previous correlation, it can be stated that Equation (3.71 and 3.72) are expected not to give right answers, as the average Reynolds number used is either equal or higher than the Reynolds number at wellbore conditions. As discussed earlier, that the Reynolds number inside the fracture is not constant, indeed, it increases toward the wellbore and it has its maximum value at the wellbore. The only correlation which is similar to the author's proposed correlation is the Guppy's correlation (Equation 3.70). Therefore, a very brief description of this correlation will be given and a comparison between its results and those of the proposed effective dimensionless fracture conductivity (Equation 3.67) will be presented.

Guppy et al. (1982) developed his correlation to account for inertial effects in Well-test analysis. They simulated series of numerical well-tests (around 250). Based on

regression analysis of their results, Equation 3.70 was proposed to calculate the effective fracture conductivity. They pointed out that their correlation is valid for the following range of wellbore Reynolds number ($1< R_{ew} >40$) and absolute dimensionless fracture conductivity ($10< C_{FD} >100$).

Figure 3.24 shows a comparison between the proposed formula of $C_{FD\text{-}eff}$ and those obtained using Guppy's correlation for the HFW-5 data set of Table 3.2. It should be mentioned that the average Well Reynolds number in here was around 45 (R_{ew} =45). It can be seen from this figure that the proposed formulation (Equation 3.67) gives better prediction compared to that of Guppy's correlation for the range of parameters used.

In conclusion, the formulation needed to calculate total fracture skin for single phase Non-Darcy flow can be summarized as follow,

$$S_{gf-eff} = \ln\left(\varepsilon_{ss} + \frac{\pi}{\left(\frac{C_{FD}}{1+0.5R_{ew}}\right)}\right) \tag{3.73}$$

$$R_{ew} = \frac{k_f \cdot \beta_f \cdot \rho \cdot V_w}{\mu} \tag{3.74}$$

$$S_t = S_{gf} + S_f = S_{gf-eff} \tag{3.75}$$

$$S_t = \ln\left(\varepsilon_{ss} + \frac{\pi}{C_{FD}} + \frac{\pi \cdot R_{ew}}{2C_{FD}}\right) \tag{3.76}$$

In Equation 3.76, the first two terms are the Darcy flow geometric skin while the third term represents the inertial effect which is a function of fluid properties, volumetric flow rate, and geometrical parameters. That is, for Darcy flow (R_{ew} is very low), and the total skin S_t equal to the geometric skin S_{gf}.

Finally, the productivity of HFW can be represented in term of VW productivity as follow,

$$m = \frac{2\pi kh\Delta\psi}{Ln\left(\frac{r_e}{r_w'}\right)}, \tag{3.77}$$

$$r_w' = x_f \times e^{-S_t} \tag{3.78}$$

Where, ψ and S_t are the pseudo pressure and total skin effect, respectively. ψ can be mathematically expressed as follows:

$$\psi = \int \frac{k_r}{\mu} dp \tag{3.79}$$

$$k_r = \frac{1}{1+R_e} \Rightarrow R_e = \frac{k_m \beta_m \rho V}{\mu}, \tag{3.80}$$

Where, the term ($k_m \cdot \beta_m$) represents the matrix permeability and matrix single phase inertial factor.

It should be mentioned that in Equation 3.76 if we have Multiple HFW then the C_{FD} should be replaced by $C_{FD\text{-}eq}$, which has been defined in Equation 3.52. Also, the fracture length in Equation 3.78 should be replaced by equivalent fracture length defined in Equation 3.49.

In conclusion, Equation 3.77 together with equations 3.78, 3.76 should produce the same flow rate as that of 2-D HFW, provided that all needed information are available. That is, using 1-D open hole simulator we can predict the same performance as that of the 2-D simulator under the same prevailing conditions. Indeed, this saves CPU time and gives more flexibility in conducting different sensitivity analysis with regard to the well performance.

However, it should be mentioned that (ψ) and $r_w'(S_t)$ are both functions of the velocity and fluid properties. That is, the productivity estimation requires an iterative procedure, which is described after discussing the structure (including the equation and solution technique) of the 1-D open simulator developed here, in order to verify the integrity of the proposed approach.

3.4.2 Steady State Single Phase 1-D Open-Hole Simulator

In this part of the study, the aim is to develop a 1-D EOH radial model, which replicates the flow performance of fine grid 2-D model under the same flow conditions. That is, the 1-D open-hole simulator simulates the steady state single phase flow around a vertical well open-hole model with constant pressure at the same external radius as that of the 2-D fine grid model. The 1-D in-house simulator has been developed using spread-sheet (VB application).

Governing Equation and Numerical Solution:

For the radial model, a combination of continuity and non-Darcy flow equations (Equation 3.5) can be written as follows:

$$\nabla . \left[\frac{1}{r} \left[\frac{k}{\mu} \right] . \frac{\rho}{1+\mathrm{Re}} . \frac{\partial p}{\partial r} \right] = 0 . \tag{3.81}$$

The numerical differential form of Equation (3.81) is given as:

$$\frac{r_{i+1/2}}{\Delta r^2}\times\left(\frac{\rho}{1+\mathrm{Re}}\frac{k}{\mu}\right)_{i+1}\times P_{i+1}-\left(\frac{r_{i+1/2}+r_{i-1/2}}{\Delta r^2}\right)\times\left(\frac{\rho}{1+\mathrm{Re}}\frac{k}{\mu}\right)_{i}\times P_i+\frac{r_{i-1/2}}{\Delta r^2}\times\left(\frac{\rho}{1+\mathrm{Re}}\frac{k}{\mu}\right)_{i-1}\times P_{i-1}=0 \tag{3.82}$$

For steady state conditions:

$$\begin{aligned} P_1 &= P_{well} \\ P_n &= P_{ext} \end{aligned} \tag{3.83}$$

Where subscript well and ext refer to wellbore and external radius.

It should be noted that the wellbore pressure, external pressure, and external radius are known. The effective wellbore radius, required for the above calculation is obtained following an iterative procedure discussed below.

3.4.3 Iterative Procedure for Effective EOH Wellbore Radius

As mentioned in the previous section, the effective wellbore radius formulation (Equation 3.78) depends on the velocity. Thus, the calculation of the effective wellbore radius needs an iterative procedure, as described below:

1) An initial guess for $r_w^{'}$, is obtained based on Darcy flow geometric skin S_{gf}, as follows:

$$r_{w1}^{'}=x_f\times e^{-S_{gf}},S_{gf}=\ln\left(\varepsilon_{ss}+\frac{\pi}{C_{FD}}\right). \tag{3.84}$$

2) Using $r_{w1}^{'}$, the pressure profile and mass flow rate of the EOH system ($\mathbf{m}_{EOH}$) are estimated by the 1-D in-house simulator. Then, using ($\mathbf{m}_{EOH}$) and the pressure profile, the pseudo pressure (ψ) is calculated from (Equation 3.77), however since (ψ) is a function of velocity, then another round of iteration is required to estimate the new pressure profile and mass flow rate.
3) The new effective wellbore radius is then estimated based on the total skin formula, Equation 3.76. That is, the mass flow rate from step 2 is used to calculate the total skin and then estimate the new effective wellbore radius (Equation 3.78).
4) The absolute deviation (AD%) between the new effective well bore radius and the previous one is estimated by:

$$AD\%=\frac{r_{w2}^{'}-r_{w1}^{'}}{r_{w1}^{'}}\times 100. \tag{3.85}$$

5) If the AD% is greater than the error tolerance threshold, defined as 0.01, then, the new effective wellbore radius is used, and the programme goes back to step 2 to re-calculate the new pressure profile mass flow rate of the system. Otherwise the iterations round will stop and the effective wellbore radius ($r_w^{'}$) and mass flow rate ($\mathbf{m}_{EOH}$) are reported.

It is important to point out that the convergence rate of the iterative procedure is acceptable. In the majority of cases studied in this thesis the solution converges after 2-3 iterations highlighting the integrity of the approach. In the next section a verification of this approach is presented.

3.4.4 Verification of EOH 1-D Simulator, Non-Darcy Flow

Single Fracture Well (SHFW), Non-Darcy Flow.

Figure 3.25 and 3.26 confirm the accuracy of the developed total skin equation (Equation 3.76) by comparing the calculated mass flow rate obtained using the EOH 1-D simulator, in which the effective wellbore radius and the iterative procedure described previously have been incorporated, with those of the HFW in-house simulator. The rocks used for data of these two Figures are a Rc1b and Texas Cream with a permeability of 0.18 and 9.1 mD and single phase inertial factor of 1.06E+12 m^{-1} and 3.29E+9 m^{-1}, respectively, more information about this (HFW6 and 7) data set are listed in Table 3.2. The AAD% (average absolute deviation error) is only 1.7% and 2.5% for 156 and 182 data points, respectively.

Multiple Fracture Well (MHFW), Non-Darcy Flow.

Figure 3.27 and 3.28 confirms the accuracy of the developed total skin equation (Equation 3.76) by comparing the calculated mass flow rate obtained using the EOH 1-D simulator, in which the effective wellbore radius and the iterative procedure described previously have been incorporated, with those of the HFW in-house simulator. The rocks used for data of these two Figures are a Rc1b and Texas Cream with a permeability of 0.18 and 9.1 mD and single phase inertial factor of 1.06E+12 m^{-1} and 3.29E+9 m^{-1}, respectively, more information about this data set are listed in Table 3.2, (HFW8 and 9).The AAD% (average absolute deviation error) is 2% and 3% for 300 and 290 data points, respectively.

Finally, more than 500 simulation runs has been done for a high permeability rock, Berea core with a permeability of 110mD and single phase inertial factor of 1.85E+8 m^{-1}, more information about this data set are listed in Table 3.2, HFW10 data set. Also, it

should be mentioned that this data set include both Single HFW and Multiple HFW runs, Figure 3.29 shows the results of this data set.

Figure 3.29 confirms the accuracy of the developed total skin equation (Equation 3.76) by comparing the calculated mass flow rate obtained using the EOH 1-D simulator, in which the effective wellbore radius and the iterative procedure described previously have been incorporated, with those of the HFW in-house simulator. The range of absolute dimensionless fracture conductivity used in here is ($0.2 < C_{FD} > 2$). The AAD% (average absolute deviation error) is only 4.2% for 500 data points.

3.5 Two-Phase Gas Condensate Flow

As mentioned earlier in this thesis, modelling gas condensate reservoirs is a real challenge due to the fact that when the pressure drops below dew point a condensate liquid bank will accumulate around the wellbore and the relative permeability in this area is a strong function of fluid properties, velocities, as well as phase behaviour. Therefore, a fine grid compositional numerical simulation is usually required in order to achieve an accurate prediction of the well performance. However, having a complex wellbore geometry such as that of HFWs, add another level of complexity to the modelling process due to the fact that the flow around HFW also requires fine grid simulation to properly capture the change in flow parameters around the wellbore.

For these reasons, a simple (yet reliable) method for HFW productivity calculation in gas condensate reservoirs is very much needed, as the above procedure is computationally cumbersome.

Accordingly, the main aim of this part of the study is to extend the single phase numerical modelling approach presented previously, to study two-phase flow around HFWs in gas condensate reservoirs. That is, an in-house simulator has been developed, simulating steady state and pseudo-steady state flow of gas and condensate around HFWs. Also, a number of, ECLIPSE E300 commercial software, numerical simulations have been used in order to verify the integrity of the two-phase in-house simulator.

3.5.1 In-House Mathematical Two-Phase Steady-State HFW Model

The 2-D geometries used here are the same as those used for single phase study in the previous section. However, the governing equations solved for this flow domain are different, as described below.

2-D Simulator Governing Equations

The equations employed in this part of the study, are the same as those described for gas condensate flow in a perforated region and around deviated wells (Jamiolahmady et al. 2006 and Ghahri 2010, both studies conducted in GCR-HWU group, GCR Final Report 2005-2008 and 2008-2011). These equations and their derivations are as follow:

1) The continuity equation for gas and condensate flow at steady state conditions

$$\nabla.\left((\rho v)_g + (\rho v)_c\right) = 0\,, \tag{3.86}$$

Where, *g* and *c* represent the gas and condensate phase respectively.

2) The flow equation for each phase:

$$v_i = \frac{k k_{ri}}{\mu_i}\nabla P\,.\; i=g,\, c \tag{3.87}$$

Combining continuity and flow equations, after some mathematical manipulation, gives:

$$\nabla.\left(\left\{\left[\frac{\rho k_r}{\mu}\right]_g + \left[\frac{\rho k_r}{\mu}\right]_c\right\} k\nabla P\right) = 0\,. \tag{3.89}$$

The total fluid composition ($\mathbf{z_j}$) is constant as the fluid flows through the porous media. However, for each component, there is mass transfer between two phases as expressed by the following equation:

$$z_j = \frac{\rho_g y_j GTR + \rho_c x_j (1-GTR)}{\rho_g GTR + \rho_c (1-GTR)} = cons.\,, \tag{3.90}$$

Where, GTR is the total gas fractional ratio defined by Equation 3.91.

$$GTR = \frac{Q_g}{Q_g + Q_c} = \frac{1}{1 + \frac{k_{rg}}{k_{rc}} \times \frac{\mu_c}{\mu_g}}\,. \tag{3.91}$$

Where, *Q* is the volumetric flow rate while *g* and *c* refer to gas and condensate.

In Equation 3.89, relative permeability, which is a function of interfacial tension and velocity, is estimated using the generalized k_r correlation by Jamiolahmady et al. (2009).

"In this correlation, gas relative permeability is interpolated between a base curve (k_{rgb}) and a miscible curve (k_{rgm}), both corrected for the effect of inertia, using a generalized interpolation function. The correlation has either universal parameters or those parameters that can be estimated from readily available petro-physical data. The correlation is based on the relative permeability ratio ($k_{rgtr} = \frac{k_{rg}}{k_{rg} + k_{rc}} = \frac{\mu_g \cdot GTR}{\mu_g \cdot GTR + \mu_c \cdot (1-GTR)}$) as the main variable, which is closely

related to fractional flow. The condensate relative permeability is calculated using the definition of relative permeability ratio.

It should be noted that in gas condensate systems, fractional flow is directly related to fluid composition and pressure at steady-state, which is generally prevailing near the wellbore, hence making it much more attractive practically, compared to saturation, which depends on core characteristics" (Jamiolahmady et al. 2009, Ghahri 2010, and GCR Final Report 2008-2011, generalized k_r correlation description).

A binary mixture of C1 (methane) and n-C4 (normal butane) was used as a model gas-condensate fluid. The fluid properties of C1-nC4 mixtures are those measured in the GCR-HW group laboratory (i.e. composition, density (ρ), viscosity (μ) and interfacial tension, *IFT*), which were implemented in the mathematical model in a tabular form, Table 3.3.

Mathematical Solution Technique

The main governing non-linear partial differential equation (PDE), Equation 3.89, and auxiliary equation (3.90) are solved using Comsol multi-physic software (Version 3.4a, 2007), which uses the finite element method. The main variables in this equation are Pressure and GTR.

The boundary conditions applied to this system are:

1) The pressure at outer boundary (external radius) is known.
2) The pressure at the inner boundary (wellbore radius) is known.
4) The total composition is constant, so either GTR or the total fluid composition is known.

3.5.2 ECLIPSE Steady-State Two Phase HFW Model

The accuracy of the two-phase mathematical in-house simulator was confirmed by comparing some of its results with those of ECLIPSE300 at the same prevailing conditions.

The reservoir model in this exercise had the core properties of Texas Cream with porosity of 0.21 and permeability of 9.1 mD. The reservoir fluid was a binary mixture of C1 (methane) and n-C4 (normal butane) Table 3.3. The reservoir was 200 m in the X and 200 m in Y directions and 10 m in the Z direction. The fracture has a length of 40 m and a width of 5mm. The fracture has a permeability of 146 D. The fracture and the core relative permeability are those measured in GCR-HW Laboratory. The very fine grid

option was used to capture the abrupt changes in flow parameters near the wellbore. It should be noted that the k_r correlations used in Comsol and ECLIPSE300 simulators are different; therefore the base curve relative permeability has been used to describe the fluid mobility around the HFW. The base curve is the relative permeability curve measured at a high IFT (above which k_r is independent of interfacial tension) and low velocity (below which k_r is independent of velocity).

In ECLIPSE 300, seventy injection wells were placed at the boundary of the reservoir to keep the reservoir pressure at the boundary constant.

It should be noted that reaching steady state for this model requires large number of (fine-in-size) time steps. This is due to the fact that capturing the abrupt changes in flow parameters near the wellbore requires small size of time step. This small time step size is required to avoid numerical convergence problems which are usually encountered in such compositional models. In fact, this highlight the added value of having a 1-D equivalent open hole (EOH) simulator for two-phase gas condensate flow as it saves CPU time and reduces troubleshooting process associated with commercial simulators.

Figure 3.30 shows the good agreement between the two results. The arithmetic average absolute percentage deviation (AAD%) of the predicted flow rate values by the ECLIPSE simulator compared to those estimated by the HFW in-house simulator was 1.7 %.

3.5.3 Two-Phase Flow STEADY STATE Total Skin

Here the objective is to introduce an EOH system, which produces the same flow performance, gas and condensate flow rates, as that of a HFW system as follows:

$$\dot{m} = \frac{2\pi kh \int_{Pw}^{Pe} \left(\frac{\rho_l k_{rl}}{\mu_l} + \frac{\rho_g k_{rg}}{\mu_g} \right) dp}{Ln\left(\frac{r_e}{r_w^{'}} \right)}, \tag{3.92}$$

$$r_w^{'} = x_f \times e^{-S_t} \tag{3.93}$$

$$S_t = S_{gf} + S_f \tag{3.94}$$

S_t total skin, (in Equation 3.94) is the summation of geometric skin and flow skin, neglecting damaged skin. S_{gf} is the geometric skin, which depends on the geometrical parameters, while S_f is the flow skin, which depends in fluid properties and volumetric flow rate.

For a gas condensate system the flow regime is controlled by coupling, which is more pronounced at moderate to high velocities, and inertia, which generally operates at high velocities. These two forces act in opposite directions, i.e. coupling improves the well productivity whilst inertia negatively reduces the well deliverability. As explained earlier, in HFW's inertia is always dominant inside the fracture while coupling effects (if exists) are mainly expected to take place inside the matrix where velocity values are much lower than those encountered inside the fracture. With these in mind, it is expected that the two phase total skin values would be smaller than those of the single-phase flow.

An approach similar to that followed for the single-phase flow system described in (Sections 3.4) has been followed. That is, a two phase total skin formulation will be proposed benefiting from the previously discussed single phase total skin. In order to do that, the competition between coupling and inertia inside the fracture region and the matrix region should be addressed first.

Figure 3.31a shows the gas relative permeability inside the fracture versus the dimensionless fracture length for HFW-11 data set in Table 3.2. In this figure the (CI) curve refers to the case where coupling and inertia has been accounted for in calculating k_{rg} while the (Iner) curve refers to the case where only inertia has been considered in calculating k_{rg} inside the fracture. The fluid used in this figure is C1-nC4 and the well total gas ratio used was 0.71 (GTR_{well} = 0.71), the external and wellbore pressures were 1850 and 1650 Psi, respectively. Figure 3.31b shows the total velocity inside the fracture versus dimensionless fracture length, for the same example.

It can be clearly seen from this figure that at this low GTR value (i.e. high condensate saturation) the curve which has both coupling and inertia effects is slightly higher than that with inertia only. This indicates that coupling has slightly improved (by around 10%) the gas relative permeability inside the fracture for this low GTR and low velocity (V_{well} = 400 mD^{-1}) case. This is consistent with Jamiolahmady et al. (2009) where they experimentally studied the coupling and inertial effects inside propped fractures. In their work they concluded that for most practical cases inertia is always dominant inside high permeability fractures. However, they pointed out that for low GTR and low velocity values(250-500mD^{-1}), the k_{rg} increase for lower interfacial tension (IFT) values (i.e. coupling improved k_{rg}). However, it should be mentioned that such low velocities are rarely realized inside the high permeability fracture.

The same exercise has been repeated but with increasing the pressure drop to 500 Psi, that is the external and wellbore pressures were 1850 and 1350 Psi respectively. Also,

the GTR_{well} was increased to (0.81), HFW-12 data set Table 3.2. These results are shown in Figures 3.32 a and 3.32b.

Figure 3.32a shows the gas relative permeability inside the fracture versus the dimensionless fracture length, for coupling and inertia, and inertia only cases. Figure 3.32b shows the total velocity inside the fracture versus dimensionless fracture length, for the same example.

It can be clearly seen that as pressure drop increased to 500Psi (i.e. the well velocity increased to $1200mD^{-1}$), the difference between the (CI) curve and inertia only curve has significantly decreased compared to (Figure 3.31a), and this indicates that inertia is more dominant at this conditions. It can also be observed in this figure that as we move away from the wellbore toward the fracture tip there is a slight increase in k_{rg} values due to the fact that the velocity around fracture tip is lower than that at the wellbore entrance.

The same exercise was repeated in Figure 3.33 (a and b) for (GTR_{well} = 0.91). In this case the pressure drop has been increased to 950Psi (P_{ext} =1850 Psi, P_{well} = 900Psi, and V_{well} =$3200mD^{-1}$), HFW-13 data set Table 3.2.

Figure 3.33a shows the gas relative permeability inside the fracture versus the dimensionless fracture length, for coupling and inertia, and inertia only cases. Also, Figure 3.33b shows the total velocity inside the fracture versus dimensionless fracture length, for the same example.

It can be seen from this figure that the difference between the (CI) and (Inertia only) curves is negligible throughout the whole length of the fracture. This indicates that inertia is dominant even in the area far away from the wellbore and near to the fracture tip.

Figure 3.34a and 3.34b show the gas relative permeability (for GTR_{well} 0.71 and 0.91) inside the fracture versus the dimensionless fracture length, for coupling and inertia and inertia only cases. These two runs were under the same pressure drop (ΔP = 200Psi) and the well velocity is almost the same (V_{well} = $400mD^{-1}$), (for GTR_{well} =0.71, P_{ext} =1850 and P_{well} =1650 Psi, while for GTR_{well} =0.91, P_{ext} =1100 and P_{well} =900 Psi), HFW-14 and 15 data sets Table 3.2. It can be seen from these two figures that (as mentioned earlier) for GTR_{well} = 0.71 (low velocity, and high condensate fractional flow/saturation) coupling helps to slightly improve k_{rg}, however, when GTR_{well} increased to 0.91 (i.e. still low velocity, but low condensate fractional flow/saturation) the improvement in k_{rg} is minimal. This confirms that coupling effect is not only related to velocity but also condensate fractional flow and IFT effects.

Based on the above discussion, it can be concluded that for most practical cases coupling inside the fracture can be ignored and inertia is dominant inside the fracture.

Considering that earlier, it has been shown that inertia is negligible for single phase flow inside the matrix, the same trend is expected for two-phase flow. However, in the two-phase flow case coupling might improve the flow inside the matrix since the velocity range encountered inside the matrix is lower than that inside the fracture.

Now, the total skin for the case of two- phase will be discussed benefiting from the expression proposed for the single phase flow case.

The single phase total skin is defined as follow (section 3.4):

$$S_t = S_{gf} + S_f = S_{gf-eff} = \ln\left(\varepsilon_{ss} + \frac{\pi}{C_{FD-eff}}\right). \tag{3.95}$$

$$C_{FD-eff} = \left(\frac{C_{FD}}{1+0.5R_{ew}}\right) \tag{3.96}$$

Initially it is proposed to extend Equation 3.96 to two-phase through replacing the single phase dimensionless fracture conductivity by a two-phase dimensionless fracture conductivity using the base relative permeability curves of gas and condensate inside the fracture and matrix (i.e. including the two-phase flow interaction terms), as follows:

$$C_{FD-eff} = \left(\frac{C_{FD-base}}{1+0.5R_{ew}}\right) \tag{3.97}$$

$$C_{FD-base} = \frac{k_f w_f}{k_m x_f} . \left(\frac{k_{rgbf} + k_{rcbf}}{k_{rgbm} + k_{rcbm}}\right) \tag{3.98}$$

Where, $(k_{rgbf} + k_{rcbf})$ and $(k_{rgbm} + k_{rcbm})$ are the summation of fracture gas and condensate base relative permeability curves and matrix gas and condensate base relative permeability curves, respectively.

Using the relative permeability ratio definition ($k_{rgtr} = \frac{k_{rg}}{k_{rg} + k_{rc}}$), Equation 3.98 can be written as,

$$C_{FD-base} = \frac{k_f w_f}{k_m x_f} . \left(\frac{\frac{k_{rgbf}}{k_{rgtr}}}{\frac{k_{rgbm}}{k_{rgtr}}}\right) \tag{3.99}$$

Because Equation 3.97 is evaluated at the wellbore condition (i.e. Reynolds number R_{ew}, is evaluated at wellbore condition) then Equation 3.99 should be evaluated at the same condition and the final form of $C_{FD\text{-}base}$ can be written as follows:

$$C_{FD-base} = \frac{k_f w_f}{k_m x_f} \cdot \left(\frac{\dfrac{k_{rgbf}}{k_{rgtr-well}}}{\dfrac{k_{rgbm}}{k_{rgtr-well}}} \right) = \frac{k_f w_f}{k_m x_f} \cdot \left(\frac{k_{rgbf}}{k_{rgbm}} \right)_{well} \tag{3.100}$$

In fact, Equation 3.97 gives the effective dimensionless fracture conductivity for gas condensate flow, however it only accounts for the effect of inertia. Therefore, this equation needs to be modified to account for the effect of coupling in order to be used in HFW gas condensate productivity calculations.

For gas condensate flow the main important (fluid/rock) properties, which may affect well productivity, are relative permeability, the density, and the viscosity of each flowing phase (i.e. gas and condensate). Thus a single parameter, total relative mass mobility (λ_{rt}), presented by Equation 3.101, can be used to express the effect of these three important properties on the effective dimensionless fracture conductivity.

$$\lambda_{rt} = \lambda_{rg} + \lambda_{rc} = \frac{\rho_g k_{rg}}{\mu_g} + \frac{\rho_c k_{rc}}{\mu_c}, \tag{3.101}$$

Where, λ_{rg} and λ_{rc} are relative mass mobility for gas and condensate, respectively.

Considering that the total skin is expected to be a function of the two-phase relative mass mobility, it is proposed to use an additional term in Equation 3.97 in the form of a multiplication factor, which accounts for the relative mass mobility effects on the HFW productivity. This term is defined as the ratio of (two-phase gas and condensate) relative mass mobility of the velocity affected flow to that of the base case, i.e. independent of velocity and IFT effects. It should be noted that a similar approach has been adopted to study flow around deviated wells in GCR-HW Group (GCR Final Report 2008-2011 and Ghahri 2010). Accordingly, Equation 3.97 can be rewritten by the following equation:

$$C_{FD-eff} = \frac{C_{FD-base}}{1+0.5R_{we}} \times \left(\frac{\lambda_{rt-EOH}}{\lambda_{rt-EOH-base}} \right)_{ave} \tag{3.102}$$

Where, λ_{rt-EOH} and $\lambda_{rt-EOH-base}$ are the average relative mass mobility for an equivalent open hole system EOH with and without considering the velocity effects, respectively. In a detailed form, Equation 3.102 can be rewritten as:

$$C_{FD-eff} = \frac{C_{FD-base}}{1+0.5R_{we}} \times \left(\frac{\left(\dfrac{\rho_g k_{rg}}{\mu_g} + \dfrac{\rho_c k_{rc}}{\mu_c} \right)_{EOH}}{\left(\dfrac{\rho_g k_{rgb}}{\mu_g} + \dfrac{\rho_c k_{rcb}}{\mu_c} \right)_{EOH}} \right)_{ave} \tag{3.103}$$

Where, (k_{rg} and k_{rc}) are the velocity affected gas and condensate relative permeabilities, and (k_{rgb} and k_{rcb}) are the base gas and condensate relative permeabilities.

It should be noticed that the above formulation includes the impact of coupling and inertial effects. Therefore, using this formula (Equation 3.103) in the total skin formulation should express the impact of two phase flow on HFW performance accurately; however for practical purposes it is possible to make it simpler.

That is, the condensate relative permeability can be estimated by the definition of fractional flow using the following equation (Jamiolahmady et. al. 2006):

$$k_{rc} = k_{rg} \times \frac{1-GTR}{GTR} \times \frac{\mu_c}{\mu_g}, \tag{3.104}$$

Where, GTR, μ_c and μ_g are the gas fractional flow, condensate and gas viscosities, respectively. Substituting the above equation into Equation 3.103 results in:

$$C_{FD-eff} = \frac{C_{FD-base}}{1+0.5R_{we}} \times \left(\frac{\left(\frac{k_{rg}}{\mu_g} \left(\rho_g + \rho_c \times \frac{1-GTR}{GTR} \right)_{EOH} \right)_{ave}}{\left(\frac{k_{rgb}}{\mu_g} \left(\rho_g + \rho_c \times \frac{1-GTR}{GTR} \right)_{EOH} \right)_{ave}} \right), \tag{3.105}$$

Rearranging Equation 3.105 gives:

$$C_{FD-eff} = \frac{C_{FD-base}}{1+0.5R_{we}} \times \left(\frac{\left(\frac{k_{rg}}{\mu_g \times GTR} \left(\rho_g \times GTR + \rho_c \times (1-GTR) \right)_{EOH} \right)_{ave}}{\left(\frac{k_{rgb}}{\mu_g \times GTR} \left(\rho_g \times GTR + \rho_c \times (1-GTR) \right)_{EOH} \right)_{ave}} \right), \tag{3.106}$$

Or

$$C_{FD-eff} = \frac{C_{FD-base}}{1+0.5R_{we}} \times \left(\frac{\left(\frac{k_{rg}}{\mu_g \times GTR} \left(\rho_{eq-s} \right)_{EOH} \right)_{ave}}{\left(\frac{k_{rgb}}{\mu_g \times GTR} \left(\rho_{eq-s} \right)_{EOH} \right)_{ave}} \right), \tag{3.107}$$

Where, ρ_{eq-s} is the equivalent single phase density, which is the fractional flow based average density of gas and condensate, defined as (Jamiolahmady et. al. 2006 and Ghahri 2010):

$$\rho_{eq-s} = \rho_g \times GTR + \rho_c \times (1-GTR) \tag{3.108}$$

The fluid properties and GTR variation in the reservoir depend on the pressure profile. Due to the velocity effects, the pressure profile distribution in the reservoir for the base EOH (without velocity and IFT effects) is different from that of the velocity/IFT dependant EOH case. However, the pressures and GTR values in both

cases are the same at the boundary conditions, i.e. the same wellbore and exterior pressures. Hence, in this case, it is expected that the effect of fluid properties would be minimal. Therefore, the relative mass mobility ratio can be approximately estimated by the following equation:

$$\frac{\left(\frac{k_{rg}}{\mu_g \times GTR}\left(\rho_{eq-s}\right)_{EOH}\right)_{ave}}{\left(\frac{k_{rgb}}{\mu_g \times GTR}\left(\rho_{eq-s}\right)_{EOH}\right)_{ave}} \cong \left(\frac{k_{rg}}{k_{rgb}}\right)_{EOH-ave} \tag{3.109}$$

Figure 3.35 shows the variation of the velocity/IFT dependent gas relative permeability to the base gas relative permeability $\left(\frac{k_{rg}}{k_{rgb}}\right)_{EOH}$, for an EOH system, HFW16 and 17 data sets in Table 3.2. The rocks used in this figure are Texas-cream and Berea with permeability of 9.1mD and 110mD, respectively. The base curve relative permeability used are those measured in GCR-HW Laboratory.

It can be seen from Figure 3.35 that the ratio between the velocity/IFT dependent gas relative permeability (k_{rg}) and the base gas relative permeability (k_{rgb}) changes mostly around the wellbore, where the velocity is high and the two important parameters, coupling and inertia, control the HFW productivity. However, far away from the wellbore, the ratio between these two curves, k_{rg} and k_{rgb}, is almost constant. Thus $\left(\frac{k_{rg}}{k_{rgb}}\right)_{EOH-avg}$ could be approximately predicted by an average value corresponding to that around the wellbore, (i.e. $\left(\frac{k_{rg}}{k_{rgb}}\right)_{EOH-avg} = \left(\frac{k_{rg}}{k_{rgb}}\right)_{well}$)

Therefore the following equation can be used to estimate approximately the effective two phase (gas condensate) dimensionless fracture conductivity:

$$C_{FD-eff} = \frac{C_{FD-base}}{1+0.5R_{we}} \times \left(\frac{k_{rg}}{k_{rgb}}\right)_{well} \tag{3.110}$$

Where, $\left(\frac{k_{rg}}{k_{rgb}}\right)_{well}$ is the ratio of velocity/IFT dependent gas relative permeability to the base gas relative permeability evaluated at wellbore conditions, which represents coupling effects inside the matrix.

Based on the previous discussion, it can be concluded that the total skin for two phase gas condensate flow can be obtained using the definition of two phase effective dimensionless conductivity as shown below:

$$S_t = S_{gf} + S_f = S_{gf-eff} = \ln\left(\varepsilon_{ss} + \frac{\pi}{C_{FD-eff}}\right). \tag{3.111}$$

$$C_{FD-eff} = \frac{C_{FD-base}}{1+0.5R_{ew}} \times \left(\frac{k_{rg}}{k_{rgb}}\right)_{well} \tag{3.112}$$

After some re-arrangement the final form of the total skin is obtained as:.

$$S_t = \ln\left(\varepsilon_{ss} + \left(\frac{k_{rgb}}{k_{rg}}\right)_{well} \cdot \left(\frac{\pi}{C_{FD-base}} + \frac{\pi \cdot R_{ew}}{2C_{FD-base}}\right)\right) \tag{3.113}$$

This form of total skin is general in the sense that for single-phase flow $\left(\frac{k_{rgb}}{k_{rg}}\right)_{well}$ will equal one, and the two-phase base dimensionless conductivity will equal to that of single phase dimensionless conductivity.

Eventually, the final form of the two-phase EOH, which should replicate the performance of 2-D HFW, can be summarized as follow,

$$m^0 = \frac{2\pi kh\Delta\psi}{Ln\left(\frac{r_e}{r_w'}\right)}, \tag{3.114}$$

$$\Delta\psi = \int_{Pw}^{Pe}\left(\frac{\rho_l k_{rl}}{\mu_l} + \frac{\rho_g k_{rg}}{\mu_g}\right)dp \tag{3.114a}$$

$$r_w' = x_f \times e^{-S_t} \tag{3.115}$$

$$S_t = \ln\left(\varepsilon_{ss} + \left(\frac{k_{rgb}}{k_{rg}}\right)_w \cdot \left(\frac{\pi}{C_{FD-base}} + \frac{\pi \cdot R_{ew}}{2C_{FD-base}}\right)\right). \tag{3.116}$$

3.5.4 In-house 1-D Two-Phase Steady State Open-Hole Simulator

In order to verify the proposed EOH system formulation presented above, a 1-D two-phase open hole in-house simulator was developed, simulating the steady state flow of gas and condensate around a vertical well, which should generate the same flow performance as that of the fine grid 2-D model. The structure of this simulator is similar to that of the single-phase 1-D simulator but the flow equations used are those governing the two-phase flow of gas and condensate, as described below. It should be noted that the 1-D simulator is based on the finite difference method.

Governing Equations and **Numerical Solution of EOH system:**

For the radial model, a combination of continuity and gas and condensate flow equations (Equation 3.89) can be written as follows:

$$\nabla.\left[\frac{1}{r}.\left(\left[\frac{\rho k_r}{\mu}\right]_g+\left[\frac{\rho k_r}{\mu}\right]_c\cdot k\right).\frac{\partial p}{\partial r}\right]=0. \tag{3.117}$$

The numerical differential form of the above equation is

$$\frac{r_{i+1/2}}{\Delta r^2}\times.\left(\left[\frac{\rho k_r}{\mu}\right]_g+\left[\frac{\rho k_r}{\mu}\right]_c.\frac{k}{\mu}\right)_{i+1}\times P_{i+1}-\left(\frac{r_{i+1/2}+r_{i-1/2}}{\Delta r^2}\right)\times\left(\left[\frac{\rho k_r}{\mu}\right]_g+\left[\frac{\rho k_r}{\mu}\right]_c.\frac{k}{\mu}\right)_i\times P_i+$$
$$\frac{r_{i-1/2}}{\Delta r^2}\times\left(\left[\frac{\rho k_r}{\mu}\right]_g+\left[\frac{\rho k_r}{\mu}\right]_c.\frac{k}{\mu}\right)_{i-1}\times P_{i-1}=0 \tag{3.117a}$$

$$z_j=\frac{\rho_g y_j GTR+\rho_c x_j(1-GTR)}{\rho_g GTR+\rho_c(1-GTR)}=cons. \tag{3.118}$$

For steady state conditions,

$P_1=P_w$

$P_n=P_{res}$, (3.119)

Where, subscripts *w* and *res* refer to wellbore and external radius.

It should be noted that the wellbore pressure, external pressure, external radius, and GTR_{well} or Z_i are known. However, the effective wellbore radius is found based on an iterative procedure as discussed below.

Iterative Procedure for Effective EOH Wellbore Radius

The total skin and effective EOH wellbore radius is a function of fluid properties, coupling and inertial effects. Therefore, an iterative method, similar to that introduced for the single phase non-Darcy flow case, can be applied here to estimate the effective EOH wellbore radius of gas condensate systems:

1) An initial guess for $r_w^{'}$, is obtained based on two phase Darcy flow (i.e. base curve, no coupling and no inertia) total skin S_{gf}, as follows:

$$r_{w1}^{'} = x_f \times e^{-S_{gf}}, S_{gf} = \ln\left(\varepsilon_{ss} + \frac{\pi}{C_{FD-base}}\right). \quad (3.120)$$

2) Based on the effective well bore radius, the pressure profile and flow rate are calculated using Equation 3.114. It should be noted that the 1-D simulator calculations are based on the pseudo pressure formula (Equation 3.114a), which itself is a function of velocity; therefore, another round of iteration is required to estimate the pressure profile and mass flow rate.
3) The new effective wellbore radius is calculated by using the mass flow rate from step 2 in the two-phase total skin formula, Equation 3.116. Then, Equation 3.115
4) If the difference between the new effective EOH wellbore radius calculated and the previous one is not negligible. That is, absolute deviation (AD%) is greater than the error tolerance threshold, defined as 0.01, then a new iteration starts from step 2. Otherwise the iteration round stops and the calculated effective well bore radius and mass flow rate are reported.

3.5.5 Verification of Steady State Two-Phase EOH formulation

Single Hydraulic Fractured Well

Figures 3.36 and 3.37 confirm the accuracy of the proposed approach by comparing the calculated mass flow rates obtained using the EOH 1-D simulator, in which the developed effective wellbore radius, Equation 3.115, and the iterative procedure described in the previous section, have been used, with those of the HFW in-house simulator. The core used in here is Berea with permeability of 110 mD, the relative permeability used was measured in GCR-HW Laboratory. In this model the fracture permeability was fixed and the fracture length was varying (i.e. different I_x) for two GTR_{well} values (0.71 and 0.81). Three mass flow rates are presented in these two Figures. These are the velocity affected mass flow rate curve using in-house simulator and EOH, and mass flow rate calculated using the base relative permeability curve only (i.e. no coupling and no inertia).The reservoir model and the range of the variables are

those listed in Table 3.2, HFW-18 and 19. In these two figures the average absolute deviation error, AAD%, between the EOH and 2-D in-house simulators is only 2.5%.

In Figure 3.36 It can be noticed that for GTR_{well} of 0.71 (with a pressure drop of 200 Psi) and for I_x lower than 0.5, the velocity affected mass flow rate curve is higher than that of calculated using the base curve which indicated that coupling is more dominant at $I_x < 0.5$. However, as penetration ratio increase (i.e. the dimensionless fracture conductivity decrease) the base curve mass flow rate is higher than the velocity affected curve mass flow rate which indicates that inertia start to become more dominant in the system. However, in Figure 3.37 with GTR_{well} of 0.81 (in this case the pressure drop has increased to 500 Psi), it can be noticed that the base curve mass flow rate is always higher than the velocity affected curve mass flow rate demonstrating that inertia is always dominant for all values of penetration ratio (I_x). From these results it can be concluded that if inertia is dominant, the well performance is poorer. In other words, the optimum geometry of fracture should preferably be in the region where impact of inertia is not very pronounced. The optimum operational conditions (i.e. GTR_{well} or P_{well}) should also be in the region where coupling is favorably improving the well performance. Finally, it can be stated that ignoring the velocity effects in the fracture performance prediction (i.e. using the base curve only) can lead to overestimation or underestimation of the HFW performance depending on the competition between coupling and inertia.

To further verify the integrity of the proposed EOH model, more two-phase simulation runs have been conducted.

Figure 3.38 and 3.39 confirm the accuracy of the developed total skin equation (Equation 3.116) by comparing the calculated mass flow rate obtained using the EOH 1-D simulator, in which the effective wellbore radius and the iterative procedure described previously have been incorporated, with those of the HFW in-house simulator. The rocks used for data of these two Figures are a Texas Cream and Berea with a permeability of 9.1 and 110 mD and single phase inertial factor of 3.29E+9 m^{-1} and 1.85E+8 m^{-1}, respectively. The fracture has a permeability of 146 D and single phase inertial factor of 3.5E+5 m^{-1}. The relative permeability curves are those measured in GCR-HW Laboratory. More information about these two data sets are listed in Table 3.2, 20 and 21. Here the AAD% (average absolute deviation error) is 1.9% for 100 data points (HFW-20) and 2.5% for 60 data points (HFW-21).

Multiple Hydraulic Fractured Well

Figures 3.40 and 3.41 confirm the accuracy of the proposed total skin formula (Equation 3.116) by comparing the calculated mass flow rates obtained using the EOH 1-D simulator, in which the developed effective wellbore radius, and the iterative procedure described in the previous section, have been used, with those of the HFW in-house simulator. These two figures represent two phase flow around vertical well intercepted by two perpendicular fractures. The rocks used for data of these two Figures are Texas Cream and Berea core with a permeability of 9.1 and 110 mD and single phase inertial factor of 3.29E+9 m-1 and 1.85E+8 m-1, respectively. The reservoir models and the range of the variables are those listed in Table 3.2, HFW-22 and 23. The AAD% (average absolute deviation error) is 1.6% for 100 data points (HFW-22) and 2.76% for 100 data points (HFW-23).

3.5.6 Pseudo Steady State Two-Phase Flow

Previously, a total skin was developed to account for the effect of flow and geometric parameters on the HFW productivity of two phase steady state conditions. This part of study is devoted to investigate the application of this total skin formulation for two-phase pseudo steady state conditions. A HFW in-house simulator was developed for this purpose, which will be described first. To confirm the integrity of the in-house simulator, its results have been compared with those of the ECLIPSE commercial simulator for the same prevailing flow conditions.

3.5.7 Mathematical Two-Phase Pseudo Steady State HFW Model

During pseudo-steady state conditions the fluid composition and properties vary with time and space. Therefore, the saturation equation needs to be solved. This will then result in a complex set of compositional calculations for the gas condensate fluid systems. Therefore the author used the equivalent single phase approach which was originally included in the generalized k_r correlation (Jamiolahmady et al. 2009) and then extended to the simulation of PSS two-phase flow around deviated wells (Ghahri 2010). In this latter approach and during each time step there is a fixed total composition travelling across the whole reservoir. This allows to easily calculate equivalent single-phase fluid properties weighted based on the total gas fractional flow (GTR). It should be noted that the total fluid composition varies with time only, and the fractional flow of gas and condensate varies with time and also through the reservoir drainage area.

The 2-D geometries used in here are the same as those presented earlier for the PSS single- phase flow case; however the equations are solved for a HFW producing at a constant total (gas and condensate) flow rates.

2-D Simulator Governing Equations

The mathematical derivations and equations which describe the PSS two-phase flow of gas and condensate around HFWs are the same as those used for gas condensate flow around deviated wells (Ghahri 2010, and Gas Condensate Recovery Final Report 2008-2011). These equations and their derivations are as follow:

1) The continuity equation for the equivalent single phase is:

$$\nabla.\left((\rho v)_{eqphase}\right)=\frac{d(\rho_{eqphase}\varphi)}{dt}, \tag{3.121}$$

Where, the equivalent single phase density is defined as follows:

$$\rho_{eqphase}=\rho_g GTR+\rho_c(1-GTR)=\frac{(\rho v)_g}{v_g+v_c}+\frac{(\rho v)_c}{v_g+v_c}, \tag{3.122}$$

$$(\rho v)_{eqphase}=\left(\rho_{eqphase}(v_g+v_c)\right)=(\rho v)_g+(\rho v)_c, \tag{3.123}$$

Substituting from Equation 3.123 into Equation 3.121 gives:

$$\nabla.\left((\rho v)_g+(\rho v)_c\right)=\frac{d(\rho_{eqphase}\varphi)}{dt}, \tag{3.124}$$

Where, *g* and *c* represent the gas and condensate phases, respectively.

2) The flow equation for each phase is:

$$v_i=\frac{kk_{ri}}{\mu_i}\nabla P \text{ . i=g,c,} \tag{3.125}$$

Combining continuity and flow equations, after some mathematical manipulation, gives:

$$\nabla.\left(\left\{\left[\frac{\rho k_r}{\mu}\right]_g+\left[\frac{\rho k_r}{\mu}\right]_c\right\}k\nabla P\right)=\frac{d(\rho_{eqphase}\varphi)}{dt}. \tag{3.126}$$

At PSS conditions, the pressure derivative with regard to time is constant across the whole drainage area. Therefore, Equation 3.126 can be written as follows:

$$\nabla.\left(\left\{\left[\frac{\rho k_r}{\mu}\right]_g+\left[\frac{\rho k_r}{\mu}\right]_c\right\}k\nabla P\right)=\frac{\left(\rho_{eq-phase}q\right)_{well}}{V}. \tag{3.127}$$

Where, $q_{well}=\left(q_g+q_c\right)_{well}$.

Furthermore, as mentioned earlier, at any time the total fluid composition (z_j) is constant as fluid flows through the porous media. However, there is a mass transfer between the two phases for each component as expressed by the following equation.

$$z_j = \frac{\rho_g y_j GTR + \rho_c x_j (1-GTR)}{\rho_g GTR + \rho_c (1-GTR)} = cons., \tag{3.128}$$

Where, GTR is the total gas fractional flow. The same binary fluid system as that used for the SS simulator was used here.

Mathematical Solution Technique

The governing non-linear partial differential equation (PDE), Equation 3.126, is solved using Comsol multi-physic software (Version 3.4a, 2007), which uses the finite element method. The main dependent variable in this equation is P (pressure).

The boundary conditions are:

1) The outer boundary (external radius) has no flow boundary :

$$\frac{\partial P}{\partial x} = 0, \tag{3.129}$$

$$\frac{\partial P}{\partial y} = 0,$$

2) The flow rate at the inner boundary (wellbore radius) is known. $q_w = q_g + q_c$.

3) Total fluid composition (Equation 3.128) is known.

3.5.8 ECLIPSE Two-Phase Pseudo Steady State HFW

The accuracy of the two-phase mathematical in-house simulator was confirmed by comparing its results with those of ECLIPSE300 at the same prevailing conditions.

The reservoir model in this exercise has the core properties of Texas Cream with porosity of 0.21 and permeability of 9.1 mD. The reservoir fluid is a binary mixture of C1 (methane) and n-C4 (normal butane) described in Table 3.3. The reservoir was 200 m in the X and 200 m in Y directions and 10 m in the Z direction. The fracture has a length of40 m and a width of 5mm. the fracture has a permeability of 146 D. The fractional flow at average reservoir pressure was the same for both simulators. In addition, the fine grid option of E300 has been used to capture the complexity of flow near the wellbore.

It should be noted that the k_r correlations used in Comsol and ECLIPSE300 simulators are different; therefore the base curve relative permeability has been used to describe the fluid mobility around the HFW. In order to achieve PSS conditions for the gas and

condensate flow in ECLIPSE (E300), first the pressure at the boundaries was kept constant by injecting gas condensate through 70 injection wells in this area, once steady state (SS) conditions were achieved, these injection wells were shut down and the HFW produces gas and condensate with a total constant reservoir flow rate. In E-300 simulator, the wellbore and volumetric average pressures were recorded at different time steps.

Then, these wellbore pressure values were used in the in-house simulator in order to calculate the volumetric average reservoir pressure for each time step.

It should be mentioned that achieving PSS conditions by natural depletion in the ECLIPSE model was very difficult. This was due to the very small size of time steps that was used to insure numerical stability and the significant time it takes for the model to complete the transient period (more than 30,000 time steps).

The volumetric average reservoir pressures (P_{ave}) calculated by ECLIPSE300 and the in-house simulator have been compared at different time steps. Figure 3.42 shows the good agreement between the two results. The arithmetic average absolute percentage deviation (AAD %) of the predicted P_{ave} (psi) values by the ECLIPSE simulator compared to those estimated by the HFW in-house simulator was 1.2 %.

3.5.9 Two-Phase Flow Pseudo-Steady State Total Skin

Earlier in this chapter, it has been shown that the skin formulation of HFW is similar under steady state (SS) and pseudo-steady state (PSS) conditions, for penetration ratio less than or equal 0.2 ($I_x \leq 0.2$). However, the skin formulations of (SS and PSS) are different for ($I_x > 0.2$), due to the difference in the parameter (ε) value (i.e. $\varepsilon_{ss} \neq \varepsilon_{pss} \rightarrow I_x > 0.2$).

Accordingly, it can be concluded that the two-phase PSS total skin formulation is similar to those of SS (presented in section 3.5.3) but with a different expression of (ε), as shown below,

$$S_t = \ln\left(\varepsilon_{pss} + \left(\frac{k_{rgb}}{k_{rg}}\right)_w \cdot \left(\frac{\pi}{C_{FD-base}} + \frac{\pi \cdot R_{ew}}{2C_{FD-base}}\right)\right). \tag{3.130}$$

For PSS conditions:

$$\varepsilon_{PSS} = 2 + \left(\frac{0.355 I_x}{1 - 0.704 I_x}\right) \tag{3.130a}$$

3.5.10 In-House 1-D Two-Phase Pseudo Steady State Open-Hole Simulator

A two-phase open-hole in-house simulator was developed to verify the integrity of the proposed approach of simulating two-phase flow around a single vertical well rather than the actual 2D geometry for PSS conditions. The modelling approach is similar to that used for single-phase flow; however the flow equations governing the gas and condensate flow were solved using finite difference method, as described below.

Governing Equations and Numerical Solution of EOH

For the radial model, a combination of continuity and gas and condensate flow equations (Equation 3.126) can be written as follows:

$$\nabla.\left[\frac{1}{r}.\left(\left[\frac{\rho k_r}{\mu}\right]_g+\left[\frac{\rho k_r}{\mu}\right]_c\cdot k\right).\frac{\partial p}{\partial r}\right]=\frac{d(\rho_{eqphase}\varphi)}{dt}. \tag{3.131}$$

The numerical differential form of above equation (3.131) is:

$$\frac{r_{i+1/2}}{\Delta r^2}\times.\left(\left[\frac{\rho k_r}{\mu}\right]_g+\left[\frac{\rho k_r}{\mu}\right]_c\cdot\frac{k}{\mu}\right)_{i+1}\times P_{i+1}-\left(\frac{r_{i+1/2}+r_{i-1/2}}{\Delta r^2}\right)\times\left(\left[\frac{\rho k_r}{\mu}\right]_g+\left[\frac{\rho k_r}{\mu}\right]_c.\frac{k}{\mu}\right)_i\times P_i+$$
$$\frac{r_{i-1/2}}{\Delta r^2}\times\left(\left[\frac{\rho k_r}{\mu}\right]_g+\left[\frac{\rho k_r}{\mu}\right]_c.\frac{k}{\mu}\right)_{i-1}\times P_{i-1}=\frac{\rho_{eqphase_w}q_w}{V} \tag{3.131}$$

$$z_j=\frac{\rho_g y_j GTR+\rho_c x_j(1-GTR)}{\rho_g GTR+\rho_c(1-GTR)}=cons. \tag{3.132}$$

The boundary conditions are:

1) At the outer boundary (external radius) there are no flow boundaries:
   $q_{ext} = 0$
2) The flow rate at the inner boundary (wellbore radius, q_{well}) is known.

Validation of PPS EOH simulator- Two Phase Flow

Figures 4.43 and 4.44 confirm the accuracy of the proposed approach by comparing the EOH calculated volumetric average reservoir pressure with those of the 2-D HFW in-house simulator. The rock used in here is Texas-cream with permeability of 9.1mD, two range of GTR_{well} has been tested (GTR_{well} =0.81 and 0.91). The reservoir model and other range of the variables are those listed in Table 3.2, HFW-24 and 25 data sets. The average absolute deviation error, AAD in this study is less than 2.2%.

3.6 SUMMARY AND CONCLUSIONS

A number of in-house simulators were developed to study the well performance of single layer hydraulically fractured wells (HFWs) in gas and gas condensate reservoirs. The simulator initially simulated both steady-state or pseudo-steady state flow around one planar HF but then for the first time, extended to two fractures intersecting the well at 90 degree angle. The models correctly account for the coupling (increase in kr by a decrease in IFT or increase in velocity) and inertia (decrease in kr by an increase in velocity) that affect the flow performance of gas condensate reservoirs. The integrity of the results of the in-house simulators were confirmed by comparing some of their results with those obtained using ECLIPSE with fine grid for the same prevailing flow conditions. Based on the assumption and results presented in chapter 3, the following conclusions can be drawn

1. Based on the pressure distribution maps around HFWs, it was shown that flow around high conductivity fractures is elliptical; however it converges to radial flow with decreasing fracture conductivity. These observations are consistent with literature studies (e.g. Prats 1961).
2. Based on the dimensionless velocity profile inside the fracture, it was shown that flow velocity across the fracture is uniform and directly proportional to dimensionless distance for high conductivity fractures ($24< C_{FD} >240$), while as fracture conductivity decreases ($0.24< C_{FD} >2.4$) the flow velocity decrease significantly in the farthest part of the fracture, however, it increases steeply in the area near to the wellbore.
3. It was shown that for small fracture conductivity ($C_{FD} \rightarrow$ zero) or small penetration ratio ($I_x < 0.2$) the geometric skin of HFW at steady-state conditions is the same as that at pseudo-steady state conditions, however, as fracture conductivity increase and the fracture penetration ratio is greater than 0.2 ($I_x > 0.2$), geometric skin of SS and PSS are different. These observations are in line with similar studies in the literature (e.g. Raghavan 1978).
4. New formulae (Equations 3.53 and 3.54) were developed for estimation of geometric skin of HFW intercepted by two perpendicular fractures at SS and PSS.
5. For Single phase Non-Darcy flow, it was explained that the inertia is dominant inside the fracture; while velocity effects inside the matrix are not

significant. These observations are consistent with literature studies (e.g. Guppy 1982).

6. Also, it was shown that Non-Darcy effects can manifest itself as a reduction in absolute fracture dimensionless conductivity $C_{FD.}$

7. A new more efficient formulation to estimate single phase effective dimensionless fracture conductivity ($C_{FD\text{-}eff}$) was proposed (Equation 3.67) based on the results of more than 1400 (Non-Darcy flow simulations) covering a wide range of pertinent geometrical and flow parameters. This approach was initially followed for a single-fracture model but then, for the first time, extended to multiple (two-perpendicular) fracture systems, which simplifies to single planner fracture system when the number of fracture is set to one.

8. A new and efficient formula (Equation 3.76) for single phase total skin of HFW was proposed benefiting from the newly developed ($C_{FD\text{-}eff}$) formula (Equation 3.67).

9. This total skin was used to estimate effective wellbore radius (Equation 3.78) for an equivalent open-hole (EOH) system replicating flow around HFWs.

10. Because of dependency of effective wellbore radius formulation to flow rate (Equation 3.78) an iterative procedure for using the developed formula for estimation of effective wellbore radius was proposed.

11. It was shown that for most practical cases of two phase flow, inertia is dominant inside the fracture, while coupling is more dominant inside the matrix. This is in line with similar observations made by Carvajal (2005) and Mahdiyar (2008) who worked in the GCR-HW research team.

12. Accordingly a new and efficient formula (Equation 3.110) was proposed to estimate two phase effective dimensionless fracture conductivity ($C_{FD\text{-}eff}$).

13. A new formula (Equation 3.113) for two phase total skin of HFW was proposed based on the newly developed two phase dimensionless fracture conductivity formula (Equation 3.110).

14. The proposed formulations are general, as it correctly extends to the single fracture case if the number of fracture is set to one. If gas fractional flow (GTR_{well}) is set to unity, it also correctly converts to the single phase gas systems under Non-Darcy flow, and if Reynolds number is small to that under Darcy flow.

15. The author developed a 1-D equivalent open-hole (EOH) simulator that incorporates the proposed effective wellbore radius formulation and associated iterative procedure to model gas condensate flow around HFW.
16. It was shown that the 1-D simulator can saves CPU time and reduces troubleshooting process associated with modelling such complex flow geometries using commercial compositional simulators.
17. The integrity of the 1-D simulator was verified by comparing its results with those of (fine grid) 2-D in-house simulator for more than (1600 simulation) covering a wide range of geometrical and flow parameters including single and two phase flow conditions for both single and two fracture systems considered here. It was also shown that the convergence rate for the incorporated iterative process acceptable (around 2-3 iterations for most studied cases), all making the proposed approach very attractive.
18. The close agreement between both simulators, highlight the added value of using 1-D simulator as a quick tool for long term performance prediction and reservoir sensitivity analysis.
19. The proposed formulations and procedures mentioned above are applicable to both steady state and pseudo-steady state conditions.

3.7 REFERENCES

McGuire, W. and Sikora V.: "The Effect of Vertical Fractures on Well Productivity" paper SPE 1618-G, JPT, **12**(10), pp.72-74, 1960.

Prats M.: "Effect of Vertical Fractures on Reservoir Behaviour-Incompressible Fluid Case", SPE Journal, **222**, pp. 105-118, June 1961.

Raghavan, R., Hadinoto, N.: "Analysis of Pressure Data for Fractured Wells: The Constant Pressure Outer Boundary" SPE 6015, SPE Journal, pp.139-149, April 1978.

Gringarten, A. C., Ramey, H.J., and Raghavan, R.: "Unsteady State Pressure Distributions Created by a Well with a Single Infinite-Conductivity Fractures" SPE Journal, pp 347-360, 1974.

Meyer B.R. and Jakot R.H.: "Pseudo-Steady State Analysis of Finite Conductivity Vertical Fractures", SPE 95941, Presented at SPE Annual Technical Conference, Texas, USA, 2005.

Holditch, S.A. and Morse, R.A.: "The Effects of Non-Darcy Flow on the Behaviour of Hydraulically Fractured Gas Wells," Journal of Petroleum Technology, pp 1169-1178, Oct. 1976.

Guppy K.H., Cinco-Ley H., Ramey Jr. H.J. and Samaneigo-V. F.: "Non-Darcy Flow in Wells with Finite-Conductivity vertical Fractures" SPE 8281, SPE Journal, pp. 681-698, Oct-1982.

Guppy K.H., Cinco-Ley H., and Ramey Jr. H. J.: "Pressure Build-up Analysis of Fractured Wells Producing at High Flow Rate" JPT, pp. 2656-2666, Nov-1982.

Giddley J.L.: "A Method for Correcting Dimensionless Fracture Conductivity for Non-Darcy Flow Effects" SPE 20710, SPE Production Engineering Journal, pp.391-394, Nov-1991.

Settari A., Bale A., Batchman R.C., Floisand V.: "General Correlation for the Effect of Non-Darcy Flow on Productivity of Fractured Wells" SPE 75715, presented at Gas Technology Symposium, Calgary, Canada, 2002.

Wang X., Indriati S., Valko P.P and Economides, M. J.: "Production Impairment and Purpose Built Design of Hydraulic Fracture in Gas Condensate Reservoirs," SPE 64749, presented at International Oil and Gas Conference and Exhibition, Beijing, China, November 2000.

Indriati, Sh., Wang, X., Economides, M., J.: "Adjustment of Hydraulic Fracture Design in Gas Condensate Wells" SPE 73751, presented at International Symposium and Exhibition on Formation Damage Control, Louisania, USA, 2002.

Mohan J., Pope G.A. and Sharma M. M.: "Effect of Non-Darcy Flow on Well Productivity of a Hydraulically Fractured Gas/Condensate Well" SPE 103025, presented at Gas Technology Symposium, Texas, USA, 2006.

Mahdiyar H., Jamiolahmadi M. and Sohrabi M.: "A New Flow Skin Factor Formulation for Hydraulically Fractured Wells in Gas Condensate Reservoirs", SPE113597, presented at Europec/EAGE Conference and Exhibition, Rome, Italy, June 2008.

Carvajal G.A., Danesh A., Jamiolahmady M. and Sohrabi M.: "The Impact of Pertinent Parameters on the Design of Hydraulic Fracturing in Gas Condensate Reservoirs" SPE 94074, presented at SPE Europech/EAGE annual Conference, Madrid, Spain, 2005.

Freddy H.; Djebbar Tiab, Sarfraz A.: "Pressure Analysis for a Well Intersected by a Hydraulic Fracture with Multiple Segments", SPE 71035 presented at SPE Rocky Mountain Petroleum Technology Conference, 21-23 May 2001, Keystone, Colorado

D.P. Restrepo, and D. Tiab:"Multiple Fractures Transient Response", SPE 121594 presented at the 2009 SPE Latin American and Caribbean Petroleum Engineering Conference held in Cartagena, Colombia, 31 May–3 June 2009.

Forchheimer, P.: Hydraulik, Chapter15, pp. 116-8, Leipzik and Berlin, 1914.

Jamiolahmady M. and Sohrabi M. , 2005: "Single-phase flow in and around perforation tunnel", IASME Transactions, Issue 7, Volume 2, pp 1288-1297.

Jamiolahmady M., Danesh A., Sohrabi M. and Duncan D. B, February 2006: "Flow around a rock perforation surrounded by damaged zone: Experiments vs. Theory", Journal of Petroleum Engineering and Science, 50 (2), pp. 102-114.

Jamiolahmady M., Sohrabi M., Ireland S., and Ghahri P., 2009: "A Generalized Correlation for Predicting Gas-Condensate Relative Permeability at near the Wellbore Conditions", Journal of Petroleum Science and Engineering.

Gas Condensate Recovery Project (2005-2008) Final Report, 2008, IPE, Heriot Watt University, UK.

Panteha Ghahri: "Modelling of Gas-Condensate Flow around Horizontal and Deviated wells and Cleanup Efficiency of Hydraulically Fractured Wells", PhD 2010, Heriot-Watt University.

Gas Condensate Recovery Project (2008-2011) Final Report, 2008, IPE, Heriot Watt University, UK.

Riley, M.F., Brigham, W.E., and Horne, R.N.: "Analytical Solutions for Elliptical Finite-Conductivity Fractures," SPE 22656, presented at SPE Annual Technical Conference and Exhibition, Dallas, USA, Oct. 1991.

Economides, M., Oligney, R., and Valko, P.: Unified Fracture Design, Orsa Press, Alvin, Texas, USA, (2002).

Jamiolahmady, M., Danesh, A., Rezaei, A., Ataei, R. and Sohrabi, M.: "Calculation of productivity of a gas condensate well: application of skin with rate dependent pseudo-pressure" SPE 94718, presented at Proceedings of the SPE European Formation Damage Conference, May 2005.

Cinco-Ley, H., Ramey Jr., H., Samaniego-V. F. and Dominguez A. N.: "Behaviour of Wells with Low-Conductivity Vertical Fractures" SPE 16776, presented at SPE Annual Technical Conference and Exhibition, Dallas, USA, 1987.

Jamiolahmady, M., Sohrabi, M. and Ireland, S.: "Gas Condensate Relative Permeabilities in Propped Fracture Porous Media: Coupling Versus Inertia", SPE 115726, Colorado, USA, September 2008.

Table 3.1: Basic Core Properties.

Core type	Porosity	Permeability (mD)	Single-phase Inertial factor (m^{-1})
RC1b	0.18	0.18	1.06E+12
Texas Cream	0.21	9.1	3.93E+9
Berea	0.185	110	1.85E+8

Table 3.1a: Basic Single Phase Gas Properties.

Specific Gravity, γ_g	Formation volume Factor B_g, Rm^3/Sm^3	Viscosity (cp)
0.7	0.0103	0.035

Table 3.2: Parameters of different HFWs studied in this work.

	HFW-1	**HFW-2**	**HFW-3**	**HFW-4**
Matrix Properties	k=9.1mD β=3.927E+9 m^{-1}	k=9.1mD β=3.927E+9 m^{-1}	k=110mD β=1.85E+8 m^{-1}	k=9.1mD β=3.927E+9 m^{-1}
Fracture Properties	k=146D β=3.5E+5 m^{-1}	k=146D β=3.5E+5 m^{-1}	k=146D β=3.5E+5 m^{-1}	k=146D β=3.5E+5
Fluid	Single phase Darcy	Single phase Darcy	Single phase Darcy	Single phase Darcy & Non-Darcy
Number of Data Points	4	19	4	12
Ix=xf/xe	0.5	0.05-0.98	0.5	0.25
W_f, mm	15	5-15	15	5-25
P_{wf}/psia	1000	1000	1000	1000
P_{ext}/psia	1500	1500	1500	1500
GTR_{well}	1	1	1	1
Comments	Single Fracture Steady-State (SS)	Single Fracture (SS)	Multiple Fracture (SS)	Single Fracture (SS)

Table 3.2: Parameters of different HFWs studied in this work.

	HFW-5	**HFW-6**	**HFW-7**
Matrix Properties	k=9.1mD β=3.927E+9 m-1	k=0.18mD β=1.06E+12 m^{-1}	k=9.1mD β=3.927E+9 m^{-1}
Fracture Properties	k=146D β=3.5E+5 m-1	k=146D β=3.5E+5 m^{-1}	k=146D β=3.5E+5 m^{-1}
Fluid	Single phase Non-Darcy	Single phase Non-Darcy	Single phase Non-Darcy
Number of Data Points	1	156	182
Ix=xf/xe	0.1-0.9	0.1-0.95	0.1-0.95
W_f, mm	5	5-15	5-15
P_{wf}/psia	1500	1000	1500
P_{ext}/psia	2000	2000	2000
GTR_{well}	1	1	1
Comments	Single Fracture (SS)	Single Fracture (SS)	Single Fracture (SS)

Table 3.2: Parameters of different HFWs studied in this work.

	HFW-8	**HFW-9**	**HFW-10**
Matrix Properties	k=0.18mD β=1.06E+12 m^{-1} 1	k=9.1mD β=3.927E+9 m^{-1}	k=110mD β=1.85E+8 m^{-1}
Fracture Properties	k=146D β=3.5E+5 m^{-1}	k=146D β=3.5E+5 m^{-1}	k=146D β=3.5E+5 m^{-1}
Fluid	Single phase Non-Darcy	Single phase Non-Darcy	Single phase Non-Darcy
Number of Data Points	300	290	500
Ix=xf/xe	0.1-0.95	0.1-0.95	0.1-0.95
W_f, mm	5-10	5-10	5-15
P_{wf}/psia	1200-800	1800-1200	1900
P_{ext}/psia	1800-1500	2000	2000
GTR_{well}	1	1	1
Comments	Multiple Fracture (SS)	Multiple Fracture (SS)	Single & Multiple Fracture (SS)

Table 3.2: Parameters of different HFWs studied in this work.

	HFW-11	**HFW-12**	**HFW-13**	**HFW-14**
Matrix Properties	k=9.1mD β=3.927E+9 m-1	k=9.1mD β=3.927E+9 m-1	k=9.1mD β=3.927E+9 m-1	k=9.1mD β=3.927E+9 m-1
Fracture Properties	k=146D β=3.5E+5 m-1	k=146D β=3.5E+5 m-1	k=146D β=3.5E+5 m-1	k=146D β=3.5E+5 m-1
Fluid	Two phase	Two phase	Two phase	Two phase
Number of Data Points	1	1	1	1
Ix=xf/xe	0.20	0.20	0.20	0.20
W_f, mm	5	5	5	5
P_{wf}/psia	1650	1350	900	1650
P_{ext}/psia	1850	1850	1850	1850
GTR_{well}	0.71	0.81	0.91	0.71
Comments	Single Fracture (SS)	Single Fracture (SS)	Single Fracture (SS)	Single Fracture (SS)

Table 3.2: Parameters of different HFWs studied in this work.

	HFW-15	**HFW-16**	**HFW-17**	**HFW-18**
Matrix Properties	k=9.1mD β=3.927E+9 m^{-1}	k=9.1mD β=3.927E+9 m^{-1}	k=110mD β=1.85E+8 m^{-1}	k=110mD β=1.85E+8 m^{-1}
Fracture Properties	k=146D β=3.5E+5 m^{-1}	k=146D β=3.5E+5	k=146D β=3.5E+5 m^{-1}	k=146D β=3.5E+5 m^{-1}
Fluid	Two phase	Two phase	Two phase	Two phase
Number of Data Points	1	1	1	10
Ix=xf/xe	0.20	0.20	0.20	0.1-0.98
W_f, mm	5	5	5	5
P_{wf}/psia	900	1700	1700	1650
P_{ext}/psia	1100	1850	1850	1850
GTR_{well}	0.71	0.683	0.683	0.71
Comments	Single Fracture (SS)	Single Fracture (SS)	Single Fracture (SS)	Single Fracture (SS)

Table 3.2: Parameters of different HFWs studied in this work.

	HFW-19	**HFW-20**	**HFW-21**	**HFW-22**
Matrix Properties	k=110mD β=1.85E+8 m^{-1}	k=9.1mD β=3.927E+9 m^{-1}	k=110mD β=1.85E+8 m^{-1}	k=9.1mD β=3.927E+9 m^{-1}
Fracture Properties	k=146D β=3.5E+5 m^{-1}	k=146D β=3.5E+5	k=146D β=3.5E+5 m^{-1}	k=146D β=3.5E+5
Fluid	Two phase	Two phase	Two phase	Two phase
Number of Data Points	10	100	60	100
Ix=xf/xe	0.1-0.98	0.1-0.98	0.1-0.98	0.1-0.98
W_f, mm	5	5-15	5-15	5-15
P_{wf}/psia	1350	900-1650	900-1650	900-1650
P_{ext}/psia	1850	1850	1850	1850
GTR_{well}	0.81	0.71-0.91	0.71-0.91	0.71-0.91
Comments	Single Fracture (SS)	Single Fracture (SS)	Single Fracture (SS)	Multiple Fracture (SS)

Table 3.2: Parameters of different HFWs studied in this work.

	HFW-23	**HFW-24**	**HFW-25**
Matrix Properties	k=110mD β=1.85E+8 m^{-1}	k=9.1mD β=3.927E+9 m^{-1}	k=110mD β=1.85E+8 m^{-1}
Fracture Properties	k=146D β=3.5E+5 m^{-1}	k=146D β=3.5E+5	k=146D β=3.5E+5 m^{-1}
Fluid	Two phase	Two phase	Two phase
Number of Data Points	100	4	4
Ix=xf/xe	0.1-0.98	0.25	0.25
W_f, mm	5-15	5-15	5-15
P_{wf}/psia	900-1650	1350	900
P_{ext}/psia	1850	--	--
GTR_{well}	0.71-0.91	0.81	0.91
Comments	Multiple Fracture (SS)	Single Fracture (PSS)	Single Fracture (PSS)

Table 3.3: Properties of the mixture C1-C4, %C1: 73.6%, P_{Dew}=1865 psi.

P(psi)	**x1**	**y1**	ρ_c **(kg/m^3)**	ρ_g **(kg/m^3)**	μ_c **cp**	μ_g **cp**	**IFT mN.m**
1865	0.4195	0.4195	223.3	223.3	0.0261	0.0261	0
1850	0.3521	0.5049	307.5	220.5	0.0398	0.0255	0.008
1840	0.343	0.5146	317.4	211.4	0.0405	0.0249	0.036
1800	0.3069	0.5535	341.1	188.7	0.0431	0.0211	0.112
1790	0.3018	0.5583	345.1	184.8	0.0474	0.0206	0.149
1750	0.2814	0.5776	359.5	171.3	0.0462	0.0195	0.2809
1700	0.2609	0.5944	374.7	157.4	0.0491	0.0184	0.4318
1650	0.2444	0.6088	387	146.5	0.052	0.0176	0.5785
1600	0.2279	0.6232	397.8	137.8	0.0549	0.017	0.7329
1565	0.2192	0.6297	404	132.6	0.0601	0.0172	0.852
1500	0.203	0.6418	421.76	118.39	0.0608	0.016	1.1106
1400	0.1821	0.655	438.62	106.44	0.0669	0.0152	1.5938
1250	0.154	0.6664	459.64	91.27	0.0762	0.0144	2.3971
1200	0.1452	0.669	466.06	86.68	0.0793	0.0141	2.6907
1000	0.1136	0.6712	487.63	69.89	0.0908	0.0133	3.9239
800	0.0859	0.664	505.63	54.71	0.1015	0.0126	5.2907
600	0.0604	0.6335	522.29	41.17	0.1121	0.012	6.8104
500	0.0484	0.605	530.06	34.86	0.1173	0.0117	7.6186
400	0.0368	0.5636	537.53	28.78	0.1234	0.0114	8.4582
300	0.0257	0.4985	544.48	22.93	0.1283	0.0111	9.3119
200	0.0152	0.3948	551.22	17.16	0.133	0.0106	10.2085
150	0.01	0.3128	554.66	14.33	0.1356	0.0101	10.6795
100	0.0049	0.1901	557.94	11.55	0.1383	0.0094	11.15
80	0.0029	0.123	559.11	10.45	0.1393	0.009	11.3299

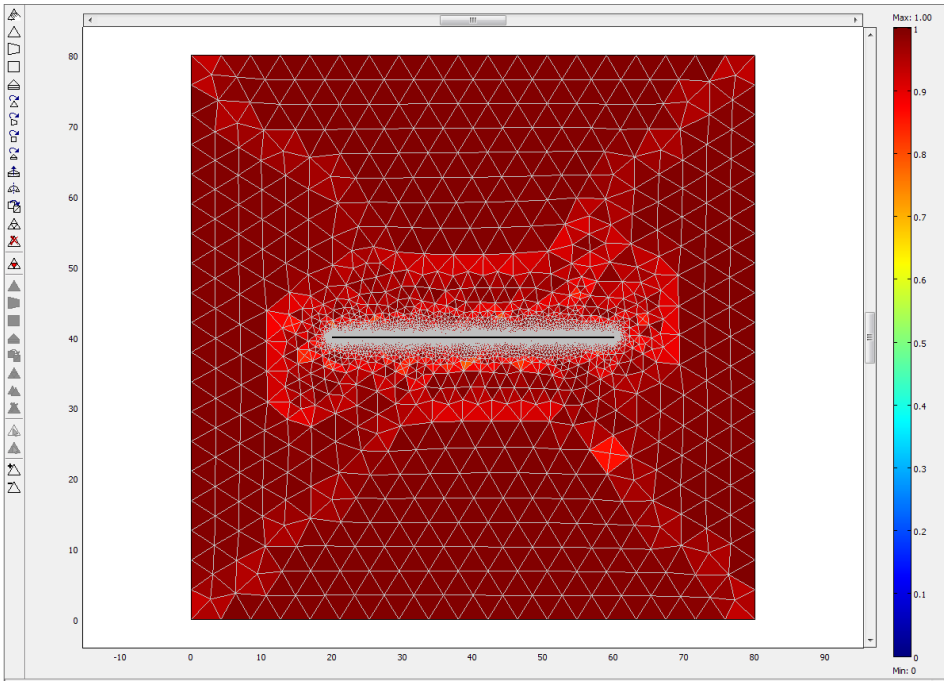

(a)

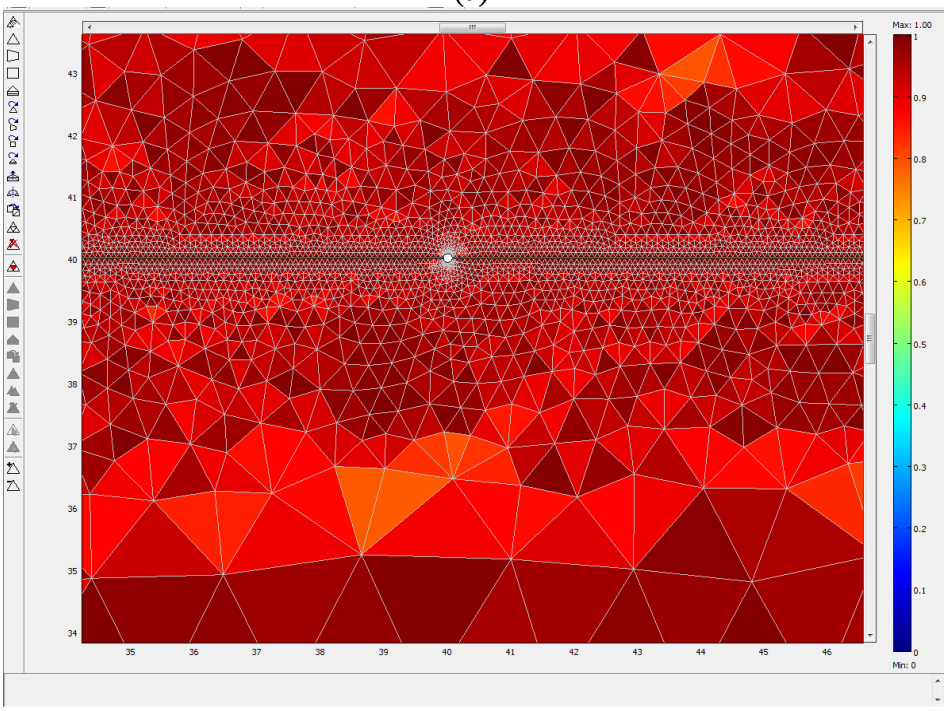

(b)

Figure 3.1 Mesh File quality for HFW (a) whole model, (b) Zoom-in in the area inside and around the fracture

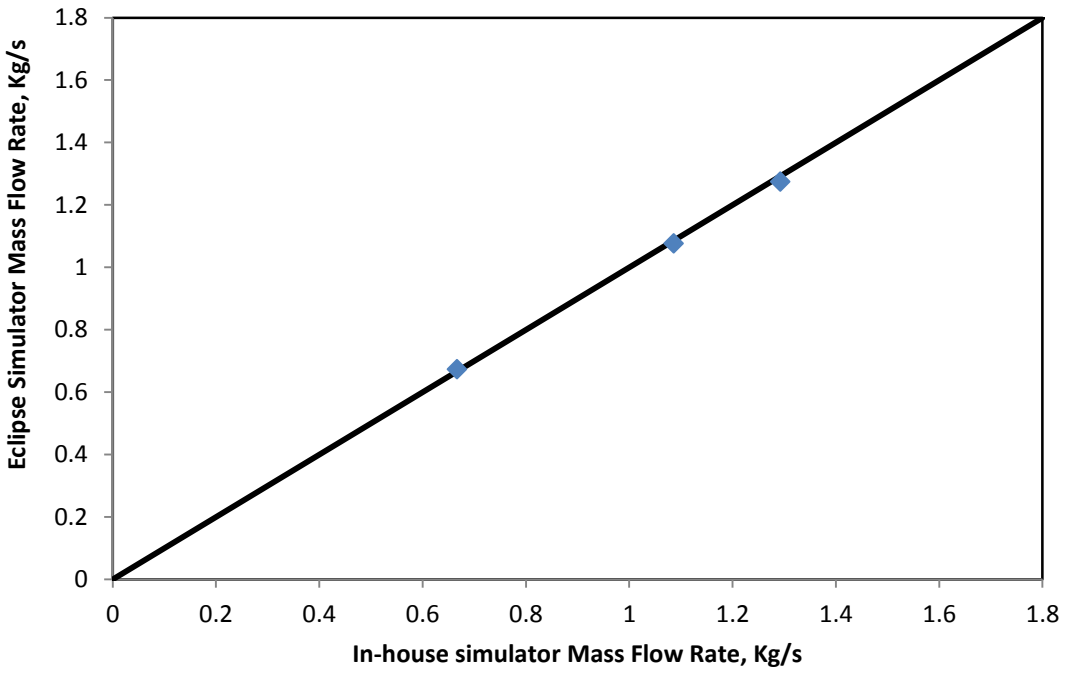

Figure 3.2 Comparison between the mass flow rates estimated using the 2D HFW in-house simulator and those of ECLIPSE E100 simulator, single phase Steady State Darcy flow.

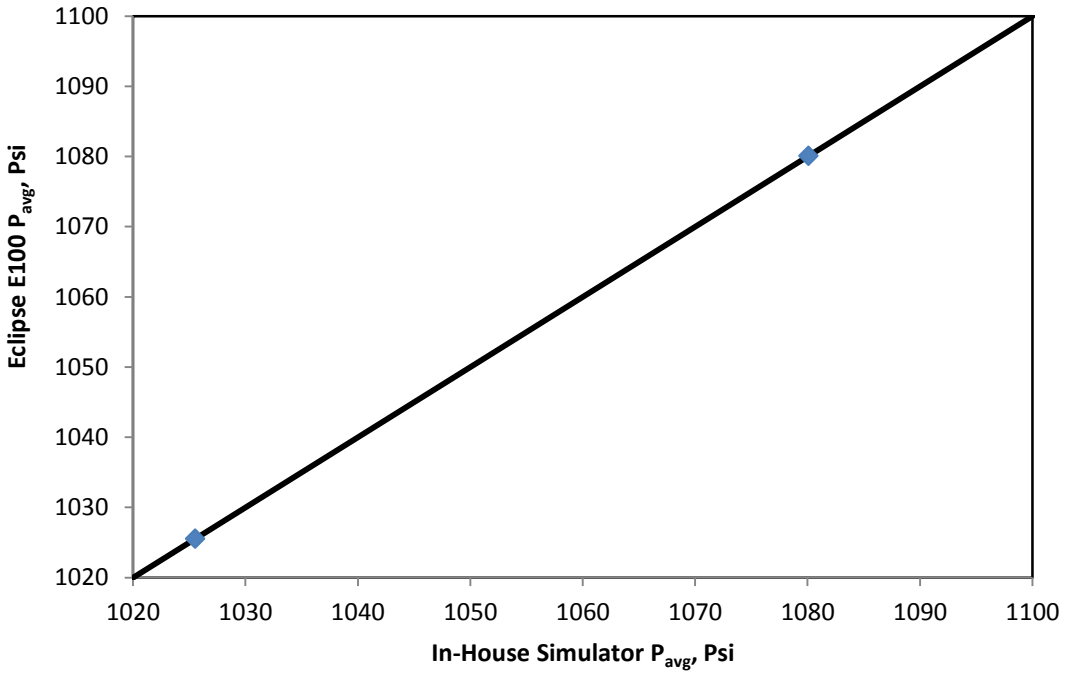

Figure 3.3 Comparison between the volumetric Average Reservoir Pressures estimated using the 2D HFW in-house simulator and those of ECLIPSE E100 simulator, single phase Pseudo-Steady State Darcy flow.

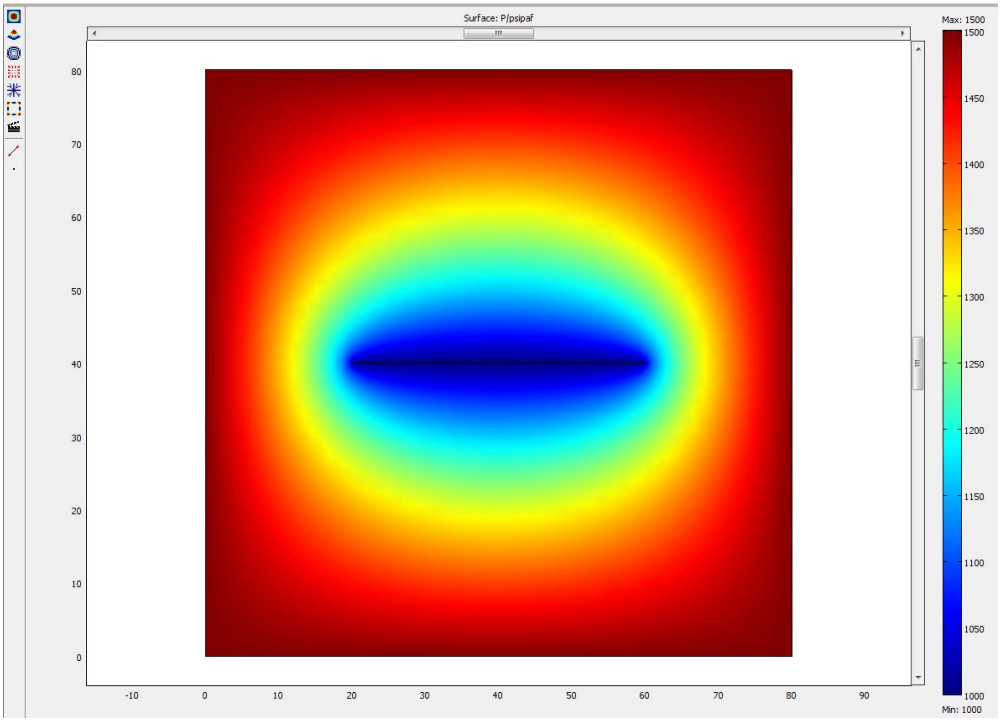

Figure 3.4 Pressure distribution around Single hydraulic Fracture intersecting vertical well, CFD =240

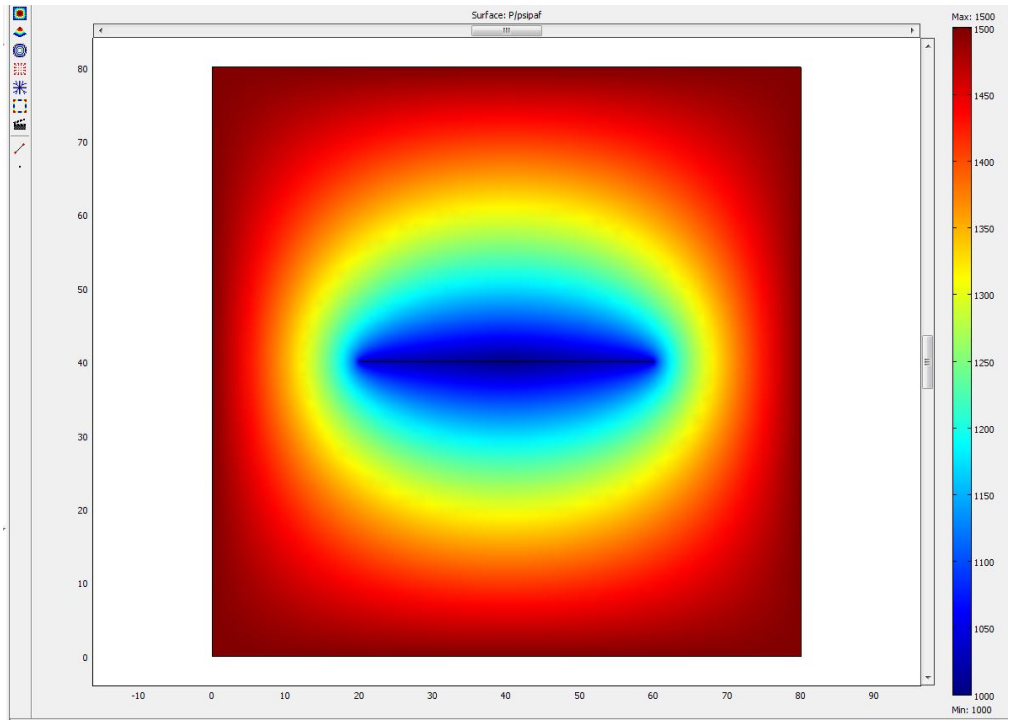

Figure 3.5 Pressure distribution around Single hydraulic Fracture intersecting vertical well, CFD =24.

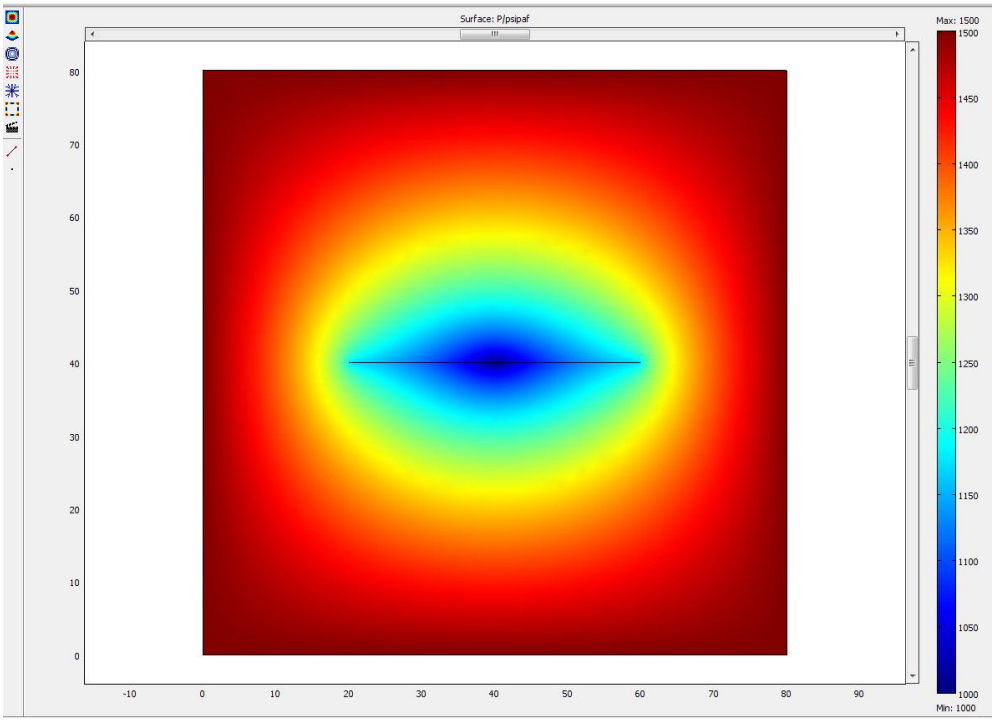

Figure 3.6 Pressure distribution around Single hydraulic Fracture intersecting vertical well, CFD =2.40.

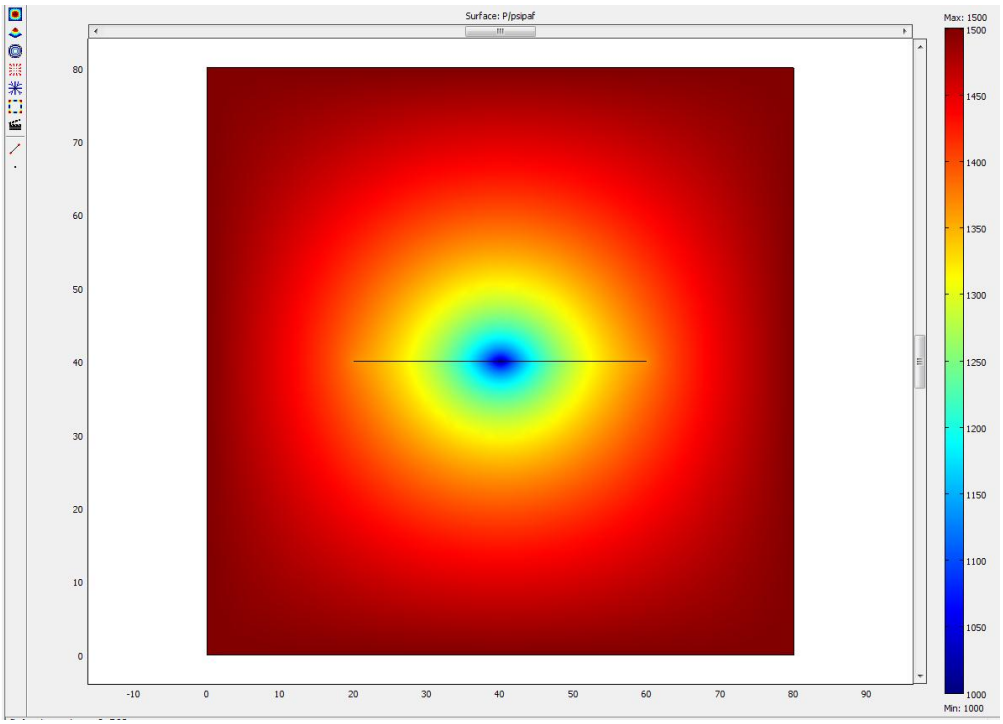

Figure 3.7 Pressure distribution around Single hydraulic Fracture intersecting vertical well, CFD =0.240.

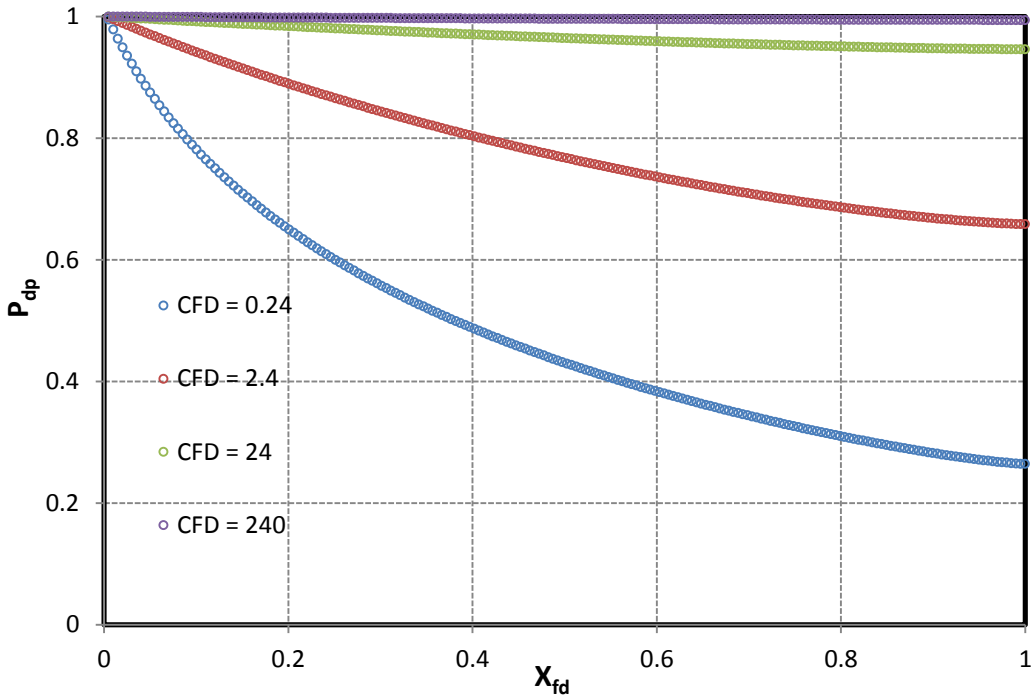

Figure 3.8 Dimensionless Pressure drop inside the fracture for different C_{FD} values

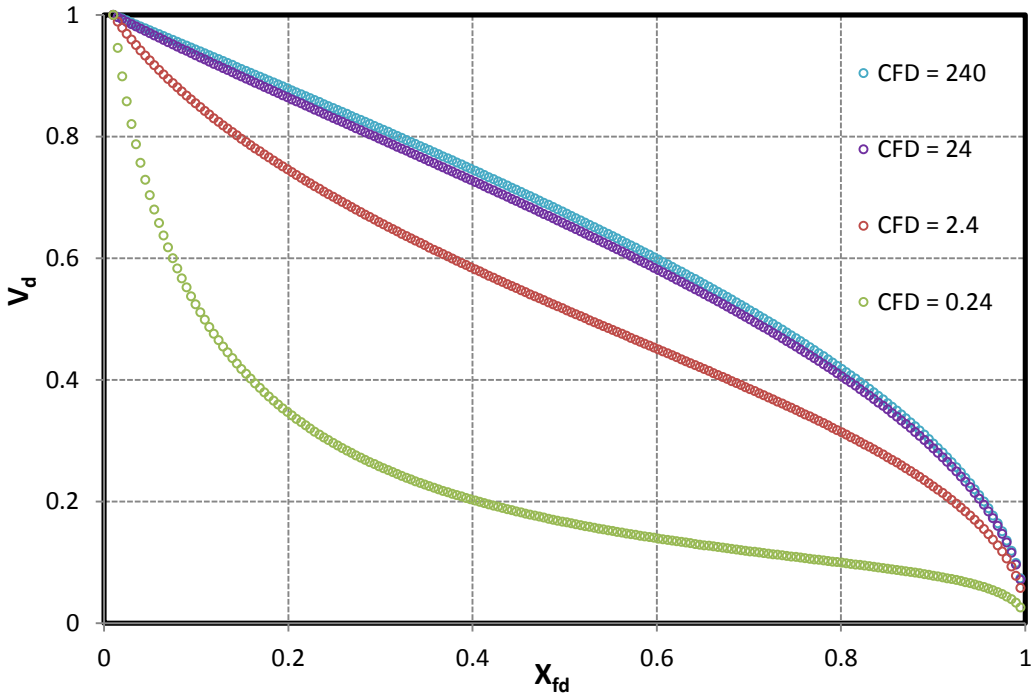

Figure 3.9 Dimensionless Velocity profile inside the fracture for different C_{FD} values

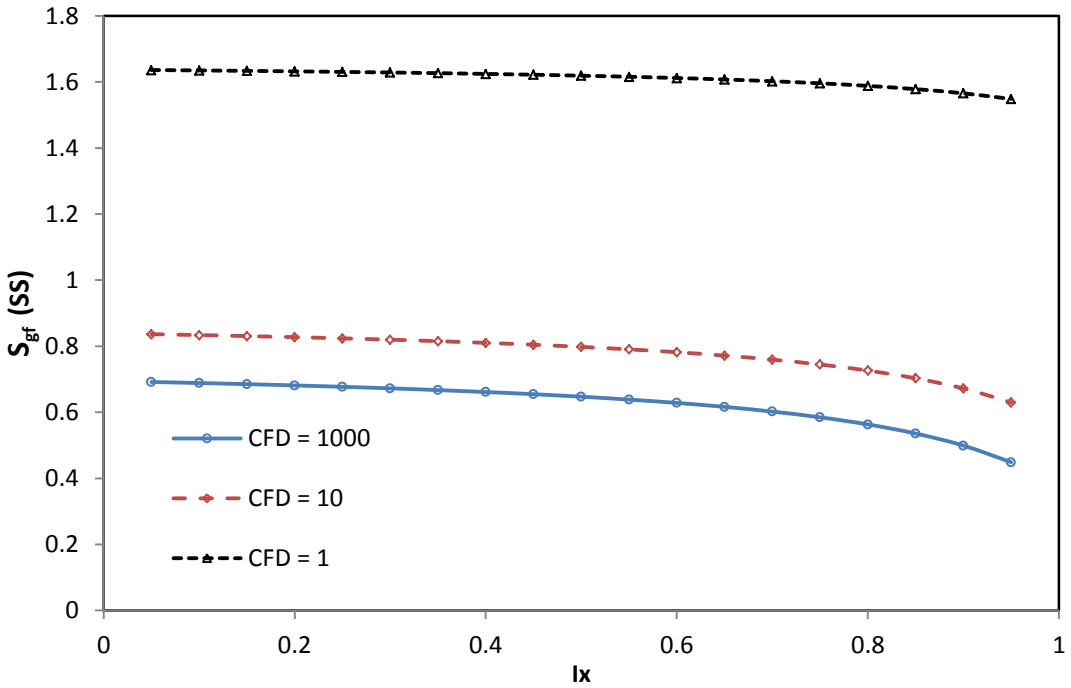

Figure 3.10 Fracture Geometric skin as a function of dimensionless fracture conductivity C_{FD} and penetration ratio $I_{x.}$ Obtained using the Steady State in-house Simulator.

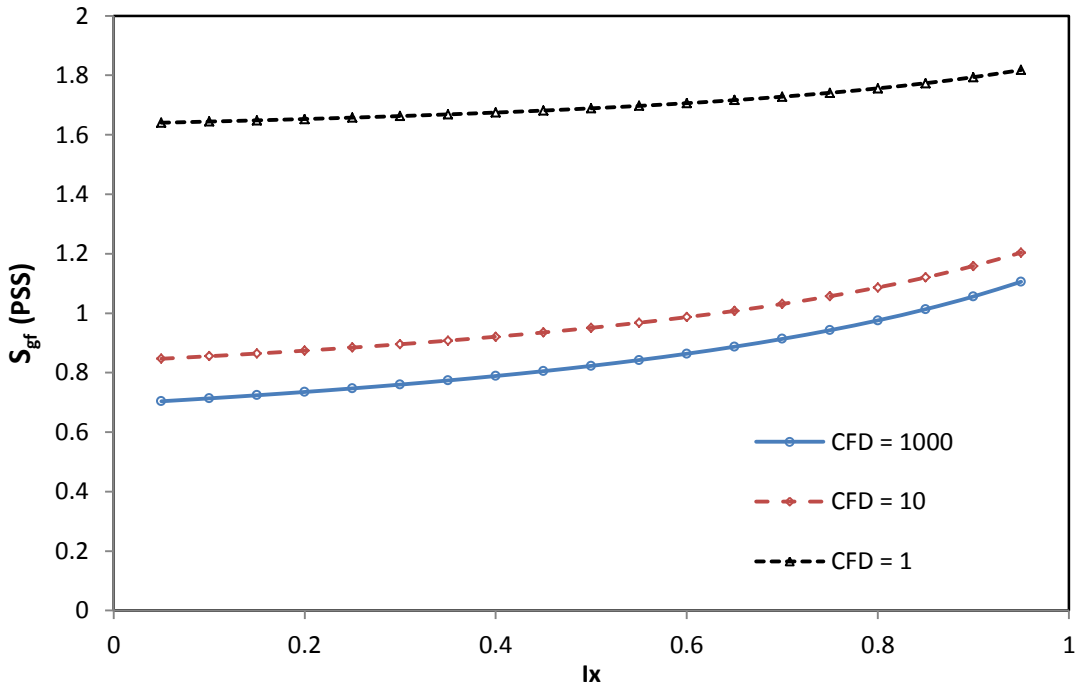

Figure 3.11 Fracture Geometric skin as a function of dimensionless fracture conductivity C_{FD} and penetration ratio $I_{x.}$ Obtained using the Pseudo-Steady State in-house Simulator.

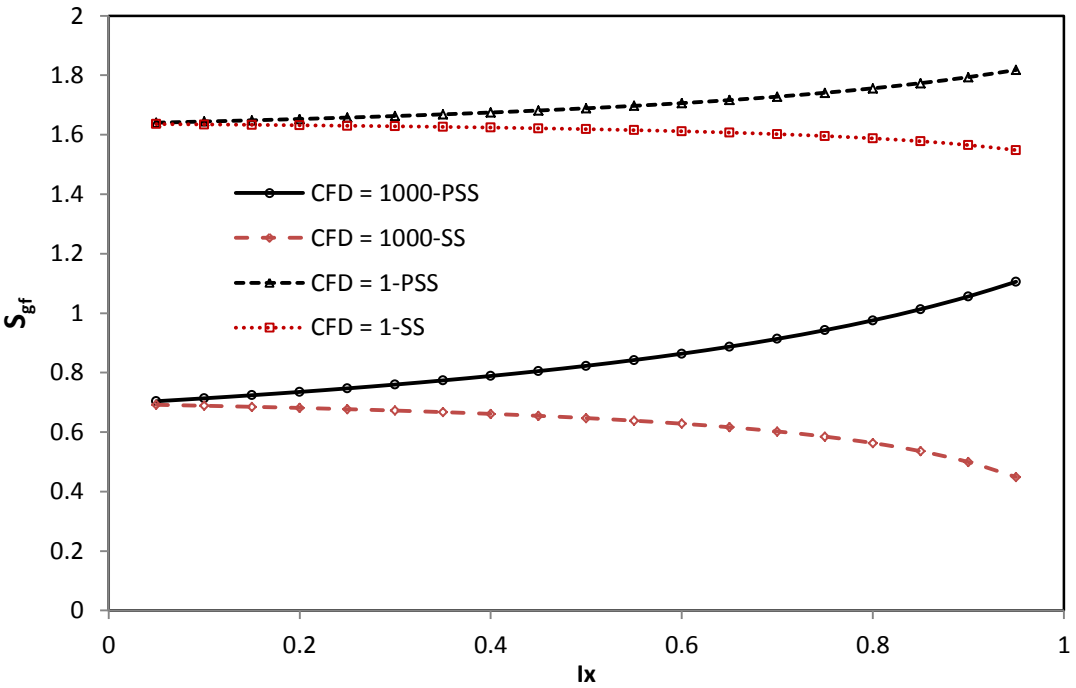

Figure 3.12 Fracture Geometric skin for high and low dimensionless fracture conductivity C_{FD} Steady State and pseudo-steady state Conditions

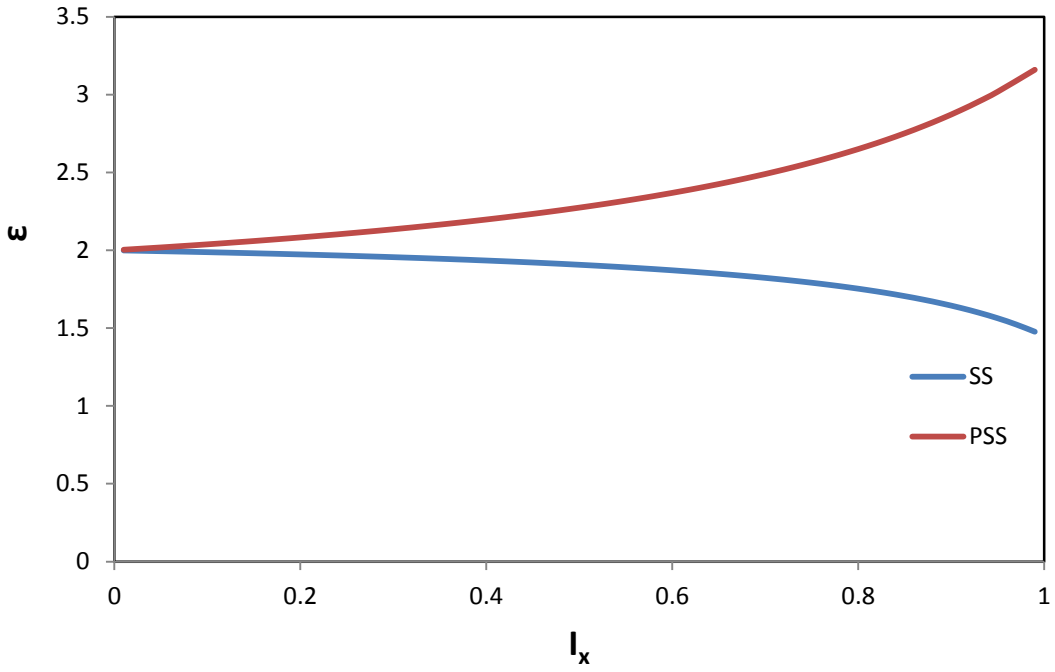

Figure 3.13 Variation of the parameter ε with penetration ratio, Equations 3.44 and 3.45.

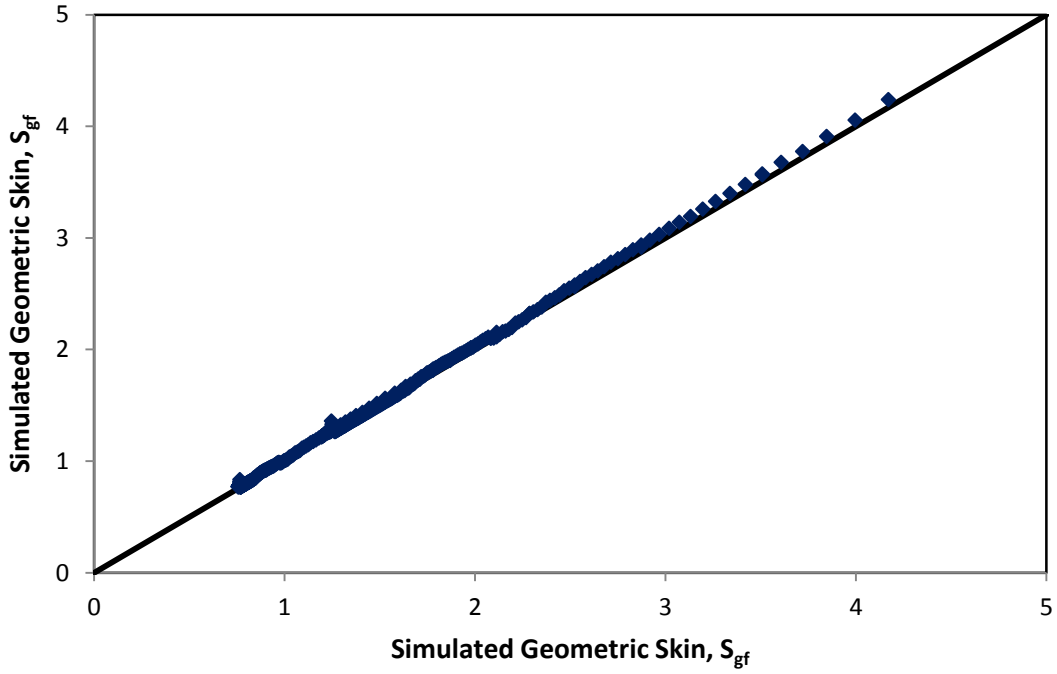

Figure 3.14 Comparison between the geometric skin obtained using the in-house and those estimated from Equation 3.46 and 3.47, single phase Darcy flow.

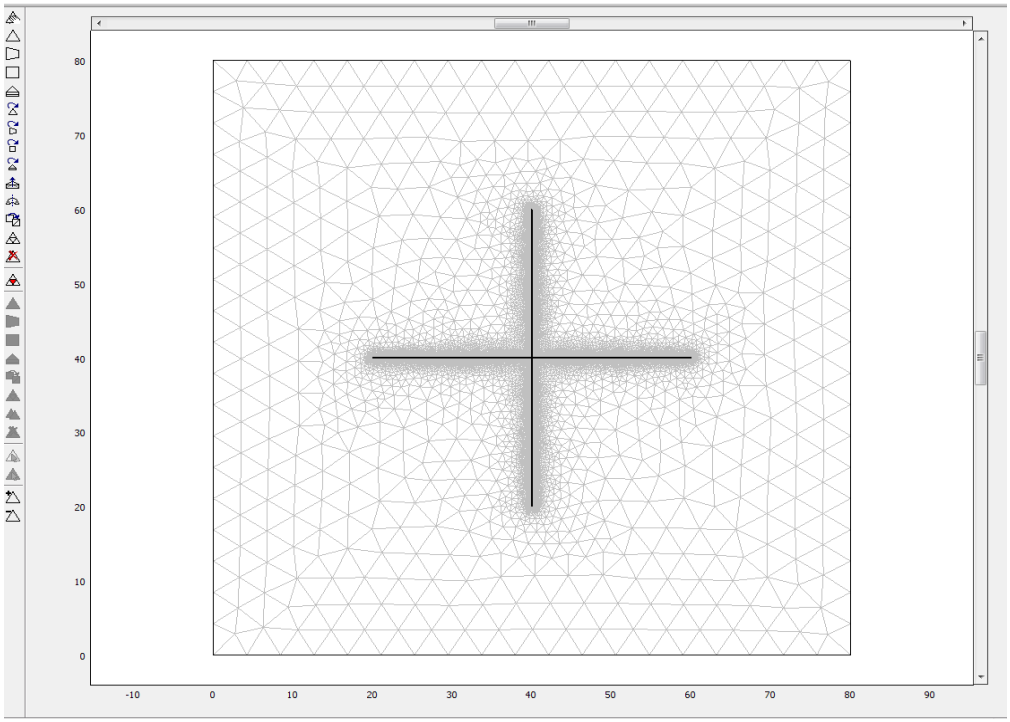

Figure 3.15 Mesh file of Multiple HFW used in this study

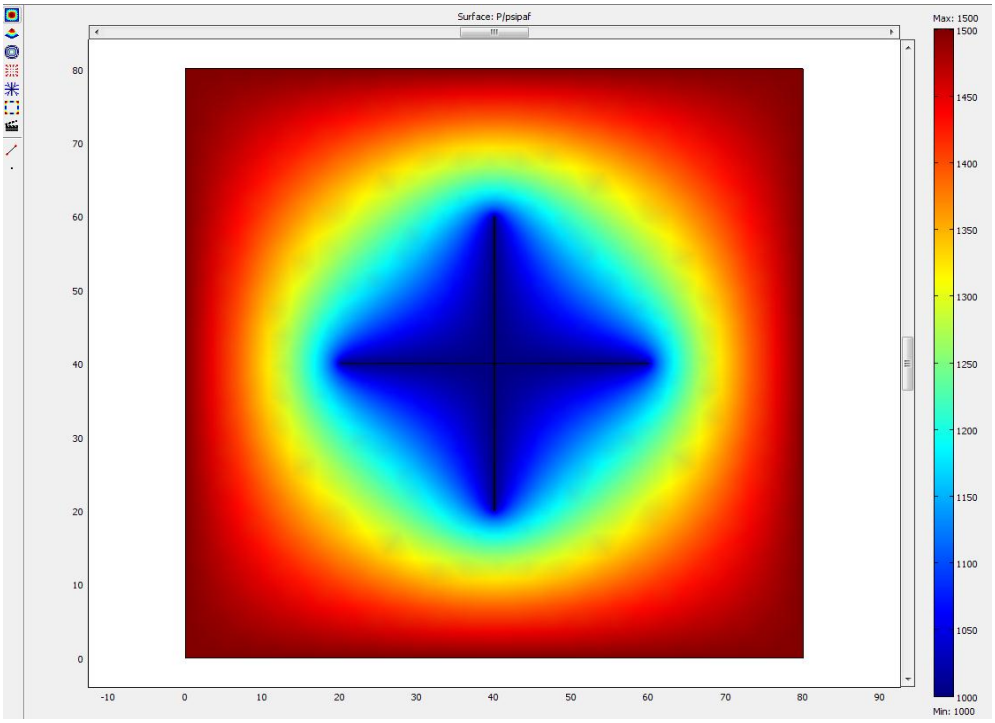

(a)

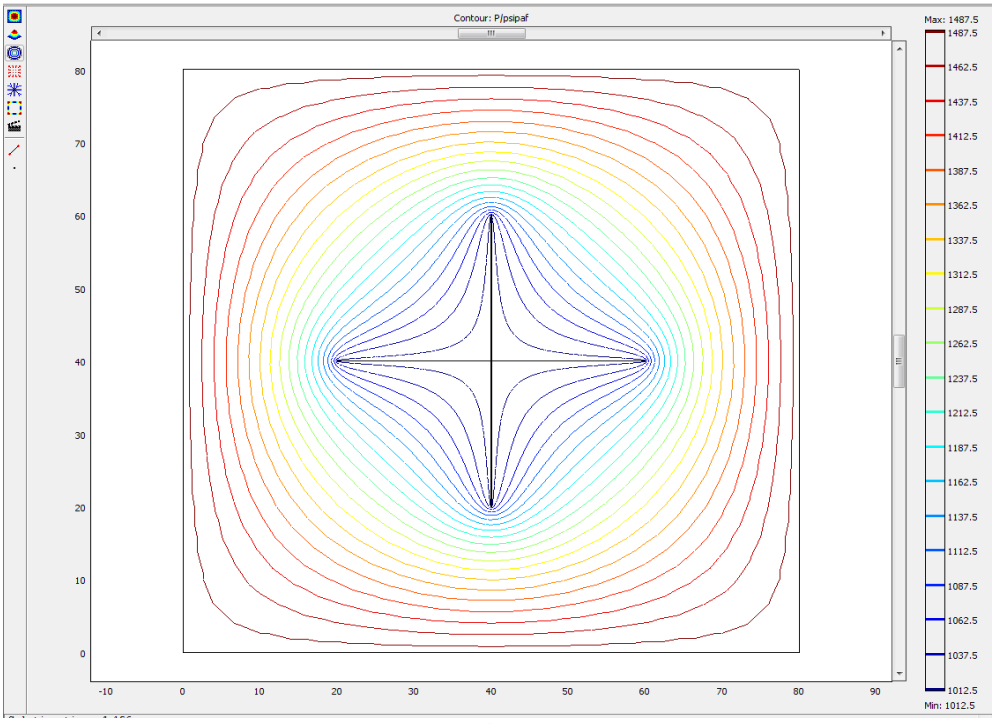

(b)

Figure 3.16 Pressure distributions around Multiple Fractured Well CFD =240, (a) surface map, (b) Counter map.

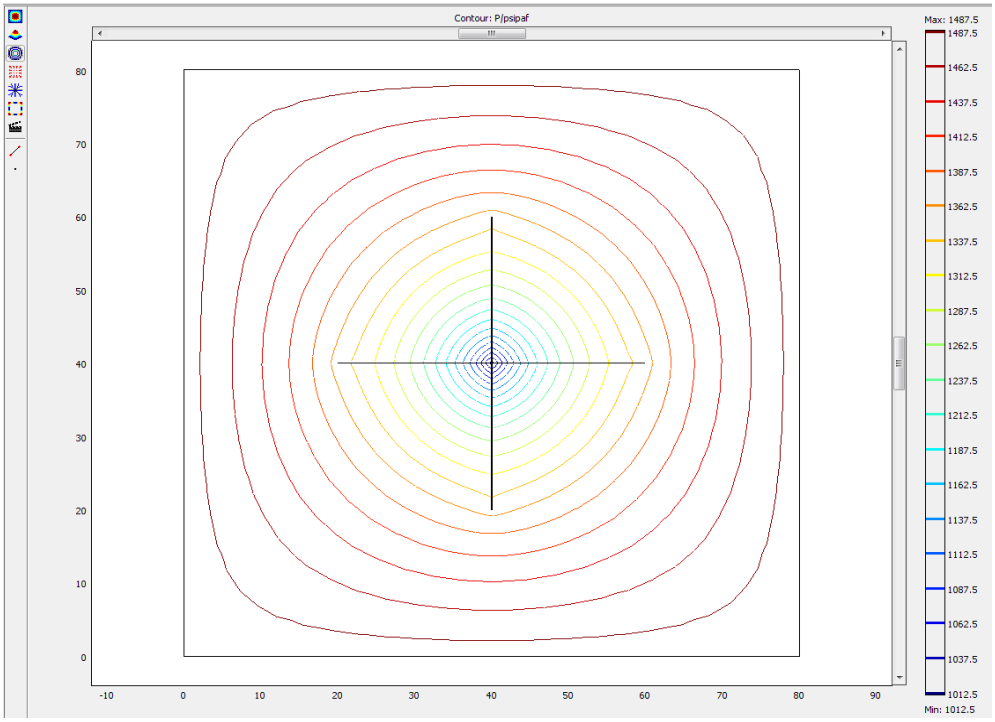

Figure 3.17 Pressure distributions around Multiple Fractured Well CFD =0.24

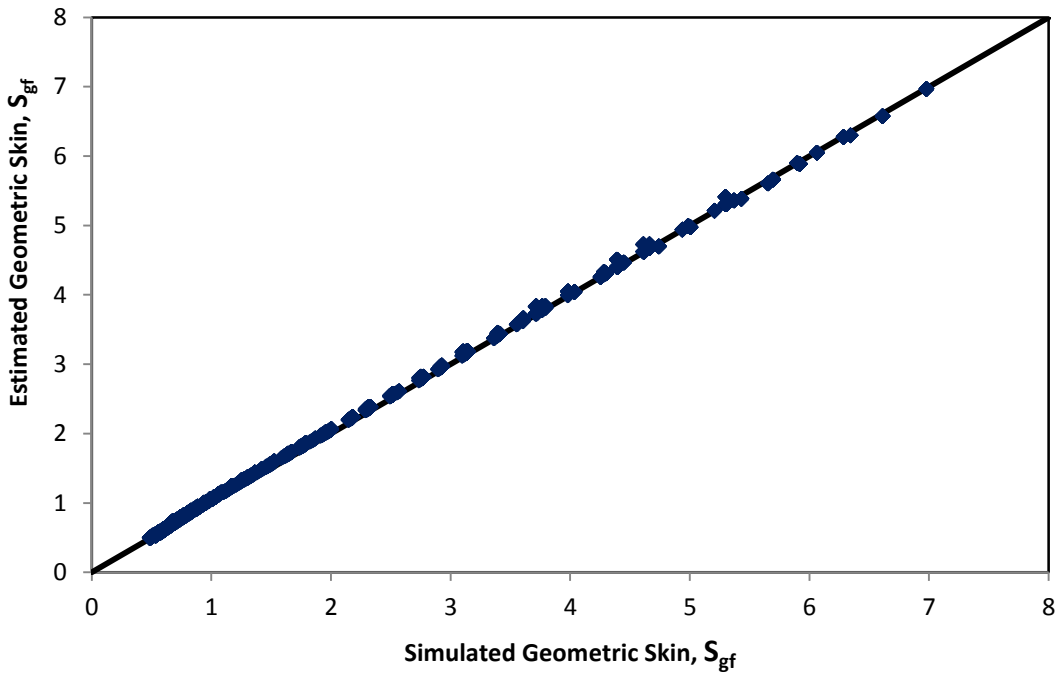

Figure 3.18 Comparison between the geometric skins obtained using the in-house and those estimated from Equations 3.53 and 54, single phase Darcy flow, (Two Identical Fractures)

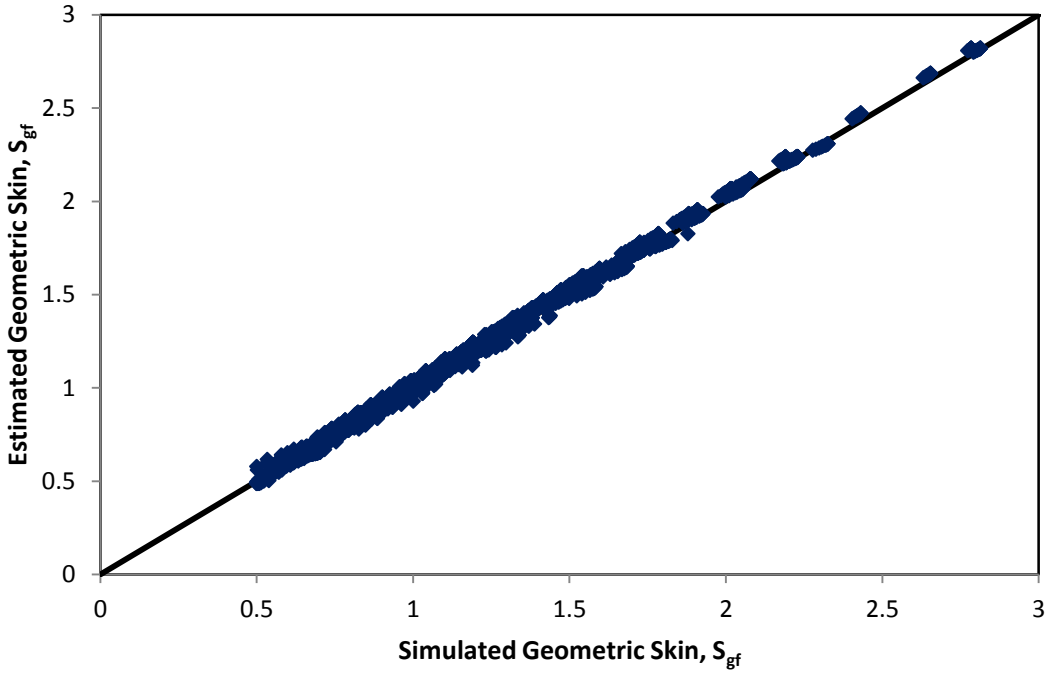

Figure 3.19 Comparison between the geometric skins obtained using the in-house and those estimated from Equations 3.53 and 54, single phase Darcy flow, (Two Non-Identical Fractures)

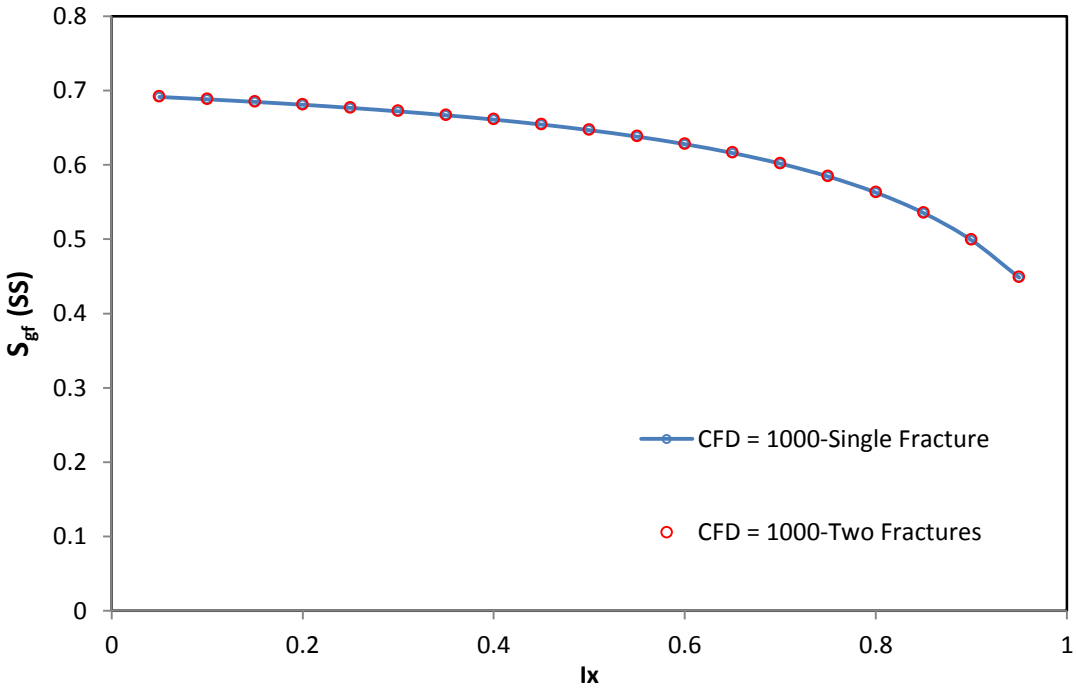

Figure 3.20 Difference between Geometric skin of Single and Multiple fractures, infinite conductivity fracture

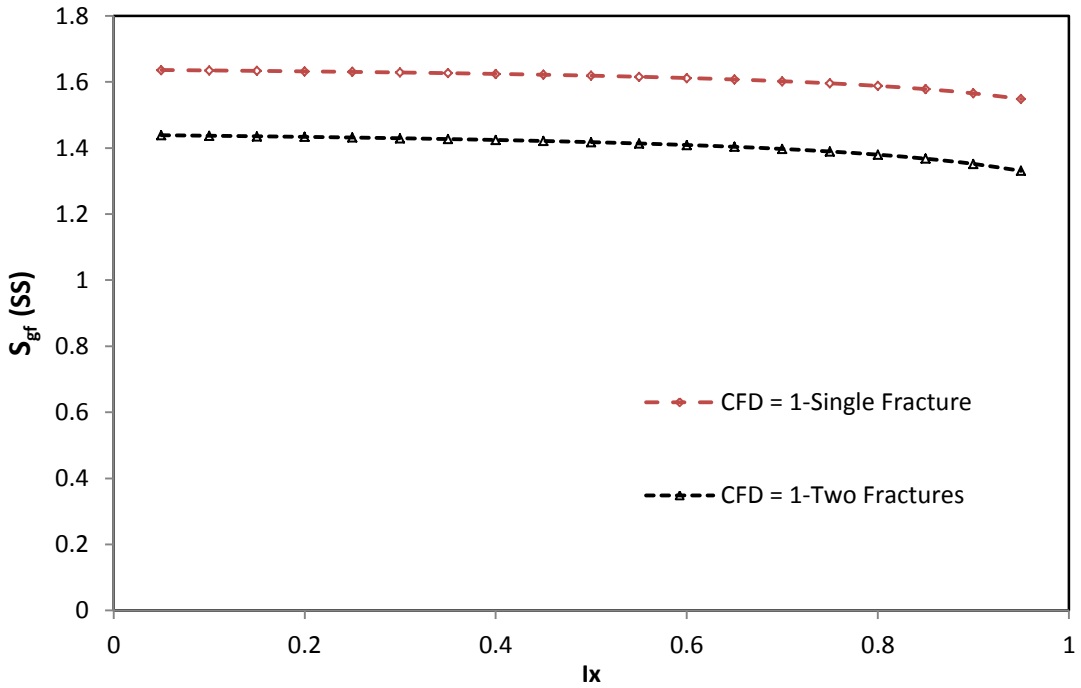

Figure 3.21 Difference between Geometric skin of Single and Multiple fractures, low conductivity fracture.

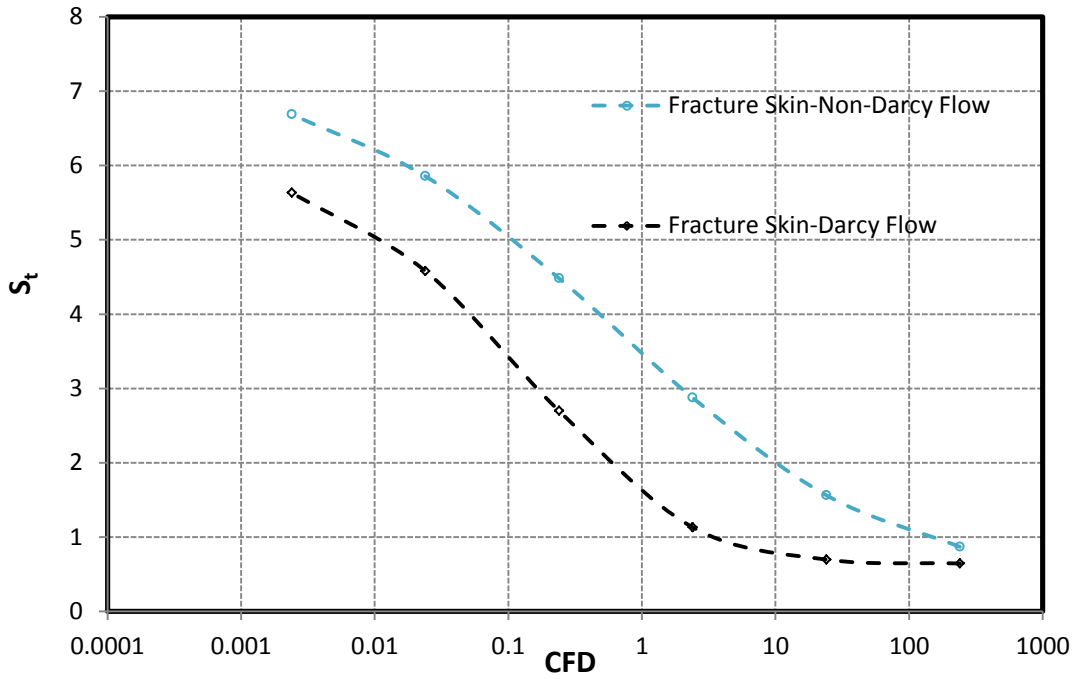

Figure 3.22 effect of Non-Darcy flow on Single phase Total skin for different fracture conductivity values, for a pressure drop of DP = 500Psi, HFW-4.

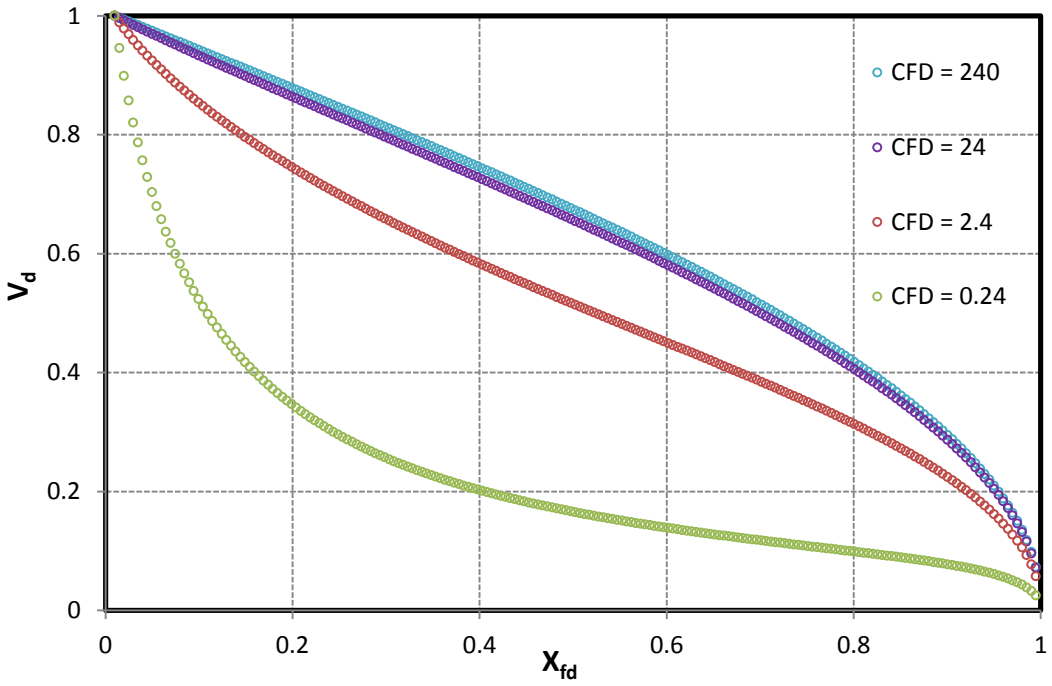

(a)

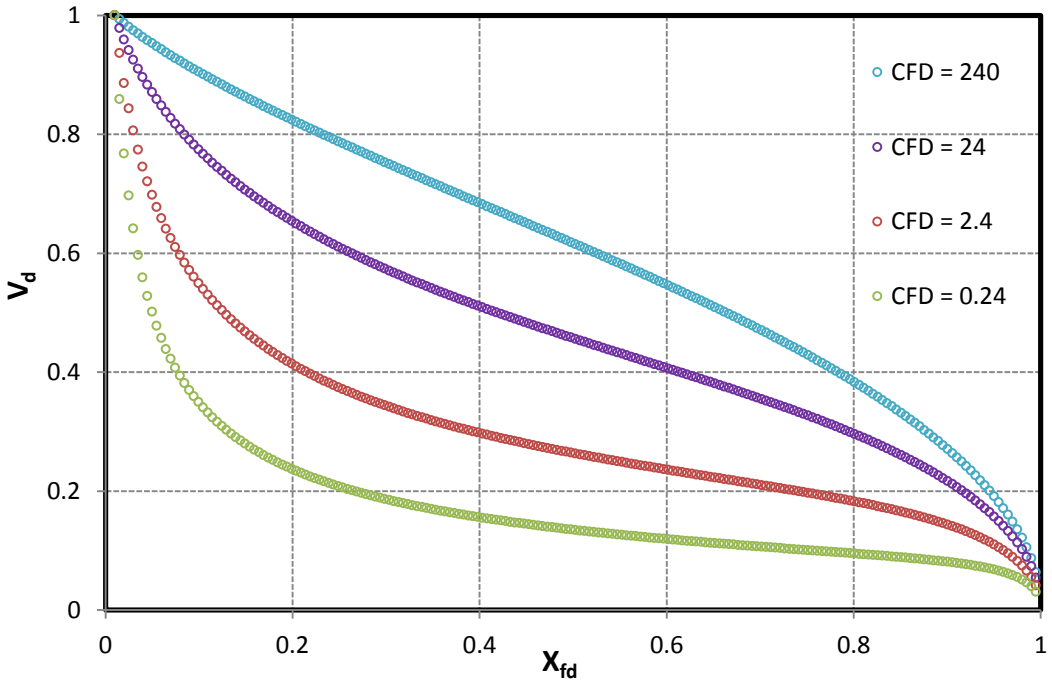

(b)

Figure 3.23 Dimensionless Velocity profiles for different absolute fracture conductivities inside the fracture (a) Darcy Flow, (b) Non-Darcy Flow.

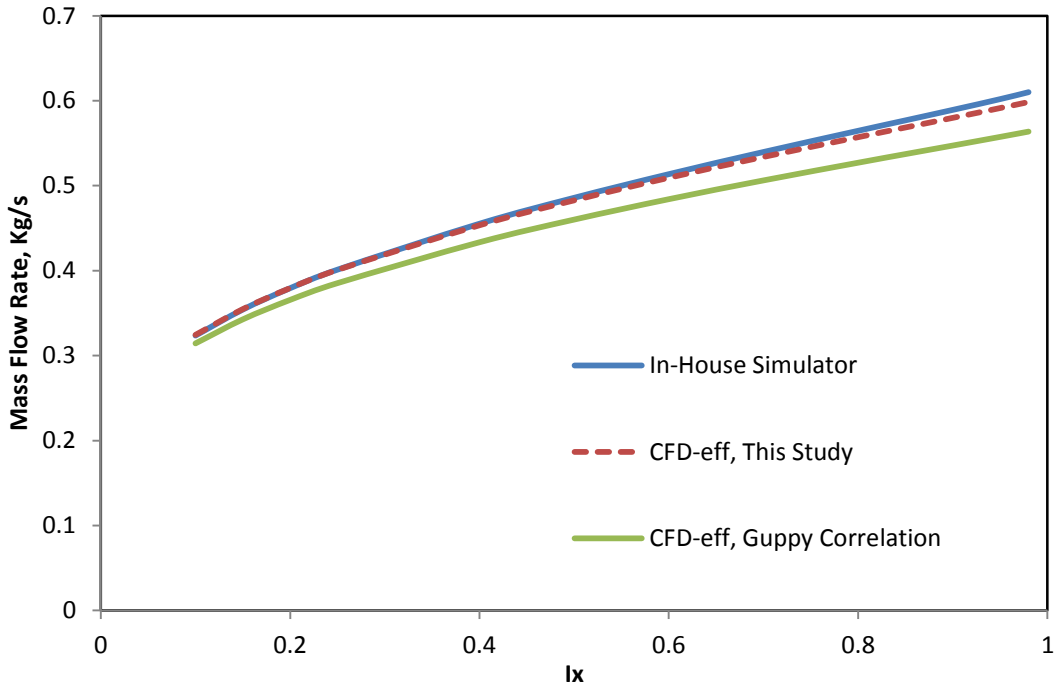

Figure 3.24 Calculated mass flow rates using EOH model with effective dimensionless fracture conductivity calculated using the proposed $C_{FD\text{-}eff}$ formulation (Equation 3.67) and Guppy's Correlation (Equation 3.70) versus the corresponding values estimated by the 2D in-house simulator, Average wellbore Reynolds Number R_{ew} = 45, HFW-5.

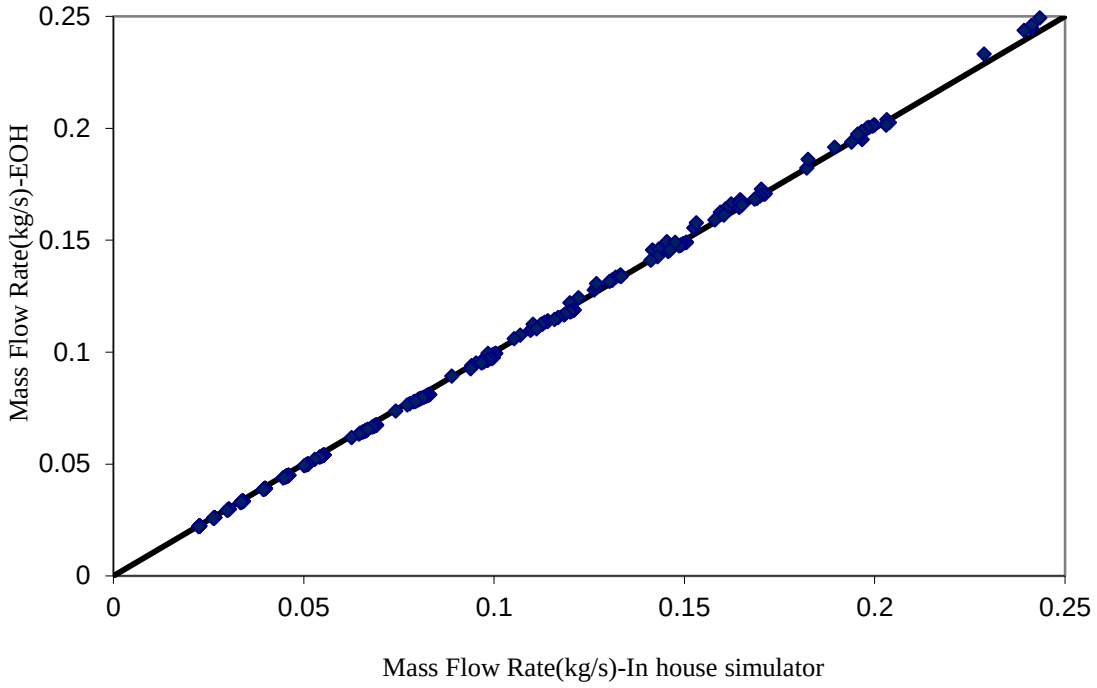

Figure 3.25 Calculated mass flow rates using EOH model with equivalent radius versus the corresponding values estimated by the HFW 2D in-house simulator, HFW-6.

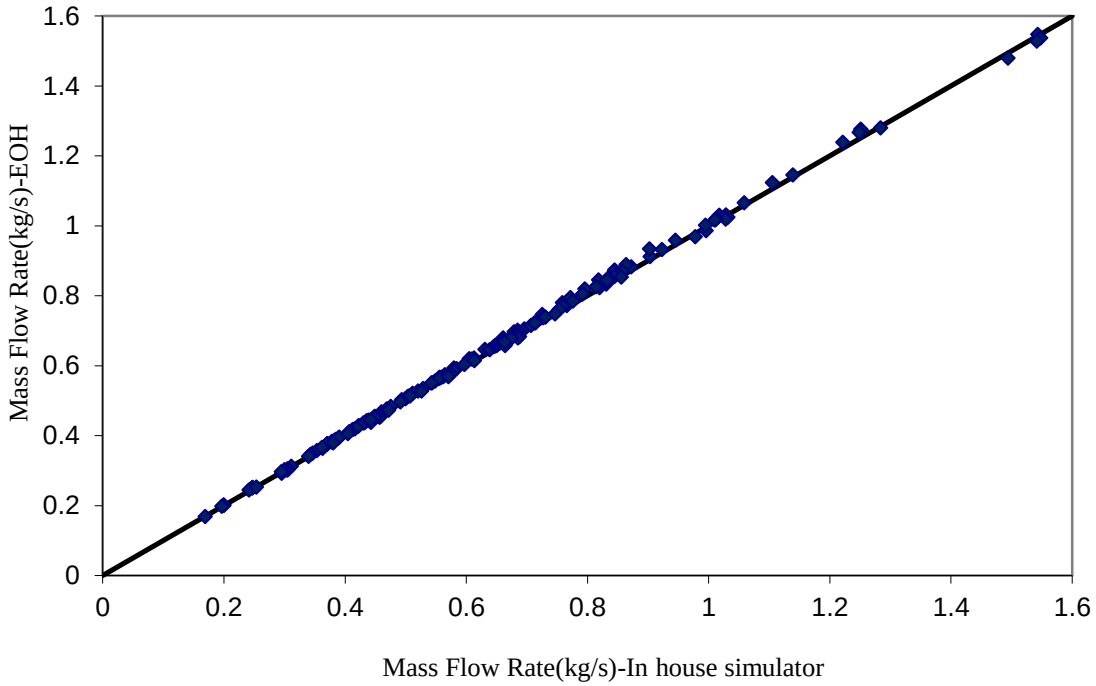

Figure 3.26 Calculated mass flow rates using EOH model with equivalent radius versus the corresponding values estimated by the HFW 2D in-house simulator, HFW-7.

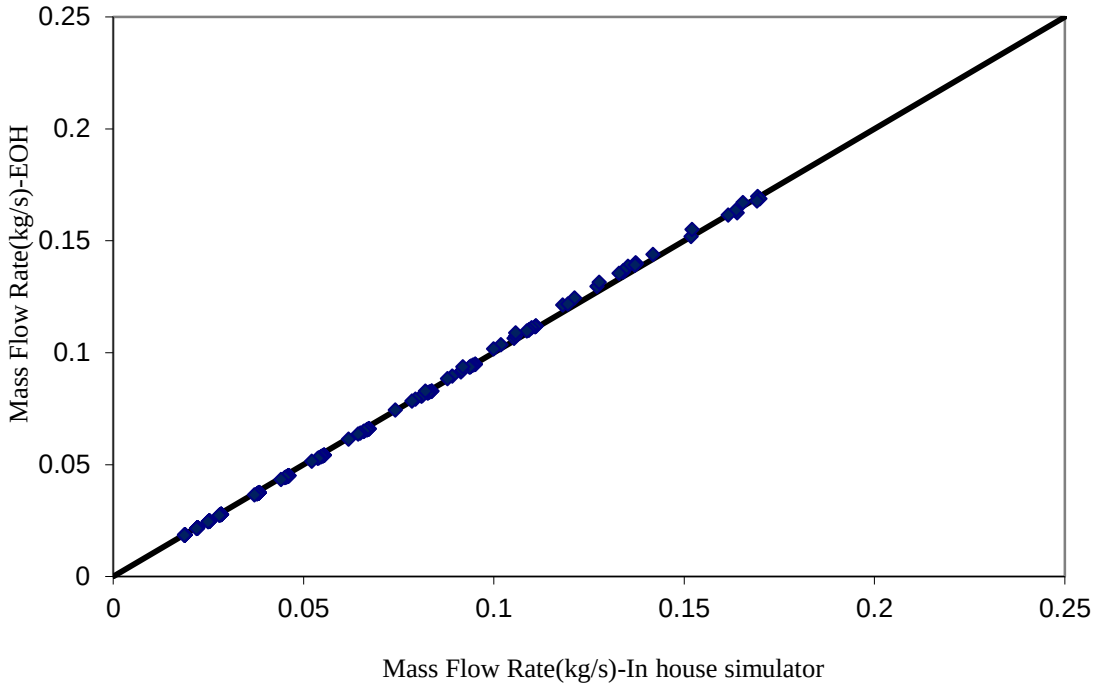

Figure 3.27 Calculated mass flow rates using EOH model with equivalent radius versus the corresponding values estimated by the HFW 2D in-house simulator, HFW-8.

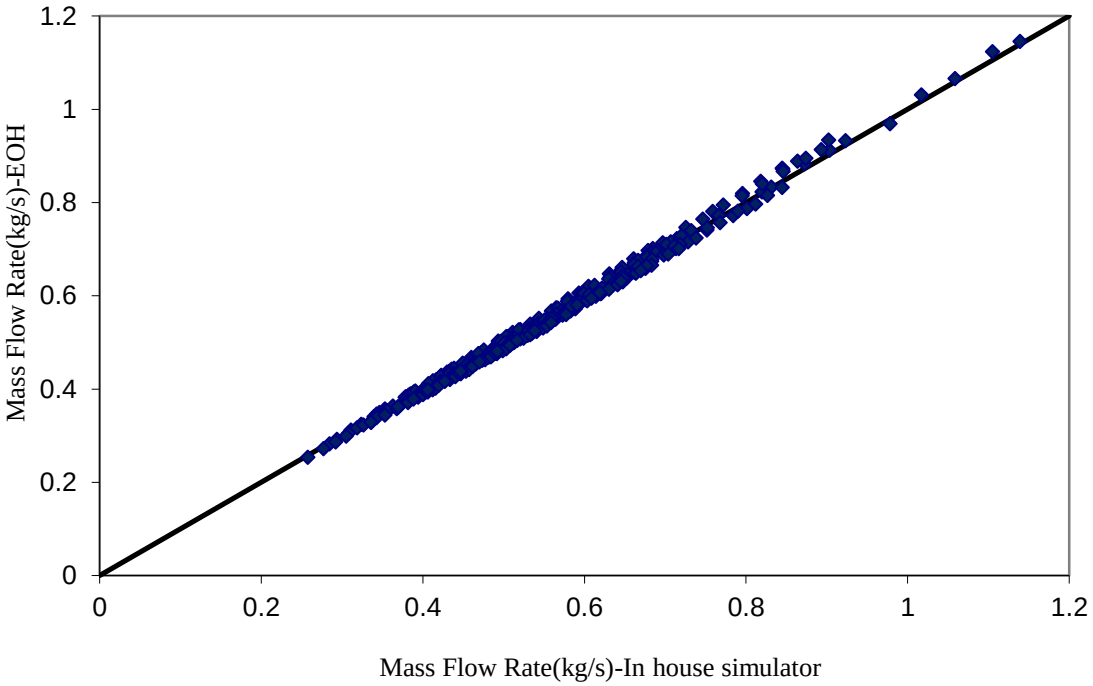

Figure 3.28 Calculated mass flow rates using EOH model with equivalent radius versus the corresponding values estimated by the HFW 2D in-house simulator, HFW-9.

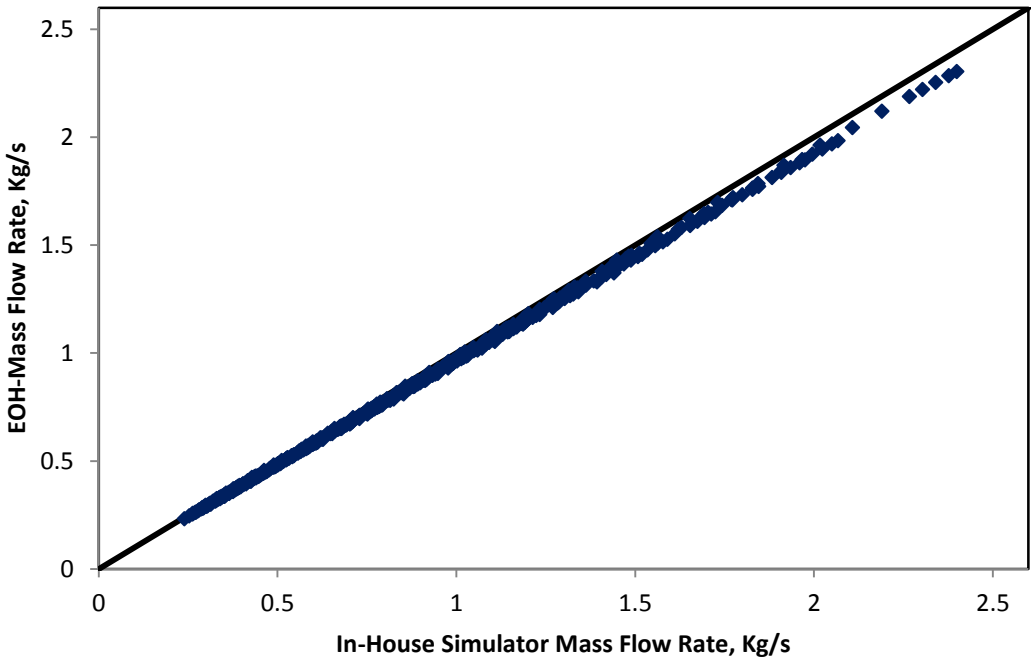

Figure 3.29 Calculated mass flow rates using EOH model with equivalent radius versus the corresponding values estimated by the HFW 2D in-house simulator, HFW-10.

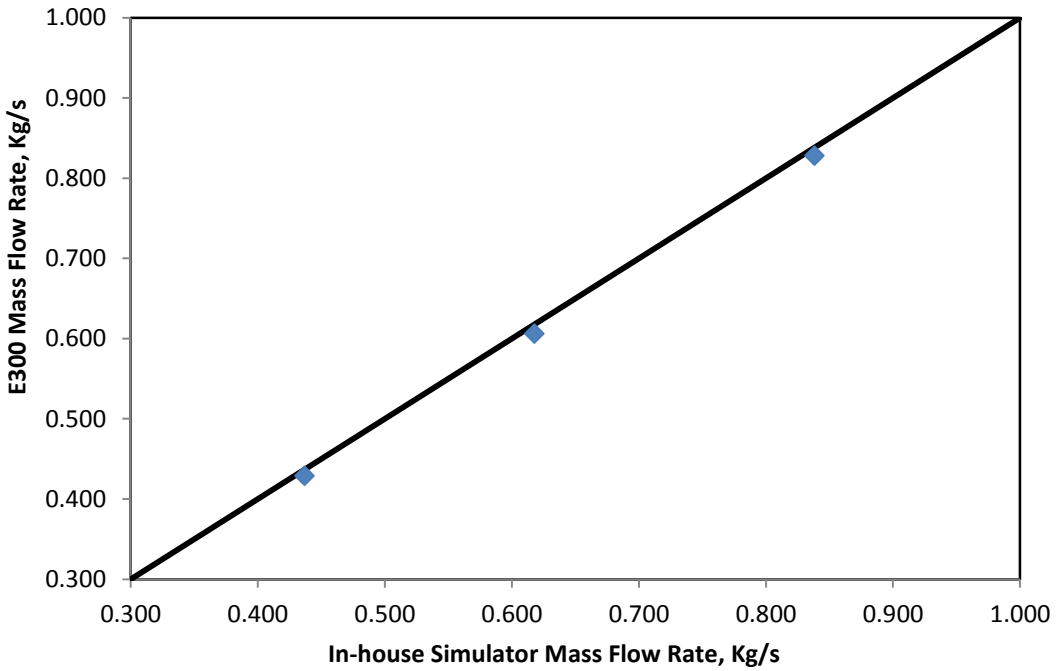

Figure 3.30 Calculated mass flow rates using Eclipse E300 versus the corresponding values estimated by the HFW 2D in-house simulator, two phase-SS.

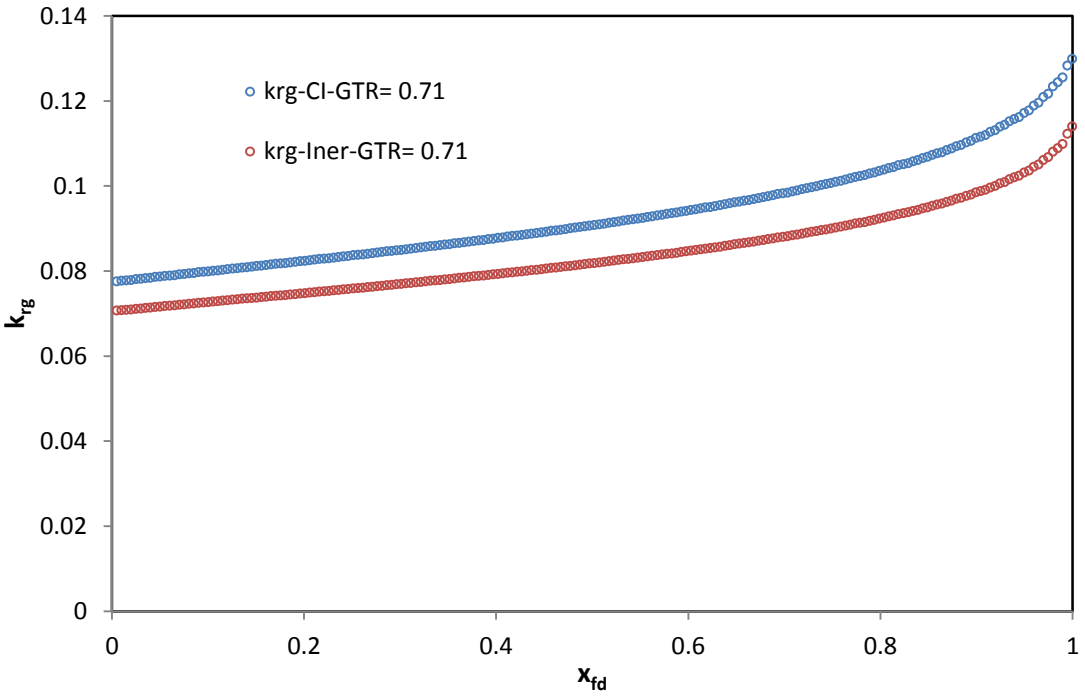

(a)

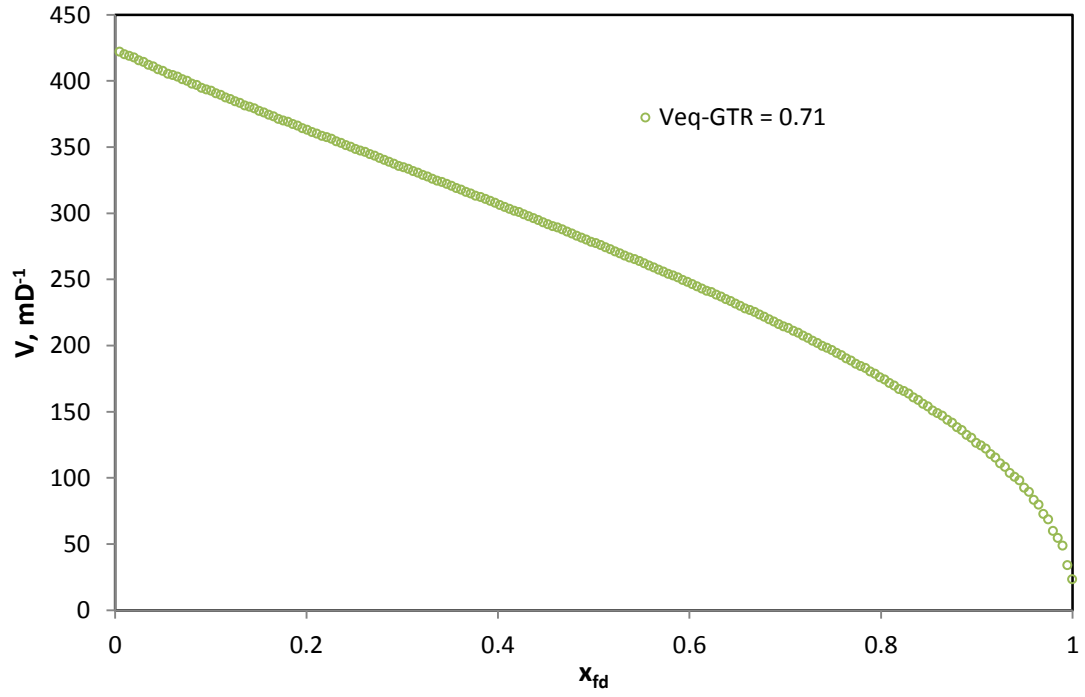

(b)

Figure 3.31 (a) - Gas relative permeability variation inside the fracture, (b)- Total Velocity variation inside the fracture for GTR_{well} 0.71, under pressure drop (DP= 200Psi), HFW-11.

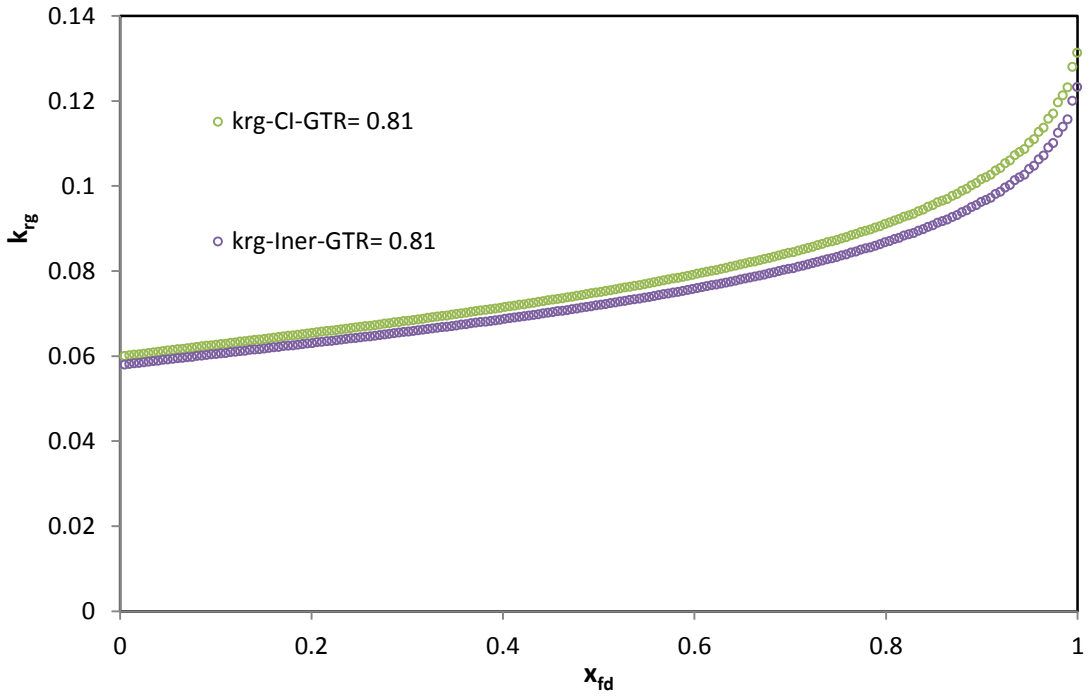

(a)

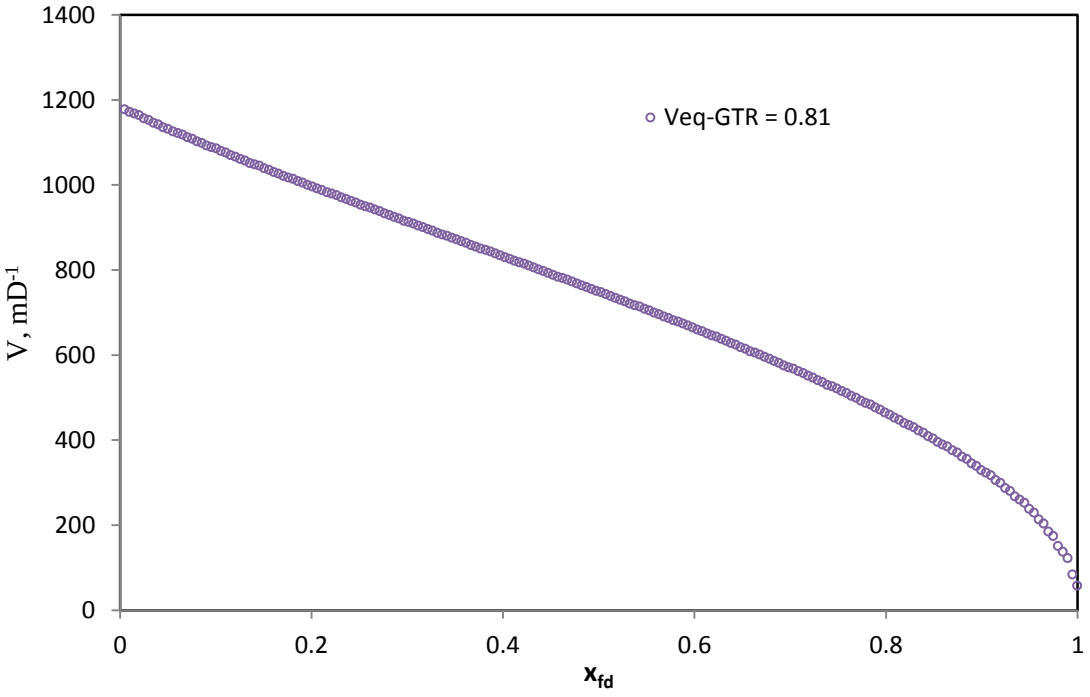

(b)

Figure 3.32 (a) - Gas relative permeability variation inside the fracture, (b)- Total Velocity variation inside the fracture for GTR_{well} 0.81, under pressure drop (DP= 500Psi), HFW-12.

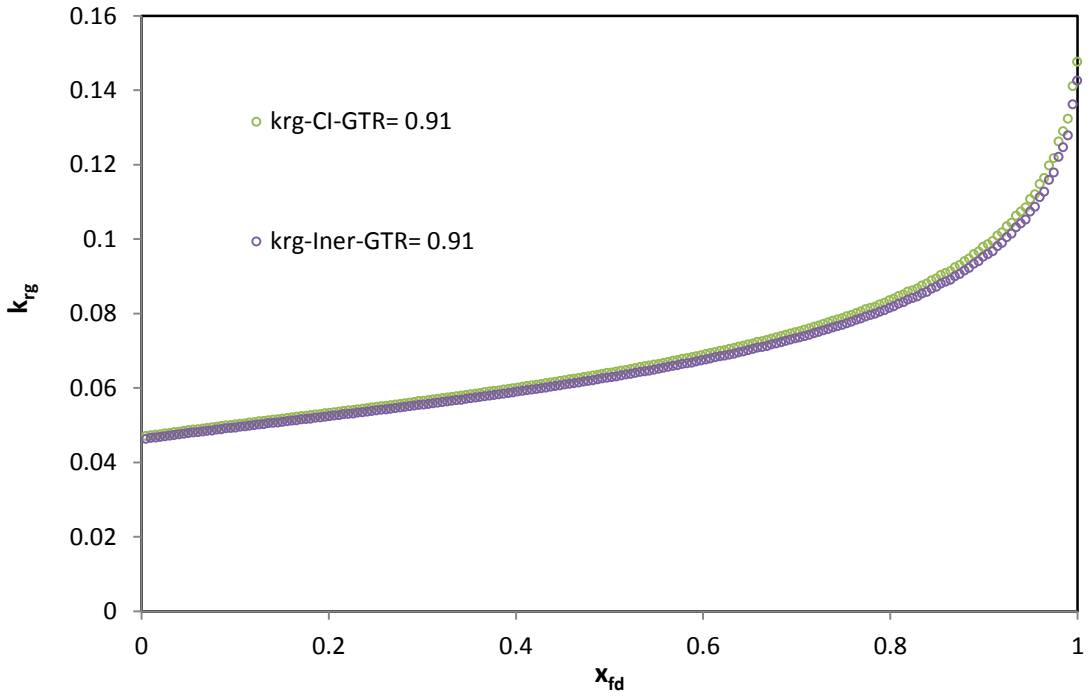

(a)

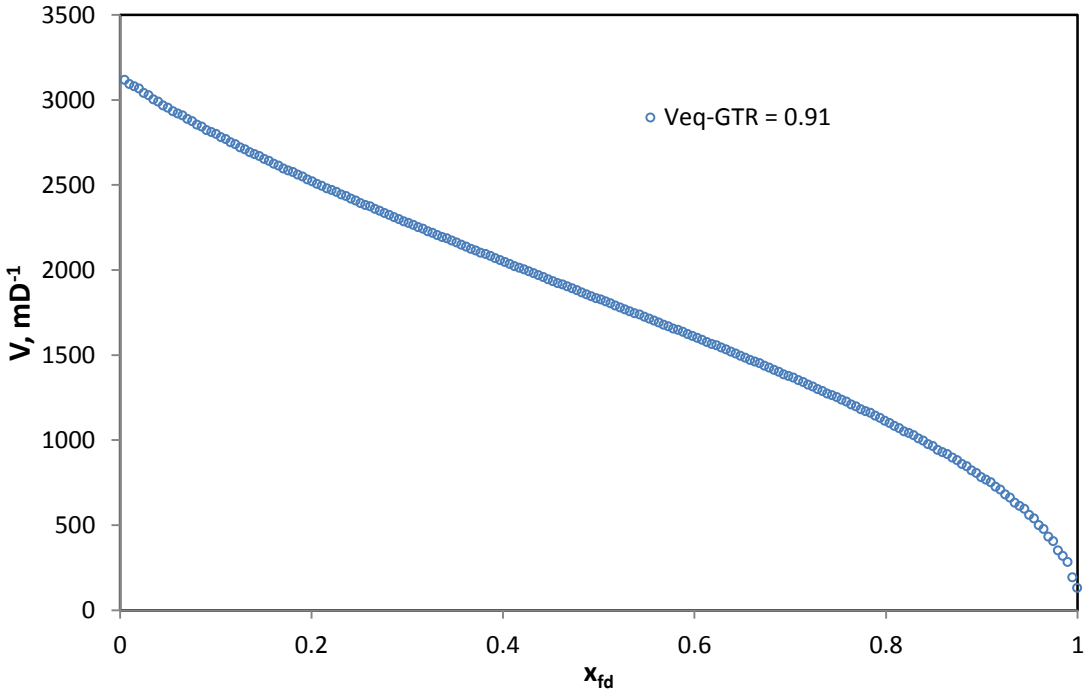

(b)

Figure 3.33 (a) - Gas relative permeability variation inside the fracture, (b)- Total Velocity variation inside the fracture for GTR_{well} 0.91, under pressure drop (DP= 950Psi), HFW-13.

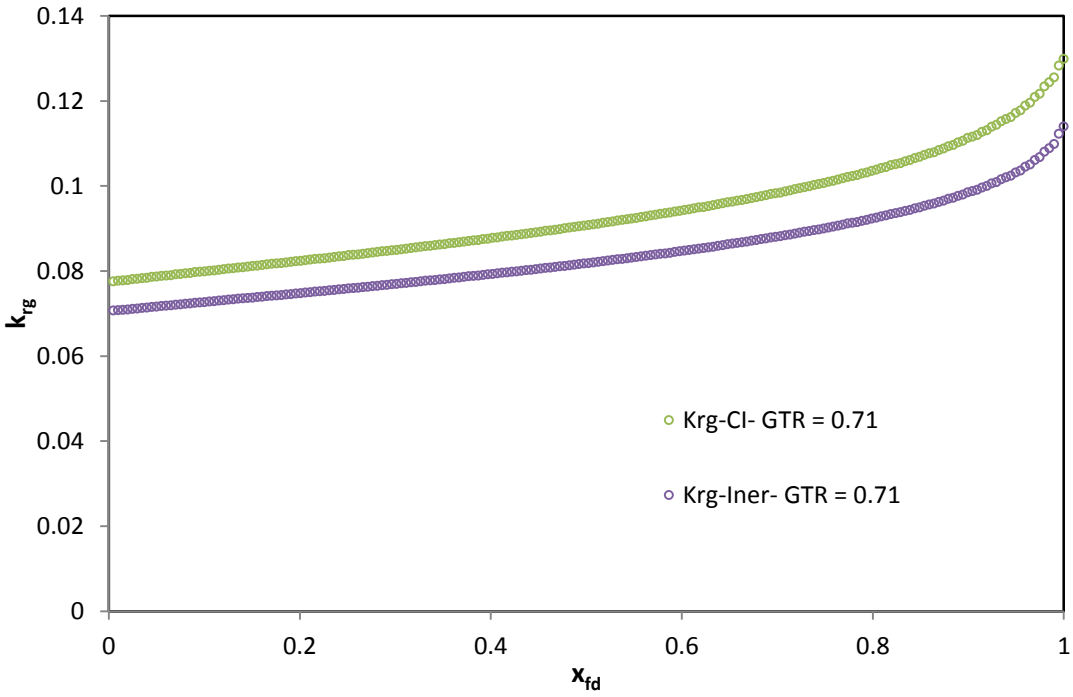

(a)

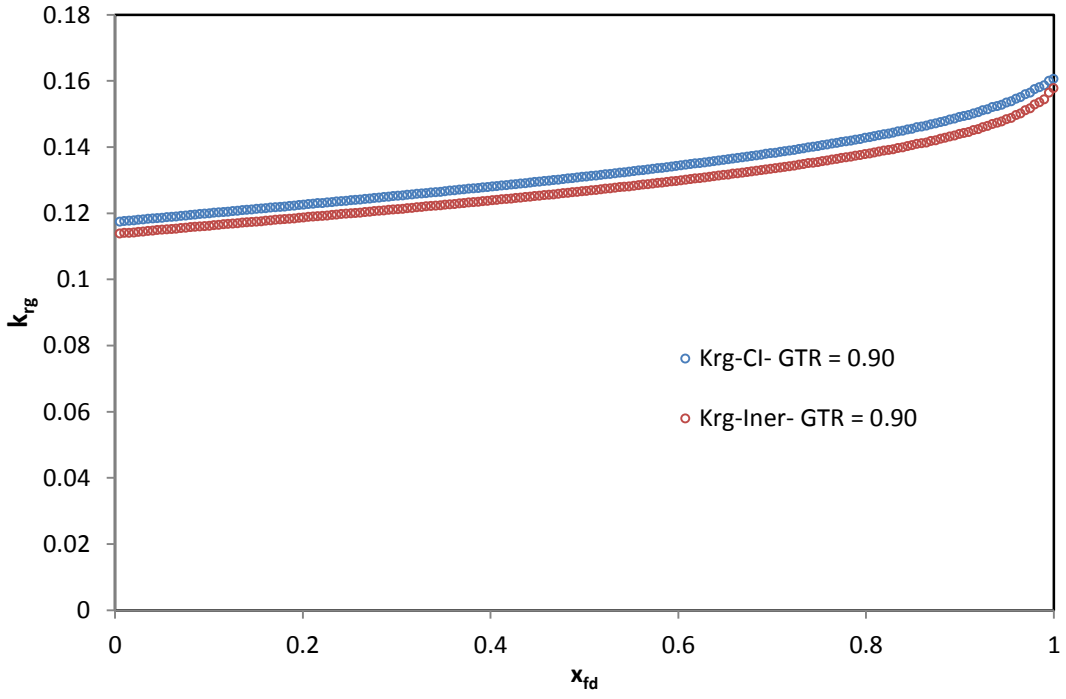

(b)

Figure 3.34 Gas relative permeability variation inside the fracture for (a)- GTR_{well} 0.71 and (b)- 0.91, both under pressure drop (DP= 200Psi), HFW-15 and HFW-14.

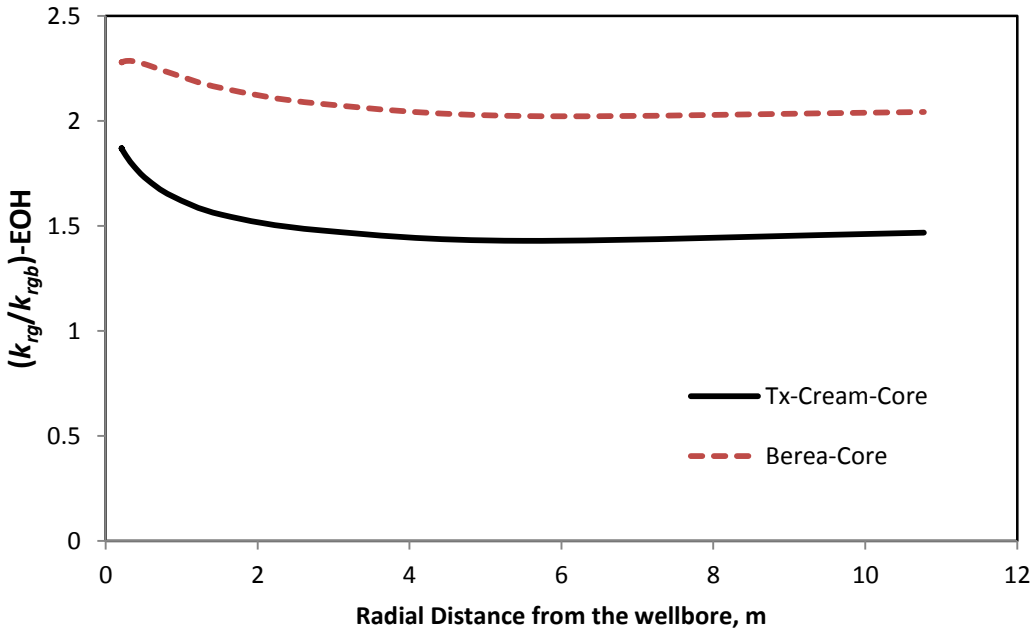

Figure 3.35 ratio of the velocity/IFT affected relative permeability to the base relative permeability for EOH system HFW-16 and HFW-17.

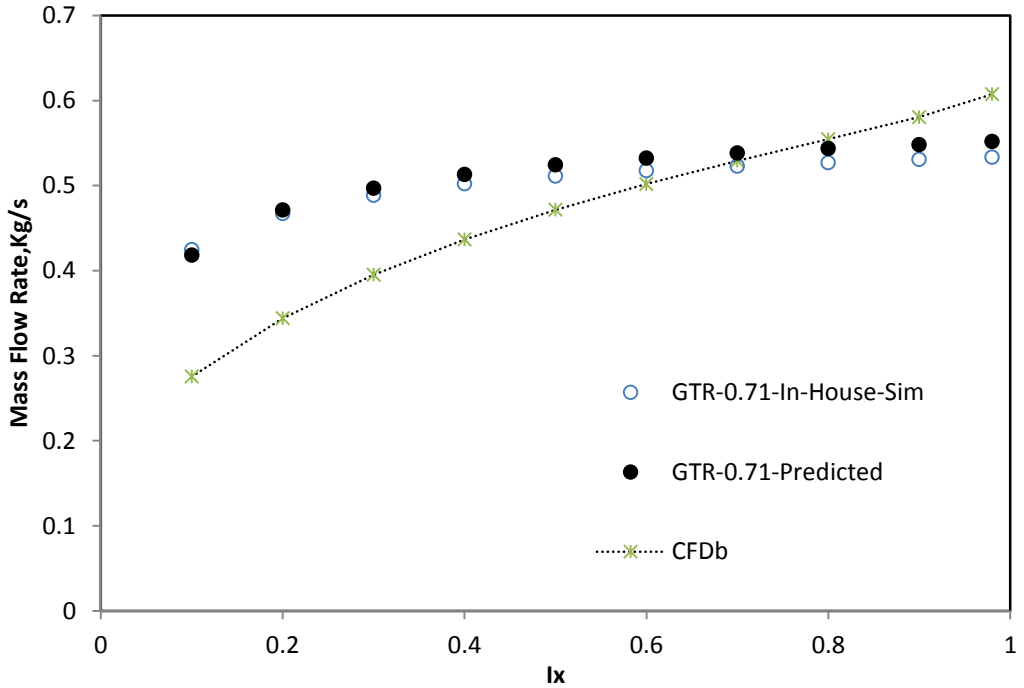

Figure 3.36 Calculated mass flow rates using EOH model with equivalent radius versus the corresponding values estimated by the HFW 2D in-house simulator, HFW-18. C_{FDb} curve is calculated using base relative permeability (No Coupling and No Inertia).

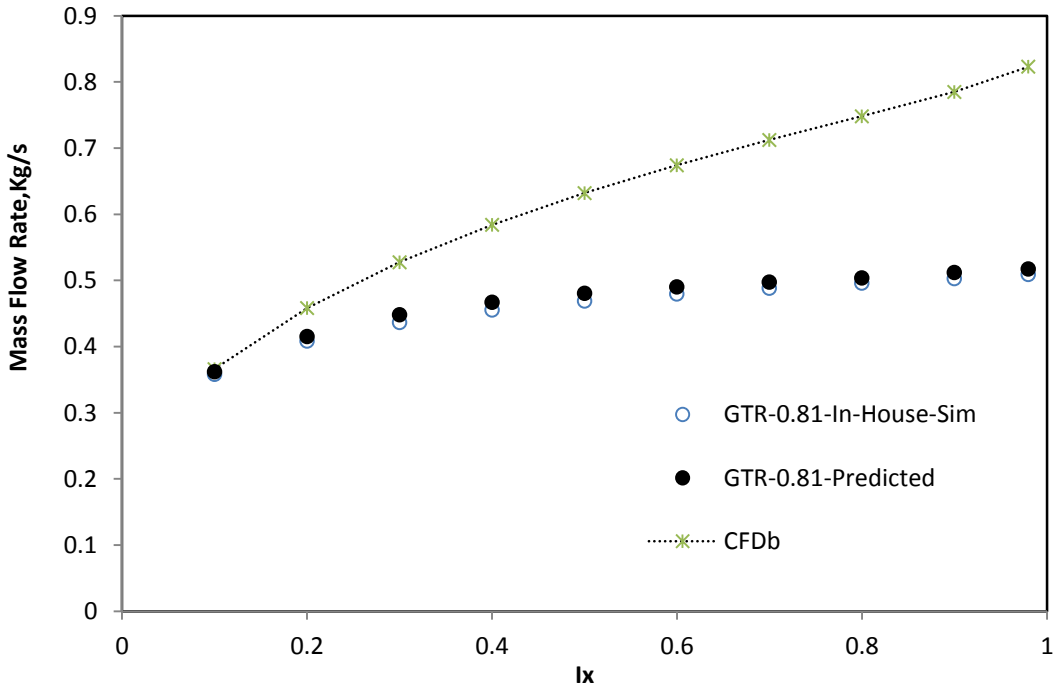

Figure 3.37 Calculated mass flow rates using EOH model with equivalent radius versus the corresponding values estimated by the HFW 2D in-house simulator, HFW-19. C_{FDb} curve is calculated using base relative permeability (No Coupling and No Inertia).

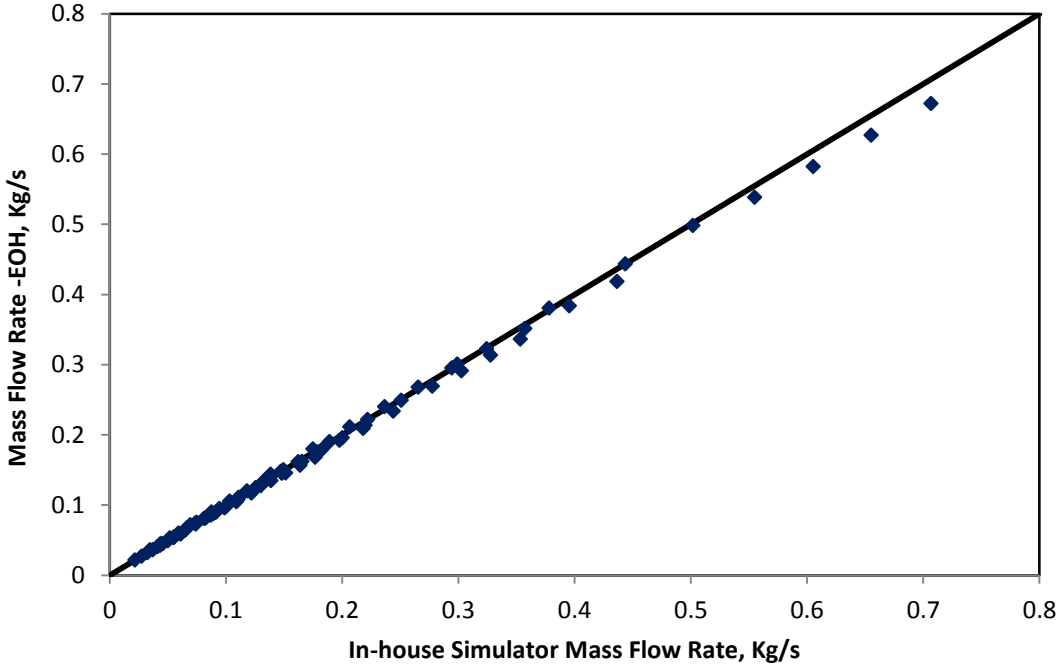

Figure 3.38 Calculated mass flow rates using EOH model with equivalent radius versus the corresponding values estimated by the HFW 2D in-house simulator, HFW-20.

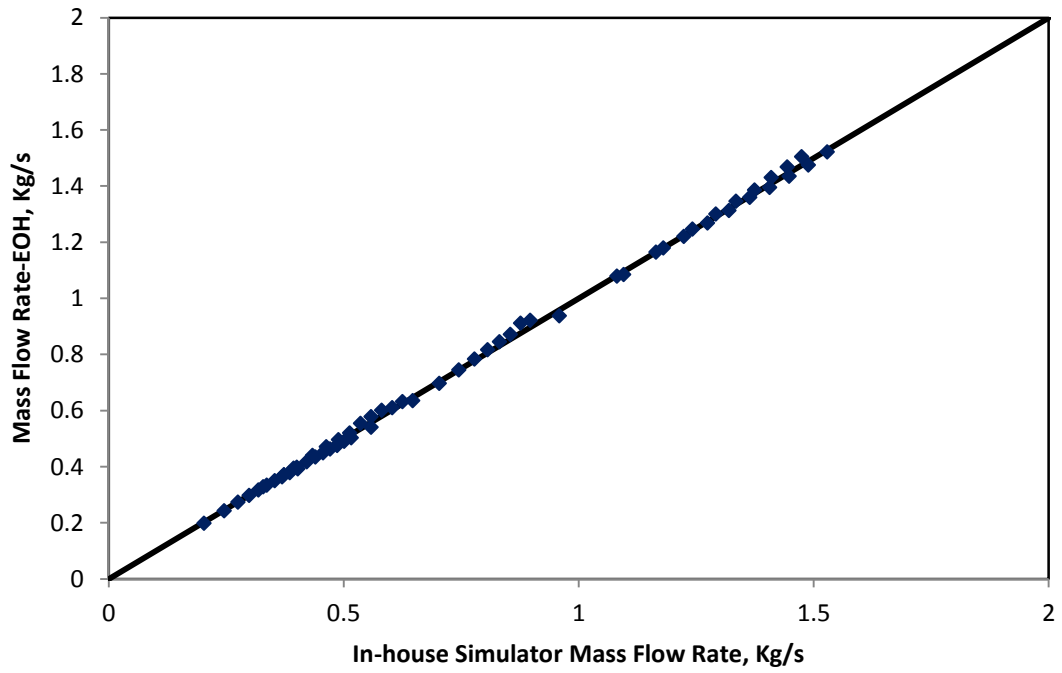

Figure 3.39 Calculated mass flow rates using EOH model with equivalent radius versus the corresponding values estimated by the HFW 2D in-house simulator, HFW-21.

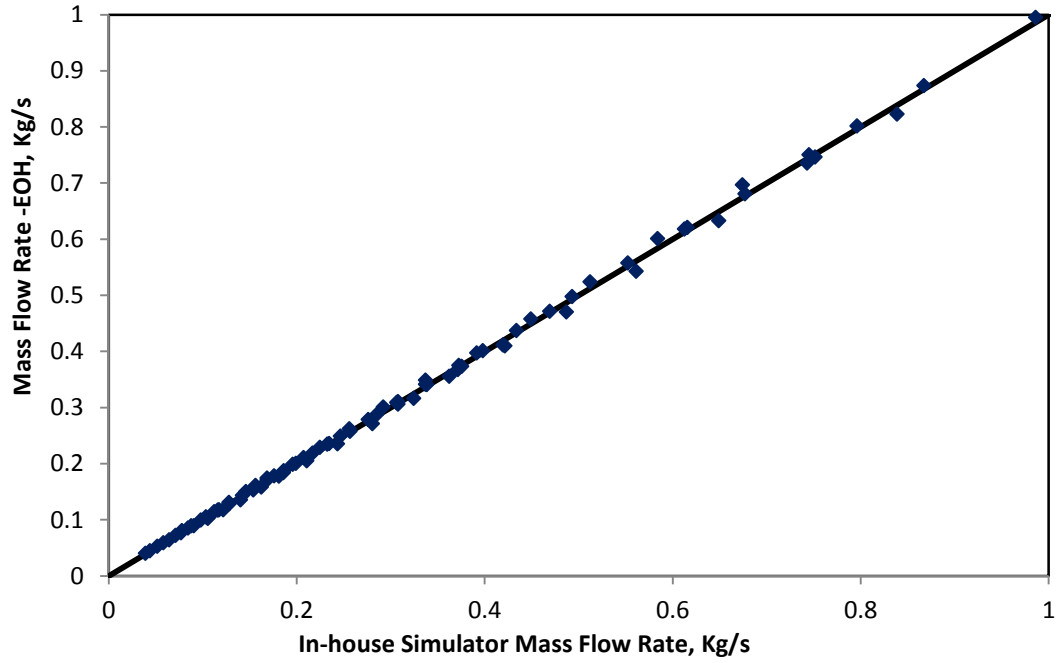

Figure 3.40 Calculated mass flow rates using EOH model with equivalent radius versus the corresponding values estimated by the HFW 2D in-house simulator, HFW-22.

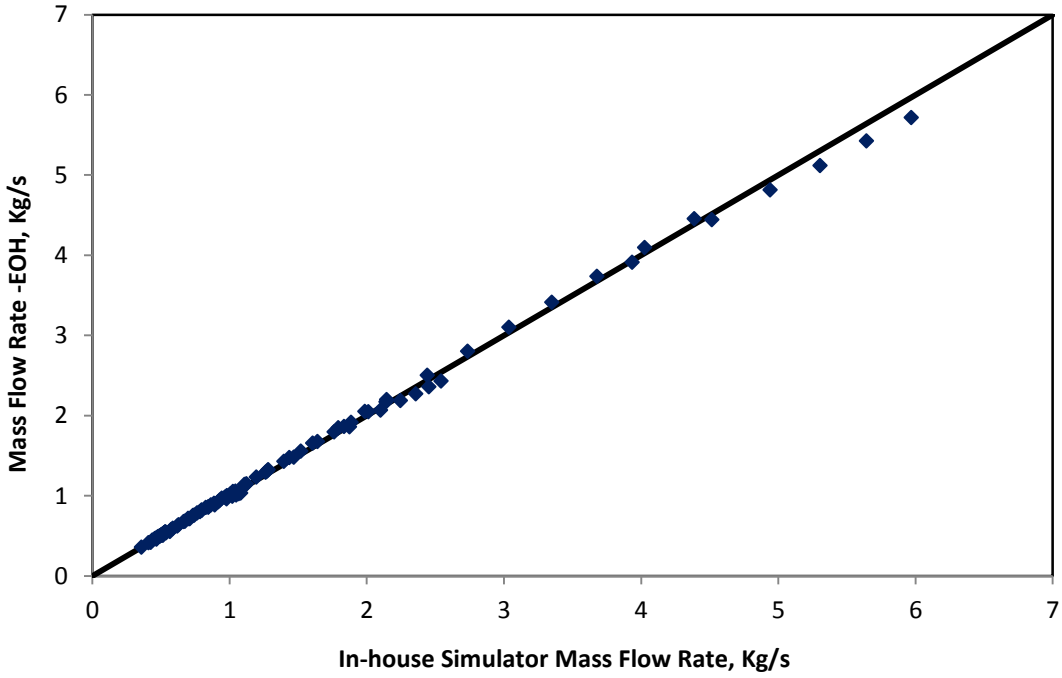

Figure 3.41 Calculated mass flow rates using EOH model with equivalent radius versus the corresponding values estimated by the HFW 2D in-house simulator, HFW-23.

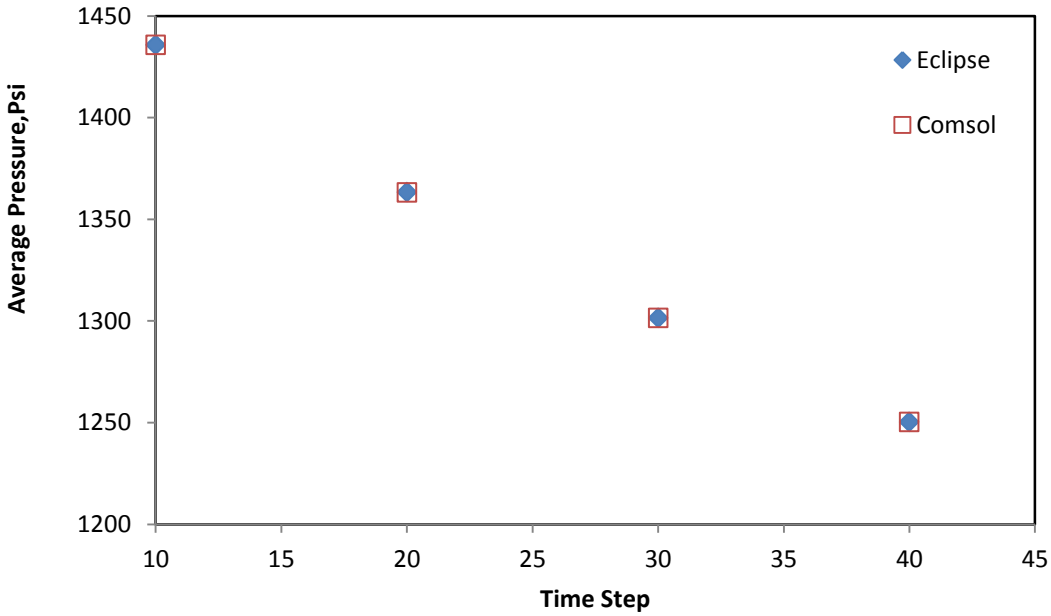

Figure 3.42 Calculated average volumetric reservoir pressure using Eclipse E300 versus the corresponding values estimated by the HFW 2D in-house simulator at different time steps, two phase-PSS.

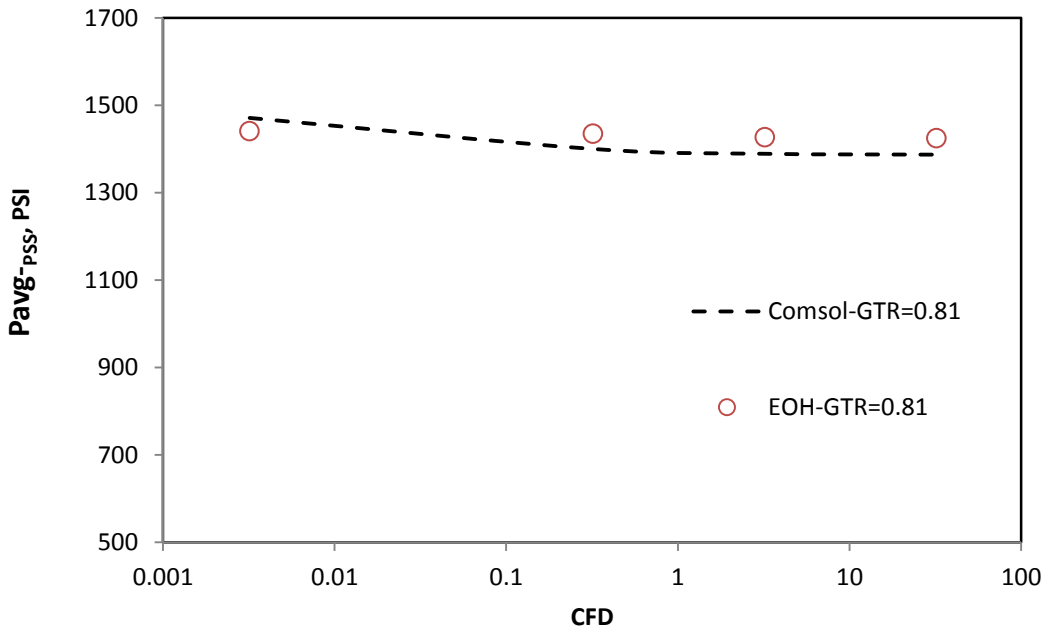

Figure 3.43 Comparison of Calculated average volumetric reservoir pressure using EOH, versus the corresponding values estimated by the HFW 2D in-house simulator for different CFD, GTRwell=0.81, HFW-24

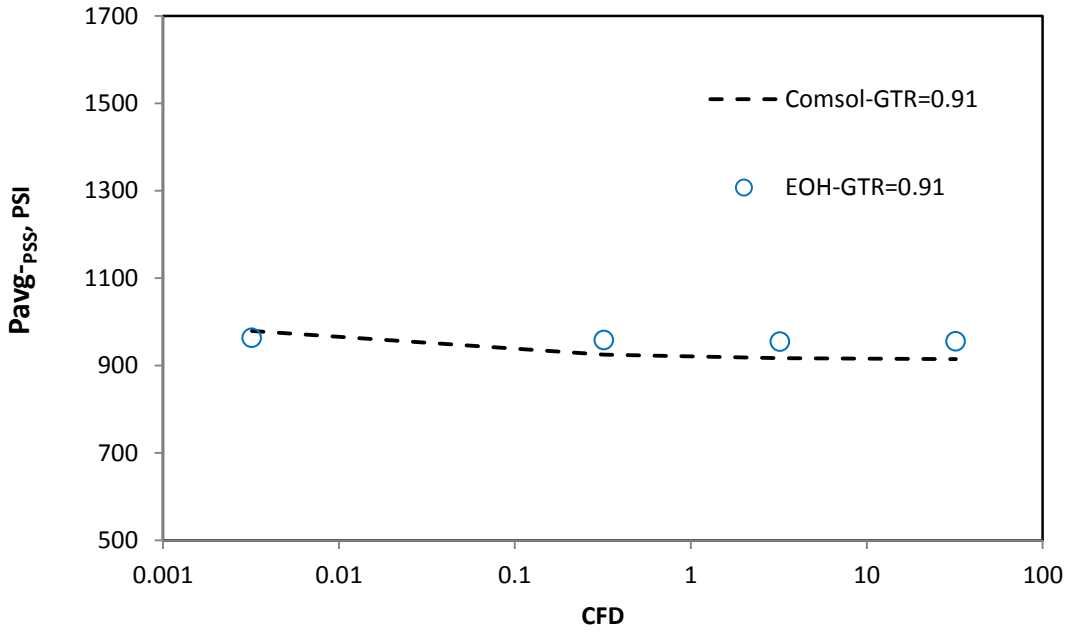

Figure 3.44 Comparison of Calculated average volumetric reservoir pressure using EOH, versus the corresponding values estimated by the HFW 2D in-house simulator for different CFD, GTR_{well}=0.91, , HFW-25

CHAPTER 4

Gas Condensate Flow around Multi-layer Hydraulically Fractured wells

4.1 PROBLEM STATEMENT AND OBJECTIVES

Flow behaviour around multi-layer HFWs is complex because of the 3-D nature of flow around such well geometries. That is, it is very difficult to obtain an analytical solution to forecast accurately the productivity of 3-D HFWs. In gas condensate reservoirs, as the pressure falls below dew point, a bank of condensate forms around the wellbore, which affects the well productivity and near wellbore flow behaviour. Fine grid compositional numerical simulation, similar to that of the in-house simulator, is usually required to predict gas-condensate well productivity and to account for high velocity phenomena, which result in variation of relative permeability due to the coupling and inertial effects. A simple and reliable method for the layered HFW productivity calculation in gas condensate reservoirs is very desirable, as the above procedure is computationally very expensive and cumbersome.

In Chapter 3, the author presented and verified a new formulation to estimate effective wellbore radius of a single layer hydraulically fractured well in gas condensate reservoirs.

With these in mind, the main aim of this part of the study is to extend this formulation for the case of Multi-Layer hydraulically fractured well. However, in order to achieve this goal, first it is needed to visit the equivalent single layer concept which is usually used to improve simulation of multi-layer systems and then propose the new formulation for effective wellbore radius in Multi-Layer HFW's.

Simulating Multi-Layer system using the equivalent single layer concept significantly reduces the required CPU time and allows more flexibility in conducting different sensitivity scenarios. However, to the best of author's knowledge all available studies in the literature were for single-phase Darcy flow conditions. That is, modelling (two-phase gas condensate and single-phase Non-Darcy flow) Multi-Layer system using the equivalent single layer concept has not been presented before for both fractured and non-fractured wells.

The main difficulties in producing an equivalent single layer for a gas or gas condensate multi-layer system are summarized in two important questions 1) – what is the effective or equivalent single phase/two phase inertial factor, 2) – what is the effective or

equivalent relative permeability curve, both in the direction of properly accounting for coupling and inertial effects in an equivalent single layer.

Accordingly, in this chapter the answer to these two questions will be given, when the corresponding expressions for estimation of effective single phase inertial factor and equivalent relative permeability curve will be presented. Then, an approach which allows simulating multi-layer (gas and gas condensate) system with the equivalent single layer concept including the effect of coupling and inertia will be proposed and verified for both fractured and non-fractured vertical wells. As mentioned above, working with 1D EOH system reduces CPU time and gives more flexibility in conducting different sensitivity analysis on the well performance as working with a 3D system is cumbersome, costly and often impractical.

In this exercise, the author has mainly focused on a two/three-layer system but the approach can equally be extended to more number of layers.

The integrity of the proposed approach is first verified for the single-phase Darcy flow conditions and then its application is extended to single-phase non-Darcy flow followed by two-phase gas condensate systems. In this exercise, several in-house simulators were developed to verify the integrity of the proposed approaches. Therefore, a brief description of their structure and the incorporated governing equations are also presented.

This exercise is first performed for flow under steady state conditions and then that under pseudo-steady-state conditions.

4.2 STEADY-STATE SINGLE PHASE DARCY FLOW

4.2.1 Geometrical Skin Factor/Effective Wellbore Radius

When a well commences to produce at a constant rate or pressure drop, the first flow regime, which develops in the reservoir is transient flow. For a system with constant flow across the exterior boundaries, which is equal to the well production rate, a transient flow is changed to steady state (SS) flow.

In chapter 3 (section 3.3), it has been shown that the productivity of HFW under single-phase Darcy flow conditions can be expressed in term of the productivity of vertical well with an effective wellbore radius ($r_w^{'}$).

$$q_{HFW} = \frac{2\pi k_m h \Delta P}{\mu\left(\ln\left(\frac{r_e}{r_w^{'}}\right)\right)} \tag{4.1}$$

$$r_w^{'} = x_f \times e^{-S_{gf}} \tag{4.2}$$

In Equation 4.2 S_{gf} is the geometric skin (also known in some of the literature studies as Pseudo-Fracture skin) given as:

$$s_{gf} = \ln\left(\varepsilon_{ss} + \frac{\pi}{C_{FD}}\right). \tag{4.3}$$

Where C_{FD} and ε_{ss}; are the fracture dimensionless conductivity and the reciprocal effective wellbore radius for infinite conductivity fracture under steady-state conditions, respectively.

$$C_{FD} = \frac{k_f w_f}{k_m x_f}. \tag{4.4}$$

For SS conditions:
$$\varepsilon_{SS} = 2 - \left(\frac{0.112 I_x}{1 - 0.796 I_x}\right) \tag{4.5}$$

The fracture geometric skin factor expressed by Equation 4.3 was introduced in Chapter 3. The validity of its application was verified for different pertinent parameters (fracture dimensions, reservoir dimensions, and fracture/reservoir rock properties) in the case of a 2-D single layer HFWs (Chapter 3, section 3.3).

Here the author proposes to alter the (fracture dimensionless conductivity, C_{FD}, and fracture half-length, x_f) when extending this formulation to multi-layer systems. This can be achieved if we reduce the multi-layer model to an equivalent single layer model with an equivalent single fracture which has a dimensionless conductivity of $C_{FD\text{-}eq}$ and fracture half-length of $x_{f\text{-}eq}$. That is, the geometric skin factor and the effective wellbore radius of a Multi-Layer fractured well could be estimated using the formula of single layer fractured well, provided that the equivalent dimensionless fracture conductivity $C_{FD\text{-}eq}$ and the equivalent fracture half-length $x_{f\text{-}eq}$ are known. In other words, the geometric skin and equivalent wellbore radius expressions of Equations 4.3 and 4.2, take the following form for multi-layered systems

$$s_{gf} = \ln\left(\varepsilon_{ss} + \frac{\pi}{C_{FD-eq}}\right). \tag{4.6}$$

$$r_w^{'} = x_{f-eq} \times e^{-S_{gf}} \tag{4.7}$$

Where, C_{FD-eq} , is the equivalent dimensionless fracture conductivity for an equivalent single layer defined as:

$$C_{FD-eq} = \frac{\overline{k_f} w_f}{\overline{k_m} x_{f-eq}}. \tag{4.8}$$

Here, ($\overline{k_f}$ and $\overline{k_m}$) are the arithmetic average permeability of fracture and matrix, respectively. Also, if fractures in all layers have the same length then $x_{f-eq} = x_f$ otherwise a separate formulation for equivalent fracture half-length should be used. This will be discussed next.

Bennent *et al.* (1986) was the first to discuss the subject of multi-layer fractured wells. They studied the transient pressure response of a commingled hydraulically fractured well (that is, they assumed that the layers communication happens only through the fracture) for a single phase incompressible fluid under Darcy flow conditions. The main outcome of this study was the introduction of a factor called reservoir conductivity (C_R). Indeed, reservoir conductivity was nothing more than the summation of individual layers matrix conductivity ($k_{mi}h_i$) divided by the total average matrix conductivity ($\overline{k_m}$ h_t). Bennent *et al.* (1986), argued that if a system consist of (n) layers where each individual layer has a permeability and height of (k_{mi} and h_i) then the reservoir conductivity factor (C_R) should always results in a value of 1,

$$C_R = \frac{\sum_{i=1}^{n} k_{mi} h_i}{\overline{k_m} h_t} = 1. \tag{4.9}$$

Later, Camatcho *et al*. (1987) used the reservoir conductivity factor (C_R) as a scaling parameter to determine the equivalent fracture half-length ($x_{f\text{-}eq}$) for multi-layer fractured well with different fracture length in each layer by introducing of the following formula.

$$x_{f-eq} = \frac{\sum_{i=1}^{n} k_{mi} \cdot h_i \cdot x_{fi}}{\overline{k_m} h_t}. \tag{4.10}$$

These two studies have mainly focused on the well testing aspect of a multi-layer fractured well during transient period for single phase Darcy flow conditions.

In this study, the ($x_{f\text{-}eq}$) formula defined in Equation 4.10 (Camatcho *et al*. 1987) will be extended and verified for the case of gas condensate reservoirs under boundary dominated flow (i.e. steady-state and pseudo-steady state condition) with the combined

effect of coupling and inertia. That is, using Equation4.10 in Equation 4.8, the author defines a single layer fractured well model equivalent to that of 3-D Multi-Layer fractured well. Then, the effective wellbore radius which will give us the same performance as that of 3-D Multi-Layer fractured well can be calculated using Equations 4.6 and 4.7. Finally, the equivalent single layer productivity can be obtained using Equation 4.11,

$$q_{HFW} = \frac{2\pi \overline{k_m} h \Delta P}{\mu \left(\ln\left(\frac{r_e}{r_w'} \right) \right)} \tag{4.11}$$

This procedure has been followed to verify the integrity of the proposed formula, as shown in the following sections. However first a brief description of the in-house simulator used for this purpose is presented.

4.2.2 3 D HFW Mathematical Simulator

The main aim of this section is to develop a 3-D simulator that can be used to create a large bank of data for Multi-Layer HFWs with different fracture geometries (different fracture lengths and widths) in a reservoir with different dimensions.

The 3-D system considered in this study consists of a HFW with fracture width $\mathbf{w_f}$ and length of $\mathbf{x_{fi}}$ in each layer, as shown in Figure 4.1. This homogenous isotropic porous medium has an absolute permeability k_{mi} and formation thickness of h_{mi} for each layer. Figure 4.2 shows the mesh quality of a selected geometry, as it can be seen from this figure that the minimum mesh quality is higher than 0.6, which is expected to improve the accuracy of the numerical model. It should be noted that the minimum acceptable mesh quality of 0.6 has been honoured for all geometries used in this study. Also, Figure 4.3 shows the pressure distribution around a selected multi-layer HFW mesh.

Because of the existing symmetry only a quarter of the HFW model has been considered in this study.

The main assumptions used in this in-house simulator are as follow:

7. The fracture and matrix are two different porous media but each one is a uniform porous medium.
8. Each matrix layer is a uniform and isotropic porous medium with a matrix permeability k_{mi} and height h_{mi}.
9. Each fracture layer is a uniform and isotropic porous medium with a fracture permeability k_{fi} and height h_{fi}.

10. All layers are in full communication.
11. The width of the fracture is constant for all layers.
12. The fracture has penetrated symmetrically in both directions along the X-axis.
13. Wellbore flow directly from the matrix is negligible, compared to that from the fracture to the well.
14. The fracture has penetrated vertically through the whole height of each layer (i.e. the fracture height in each layer equal to the height of the layer $h_{mi} = h_{fi}$).
15. Gravity force is neglected in this 3-D system.

The governing equations employed in this model, are the same as those presented in Chapter 3 (section 3.2.1), for the (SS) single-phase flow around 2-D single layer HFWs, however in here the governing equations have been solved for 3-D Multi-Layer space. The main governing equation is shown below, which is the final form of combining the single phase continuity equation and the Forchheimer equation (Jamiolahmady et al. 2006, Ghahri 2010, Gas Condensate Recovery Final Report 2005-2008 and 2008-2011):

$$\nabla.\left[2\left[\frac{k}{\mu}\right].\frac{\rho\nabla P}{1+\sqrt{1+4\beta\rho\left(\frac{k}{\mu}\right)^2\left|\nabla P\right|}}\right]=0. \qquad (4.12)$$

More information about the set of (SS) single phase governing equations as well as their source, and their full derivations can be found in Chapter 3, section 3.2.1. Furthermore, the mathematical solution technique used to solve the above equation is similar to that presented in Chapter 3, section 3.2.1.

4.2.3 ECLIPSE Single Phase HFW Model

In order to confirm the integrity of the in-house single phase mathematical simulator, a HFW model was constructed using the fine grid option of ECLIPSE 100.

The core properties of Texas Cream (Table 4.1) with porosity 0.21 and permeability 9.1 mD were used to describe the reservoir in this model. The single phase fluid properties are those listed in Table 3.1a. The reservoir consist of two layers with equal thickness, but different fracture lengths (i.e. $h_1 = h_2$, $x_{f1} = 0.5x_{f2}$). The reservoir was 100 m in the X and 100 m in Y directions and 8 m in the Z direction. The fracture has a length of 25 m and a width of 5mm. The fracture has a permeability of 146 D. The

reservoir pressure was 1200 Psi and the HFW was producing under a controlled bottom-hole pressure of 1000 Psi. Fine grids were used to capture the flow complexity near the wellbore.

Sixty injection wells were located in the boundary of the reservoir to make the reservoir pressure at the drainage boundary constant (P_{ext} = 1200 Psi).

The results of the in-house mathematical simulator were compared with those of similar simulations conducted using the ECLIPSE simulator. Figure 4.4 shows the good agreement between the two results. The arithmetic average absolute deviations (AAD%) of the predicted mass flow rates values by the ECLIPSE simulator compared to those estimated by the HFW in-house simulator was 2.1 % for the simulation with a constant pressure drop (ΔP) of 200 psi maintained over the drainage area.

4.2.4 Verification of the Equivalent Single Layer Geometric Skin

In this section a verification of the proposed geometric skin and effective wellbore radius formulae will be given by comparing the equivalent single layer HFW mass flow rate with those of the 3-D HFW in-house simulator (described above).

Figure 4.5 shows the good level of accuracy of Equation 4.11 by comparing its results with the outcomes of the steady state 3-D in-house simulator. In this example the two layers have the same thickness with equal fracture width and half-length. However, the fracture permeability and matrix permeability corresponding to each layer are different. Wide ranges of variation of the pertinent parameters were considered as listed below:

Fracture width ($w_{f1} = w_{f2}$): 5, 10, 15 mm

Fracture half length ($x_{f1} = x_{f2}$): 20, 40, 80 and 100 m

Fracture permeability (k_{f1}): 10, 100, 200 D

Reservoir permeability (k_{m1}): 0.1, 1, 10, 100 mD

Fracture permeability ratio (k_{f1}/ k_{f2}): 0.1, 0.25, 0.5, 0.75, and 1

Reservoir permeability ratio (k_{m1}/ k_{m2}): 0.1, 0.25, 0.5, 0.75, 1

Here the Average Absolute Deviation (AAD%) is less than 2.2%, confirming the applicability of Equation 4.6 for the calculation of Multi-Layer geometric fracture skin at steady state conditions.

Figure 4.6 compare the mass flow rate of the steady state in-house simulator with those obtained using Equation 4.11. In this example the two layers have different thickness and fracture half-length. Similar to the previous data set, the fracture permeability and

matrix permeability corresponding to each layer are also different. The ranges of variation of the pertinent parameters used are listed below:

Fracture width ($w_{f1} = w_{f2}$): 5, 10, 15 mm

Fracture half length (x_{f1}): 20, 40, 80 and 100 m

Fracture permeability (k_{f1}): 10, 100, 200 D

Reservoir permeability (k_{m1}): 0.1, 1, 10mD

Fracture permeability ratio (k_{f1}/ k_{f2}): 0.1, 0.5, and 0.75

Reservoir permeability ratio (k_{m1}/ k_{m2}): 0.1, 0.5, and 0.75

Layer height ratio (h_1/h_2): 0.25, 0.5, 0.75, and 1

Fracture length ratio (x_{f1}/x_{f2}): 0.25, 0.5, 0.75, and 1

Here the Average Absolute Deviation (AAD%) is less than 3%, confirming the applicability of Equation 4.6 for the calculation of Multi-Layer geometric fracture skin for the case of (Un-equal fracture length in each layer) at steady state conditions.

Figure 4.7 shows the results of the in house simulator mass flow rate compared to those of Equation 4.11 for a three layer system with (un-equal fracture length in each layer), the details of this run is given in Table 4.2, HWF-M1 data set. Here the average absolute deviation was 3.5%.

This result confirms the integrity of the approach by applying Equation 4.6 for the calculation of Multi-Layer geometric fracture skin for the case of three layers with (Un-equal fracture length in each layer) under steady state Darcy flow conditions.

4.3 STEADY-STATE SINGLE PHASE NON-DARCY FLOW

4.3.1 Total Skin Factor/Effective Wellbore Radius

For single phase flow under Non-Darcy conditions, the total skin is equal to,

$$S_t = S_{gf} + S_f \,. \tag{4.13}$$

In this equation, S_{gf} and S_f are the geometrical and flow skin, respectively. For Darcy flow, the effect of inertia is minimal; therefore the flow skin (S_f) is zero. S_f depends on the fluid properties and velocities, in addition to geometrical parameters.

In Chapter 3 (section 3.4) a detailed analysis of Non-Darcy flow around hydraulically fractured wells was presented. Some of the main conclusions can be summarized as follow:

1. The Non-Darcy flow mainly takes place inside the fracture. That is, inertial effects inside the matrix can be neglected for most practical cases.
2. The Non-Darcy effects can manifest itself as a reduction in absolute fracture dimensionless conductivity C_{FD}. Therefore, effective dimensionless fracture conductivity ($C_{FD\text{-}eff}$) should be used instead of the absolute one (i.e. C_{FD}) inside the geometric skin equation (Equation 4.3), in order to account for the negative impact of inertia.
3. The effective dimensionless fracture conductivity can be obtained by correcting the fracture permeability for the effect of inertia using a relative permeability term, refer to Equation 3.65a in Chapter 3.

Accordingly, in Chapter 3 of this thesis, the following formula of total skin has been developed for single layer HFWs:

$$S_t = \ln\left(\varepsilon_{ss} + \frac{\pi}{C_{FD}} + \frac{\pi \cdot R_{ew}}{2C_{FD}}\right) \tag{4.14}$$

$$R_{ew} = \frac{k_f \cdot \beta_f \cdot \rho \cdot V_w}{\mu} \tag{4.15}$$

In Equation 4.14, the first two terms are the Darcy flow geometric skin while the third term represents the inertial effect which is a function of fluid properties, volumetric flow rate, and geometrical parameters. That is, for Darcy flow (R_{ew} is very low), and the total skin S_t equal to the geometric skin S_{gf}.

Now, the total skin of an equivalent single layer that should give the same performance as that of the 3-D Multi-Layer HFW is shown in Equation 4.16. This equation has been derived by combining Equation 4.8 and 4.14, as follow.

$$S_t = \ln\left(\varepsilon_{ss} + \frac{\pi}{C_{FD-eq}} + \frac{\pi \cdot R_{ew-eq}}{2C_{FD-eq}}\right) \tag{4.16}$$

$$R_{ew-eq} = \frac{\bar{k}_f \cdot \beta_{f-eff} \cdot \rho \cdot V_w}{\mu}. \tag{4.17}$$

Where, the term ($\bar{k}_f \cdot \beta_{f-eff}$) represents the average fracture permeability, and effective fracture single phase inertial factor product.

Also, the mass flow rate of the equivalent single layer can be written as follow,

$$m = \frac{2\pi \overline{k_m} h \Delta\psi_{eq}}{Ln\left(\frac{r_e}{x_{f-eq}}\right) + S_t} = \frac{2\pi \overline{k_m} h \Delta\psi_{eq}}{Ln\left(\frac{r_e}{r_w^{'}}\right)} \tag{4.18}$$

Where, $\psi_{eq}, r_w^{'}$ and S_t are the equivalent single layer pseudo pressure effective wellbore radius and total skin, respectively. ψ_{eq} , $r_w^{'}$ can be mathematically expressed as follows:

$$\psi_{eq} = \int \frac{k_{r-eq}}{\mu} dp \tag{4.19}$$

$$k_{r-eq} = \frac{1}{1+R_{e-eq}} \Rightarrow R_{e-eq} = \frac{\overline{k}_m \beta_{m-eff} \rho V}{\mu} \tag{4.20}$$

$$r_w^{'} = x_{f-eq} \times e^{-S_t} \tag{4.21}$$

Where, the term ($\overline{k}_m \cdot \beta_{m-eff}$) represents the average matrix permeability, and effective matrix single phase inertial factor product.

Equation 4.18 should produce the same flow rate as that of 3-D Multi-layer fractured well both flowing under same pressure drop, provided that all required information are available. That is, a 1-D open-hole simulator is used to predict the performance of the 3-D simulator both under the same prevailing conditions. This saves CPU time and gives more flexibility in conducting different sensitivity analysis on the well performance as working with a 3D system is cumbersome, costly and often impractical. Therefore, the author developed a 1-D open-hole simulator for this purpose, which will be discussed in the next section.

However, there are two main points which should be highlighted beforehand. The first one is the fact that (ψ_{eq}) and $r_w^{'}(S_t)$ are both functions of the volumetric flow rate and fluid properties. That is, the productivity estimation requires an iterative procedure, which will be discussed in the forthcoming sections.

The second important point is the fact that there is no available formula to estimate the effective single phase inertial factor in both matrix and fracture (β_{f-eff} and β_{m-eff}). That is, in Multi-Layer systems it is simple to average the permeability (k) however the same is not true for the single phase inertial factor (β). As will be shown later in this chapter, that most available averaging techniques can lead to erroneous results if used to estimate an effective or average (β). This is due to the fact that in Layered system

(under Non-Darcy flow) the individual layer velocity ($\boldsymbol{v}_i$) is not readily known and therefore an iterative procedure is required to estimate (β_{eff}).

Accordingly, there is a need to propose an approximation to calculate the effective single phase inertial factor (β_{eff}) for multi-layer system, which will be proposed and verified later in the following sections.

4.3.2 Single Phase 1-D Open-Hole Simulator

In this section, the aim is to develop a 1-D EOH radial model, which replicates the flow performance of fine grid 3-D model under the same flow conditions. Therefore a 1-D open-hole simulator which simulates the steady state single phase flow around a vertical well open-hole model with constant pressure at the same external radius as that of the 3-D model was developed.

The 1-D simulator was developed using spread-sheet (VB application). Description of this simulator is given below.

Governing Equations and Numerical Solution

For the radial model, a combination of continuity and non-Darcy flow equations (Equation 4.16) can be written as follows:

$$\nabla.\left[\frac{1}{r}\left[\frac{\bar{k}}{\mu}\right].\frac{\rho}{1+R_{e-eq}}.\frac{\partial p}{\partial r}\right]=0\,. \tag{4.22}$$

The numerical differential form of Equation (4.22) is given as:

$$\frac{r_{i+1/2}}{\Delta r^2}\times.\left(\frac{\rho}{1+R_{e-eq}}\frac{\bar{k}}{\mu}\right)_{i+1}\times P_{i+1}-\left(\frac{r_{i+1/2}+r_{i-1/2}}{\Delta r^2}\right)\times\left(\frac{\rho}{1+R_{e-eq}}\frac{\bar{k}}{\mu}\right)_{i}\times P_i+\frac{r_{i-1/2}}{\Delta r^2}\times\left(\frac{\rho}{1+R_{e-eq}}\frac{\bar{k}}{\mu}\right)_{i-1}\times P_{i-1}=0 \tag{4.23}$$

For steady state conditions:

$P_1 = P_{well}$

$P_n = P_{ext}$

Where subscript well and ext refer to wellbore and external radius.

It should be noted that the wellbore pressure, external pressure, and external radius are known. However, the effective wellbore radius formulation in (Equation 4.21) depends on the velocity. Thus, the 1-D simulator calculation needs an iterative procedure. This iterative procedure is similar to that presented for single phase (SS) flow around single layer HFWs (refer to Chapter 3, section 3.4.3). However, the

equations used in here are those suitable for multi-layer HFWs (i.e. Equations 4.16, 4.18, 4.19). Also, it is important to point out that the convergence rate of the iterative procedure is acceptable. Hence, for majority of cases studied in this thesis the solution converges after 2-3 iteration rounds highlighting the integrity of the approach.

Validation of the 1-D EOH simulator will be given later in the verification section, but in order to complete the 1-D EOH description the effective single phase inertial factor (β_{eff}) will be discuss first.

4.3.3 Effective Single Phase Inertial Factor in Layered Systems

As mentioned earlier, the main difficulty in modelling layered system with an equivalent single layer is the fact that effective single phase inertial factor (β_{eff}) should be determined in an iterative way. This adds another level of complexity to the process since finding the effective wellbore radius is iterative in nature; because it is a function of Reynolds number (and thus a function of β_{eff}).

Ganesh *et.al.* and Cooper *et.al.* (1999) both studied the subject of effective single phase inertial factor (β_{eff}) in layered reservoirs. The main conclusions from these studies are a) estimating (β_{eff}) using any averaging techniques (e.g. arithmetic thickness based averaging) will always lead to erroneous results, b) estimating (β_{eff}) by using ($\overline{k}$) in a single phase inertial factor correlation (e.g. Greetsma, or Jones correlation, or any other correlation) will also lead to erroneous results. Therfore, it is recommended to use an iterative procedure to calculate (β_{eff}).

In this study, the author confirmed the previous conclusions (i.e. conclusions a and b), this will be shown in next section. However, the author propose a simple approximation to estimate (β_{eff}) for layered systems instead of the iterative procedure.

In order to propose (β_{eff}) formulation, a large data bank of more than 400 simulation (Non-Darcy flow) runs of Multi-Layer fractured and Non-fractured vertical wells was prepared. The author tried to match the mass flow rate of the EOH 1-D simulator with those of the 3-D in-house simulator by using different expressions of (β_{eff}). Here the validity of the arithmetic averaging technique, or the single phase (β) correlations available in literature were first examined with no success.

After a careful examination of these (Non-Darcy flow)simulations of Multi-Layer fractured and Non-fractured vertical wells, the author concluded that the results of the 3-

D simulator and those of the 1-D EOH simulator can be matched if the thickness averaged value of the ($k \cdot \beta$) product is used in estimating (β_{eff}). This is due to the fact that the inertial impact is always controlled by the ($k \cdot \beta$) product. That is, rocks with higher ($k \cdot \beta$) product have more negative impact of inertia (in term of well productivity). (β_{eff}) mathematical expression can be shown as follow,

$$\beta_{eff} = \frac{\sum_{i=1}^{n} k_i \cdot \beta_i \cdot h_i}{\overline{k} \cdot h_t}. \qquad (4.24)$$

($\overline{k}$) is the equivalent single layer permeability which can be calculated separately (using the Arithmetic averaging method) and then applied in Equation 4.24.

Up to this point, the 1-D EOH description has been completed and all the needed equations has been defined and explained. Therefore, in the next section a verification of the EOH 1-D simulator will be presented.

4.3.4 Verification of the Proposed Equivalent Open-Hole Approach

Layered (Non-Fractured) Vertical well

Figure 4.8 shows a comparison of the calculated Non-Darcy mass flow rate obtained using the EOH 1-D simulator with those of the 3-D in-house simulator for vertical layered Non-fractured well. This Vertical well consists of three layers. The three layers are (RC3 core with k of 3.9mD and β of 1E+11, Texas Cream with k of 11mD and β of 3.93E+9, Clashach with k of 553mD and β of 3.05E+5); more description of the layers properties is shown in Table 4.2, VW-M1 data set.

Figure 4.8 confirm a good accuracy of Equation 4.24. That is using (β_{eff}) calculated from Equation 4.24 in the EOH simulator give almost the same results as those of the 3-D simulator with an average absolute deviation error of (2%) for a wide range of pressure drop (50 < DP > 2500 Psi) and well velocities (50 < V_{well} > 4500 mD^{-1}). It should be noted that well velocities has been calculated by dividing the volumetric flow rate by the well surface area. Furthermore, it can be noticed (from the same figure) that using an arithmetic average method to estimate (β_{eff}) can lead to AAD as high as (80%).

Figure 4.9 shows the same comparison between EOH and those of the 3-D simulator shown in Figure 4.8. However, the mass flow rate was calculated using (β_{eff}) from

Greetsma correlation (Equation 4.25) instead of (β_{eff}) calculated using an arithmetic average method.

$$\beta_{eff} = \frac{C}{\bar{k}^{0.5}\phi^{5.5}}. \tag{4.25}$$

Where, ϕ is the rock porosity, $\bar{k}$ is the average permeability, and C is a constant equal to 4.8E+4.

It can be seen from Figure 4.9 that using ($\bar{k}$) in Greetsma correlation to estimate (β_{eff}) can lead to AAD as high as (35%). It should be noted that using any other available correlation in the literature will more or less lead to high AAD values.

The accuracy of the proposed formulation for (β_{eff}) was further verified by applying it to another layered vertical well model, with different layers rock properties and well velocities. Here, Texas Cream, Berea and RC1b core properties were used, VW-M2 data set in Table 4.2. Figure 4.10 compares the calculated mass flow rates using the EOH 1-D simulator, incorporating the effective single phase inertial factor formulation Equation 4.24, with those of the 3-D in-house simulator. This figure shows the good accuracy of the developed formulation and proposed EOH, with an average absolute deviation (AAD) of 2.6% for 100 data points used in this study.

Layered Vertical well (Hydraulically Fractured- Equal Fractures Length)

In this section the proposed EOH formulation (S_t and r_w', Equation 4.16 and 4.21) will be verified for a layered HFW model with equal fracture length in all layers (i.e. $x_{f\text{-}eq} = x_f$). The model consists of two layers. For this model three possible scenarios have been considered. That is, the first scenario is when the fracture and matrix permabilities in the two layers are un-equal. The second scenario is when the fracture permability in the two layers are un-equal but the matrix permeability in both layers is the same. The third scenario is when the fracture permeability in both layers is the same while the matrix permability in the two layers are different.

Figures 4.11 to 4.13 confirms the accuracy of the developed total skin equation (Equation 4.16) by comparing the calculated mass flow rate obtained using the EOH 1-D simulator, in which the effective wellbore radius and the iterative procedure have been incorporated, with those of the HFW 3-D in-house simulator. The reservoir models and range of variables are those listed in Table 4.2, M-HFW2, 3, and 4 data sets. The AAD% (average absolute deviation error) is only 2% for 50 data points.

Layered Vertical well (Hydraulically Fractured, Un-Equal Fractures Length)

In this section the proposed EOH formulation (S_t, Equation 4.16) will be verified for a layered HFW model with un-equal fracture length in different layers. The model used for this purpose consists of two layers. The same scenarios as those shown in the previous example have been considered plus a fourth scenario where fracture and matrix permeability in both layers are the same. In all these four scenarios, the fracture length is different in the two layers.

Figures 4.14 to 4.17 confirms the accuracy of the developed total skin equation (Equation 4.16) by comparing the calculated mass flow rate obtained using the EOH 1-D simulator, in which the effective wellbore radius and the iterative procedure described previously have been incorporated, with those of the HFW 3-D in-house simulator. The reservoir models and range of variables are those listed in Table 4.2, M-HFW5, 6, 7 and 8 data sets. The AAD% (average absolute deviation error) is only 3% for 100 data points.

4.4 STEADY-STATE TWO-PHASE GAS CONDENSATE FLOW

The main aim of this study is to extend the single phase mathematical modelling approach discussed earlier, to study two-phase flow around Layered HFWs in gas condensate reservoirs. To achieve this goal, an in-house simulator has been developed, simulating steady state flow of gas and condensate around multi-layer HFWs. A number of, ECLIPSE E300 commercial software, numerical simulations have been used in order to verify the integrity of the in-house simulator, which will be discussed later in this section. However, the development of two-phase 1-D EOH system will be discussed first.

4.4.1 Total Skin Factor/Effective Wellbore Radius

Here the objective is to introduce an EOH system, which produces the same flow performance, gas and condensate production rate, as that of a layered HFW system.

Actually, it was demonstrated in (Chapter 3, section 3.5.3), that in HFWs inertia is always dominant inside the fracture while coupling effects (if exists) are mainly expected to take place inside the matrix where velocity values are much lower than those encountered inside the fracture. With these in mind, it is expected that the two phase total skin values would be smaller than that of the single-phase flow (presented in the previous section).

In chapter 3, the following form of total skin has been developed for two-phase flow around single layer HFWs:

$$S_t = S_{gf} + S_f = S_{gf-eff} = \ln\left(\varepsilon_{ss} + \frac{\pi}{C_{FD-eff}}\right). \tag{4.26}$$

Where $C_{FD\text{-}eff}$ is the two-phase dimensionless fracture conductivity corrected for both coupling and inertia.

For the effect of inertia only, the following form of two-phase dimensionless fracture conductivity has been developed in Chapter 3, section 3.5:

$$C_{FD-eff} = \left(\frac{C_{FD-base}}{1+0.5R_{ew}}\right) \tag{4.27}$$

$$C_{FD-base} = \frac{k_f w_f}{k_m x_f} \cdot \left(\frac{k_{rgbf}}{k_{rgbm}}\right)_{well} \tag{4.28}$$

Where, k_{rgbf} and k_{rgbm} are the base relative permeability curves for fracture and matrix, both evaluated at wellbore pressure.

Also, it has been shown that the coupling effects can be included as a multiplication factor in the definition of the two-phase effective dimensionless fracture conductivity, Equation 4.27 (refer to Chapter 3, section 3.5).

This multiplication factor can be approximately estimated as the ratio between the velocity/IFT dependent matrix gas relative permeability to the base (No velocity/IFT effects) matrix gas relative permeability, both evaluated at wellbore condition, $\left(\frac{k_{rg}}{k_{rgb}}\right)_{well}$.

Therefore the following equation can be used to estimate approximately the effective two-phase dimensionless fracture conductivity (i.e. corrected for both coupling and inertia effects):

$$C_{FD-eff} = \frac{C_{FD-base}}{1+0.5R_{we}} \times \left(\frac{k_{rg}}{k_{rgb}}\right)_{well} \tag{4.29}$$

Based on the previous discussion, it is proposed that the total skin for two phase gas condensate flow in an equivalent single layer, which should give the same flow performance as that of a 3-D Mulit-Layer HFW, be obtained by replacing the ($C_{FD-base}$) by ($C_{FD-base\text{-}eq}$) and the relative permeability terms with an equivalent single layer relative permeability, as shown below.

$$S_t = S_{gf} + S_f = S_{gf-eff} = \ln\left(\varepsilon_{ss} + \frac{\pi}{C_{FD-eff}}\right). \tag{4.30}$$

$$C_{FD-eff} = \frac{C_{FD-base-eq}}{1+0.5R_{we}} \times \left(\frac{k_{rg-eq}}{k_{rgb-eq}}\right)_{well} \tag{4.31}$$

The final form of the total skin of an equivalent single layer that should give the same performance as the 3-D Multi-Layer HFW is shown in Equation 4.32.

$$S_t = \ln\left(\varepsilon_{ss} + \left(\frac{k_{rgb-eq}}{k_{rg-eq}}\right)_{well} \cdot \left(\frac{\pi}{C_{FD-base-eq}} + \frac{\pi \cdot R_{ew-eq}}{2C_{FD-base-eq}}\right)\right) \tag{4.32}$$

This form of total skin is general in the sense that for single phase flow $\left(\frac{k_{rgb-eq}}{k_{rg-eq}}\right)_w$ will equal 1 and the two-phase dimensionless conductivity will be equal to the single phase dimensionless conductivity. And therefore Equation 4.32 will correctly convert to Equation 4.16 (i.e. Single phase total skin equation).

However, in order to solve Equation 4.32, a formulation of for (k_{rgb-eq}) estimation should be proposed.

In other words, the main question here is "what is the equivalent base relative permeability curve that should be used in Equation 4.32".

As discussed earlier, the gas condensate near wellbore flow is a steady state process due to the fact that total composition is constant across the reservoir. Furthermore, in low IFT gas condensate systems capillary pressure is set to zero. Considering that the total gas ratio (GTR) across layers is the same, one can calculate the equivalent base relative permeability curve based on the thickness averaged effective layers permabilities, as follows:

$$k_{rgb-eq} = \frac{\sum_{i=1}^{n} k_i k_{rgbi} h_i}{\bar{k} h_t} \tag{4.33}$$

Therefore, the final form of the equations for estimation of productivity of the two-phase 1-D EOH, which should replicate the performance as that of 3-D HFW can be summarized as follows:

$$m = \frac{2\pi kh \int_{Pw}^{Pe} \left(\frac{\rho_l k_{rc-eq}}{\mu_c} + \frac{\rho_g k_{rg-eq}}{\mu_g} \right) dp}{Ln\left(\frac{r_e}{r_w^{'}} \right)} \tag{4.34}$$

$$r_w^{'} = x_f \times e^{-S_t} \tag{4.35}$$

4.4.2 Two-Phase 1-D Open-Hole Simulator

In order to verify the proposed EOH system formulation presented above, a 1-D two-phase open hole in-house simulator was developed, simulating the steady state flow of gas and condensate around a vertical well, which should generate the same flow performance as that of the 3-D model. It should be noted that the 1-D simulator is based on the finite difference method.

Governing Equations and Numerical Solution

For the radial 1-D model, a combination of continuity equation, and (gas and condensate) flow equations can be solved as follows:

$$\nabla . \left[\frac{1}{r} . \left(\left[\frac{\rho k_{r-eq}}{\mu} \right]_g + \left[\frac{\rho k_{r-eq}}{\mu} \right]_c \cdot \bar{k} \right) . \frac{\partial p}{\partial r} \right] = 0 . \tag{4.36}$$

The numerical differential form of the above equation is

$$\frac{r_{i+1/2}}{\Delta r^2} \times . \left(\left[\frac{\rho k_{r-eq}}{\mu} \right]_g + \left[\frac{\rho k_{r-eq}}{\mu} \right]_c . \frac{\bar{k}}{\mu} \right)_{i+1} \times P_{i+1} - \left(\frac{r_{i+1/2} + r_{i-1/2}}{\Delta r^2} \right) \times \left(\left[\frac{\rho k_{r-eq}}{\mu} \right]_g + \left[\frac{\rho k_{r-eq}}{\mu} \right]_c . \frac{\bar{k}}{\mu} \right)_i \times P_i +$$
$$\frac{r_{i-1/2}}{\Delta r^2} \times \left(\left[\frac{\rho k_{r-eq}}{\mu} \right]_g + \left[\frac{\rho k_{r-eq}}{\mu} \right]_c . \frac{\bar{k}}{\mu} \right)_{i-1} \times P_{i-1} = 0$$

$$z_j = \frac{\rho_g y_j GTR + \rho_c x_j (1 - GTR)}{\rho_g GTR + \rho_c (1 - GTR)} = cons. \tag{4.37}$$

The total fluid composition ($\mathbf{z_j}$) is constant as the fluid flows through the porous media. However, for each component, there is mass transfer between two phases.

For steady state conditions,
$P_1 = P_w$
$P_n = P_{res}$,

Where, subscripts *w* and *res* refer to wellbore and external radius.

It should be noted that the wellbore pressure, external pressure, external radius, and GTR_{well} or Z_j are known. However, the effective wellbore radius formulation (Equation 4.35) depends on the velocity. Thus, the 1-D simulator calculation needs an iterative procedure. These iterative procedures are similar to those presented for two phase (SS) flow around single layer HFWs (refer to Chapter 3, section 3.5.4). However, the equations used in here are those suitable for two phase multi-layer HFWs (i.e. Equations 4.32, 4.34, 4.35). Also, it is important to point out that the convergence rate of the iterative procedure is acceptable. Hence, for majority of cases studied in this thesis the solution converges after 2-3 iteration rounds highlighting the integrity of the approach.

4.4.3 HFW 3D Mathematical Simulator

A fine grid 3-D two-phase (gas and condensate) in-house simulator was developed in order to verify the integrity of the proposed 1-D in-house simulator. The 3-D geometries used here are the same as those used for single phase flow in section 4.2.2. However, the governing equations solved for this flow domain are different, as described below.

The governing equations employed in this part of the study, are the same as those presented in Chapter 3 (section 3.5.1), for the (SS) two-phase flow around 2-D single layer HFWs, however in here the governing equations have been solved for 3-D Multi-Layer space. The main governing equation is shown below, which is the final form of combining the two phase flow and continuity equations (Jamiolahmady et al. 2006, Ghahri 2010, Gas Condensate Recovery Final Report 2005-2008 and 2008-2011):

$$\nabla.\left(\left\{\left[\frac{\rho k_r}{\mu}\right]_g+\left[\frac{\rho k_r}{\mu}\right]_c\right\}k\nabla P\right)=0\,. \tag{4.38}$$

More information about the set of (SS) two phase governing equations as well as their source, and their full derivations can be found in Chapter 3, section 3.5.1. Furthermore, the mathematical solution technique used to solve the above equation is similar to that presented in Chapter 3, section 3.5.1.

The relative permeability term in Equation 4.38 is estimated using the generalized k_r correlation by Jamiolahmady et al. (2009). Also, the total fluid composition ($\mathbf{z_j}$) is constant as the fluid flows through the porous media. However, for each component, there is mass transfer between the two phases. Finally, the gas condensate fluid used in this study is the same as that presented in Chapter 3, Table 3.3.

4.4.4 ECLIPSE 3-D Two Phase HFW Model

The accuracy of the two-phase mathematical in-house simulator was confirmed by comparing some of its results with those of ECLIPSE300 at the same prevailing conditions.

The reservoir model in this exercise had the core properties of Texas Cream with porosity of 0.21 and permeability of 9.1 mD. The reservoir fluid was a binary mixture of C1 (methane) and n-C4 (normal butane), refer to Table 3.3. The reservoir consist of two layers with equal thickness, but different fracture lengths (i.e. $h_1 = h_2$, $x_{f1} = 0.5x_{f2}$). The reservoir was 100 m in the X and 100 m in Y directions and 8 m in the Z direction. The fracture has a length of 25 m and a width of 5mm. The fracture has a permeability of 146 D. The fracture and the core relative permeability are those measured in GCR-HW Laboratory. The very fine grid option was used to capture the abrupt changes in flow parameters near the wellbore. It should be noted that the k_r correlations used in Comsol and ECLIPSE300 simulators are different; therefore the base curve relative permeability has been used to describe the fluid mobility around the HFW. The base curve is the relative permeability curve measured at a high IFT (above which k_r is independent of interfacial tension) and low velocity (below which k_r is independent of velocity).

In ECLIPSE 300, seventy injection wells were placed at the boundary of the reservoir to keep the reservoir pressure at the drainage boundary constant.

Figure 4.18 shows the good agreement between the two results. The arithmetic average absolute percentage deviation (AAD%) of the predicted flow rate values obtained by the ECLIPSE simulator compared to those estimated by the HFW 3-D in-house simulator was 2.8 %.

4.4.5 Verification of the Proposed Equivalent Open-Hole Approach

In this section a verification of the two-phase EOH 1-D simulator will be given, by comparing the 1-D EOH results with those of the 3-D HFW in-house simulator under the same prevailing conditions.

Layered Vertical Well- Non-fractured

Figures 4.19 and 4.20 confirm the accuracy of the proposed approach by comparing the calculated mass flow rates obtained using the EOH 1-D simulator, in which the developed effective wellbore radius, Equation 4.35, and the iterative procedure have been used, with those of the 3-D in-house simulator. The reservoir models and the range

of the variables are those listed in Table 4.2, VW-M9 and 10 data sets. The average absolute deviation error, AAD% for 38 data points is 2.5%.

Layered Vertical Well- Fractured

Figures 4.21 and 4.22 confirm the accuracy of the proposed approach by comparing the calculated mass flow rates obtained using the EOH 1-D simulator, in which the developed effective wellbore radius, Equation 4.35, and the iterative procedure have been used, with those of the HFW3-D in-house simulator. The reservoir models and the range of the variables are those listed in Table 4.2, HFW-M11 and 12 data sets. It should be mentioned that HFW-M11 is a two layer model with equal fracture length in both layers, while HFW-M12 is a two layer model with un-equal fracture length in each layer. The average absolute deviation error, AAD% for HFW-M11 was 1.82% for 100 data points while for HFW-M12 it was 3.5% for 100 data points.

4.5 PSEUDO STEADY STATE SINGLE PHASE FLOW

Earlier, a steady state geometric skin was developed to account for the effect of geometric parameters on the multi-layer HFW productivity. This part of study is devoted to investigate the application of this geometric skin formulation for pseudo steady state conditions. Accordingly, a multi-layer HFW pseudo steady in-house simulator was developed, which will be described first. Then its integrity will be confirmed by comparing some of its results with those of the ECLIPSE commercial simulator for the same prevailing flow conditions.

4.5.1 Geometric Skin/Effective Wellbore Radius

It has been shown in chapter 3, that the geometric skin of HFW under SS and PSS are the same as long as the penetration ratio is less than 0.2 (I_x <0.2). However, for higher penetration ratio the two skins are different. This difference is due to the fact that the reciprocal effective wellbore radius of infinite conductivity fracture (ε) is different under SS and PSS. That is, for SS (ε) decrease as penetration ratio increases while in case of PSS it increases as penetration ratio increase.

In summary, the PSS total skin functional form is similar to SS but with different formulation of (ε), as follows:

$$S_t = \ln\left(\varepsilon_{pss} + \frac{\pi}{C_{FD-eq}} + \frac{\pi \cdot R_{ew-eq}}{2C_{FD-eq}}\right) \tag{4.39}$$

For PSS conditions:
$$\varepsilon_{PSS} = 2 + \left(\frac{0.355 I_x}{1 - 0.704 I_x} \right) \tag{4.40}$$

It should be noted that for Darcy flow (i.e. effect of Reynolds number R_{ew}, is minimal), the third term in Equation 4.39 is negligible and the total skin S_t converts to PSS geometric skin S_{gf} which has the effect of geometry only.

Accordingly, for PSS Darcy flow a HFW can be represented by a vertical well with an effective wellbore radius as below:

$$q_{HFW} = \frac{2\pi \overline{k_m} h \Delta \psi_{eq}}{\mu \left(\ln \left(\frac{r_e}{r_w^{'}} \right) - 0.75 \right)}, \tag{4.41}$$

$$\psi_{eq} = \int \frac{k_{r-eq}}{\mu} dp \tag{4.42}$$

$$r_w^{'} = x_{f-eq} \times e^{-S_t} \tag{4.43}$$

It should be noted that for PSS, the flow rate and wellbore pressure are known and we are solving the equation for average reservoir pressure (P_{avg}). Accordingly, no iteration process is required as seen in the Steady-State case. Next, an EOH PSS simulator will be introduced.

5.4.2 Single phase 1-D Open-Hole simulator

A single-phase open-hole in-house simulator was also developed to verify the integrity of the proposed approach of simulating (single phase Darcy and Non-Darcy) flow around a single vertical well rather than the actual 3D geometry for PSS conditions. The modelling approach is similar to that used for single-phase SS flow but flow equations governing the PSS conditions were solved by the finite difference method, as described below.

Governing Equation and Numerical Solution

For the 1-D radial model, a combination of continuity equation and non-Darcy flow equation can be solved as follows:

$$\nabla . \left[\frac{1}{r} \left[\frac{\bar{k}}{\mu} \right] . \frac{\rho}{1 + R_{ew-eq}} . \frac{\partial p}{\partial r} \right] = \left(\frac{\rho_w q_w}{V_t} \right) \tag{4.44}$$

The differential form of Equation (4.44) is:

$$\frac{r_{i+1/2}}{\Delta r^2}\times.\left(\frac{\rho}{1+R_{ew-eq}}\frac{\bar{k}}{\mu}\right)_{i+1}\times P_{i+1}-\left(\frac{r_{i+1/2}+r_{i-1/2}}{\Delta r^2}\right)\times\left(\frac{\rho}{1+R_{ew-eq}}\frac{\bar{k}}{\mu}\right)_{i}\times P_i+\frac{r_{i-1/2}}{\Delta r^2}\times\left(\frac{\rho}{1+R_{ew-eq}}\frac{\bar{k}}{\mu}\right)_{i-1}\times P_{i-1}=\left(\frac{\rho_w q_w}{V_t}\right)$$

The boundary conditions are:

1) At the outer boundary (external radius) there is no flow boundary, (q_{ext} = 0)

2) The flow rate at the inner boundary (wellbore radius, q_{well}) is known.

Similarly, to the steady-state case, the main dependent variable here is pressure. After solving Equation 4.75, the pressure profile within the specified drainage area is calculated. Then volumetric average reservoir pressure is determined.

4.5.3 Mathematical HFW 3-D Simulator

Here the 3-D HFW geometries, which were developed to study the flow behaviour at steady state conditions, were used in this study. However, the governing equations are those for pseudo-steady state conditions, as described next.

The 3-D PSS governing equations used here, are the same as those presented in Chapter 3 (section 3.2.3), for the (PSS) single-phase flow around 2-D single layer HFWs, however in here the governing equations have been solved for 3-D Multi-Layer space. The main governing equation is shown below, which is the final form of combining the Forchheimer equation and the continuity equation for a single phase compressible fluid (Gas Condensate Recovery Final Report 2008-2011 and Ghahri 2010):

$$\nabla.\left[2\left[\frac{k}{\mu}\right].\frac{\rho\nabla P}{1+\sqrt{1+4\beta\left(\frac{k}{\mu}\right)^2|\nabla P|}}\right]=\frac{\rho_{well}q_{well}}{V_t}. \qquad (4.45)$$

It should be noted that the equation is for the general case of non-Darcy flow, which will converts to Darcy flow at lower velocities where inertia is negligible.

More information about the set of (PSS) single phase governing equations as well as their source, and their full derivations can be found in Chapter 3, section 3.2.3. Also, the mathematical solution technique is the same as that presented for the PSS (single phase) single layer HFWs study in Chapter 3, section 3.2.3.

4.5.4 ECLIPSE PSS Single-Phase HFW Model

The accuracy of the pseudo steady state HW in-house simulator was confirmed by comparing its results with those of a similar model constructed using ECLIPSE. The core properties of Texas Cream, with porosity 0.21 and permeability 9.1 mD, were used to describe the reservoir in this model. The single phase gas properties are listed in Table 3.1a. The reservoir consist of two layers with equal thickness, but different fracture lengths (i.e. $h_1 = h_2$, $x_{f1} = 0.5x_{f2}$). The reservoir was 100 m in the X and 100 m in Y directions and 8 m in the Z direction. The fracture has a length of 25 m and a width of 5mm. The fracture has a permeability of 146 D.

In ECLIPSE simulations, to simulate pseudo steady state condition, the flow at the outer boundary of the steady state model described in Section 4.2.3 was set to zero. The flow rate at the wellbore was kept constant during production time. The volumetric average pressure derivative with time was monitored and once stabilised, it was concluded that the pseudo steady state conditions had been achieved, and then the wellbore pressure and the volumetric average reservoir pressure are recorded.

Using the in-house simulator, for each time step, the same wellbore pressure as that of Eclipse simulator was used, and then the volumetric average reservoir pressure was calculated.

The average pressures calculated by the in-house mathematical simulator were compared with those of similar simulations conducted using the ECLIPSE simulator. Figure 4.23 shows the good agreement between the two results. The arithmetic average absolute percentage deviation (AAD %) of the predicted P_{avg} values by the ECLIPSE simulator compared to those estimated by the HW simulator was 1.2 %.

5.4.5 Verification of the Proposed PSS Equivalent Open-Hole Approach

Single phase Darcy Flow

Figure 4.24 shows the good level of accuracy of Equation 4.41 by comparing its volumetric average reservoir pressure results with the outcomes of the steady state 3-D in-house simulator. The reservoir model used is given in Table 4.2 VW-M13 data set. Here the Average Absolute Deviation (AAD %) is less than 2%, confirming the applicability of Equation 4.39 for the calculation of Multi-Layer geometric fracture skin at pseudo-steady state conditions.

Single phase Non-Darcy Flow

Figure 4.25 confirms the accuracy of the developed total skin equation (Equation 4.39) by comparing the calculated volumetric average reservoir pressure obtained using the EOH 1-D simulator with those of the HFW 3-D in-house simulator. The reservoir models and the range of variables are those listed in Table 4.2, HFW-M14 data set. The AAD% (average absolute deviation error) is 3 %.

4.6 PSEUDO STEADY STATE TWO PHASE FLOW

4.6.1 Total Skin/Effective Wellbore Radius

In Chapter 3 (section 3.5), it has been shown that the two-phase (pseudo-steady state) total skin formulation is similar to those of (steady state), but with a different expression of (ε), as shown below,

$$S_t = \ln\left(\varepsilon_{pss} + \left(\frac{k_{rgb}}{k_{rg}}\right)_w \cdot \left(\frac{\pi}{C_{FD-base}} + \frac{\pi \cdot R_{ew}}{2C_{FD-base}}\right)\right). \tag{4.46}$$

Where, ε_{pss} is given by Equation 4.40.

4.6.2 Two-Phase 1-D Open-Hole Simulator

A two-phase 1-D open-hole in-house simulator was also developed to verify the integrity of the proposed approach of simulating two-phase flow around a vertical well rather than the actual 3D geometry for PSS conditions. The model is based on finite difference method, as described below.

Governing Equations and Numerical Solution

For the radial 1-D model, a combination of continuity equation, and (gas and condensate) flow equations can be solved as follows:

$$\nabla.\left[\frac{1}{r}.\left(\left[\frac{\rho k_r}{\mu}\right]_g + \left[\frac{\rho k_r}{\mu}\right]_c \cdot k\right).\frac{\partial p}{\partial r}\right] = \frac{d(\rho_{eqphase}\varphi)}{dt}. \tag{4.47}$$

The numerical differential form of Equation (4.82) is

$$\frac{r_{i+1/2}}{\Delta r^2} \times .\left(\left[\frac{\rho k_r}{\mu}\right]_g + \left[\frac{\rho k_r}{\mu}\right]_c \cdot \frac{k}{\mu}\right)_{i+1} \times P_{i+1} - \left(\frac{r_{i+1/2} + r_{i-1/2}}{\Delta r^2}\right) \times \left(\left[\frac{\rho k_r}{\mu}\right]_g + \left[\frac{\rho k_r}{\mu}\right]_c . \frac{k}{\mu}\right)_i \times P_i +$$

$$\frac{r_{i-1/2}}{\Delta r^2} \times \left(\left[\frac{\rho k_r}{\mu}\right]_g + \left[\frac{\rho k_r}{\mu}\right]_c . \frac{k}{\mu}\right)_{i-1} \times P_{i-1} = \frac{\rho_{eqphase w} q_w}{V}$$

$$z_j = \frac{\rho_g y_j GTR + \rho_c x_j (1-GTR)}{\rho_g GTR + \rho_c (1-GTR)} = cons. \tag{4.48}$$

The boundary conditions are:

3) At the outer boundary (external radius) there are no flow boundaries, $q_{ext} = 0$

4) The flow rate at the inner boundary (wellbore radius, q_{well}) is known.

4.6.3 Mathematical 3-D HW Model

Similar to the two-phase (PSS) flow around single layer HFWs study, presented in Chapter 3 section 3.5.7, the equivalent single phase approach concept has been used in order to simplify the calculation process. A mathematical simulator was constructed to verify the integrity of this approach in multi-layer HFWs simulation. Accordingly, the 3-D geometries used in this section are the same as those used for the single- phase PSS flow case. However the governing equations are those suitable for two-phase PSS flow. The HFW is producing at a constant total flow rate (i.e. gas and condensate).

The 3-D PSS governing equations used here, are the same as those presented in Chapter 3 (section 3.5.7), for the (PSS) two-phase flow around 2-D single layer HFWs, however in here the governing equations have been solved for 3-D Multi-Layer space. The main governing equation is shown below, which is the final form of combining the PSS two-phase continuity and flow equations (Gas Condensate Recovery Final Report 2008-2011 and Ghahri 2010):

$$\nabla.\left(\left\{\left[\frac{\rho k_r}{\mu}\right]_g + \left[\frac{\rho k_r}{\mu}\right]_c\right\} k \nabla P\right) = \frac{\rho_{eqphase_w} q_w}{V}. \tag{4.49}$$

Where, $q_w = \left(q_g + q_c\right)_w$.

More information about the set of (PSS) two phase governing equations as well as their source, and their full derivations can be found in Chapter 3, section 3.5.7. Furthermore, the mathematical solution technique used to solve the above equation is similar to that presented in Chapter 3, section 3.5.7. Similar to the two-phase (SS) model, the total fluid composition (z_j) is constant at any time as fluid flows through the porous media, and the k_r term in the above equation is estimated using the generalized

correlation of (Jamiolahmady *et al.* 2009). The same binary fluid system as that used for the SS simulator was used here (Table 3.3).

4.6.4 ECLIPSE Two-Phase Pseudo Steady State HFW Model

The accuracy of the two-phase mathematical in-house simulator was confirmed by comparing its results with those of ECLIPSE300 at the same prevailing conditions.

The reservoir model in this exercise had the core properties of Texas Cream with porosity of 0.21 and permeability of 9.1 mD. The reservoir fluid was a binary mixture of C1 (methane) and n-C4 (normal butane) described in Table 3.3. The reservoir consist of two layers with equal thickness, but different fracture lengths (i.e. $h_1 = h_2$, $x_{f1} = 0.5x_{f2}$). The reservoir was 100 m in the X and 100 m in Y directions and 8 m in the Z direction. The fracture has a length of 25 m and a width of 5mm. The fracture has a permeability of 146 D. The fracture and the core relative permeability are those measured in GCR-HW Laboratory. The fine grid has been used to capture the complexity of flow near the wellbore. It should be noted that the k_r correlations used in Comsol and ECLIPSE300 simulators are different; therefore the base curve relative permeability has been used to describe the fluid mobility around the HFW. In order to achieve PSS conditions for the gas and condensate flow in ECLIPSE (E300), first the pressure at the boundaries was kept constant by injecting gas condensate through 70 injection wells in this area, once steady state (SS) conditions were achieved, these injection wells were shut down and the HFW produces gas and condensate with a total constant reservoir flow rate. In E-300 simulator, the wellbore and volumetric average pressures were recorded at different time steps.

Then, these wellbore pressure values were used in the in-house simulator in order to calculate the volumetric average reservoir pressure for each time step.

The volumetric average reservoir pressures (P_{ave}) calculated by ECLIPSE300 and the in-house simulator have been compared at different time steps. Figure 4.26 shows the good agreement between the two results. The arithmetic average absolute percentage deviation (AAD %) of the predicted P_{ave} (psi) values by the ECLIPSE simulator compared to those estimated by the HFW in-house simulator was 1.3 %.

4.6.5 Verification of the Proposed Equivalent Open-Hole Approach

Figure 4.27 confirm the accuracy of the proposed approach by comparing the two-phase EOH calculated volumetric average reservoir pressure with those of the HFW 3-D in-house simulator. The reservoir models and the range of the variables are those listed in Table 4.2, M-HFW15 and 16 data sets. The average absolute deviation error, AAD% in this study is 3%.

4.7 SUMMARY AND CONCLUSIONS

A number of in-house simulators were developed, for the first time, to study the well performance of Multi-Layer hydraulically fractured wells (HFWs) in gas and gas condensate reservoirs under both steady-state and pseudo-steady state conditions. The models correctly account for the coupling and inertial effects. The integrity of the results of the in-house simulators were confirmed by comparing some of their results with those obtained using ECLIPSE with fine grid for the same prevailing flow conditions. Based on the assumption and results presented in chapter 4, the following conclusions can be drawn.

1. The developed single layer geometric skin factor (presented in Chapter 3) can be extended to multi-layer HFW using an equivalent single layer with equivalent dimensionless fracture conductivity ($C_{FD\text{-}eq}$) and equivalent fracture length ($x_{f\text{-}eq}$).
2. The needed formulation for equivalent dimensionless fracture conductivity ($C_{FD\text{-}eq}$) (Equation 4.8) and equivalent fracture length ($x_{f\text{-}eq}$) (Equation 4.10) has been verified for a wide range of pertinent geometrical parameters.
3. For Non-Darcy flow, multi-layer systems can be modelled using an equivalent single layer concept, provided that an appropriate expression of effective or equivalent single phase inertial factor (β_{eff}) is available.
4. In this study an approximation for effective or equivalent single phase inertial factor (β_{eff}) (Equation 4.24) has been proposed and verified for Multi-layer fractured and Non-Fractured wells over a wide range of geometrical and flow parameters.
5. For the case of two-phase gas condensate flow, an equivalent single layer (base curve) relative permeability (Equation 4.33) has been presented and its applicability for the calculation of coupling and inertia effects has been verified over a wide range of geometrical and flow parameters.
6. The proposed formulations are general, as it correctly extends to a single layer system if the number of layers is set to one. If gas fractional flow (GTR_{well}) is set to unity, it also correctly converts to the single phase gas systems under Non-Darcy flow, and if Reynolds number is small to that under Darcy flow.
7. A 1-D in-house simulator was developed by the author to study gas condensate flow in multi-layer systems (fractured and Non-fractured wells).

The integrity of this simulator has been verified by comparing its results with those obtained using the fine grid 3-D in-house mathematical simulator.

8. The added value of using the 1-D in-house simulator was confirmed by demonstrating the close agreement between its results and those obtained from the fine grid 3-D in-house simulator. That is, the 1-D simulator produces the same results as those of the 3-D simulator with less computational time and minimal troubleshooting process.
9. The proposed formulations and procedures mentioned above are applicable to both steady state and pseudo-steady state conditions.

4.8 REFERENCES

Bennett C., Raghavan R., Reynolds, A., 1986: "Analysis of Finite-Conductivity Fractures Intercepting Multilayer Commingled Reservoirs", SPE11030-PA

Camacho V., Raghavan R., Reynolds, A., 1987: "Response of Wells Producing Layered Reservoirs: Unequal Fracture Length", SPE12844-PA

Ganesh N., Mukul S., Pope G., 1999: "Effect of heterogeneity on the Non-Darcy flow coefficient", SPE Reservoir Eval. & Eng. 2 (3), June 1999.

Cooper J., Xiuli W., Mohanty K., 1999: "Non-Darcy flow studies in Anisotropic porous media", SPE Journal 4 (4), December 1999.

Jamiolahmady M. and Sohrabi M. , 2005: "Single-phase flow in and around perforation tunnel", IASME Transactions, Issue 7, Volume 2, pp 1288-1297.

Jamiolahmady M., Danesh A., Sohrabi M. and Duncan D. B, February 2006: "Flow around a rock perforation surrounded by damaged zone: Experiments vs. Theory", Journal of Petroleum Engineering and Science, 50 (2), pp. 102-114.

Jamiolahmady M., Sohrabi M., Ireland S., and Ghahri P., 2009: "A Generalized Correlation for Predicting Gas-Condensate Relative Permeability at near the Wellbore Conditions", Journal of Petroleum Science and Engineering.

Panteha Ghahri: "Modelling of Gas-Condensate Flow around Horizontal and Deviated wells and Cleanup Efficiency of Hydraulically Fractured Wells", PhD 2010, Heriot-Watt University.

Gas Condensate Recovery Project (2005-2008) Final Report, 2008, IPE, Heriot Watt University, UK.

Gas Condensate Recovery Project (2008-2011) Final Report, 2008, IPE, Heriot Watt University, UK.

Table 3.1: Basic Core Properties.

Core type	Porosity	Permeability (mD)	Single-phase Inertia factor (1/m)
RC1b	0.08	0.18	1.06E+12
RC3	0.2	3.9	1.55E+11
Texas Cream	0.21	11.1	3.93E+9
Berea	0.185	100	1.08E+8

Table 4.2: Parameters of different HFWs studied in this work.

	HFW-M1	**VW-M1**	**VW-M2**
Matrix Core Properties	k_1=3.9mD β_1=1.55E+11 k_2=9.1mD β_2=3.927E+9 k_3=110mD β_3=1.85E+8	k_1=3.9mD β_1=1.55E+11 k_2=9.1mD β_2=3.927E+9 k_3=553mD β_3=1.04E+8	k_1=0.18mD β_1=1 E+12 k_2=9.1mD β_2=3.927E+9 k_3=110mD β_3=1.85E+8
Fluid	Single phase	Single phase	Single phase
Number of Data Points	16	12	100
Thickness	$h_1=h_2=h_3$=2m $k_{f1}=k_{f2}=k_{f3}$=146D $x_{f2}=0.5x_{f1}$, $x_{f3}= 0.5x_{f2}$	h_1=2m h_2=8m h_3=20m	h_1=8m h_2=16m h_3=20m
DP/psia (range)	350	50-2000	50-2400
Comment	$h_1=h_2=h_3$=2m $k_{f1}=k_{f2}=k_{f3}$=146D		

Table 4.2: Parameters of different HFWs studied in this work.

	HFW-M2	**HFW-M3**	**HFW-M4**	**HFW-M5**
Matrix Core Properties	k_1=9.1mD β_1=3.927E+9 k_2=110mD β_2=1.85E+8	k_1=9.1mD β_1=3.927E+9 k_2=9.1mD β_2=3.927E+9	k_1=9.1mD β_1=3.927E+9 k_2=110mD β_2=1.85E+8	k_1=9.1mD β_1=3.927E+9 k_2=110mD β_2=1.85E+8
Fracture Core Properties	k_1=146D β_1=3.5E+5 k_2=15D β_2=1E+6	k_1=146D β_1=3.5E+5 k_2=15D β_2=1E+6	k_1=146D β_1=3.5E+5 k_2=146D β_2=3.5E+5	k_1=146D β_1=3.5E+5 k_2=15D β_2=1E+6
Number of Data Points	16	16	16	90
$\mathbf{h_1/h_2}$	0.5-1	1	0.5-1	0.5-1
$\mathbf{X_{f1}/X_{f2}}$	1	1	1	0.25-0.75
Fluid	Single phase	Single phase	Single phase	Single phase
DP/psia (range)	850	500	200	500-1000

Table 4.2: Parameters of different HFWs studied in this work.

	HFW-M6	**HFW-M7**	**HFW-M8**
Matrix Core Properties	k_1=9.1mD β_1=3.927E+9 k_2=9.1mD β_2=3.927E+9	k_1=9.1mD β_1=3.927E+9 k_2=110mD β_2=1.85E+8	k_1=9.1mD β_1=3.927E+9 k_2=9.1mD β_2=3.927E+9
Fracture Core Properties	k_1=146D β_1=3.5E+5 k_2=15D β_2=1E+6	k_1=146D β_1=3.5E+5 k_2=146D β_2=3.5E+5	k_1=146D β_1=3.5E+5 k_2=146D β_2=3.5E+5
Number of Data Points	16	16	16
$\mathbf{h_1/h_2}$	0.5-1	0.5-1	0.5-1
$\mathbf{X_{f1}/X_{f2}}$	0.25-0.75	0.25-0.75	0.25-0.5
Fluid	Single phase	Single phase	Single phase
DP/Psia (range)	750	150	500
$\mathbf{P_{well}}$**/Psia**	1000	1000	1000
$\mathbf{GTR_{well}}$	1	1	1

Table 4.2: Parameters of different HFWs studied in this work.

	VW-M9	**VW-M10**	**HFW-M11**	**HFW-M12**
Matrix Core Properties	k_1=0.18mD β_1=1.06E+12 k_2=9.1mD β_2=3.93E+9	k_1=9.1mD β_1=3.927E+9 k_2=110mD β_2=1.85E+8	k_1=9.1mD β_1=3.927E+9 k_2=9.1mD β_2=3.927E+9	k_1=9.1mD β_1=3.927E+9 k_2=110mD β_2=1.85E+8
Fracture Core Properties	--	--	k_1=146D β_1=3.5E+5 k_2=146D β_2=3.5E+5	k_1=146D β_1=3.5E+5 k_2=15D β_2=1E+6
Number of Data Points	22	16	100	100
h_1/h_2	0.5-1	0.5-1	1	0.5-1
X_{f1}/X_{f2}	--	--	1	0.25-0.75
Fluid	Two phase	Two phase	Two phase	Two phase
DP/Psia (range)	200	200	65-665	65-665
P_{well}/Psia	1365	1365	1665-900	1665-900
GTR_{well}	0.816-0.913	0.816-0.913	0.716-0.91	0.716-0.91

Table 4.2: Parameters of different HFWs studied in this work.

	VW-M13	**HFW-M14**	**HFW-M15**	**HFW-M16**
Matrix Core Properties	k_1=9.1mD β_1=3.927E+9 k_2=110mD β_2=1.85E+8	k_1=9.1mD β_1=3.927E+9 k_2=110mD β_2=1.85E+8	k_1=9.1mD β_1=3.927E+9 k_2=110mD β_2=1.85E+8	k_1=9.1mD β_1=3.927E+9 k_2=110mD β_2=1.85E+8
Fracture Core Properties	--	k_1=146D β_1=3.5E+5 k_2=15D β_2=1E+6	k_1=146D β_1=3.5E+5 k_2=15D β_2=1E+6	k_1=146D β_1=3.5E+5 k_2=15D β_2=1E+6
Number of Data Points	16	16	16	16
$\mathbf{h_1/h_2}$	0.5-1	0.5-1	0.5-1	0.5-1
$\mathbf{X_{f1}/X_{f2}}$	1	0.25-0.75	0.25-0.75	1
Fluid	Single phase	Single phase	Two phase	Two phase
$\mathbf{q_{well}/m^3/s}$	0.01-0.4	0.001	0.001	0.001
$\mathbf{GTR_{well}}$	1	1	0.71-0.81	0.71-0.81

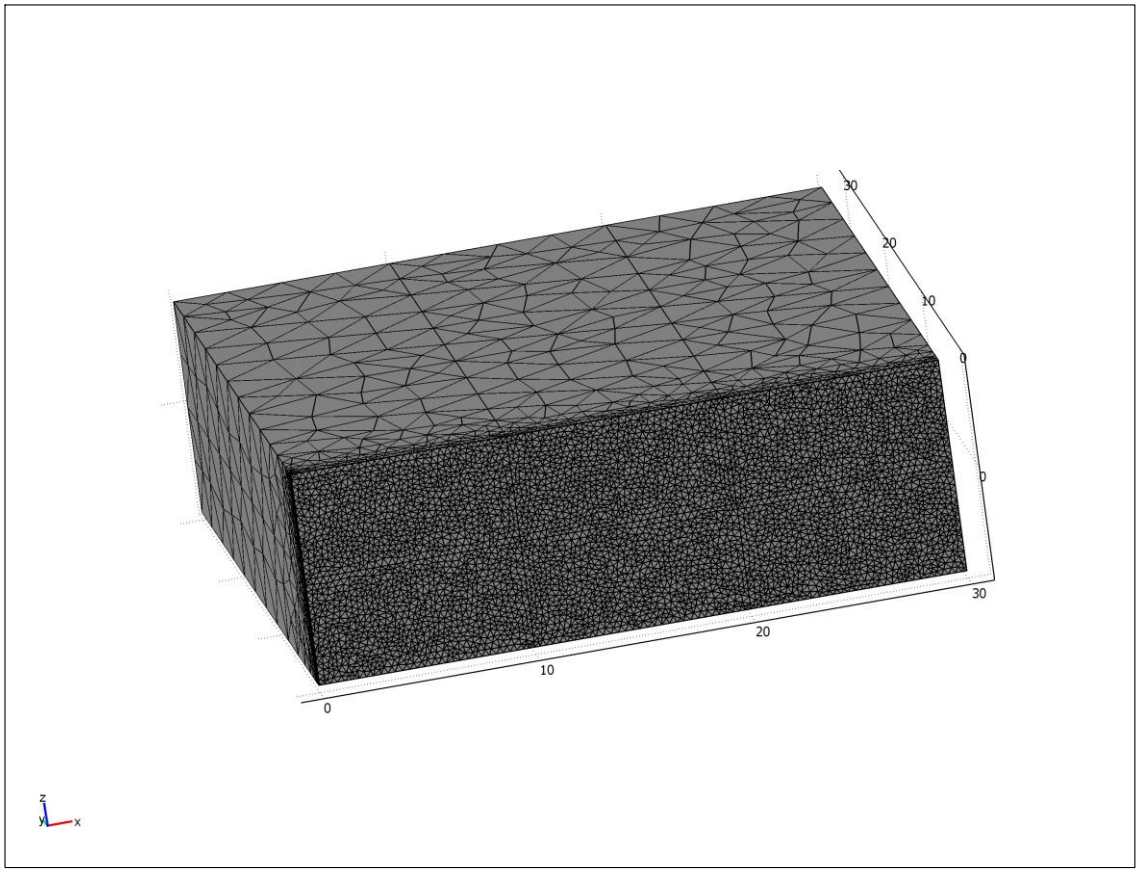

Figure 4.1 An example of 3-D Geometry used to study Multi-layer HFWs.

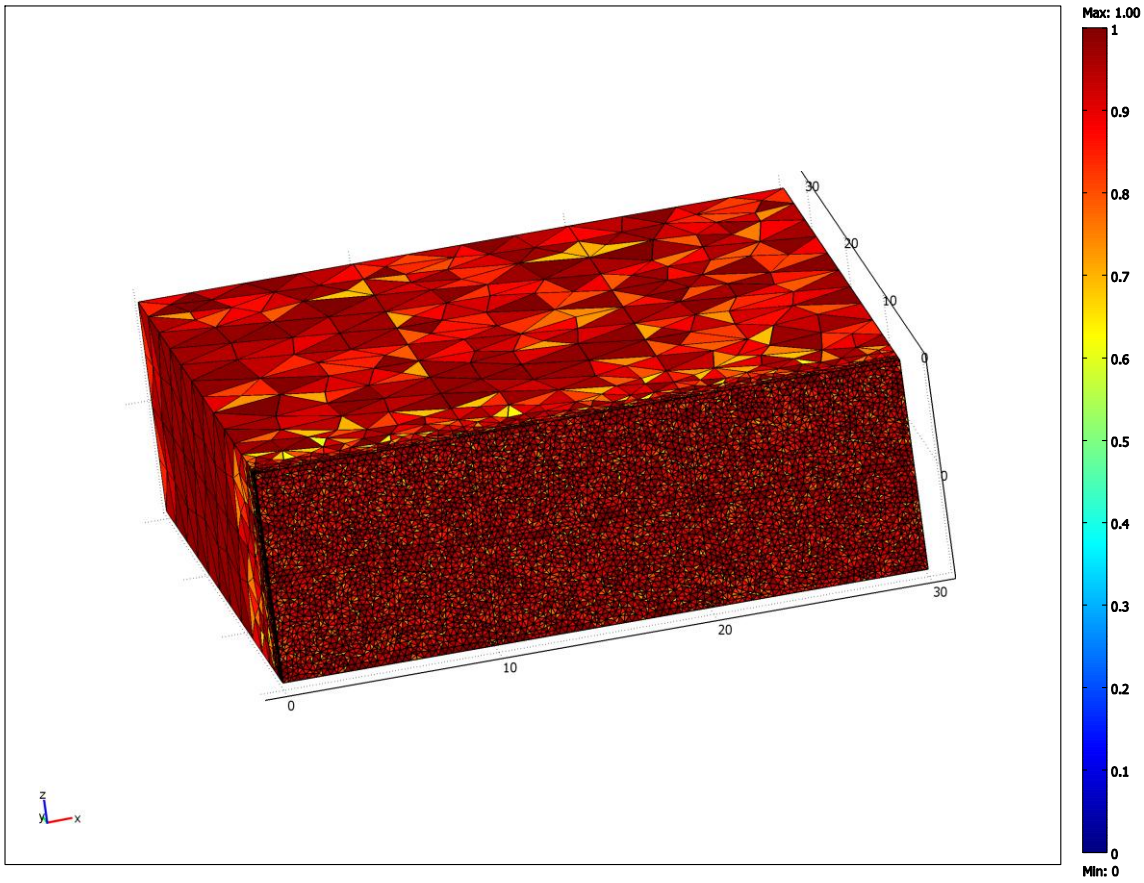

Figure 4.2 Mesh Quality of the Multi-layer 3-D geometry

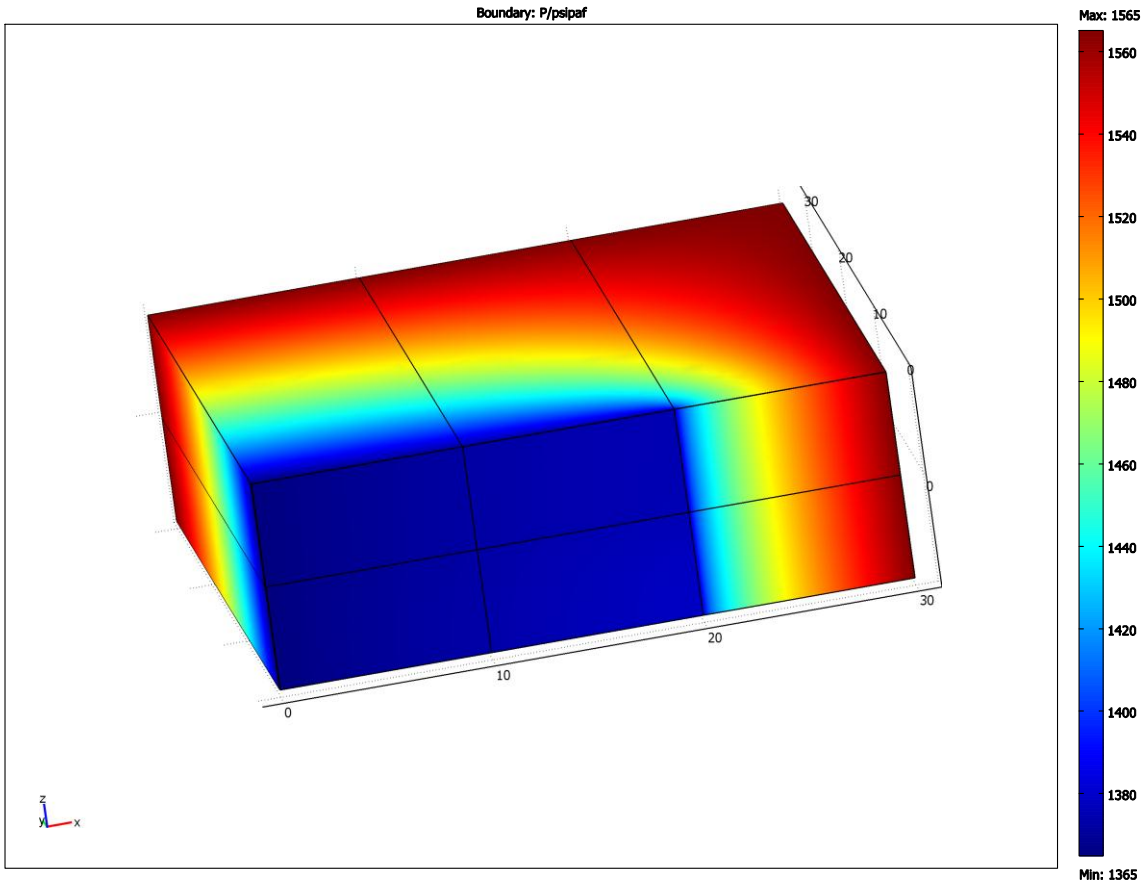

Figure 4.3 An example of pressure distribution around the 3-D HFW, (For Demonstration Purposes).

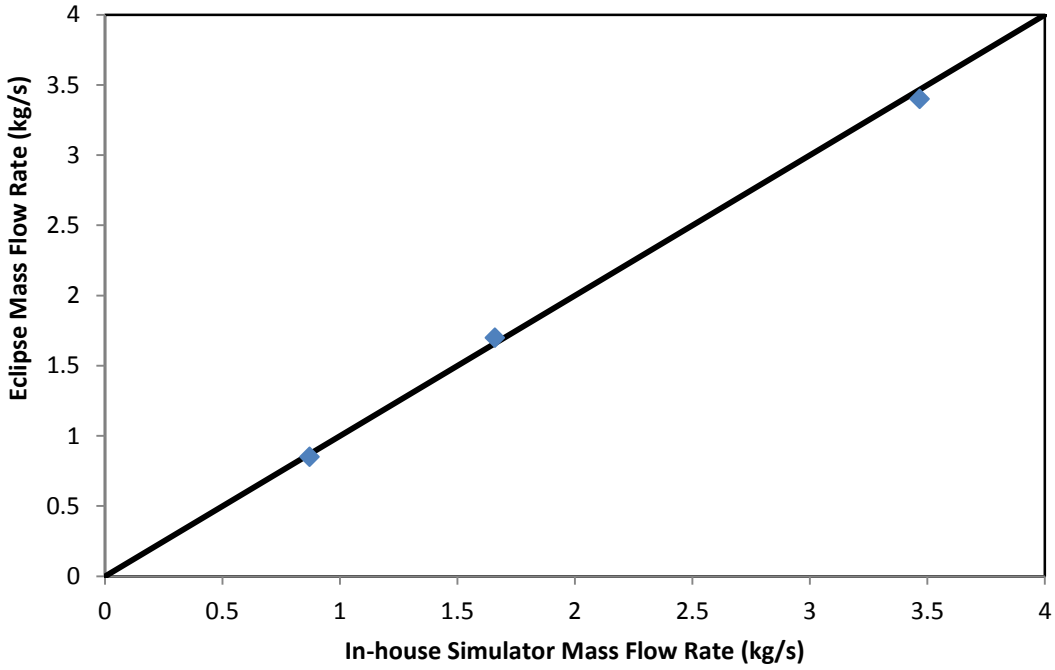

Figure 4.4 Comparison between the mass flow rates estimated using the in-house and that of ECLIPSE simulators under the same prevailing conditions, single phase Darcy flow SS conditions.

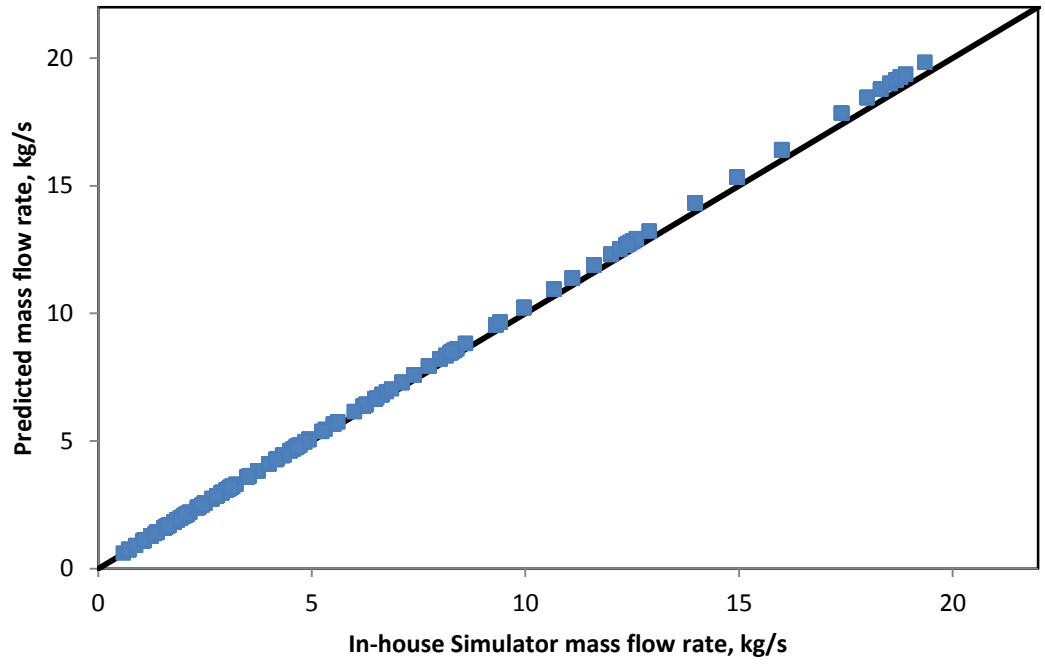

Figure 4.5 Calculated mass flow rates using EOH model with equivalent radius versus the corresponding values estimated by the HFW 3D in-house simulator, Single phase Darcy Flow.

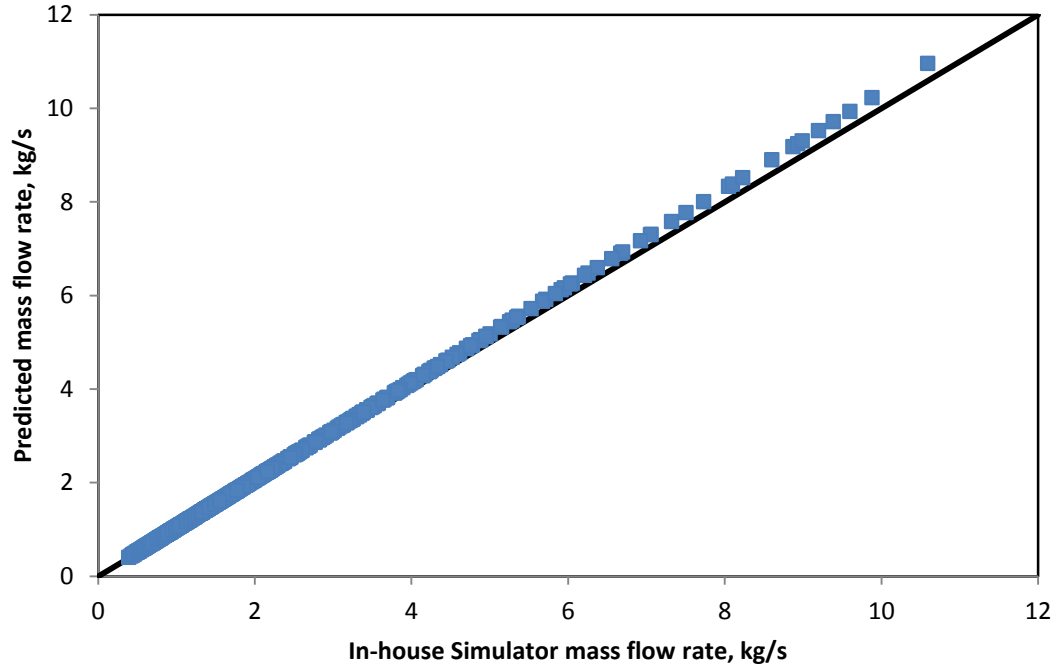

Figure 4.6 Calculated mass flow rates using EOH model with equivalent radius versus the corresponding values estimated by the HFW 3D in-house simulator, Single phase Darcy Flow.

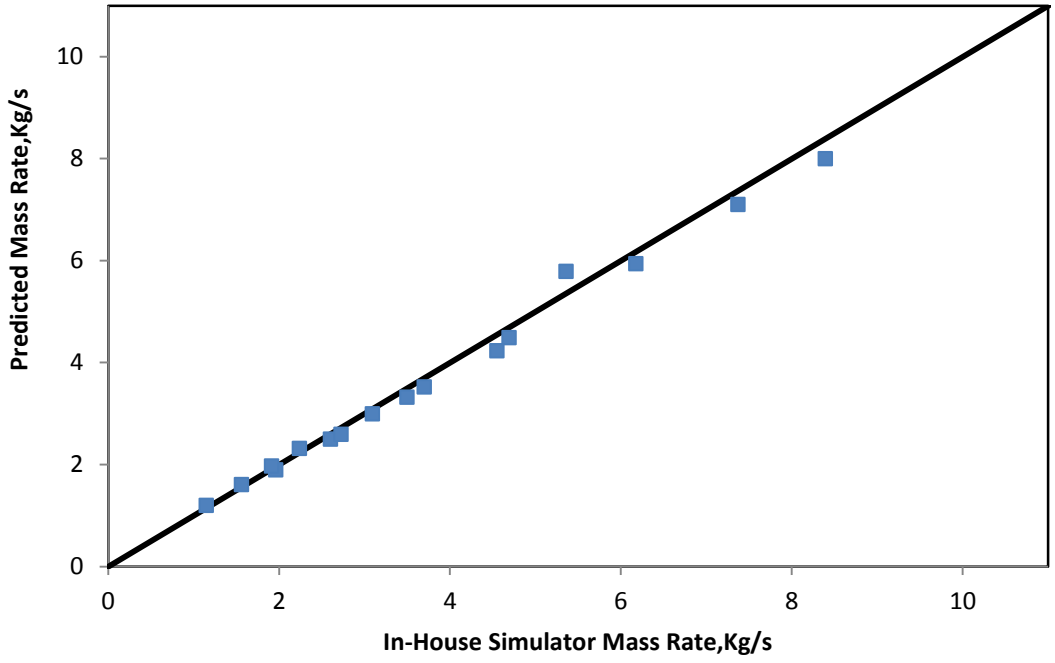

Figure 4.7 Calculated mass flow rates using EOH model with equivalent radius versus the corresponding values estimated by the HFW 3D in-house simulator, HFW-M1.

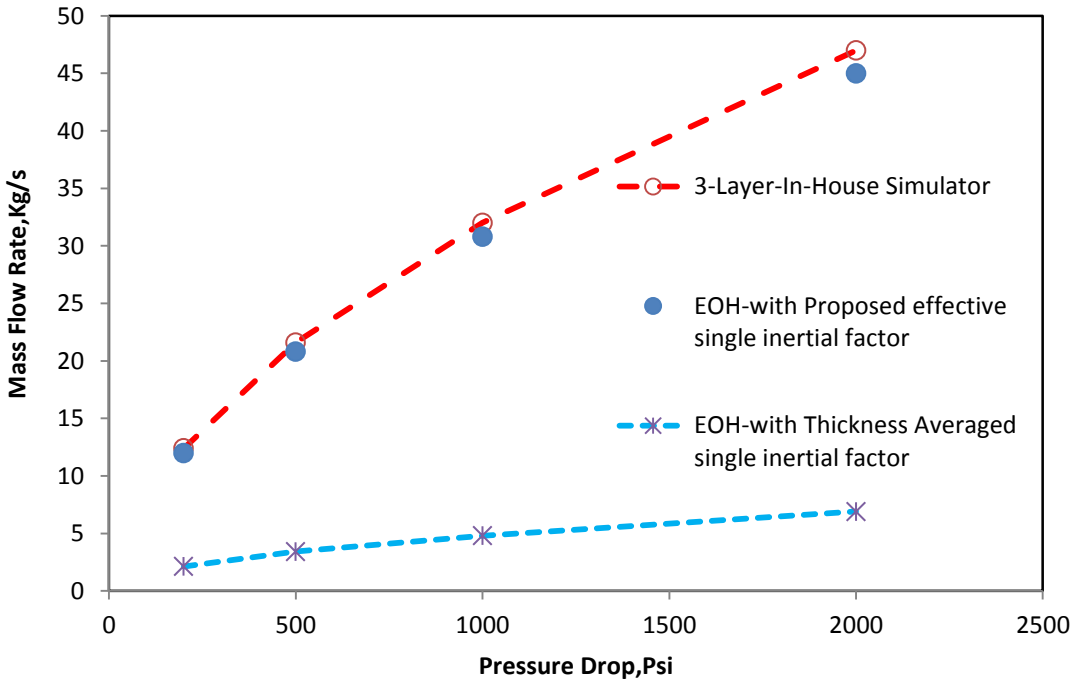

Figure 4.8 Calculated mass flow rates using EOH model with equivalent radius versus the corresponding values estimated by the VW 3D in-house simulator, VW-M1

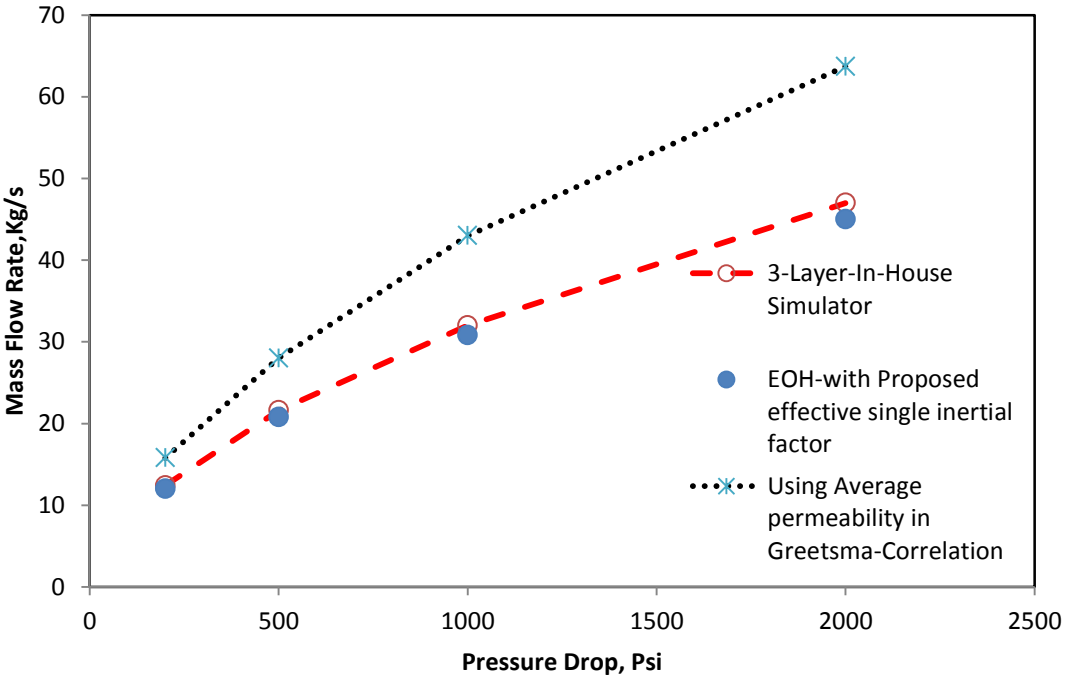

Figure 4.9 Calculated mass flow rates using EOH model with equivalent radius versus the corresponding values estimated by the VW 3D in-house simulator, VW-M1

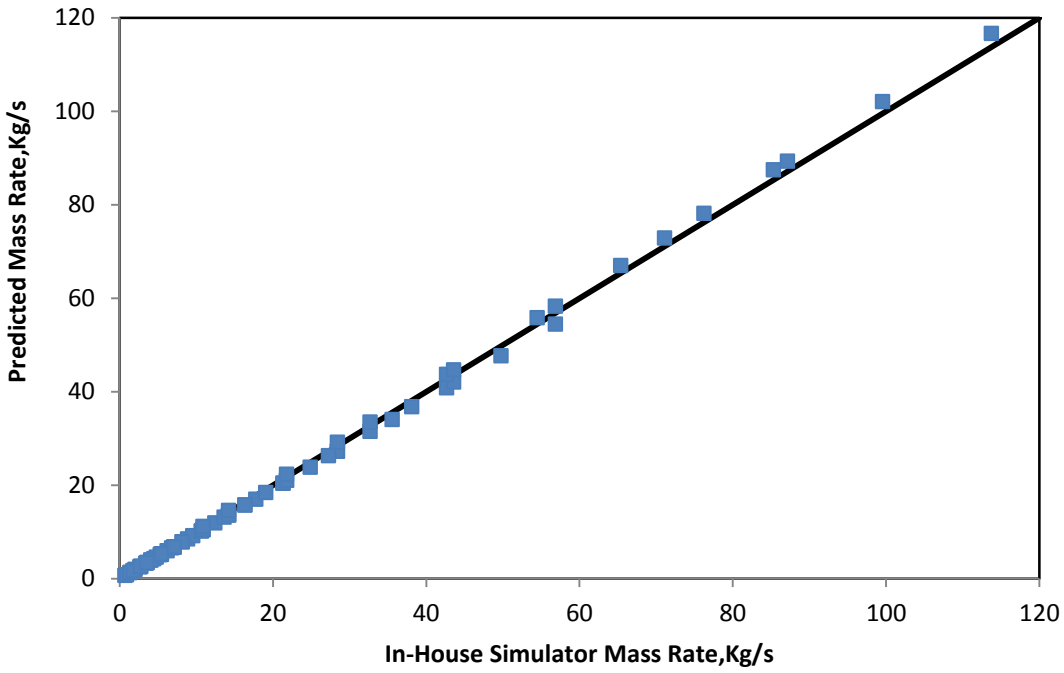

Figure 4.10 Calculated mass flow rates using EOH model with equivalent radius versus the corresponding values estimated by the VW 3D in-house simulator, VW-M2.

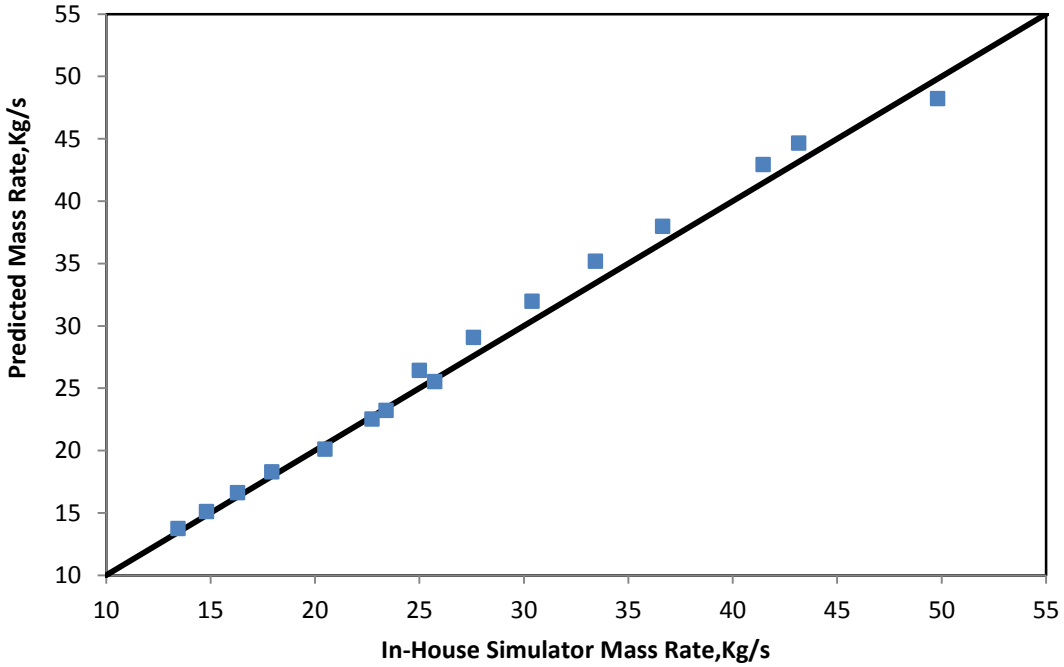

Figure 4.11 Calculated mass flow rates using EOH model with equivalent radius versus the corresponding values estimated by the HFW 3D in-house simulator, HFW-M2.

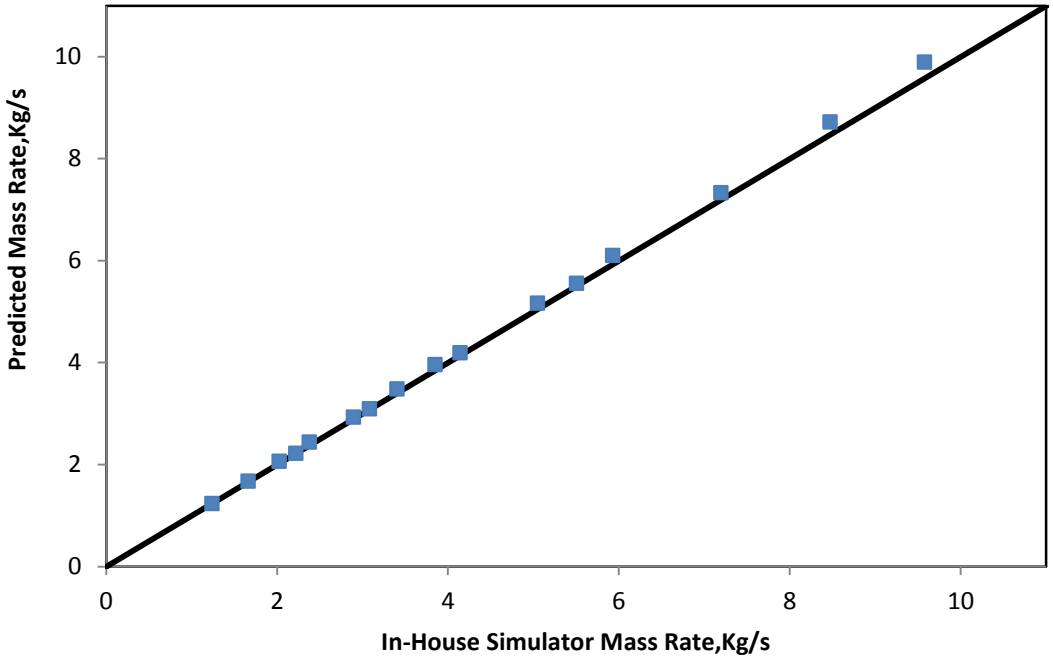

Figure 4.12 Calculated mass flow rates using EOH model with equivalent radius versus the corresponding values estimated by the HFW 3D in-house simulator, HFW-M3.

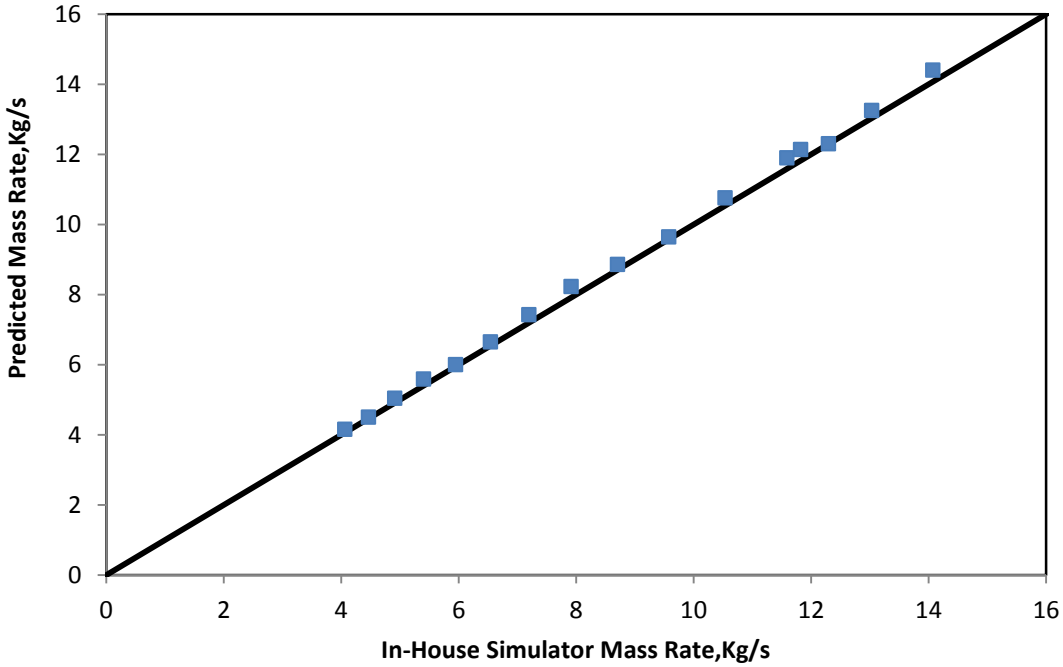

Figure 4.13 Calculated mass flow rates using EOH model with equivalent radius versus the corresponding values estimated by the HFW 3D in-house simulator, HFW-M4.

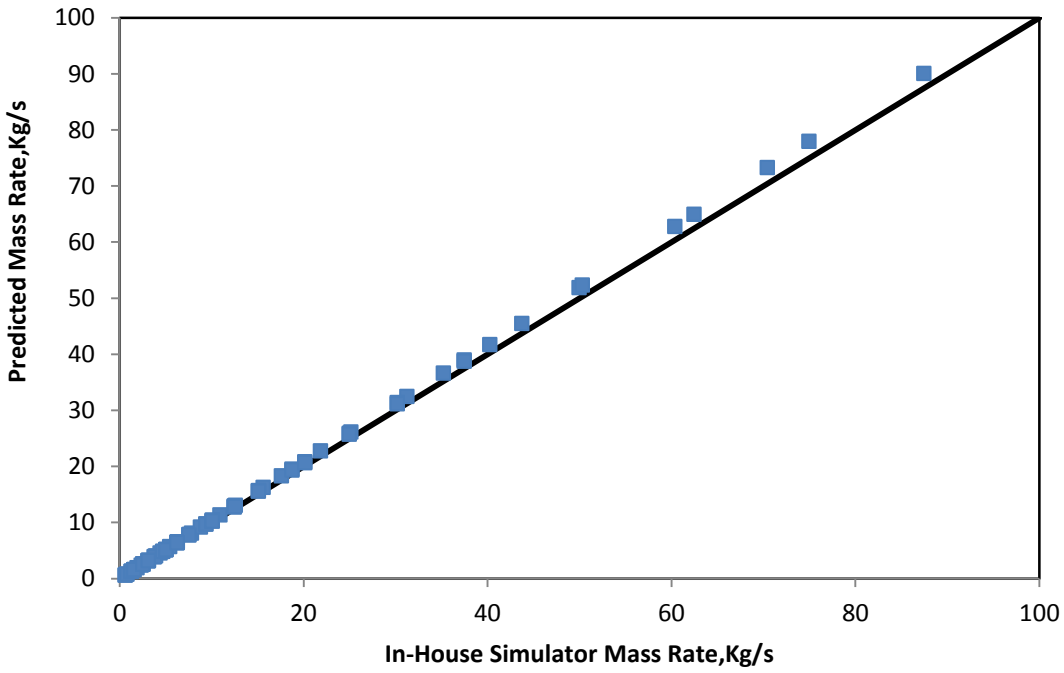

Figure 4.14 Calculated mass flow rates using EOH model with equivalent radius versus the corresponding values estimated by the HFW 3D in-house simulator, HFW-M5.

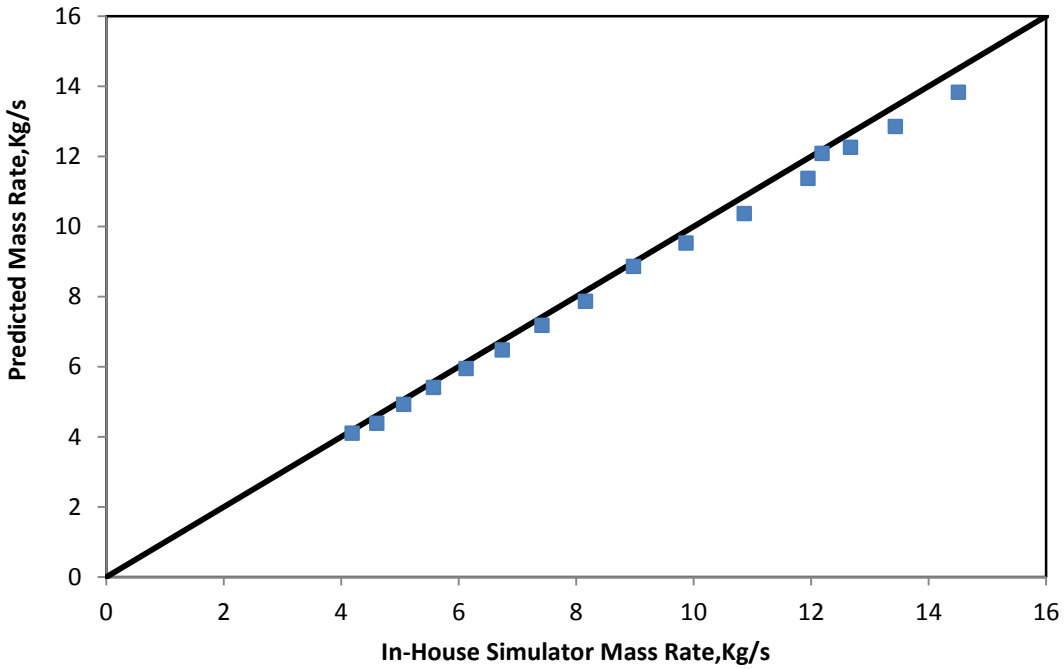

Figure 4.15 Calculated mass flow rates using EOH model with equivalent radius versus the corresponding values estimated by the HFW 3D in-house simulator, HFW-M6.

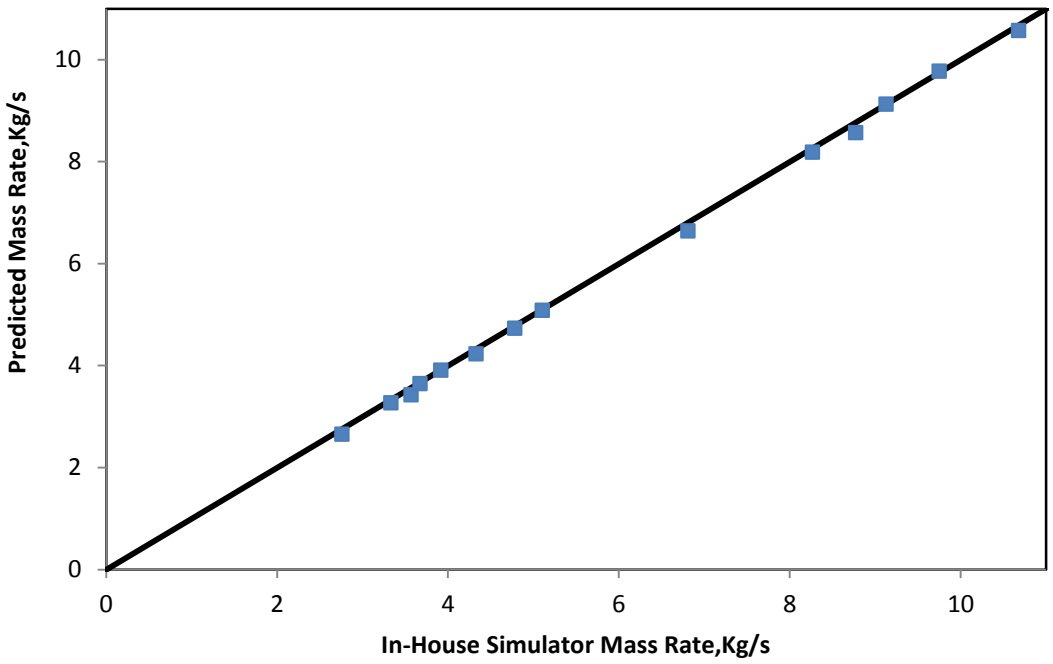

Figure 4.16 Calculated mass flow rates using EOH model with equivalent radius versus the corresponding values estimated by the HFW 3D in-house simulator, HFW-M7.

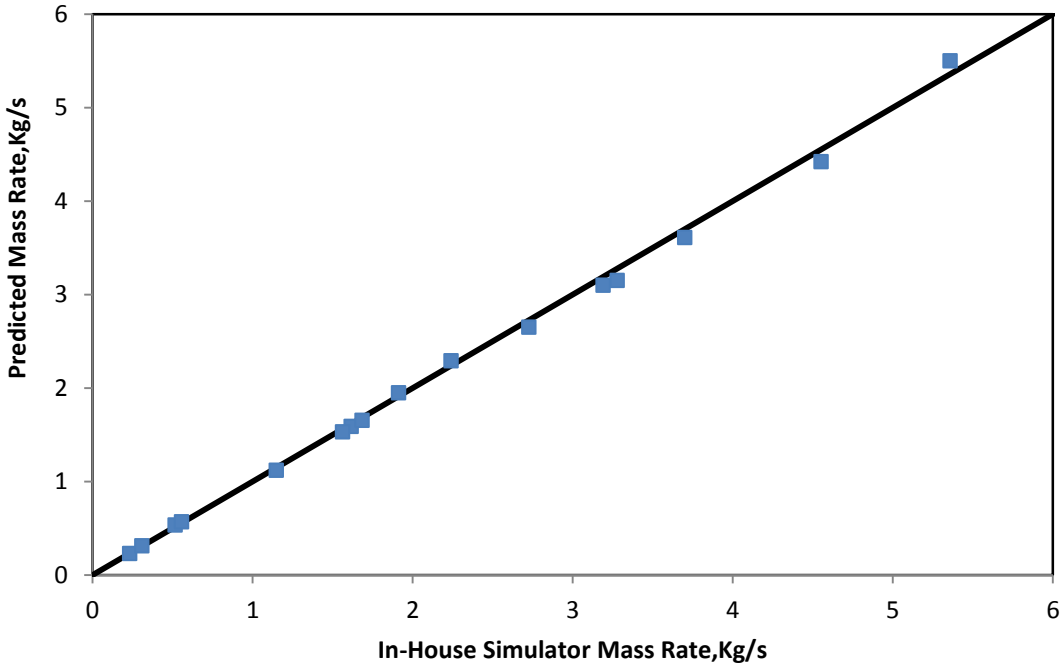

Figure 4.17 Calculated mass flow rates using EOH model with equivalent radius versus the corresponding values estimated by the HFW 3D in-house simulator, HFW-M8.

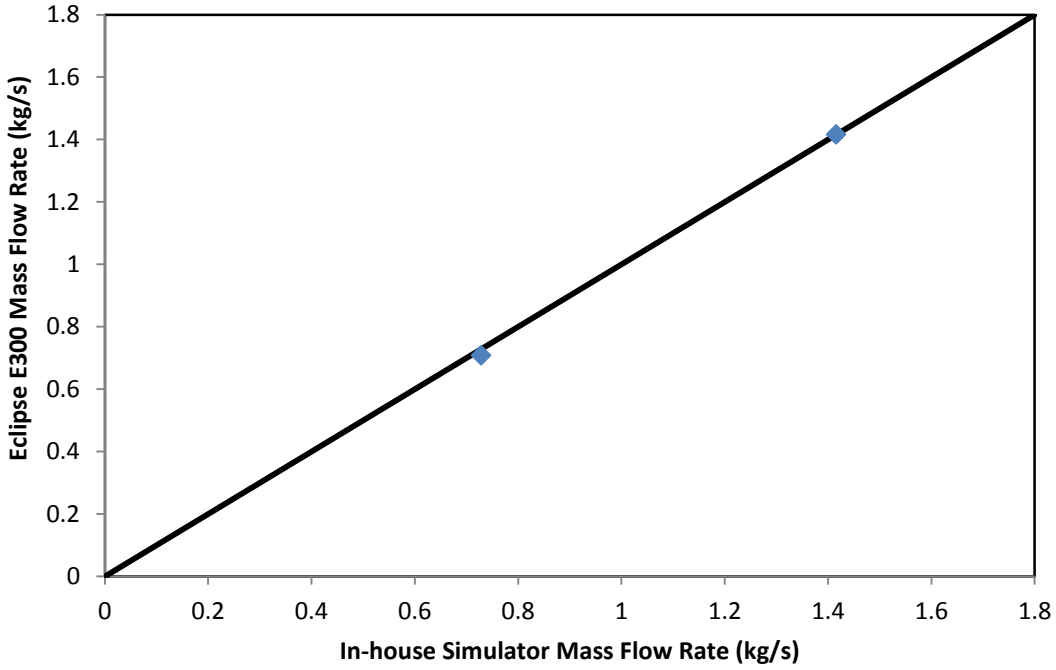

Figure 4.18 Calculated mass flow rates using Eclipse E300 versus the corresponding values estimated by the HFW 3D in-house simulator, Two phase-SS.

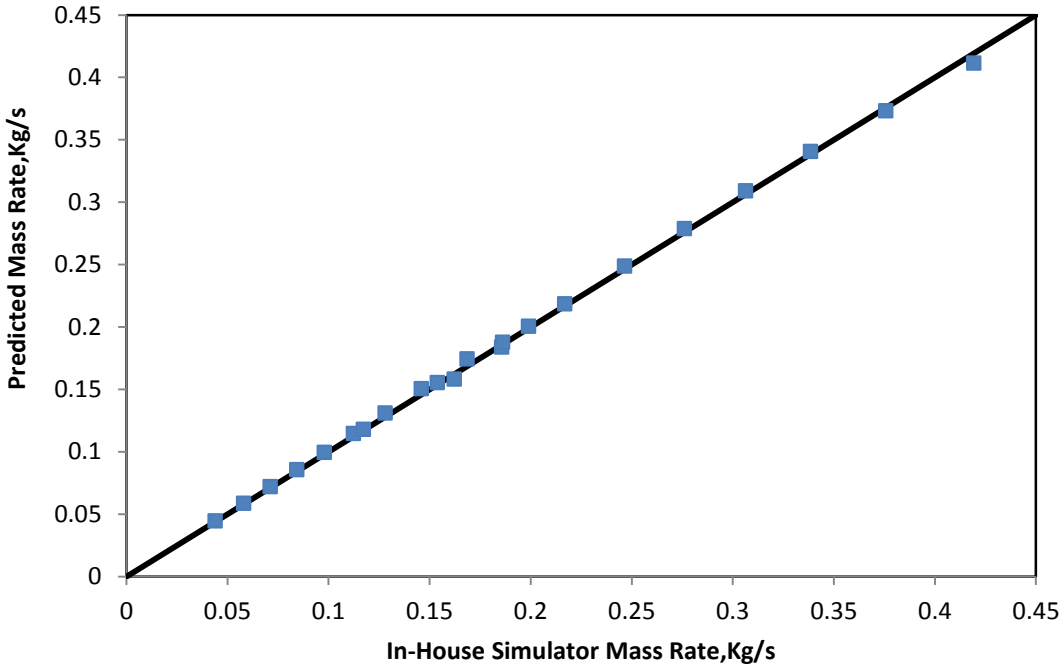

Figure 4.19 Calculated mass flow rates using EOH model with equivalent radius versus the corresponding values estimated by the VW 3D in-house simulator, VW-M9.

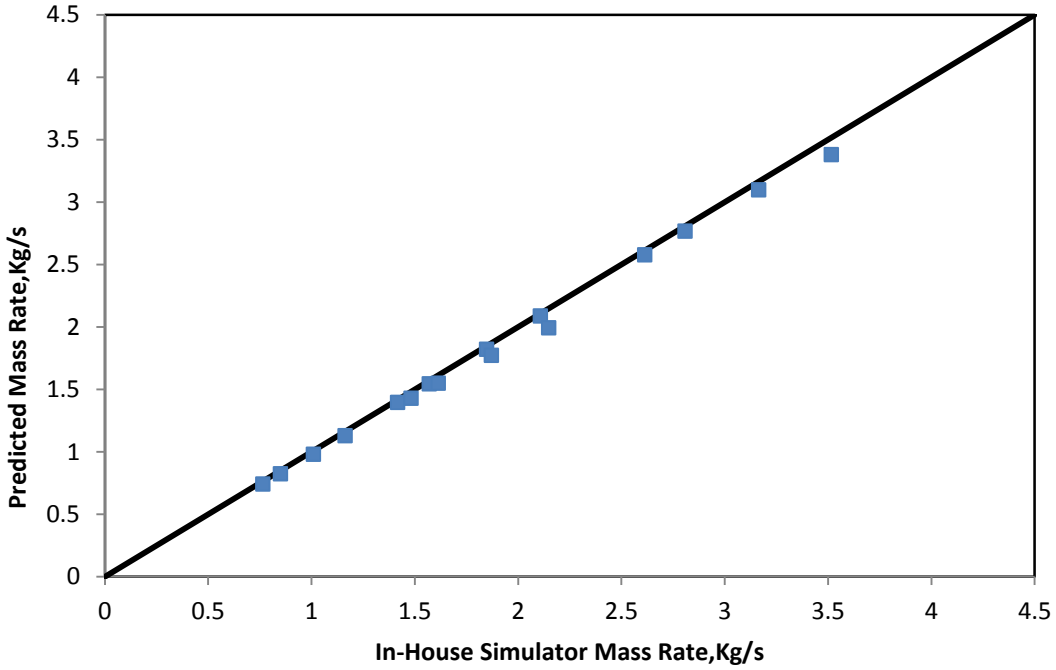

Figure 4.20 Calculated mass flow rates using EOH model with equivalent radius versus the corresponding values estimated by the VW 3D in-house simulator, VW-M10.

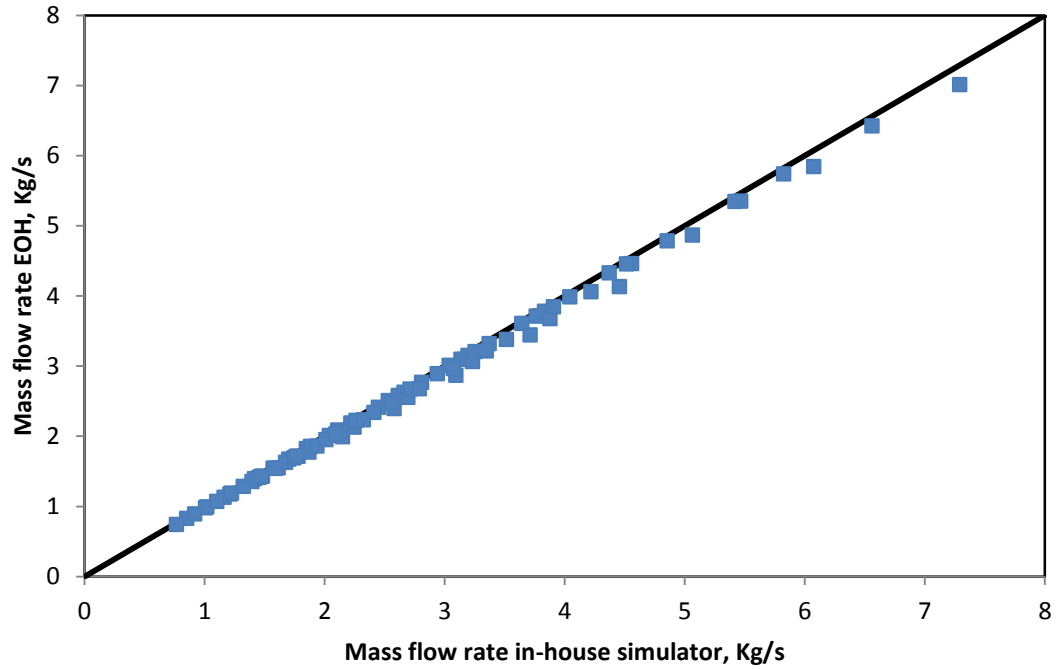

Figure 4.21 Calculated mass flow rates using EOH model with equivalent radius versus the corresponding values estimated by the HFW 3D in-house simulator, HFW-M11.

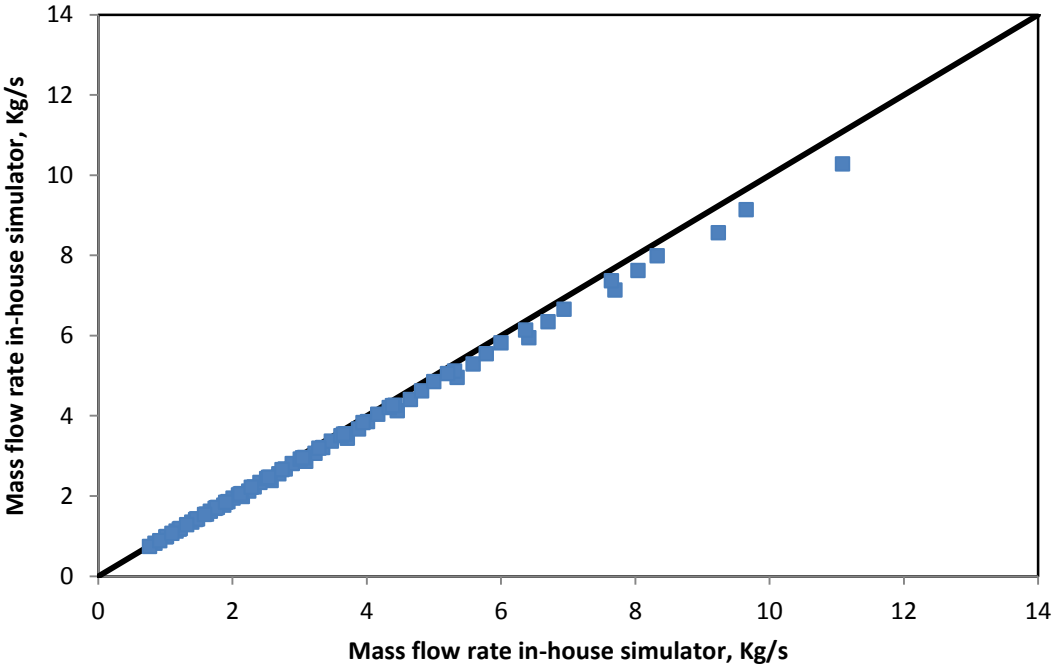

Figure 4.22 Calculated mass flow rates using EOH model with equivalent radius versus the corresponding values estimated by the HFW 3D in-house simulator, HFW-M12.

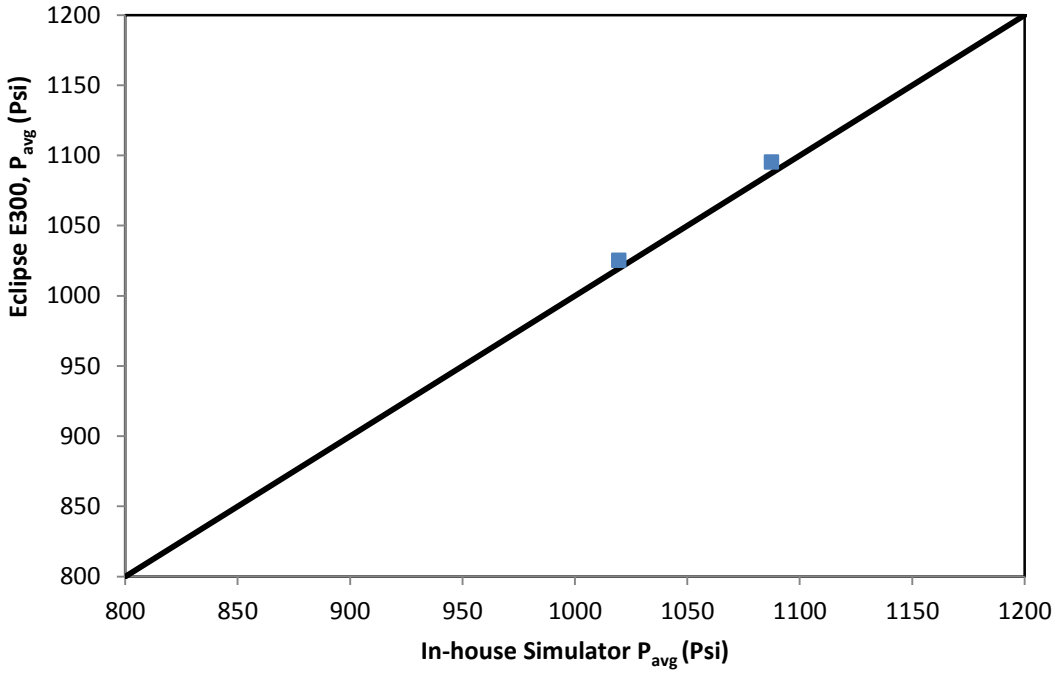

Figure 4.23 Comparison between calculated Average Reservoir Pressure (P_{avg}) using Eclipse (E300) simulators with those of the HFW 3D in-house simulator under the same prevailing conditions.

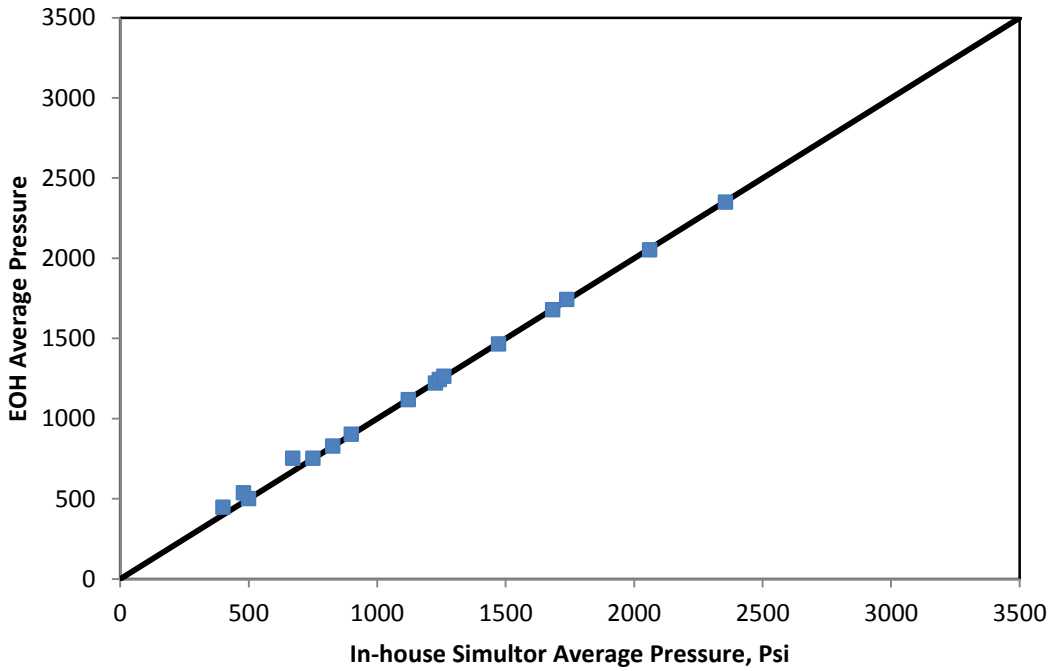

Figure 4.24 Calculated volumetric average reservoir pressure using EOH model with equivalent radius versus the corresponding values estimated by the HFW3D in-house simulator, HFW-M13.

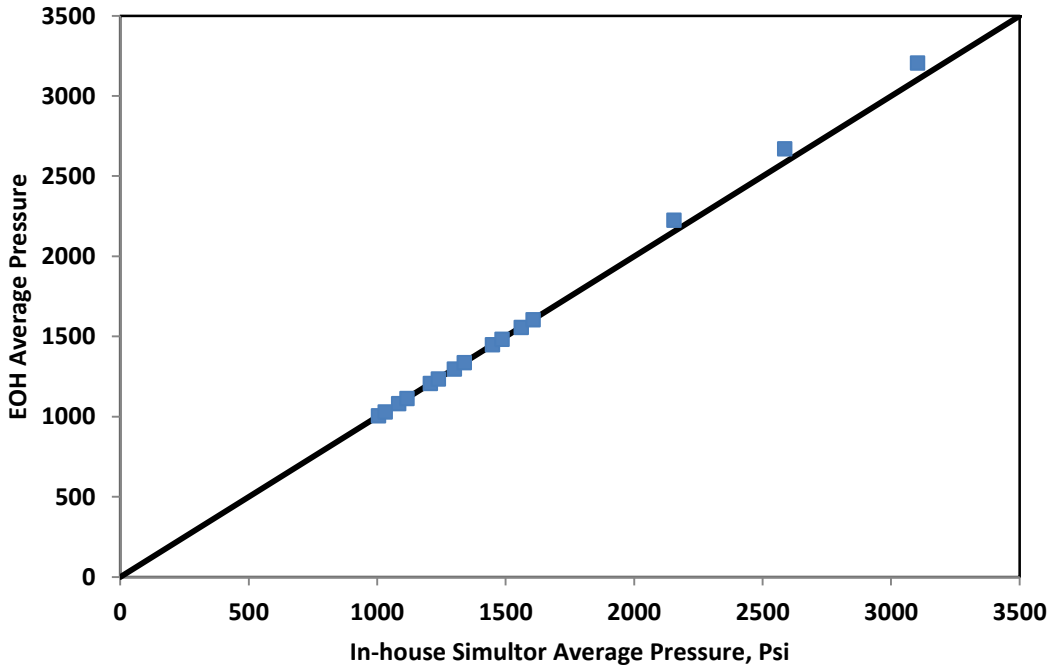

Figure 4.25 Calculated volumetric average reservoir pressure using EOH model with equivalent radius versus the corresponding values estimated by the HFW 3D in-house simulator, HFW-M14.

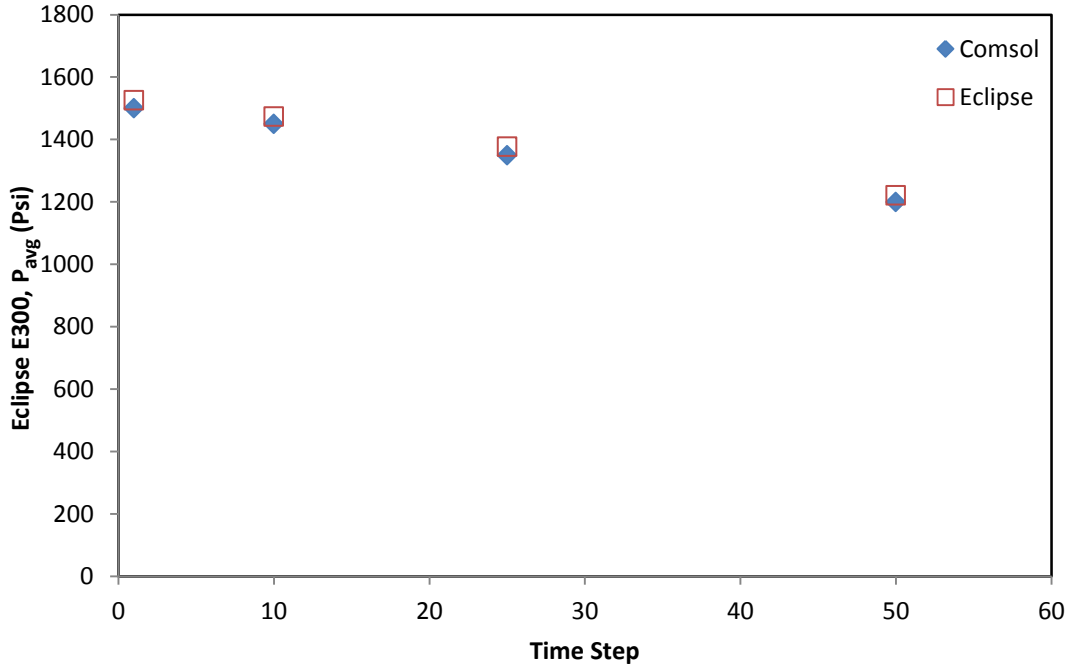

Figure 4.26 Comparison between calculated volumetric Average Reservoir Pressure (P_{avg}) using Eclipse (E300) simulator with those of the HFW 3D in-house simulator.

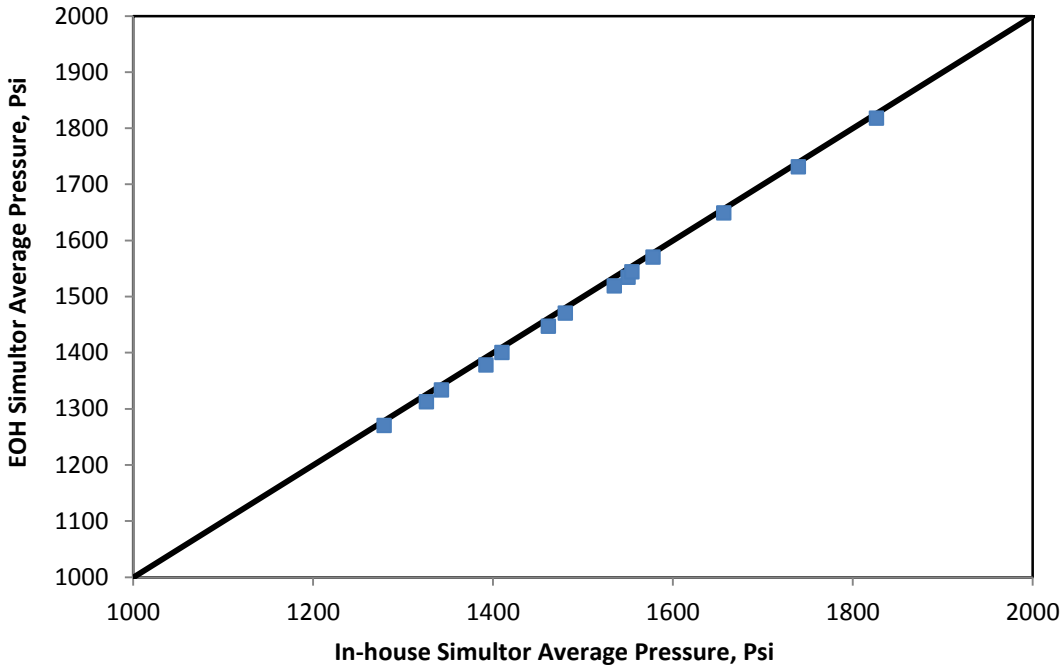

Figure 4.27 Calculated volumetric average reservoir pressure using EOH model with equivalent radius versus the corresponding values estimated by the HFW-in house simulator, HFW-M15 and 16.

CHAPTER 5
FRACTURE OPTIMIZATION IN GAS CONDENSATE RESERVOIRS

5.1 PROBLEM STATEMENT AND OBJECTIVES

Up to this part of the study, the author discussed the post fracture treatment performance in term of skin factor or equivalent wellbore radius. That is, the author has shown the impact of single phase non-Darcy flow, and two-phase gas and condensate flow on the hydraulic fracture performance. However, this research will not be complete the post fracture performance knowledge (presented earlier in this thesis) is not integrated with the fracture optimization and design phase.

Fracture optimization has gained an extensive research in the last decade, especially after the introduction of Unified Fracture Design (UFD) by (Valko and Economides 2002). UFD is a physical optimization method, which provides a tool to find optimum fracture penetration ratio and maximum achievable productivity index using a parameter called proppant number. The main advantage of proppant number that it is simple, general, and can be calculated using readily available information (i.e. reservoir and proppant volumes, as well as fracture and matrix permeabilities). In this method, for each proppant number there is a single optimum fracture penetration ratio, conductivity, and dimensionless productivity index.

However, the main pitfall of this method is that it only applies for single phase Darcy flow, under Pseudo-Steady conditions.

Accordingly, in this part of the study the author will introduce a new optimum fracture design formula for single phase gas (under both Darcy and non-Darcy conditions) and two-phase gas condensate reservoirs using the effective proppant number concept (that is correcting the absolute proppant number for the effect of coupling and inertia). The proposed effective proppant number formula is general, as it correctly converts to that suitable for single-phase Non-Darcy flow when total gas fractional flow (GTR) is unity and to Darcy flow when velocity is low. In this new formula the maximum productivity index and optimum penetration ratio can be calculated for a certain proppant number.

Furthermore, using the effective proppant number formula proposed here, the well-known UFD (Valko and Economides 2002) formula has been modified to account for Non-Darcy single phase and gas condensate flow conditions.

5.1.1 Single phase optimization previous studies

Prats introduced, for the first time, the concept of optimum fracture design, i.e. optimum length-to-width ratio, for a given fracture volume which maximizes productivity. He also showed that the optimum fracture conductivity of a HFW in a square reservoir is equal to 1.26 ($C_{FD\text{-}opt} = 1.26$), provided that the penetration ratio is small (i.e. less than 0.2). Following his approach, optimum fracture design has gained extensive research by many investigators in the last fifty years.

Valko *et al.* (1998) developed a numerical algorithm based on direct boundary element methods, to present the dimensionless productivity index of hydraulically fractured well as a function of penetration ratio and fracture conductivity for square and rectangular reservoirs with different aspect ratio. The presented results were a good tool to show the fold of increase in productivity as a result of using hydraulic fracturing. However, it was not as helpful in the optimization process.

Accordingly, Valko and Economides (2002) introduced a physical optimization approach called Unified Fracture Design (UFD). Using this approach, they presented the dimensionless productivity index of hydraulically fractured wells at Pseudo-Steady State (PSS) conditions as functions of Proppant Number. In this approach, it is also shown that for each Proppant number there is an optimum fracture geometry at which the productivity index is at its maximum achievable value.

Meyer and Jacot (2005) developed a new semi-analytical formula for the estimation of effective wellbore radius in HFWs under single-phase Darcy flow at PSS conditions. They also used their new effective wellbore radius formula to mathematically derive an expression for optimum fracture conductivity. In this expression, they correlate the optimum fracture conductivity to the drainage area aspect ratio. However, their expression is only applicable for HFWs with fracture penetration ratio less than 0.2.

The optimization of hydraulic fracture in a non-Darcy flow system has gained some interest in recent years.

For instance, Lopez-Hernandez *et al.* (2004) introduced the concept of using effective proppant number in the UFD formula in order to estimate the optimum fracture geometry under non-Darcy flow conditions. Here, the fracture permeability is corrected for the effect of inertia and then used in the absolute proppant number definition in order to find the effective proppant number, which then is used in the UFD formula to predict the optimum fracture geometry. In this this work, the author used Gidley's approximation (Equation 3.72 in Chapter 3 section 3.4, in this thesis) to estimate the effective or corrected fracture permeability. However, there was no explanation on why

to use such approximation nor there was an explanation on how to derive the formula of the effective proppant number. It was highlighted (in Chapter 3, section 3.4) of this thesis that Gidley's formula overestimate the inertial effect is in HFWs.

5.1.2 Gas Condensate optimization previous studies

Many literature studies have been devoted to the optimization of fracture design in Gas Condensate reservoirs. However, to the best of author's knowledge, most of available studies (e.g. Wang *et al.* 2000, Indriati *et al.* 2002, and Mohan *et al.* 2006), are based on a Non-physical assumption, since they consider the condensate bank region around the wellbore as a damage zone. This damage zone has a permeability of (kk_{rg}) and a thickness equal to the extent of the two-phase region around the wellbore.

Based on this assumption, these studies estimate the condensate bank damage using a damage skin formula (Cinco-Ley and Samaniego 1981) which has been developed for the fracture face damage in HFWs due to fracture fluid invasion into the matrix region. This would clearly lead to erroneous results as Cinco-Ley formula has been used out with its own limits. That is, the gas-condensate region around the wellbore is not a static or constant region, indeed, it is a function of pressure; and therefore it is impractical to use this method since pressure profile around the fracture is not a readily available piece of information. Needless to say, these studies have neglected the inertial effect inside the fracture which could also lead to erroneous results in term of optimum fracture geometry. Mahdiyar *et al.* (2009) have developed an expression to calculate the effective optimum fracture conductivity in gas condensate reservoir taking coupling and inertia effects into account. This expression was based on extending Guppy's correlation (Equation 3.70 in Chapter 3 section 3.4), developed for single phase flow, to two-phase gas condensate flow. Although this method account for the effect of coupling and inertia, however, it lacks a general parameter such as the proppant number which allow for different sensitivity analysis of optimum design. Also, it has been shown in Chapter 3 (section 3.4) that Guppy's correlation was developed for a limited range of absolute fracture conductivity and therefore using this method beyond its range could lead to misleading results.

To the best of author's knowledge there is not an appropriate methodology for predicting the effective proppant number in gas condensate reservoirs.

Here in this chapter the author shows that the formula for effective wellbore radius of HFWs, introduced in Chapter 3, provides a good tool for finding optimum fracture geometry (if linked with the idea of effective proppant number).

5.1.3 Proppant Number Concept

(Valko and Economides 1998) developed a numerical algorithm to calculate J_D. Using this algorithm they were able to plot the productivity index as a function of dimensionless fracture conductivity for both square and rectangular reservoirs. An example of such results is shown in Figure 5.1 where J_D is presented as a function of dimensionless fracture conductivity for different penetration ratio in a square reservoir. However, these type of figures, which are useful to show the fold of increase or "Productivity increase" of a fractured well (i.e. show the performance of HFW as a function of C_{FD} and I_x), are not useful to optimize the fracture geometry.

Based on this fact, (Valko and Economides 2002, Valko 2006) concluded that "the key to formulating a meaningful technical optimization problem is to realize that penetration and dimensionless fracture conductivity (through width) are competing for the same resource, the propped volume. Once the reservoir and proppant properties and the amount of proppant are fixed, one has to make the optimal compromise between width and length. The available propped volume puts a constraint on the two dimensionless numbers". To handle this constraint easily (Valko and Economides 2002) introduced the dimensionless proppant number:

$$N_P = I_x^2 C_{fD} = \frac{k_f}{k}\frac{w_f x_f}{x_e^2} = 2\frac{k_f}{k}\frac{V_f}{V_e} = cons \tag{5.1}$$

The Dimensionless Proppant Number, N_p, is the product of two ratios, the proppant volume to the reservoir volume ratio, and the fracture to formation permeability ratio, respectively. As described by (Valko and Economides 2002), the proppant number is the *most important* parameter in fracture design.

Figure 5.2a and 5.2b, presents the dimensionless productivity index as a function of dimensionless proppant number (N_P). The individual curves in both figures correspond to J_D at a fixed value of the proppant number, N_p, in these two Figures N_p ranges from 0.0001 to 0.1.

It can be clearly seen from Figure 5.2a and 5.2b that for each value of N_P, there is optimum fracture geometry (i.e. optimum dimensionless fracture conductivity and penetration ratio), which gives maximum dimensionless productivity index.

Also, it should be noted that Figure 5.2a and 5.2b should always give the same results. That is, we only need to use one of them (e.g. we can use figure 5.2a to find $C_{FD\text{-}opt}$, then from the proppant number (N_P) definition equation (5.1) we can calculate $I_{x\text{-}opt}$).

Figure 5.3, presents the dimensionless productivity index as a function of dimensionless proppant number for $N_P > 0.1$. Comparing this figure with Figure 5.2a, it can be concluded that for low proppant ($N_P < 0.1$) the optimal point occurs at C_{FD}=1.6. However, when the proppant number increases, the optimal point happens at larger dimensionless fracture conductivities because the penetration ratio cannot exceed unity. Furthermore, at large N_P numbers ($N_P > 10$) the optimum fracture penetration ratio will be equal to one and the optimum fracture conductivity will be equal to N_P value.

Accordingly, (Valko and Economides 2002) developed a general correlation to calculate optimum fracture conductivity ($C_{FD\text{-}opt}$) or penetration ratio ($I_{x\text{-}opt}$), and maximum achievable dimensionless productivity index ($J_{D\text{-}max}$) for a fixed proppant number.

For finding optimum fracture conductivity ($C_{FD\text{-}opt}$) for fixed proppant number (Economides *et al.* 2004):

$$C_{FD-opt}(N_P) = \begin{cases} 1.6 \Rightarrow N_P < 0.1 \\ 1.6 + \exp\left[\dfrac{-0.583 + 1.48\ln(N_P)}{1 + 0.142\ln(N_P)}\right] \Rightarrow 0.1 \le N_P \le 10 \\ N_P \Rightarrow N_P > 10 \end{cases} \quad (5.2a)$$

For finding maximum achievable dimensionless productivity index ($\mathbf{J_{D\text{-}max}}$) for fixed proppant number (Economides *et al.* 2004):

$$J_{D-\max}(N_P) = \begin{cases} \dfrac{1}{0.99 + 0.5\ln(N_P)} \Rightarrow N_P \le 0.1 \\ \dfrac{6}{\pi} - \exp\left[\dfrac{0.423 - 0.311N_P - 0.089N_P^2}{1 + 0.667N_P + 0.015N_P^2}\right] \Rightarrow N_P > 0.1 \end{cases} \quad (5.2b)$$

As mentioned earlier, these two formulations are valid only for single-phase flow under Pseudo-Steady state conditions.

Practical ranges of proppant number:

It is very important to have a sense of the practical range of proppant number as it is the most important factor in fracture optimization process. Even though, in academic research we tend to cover the whole theoretical range of any variable in order to properly present the concepts and generalize the conclusions. The next few paragraphs will give details of some practical aspect related to the proppant number concept.

Valko (2006) claimed that in "medium and high permeability formations, that is above 50 md, it is practically impossible to achieve a proppant number larger than 0.1. For example, the Frac-and Pack typical proppant numbers range between 0.0001 and 0.01". Therefore, using (Equation 5.2a) it can be stated that for medium and high permeability formations (k_{matrix} = 50mD), the optimum dimensionless fracture conductivity is always 1.6 ($C_{FD\text{-}opt}$=1.6).

Also, he mentioned that "in tight gas it is possible to achieve large dimensionless proppant numbers, at least in principle. If one calculates the proppant number with a limited drainage area and does not question whether the proppant really reached the pay layer, dimensionless proppant number of 1 can be achieved" (Valko 2006).

Nonetheless, Valko (2006) stated that "proppant numbers larger than one are impossible to realize. The reason is that for large treatments there is a great uncertainty of where the proppant goes both in horizontal and vertical directions".

Finally, he concluded his discussion about proppant number with the following important statement "dimensionless proppant number larger than 0.5 is rarely realized because the proppant cannot be contained in the pay and within the drainage area" (Valko 2006).

Therefore, using (Valko and Economides 2002) UFD method (i.e. Equation 5.2b), it can be stated that the maximum achievable dimensionless Productivity Index ($J_{D\text{-}max}$) for N_P = 0.5 is 0.71($J_{D\text{-}max}$ = 0.71 at N_P =0.5). Considering that the dimensionless productivity index for an undamaged (Zero skin) un-fractured vertical well is roughly in the range of (0.10 to 0.14), assuming that the typical ranges of wellbore and drainage radii are as follow, (1000 < r_e > 5000-ft and 2.75 < r_w > 8-inches).

Therefore, the maximum practical "productivity ratio" or "fold of increase" (i.e. $J_{D\text{-}\mathbf{Fractured\ well}}$ to $J_{D\text{-}\mathbf{Vertical\ well}}$) will be in the range of (5 to 7). That is, literature studies which reports high values of "productivity ratio" based on using large proppant number should be considered as theoretical rather than realistic and practical reports. However, higher productivity ratio should be expected if the vertical well was already damaged prior to fracture treatment (i.e. it has a positive pre-treatment skin). For instance, if a well has a damage skin of two (S = 2), then the aforementioned "productivity ratio" range will increase from (5 to 7) to reach a range of (6.5 to 8.5).

One final question that always in every engineer's mind is why do we need to do the optimization design based on Pseudo-Steady State conditions, while sometimes in tight reservoir transient period can be as long as several months, if not, years.

(Valko and Economides 2002, and Valko 2006) commented that "In transient regime the Productivity Index (and hence the production rate) is larger than in pseudo-steady state. With this qualitative picture in mind it is easy to discard the pseudo-steady state optimization procedure and to shoot for very high dimensionless fracture conductivity and/or to anticipate much more folds of increase in the transient period. In reality, the existence of the transient period does not change the previous conclusions on optimal dimensions and should not induce too high anticipations. Our calculations show, that there is no reason to depart from the optimum compromise, even if the well will produce in transient regime for a considerable time (several months or even years)".

5.2 Single Phase Darcy Flow Optimization

In this section the author will mathematically derive an expression for optimum fracture design, this expression will benefit from the effective wellbore radius formulation which has been presented and verified in Chapter 3.

Optimum fracture design can be defined as the geometry of a given proppant number that provides the maximum achievable dimensionless productivity index ($\mathbf{J}_{Dmax}$). Also, for this ($\mathbf{J}_{Dmax}$) there should be single optimum penetration ratio and fracture conductivity.

For hydraulically fractured wells a general dimensionless productivity index is defined as:

$$J_D = \frac{1}{\ln\left(\frac{r_e}{x_f}\right) + S_f^{'} + S + \frac{r_{wD}^2}{2} + \frac{r_{wD}^4}{4} - c} = \frac{1}{\ln\left(\frac{r_e}{r_w^{'}}\right) + S + \frac{r_{wD}^2}{2} + \frac{r_{wD}^4}{4} - c} \tag{5.3}$$

Where $r_w^{'}$ the effective wellbore radius and r_{wD} is is the dimensionless effective wellbore radius.

$$r_{wD} = \frac{r_w^{'}}{r_e} \tag{5.3a}$$

For most practical cases $r_w^{'}$ is much smaller than r_e so the third and fourth terms in the denominator of Equation 5.3 are neglected and it is simplified as follows:

$$J_D = \frac{1}{\ln\left(\frac{r_e}{r_w^{'}}\right) + S - c} \tag{5.4}$$

Here S would represent the summation of damage and shape skin factor. Shape skin factor, which depends on the shape of the drainage area and the well location, is zero for

cylindrical or square drainage area. Damage skin is considered as zero in this study. *c* is a constant which is ½ for steady-state systems and ¾ for pseudo-steady systems.

Accordingly, it can be stated that the maximum productivity index ($\mathbf{J}_{Dmax}$) is achieved when the variation of dimensionless productivity index with respect to penetration ratio reaches its maximum possible value. Mathematically, this can be represented as follow:

$$\left.\frac{\partial J_D}{\partial I_x}\right|_{N_P} = 0 \tag{5.5}$$

Where, N_P is the proppant number.

According to this equation, we are looking for an optimum fracture design, which, for a certain proppant number, provides the maximum possible dimensionless productivity index ($\mathbf{J}_{Dmax}$).

However, since J_D is a function of effective wellbore radius $r_w^{'}$, then it is mathematically more convenient to solve equation 5.5 based on $r_w^{'}$. Thus, it can be stated that the maximum dimensionless productivity index is achieved when effective wellbore radius reaches its maximum possible value with respect to the fracture length. That is, for the optimization of fracture design, the following equation should be solved:

$$\left.\frac{\partial r_w^{'}}{\partial x_f}\right|_{N_P} = 0 \tag{5.6}$$

It should be noted that, a similar approach (i.e. solving Equations 5.5 or 5.6 to find the optimum fracture geometry) has been followed in the letrature, (e.g. Meyer and Jacot 2005 for single phase gas Darcy flow) and (Mahdiyar *et al.* 2009 for gas condensate flow which has been conducted in GCR-HW group; Gas Condensate Recovery Final Report 2008-2011). However, the gas and gas condensate effective wellbore radius formulae used in the aforementioned studies are different from the ones developed and used in this current work. Furthermore, both studies (i.e. Meyer and Jacot 2005 and Mahdiyar *et al.* 2009) have their own limitations which have been highlighted in sections (5.1.1 and 5.1.2) of this chapter.

In chapter 3 (section 3.3), the author has developed the following formula for effective wellbore radius under single phase Darcy flow conditions:

$$r_w^{'} = x_f \cdot e^{-S_{gf}} = \frac{x_f}{\varepsilon + \frac{\pi}{C_{FD}}} \tag{5.7}$$

Where, ε is

For SS conditions:
$$\varepsilon_{SS} = 2 - \left(\frac{0.112 I_x}{1 - 0.796 I_x} \right) \tag{5.8}$$

For PSS conditions:
$$\varepsilon_{PSS} = 2 + \left(\frac{0.355 I_x}{1 - 0.704 I_x} \right) \tag{5.9}$$

Combining equation (5.7) with the proppant number equation (5.1) will give the following definition of effective wellbore radius:

$$r_w' = \frac{X_e \cdot I_x}{\varepsilon + \frac{\pi \cdot I_x^2}{N_p}} \tag{5.10}$$

Then equation (5.10) is used to solve equation (5.6) as follow:

$$\frac{\partial}{\partial x_f} \left(\frac{X_e \cdot I_x}{\varepsilon + \frac{\pi \cdot I_x^2}{N_p}} \right)_{N_P} = 0 \tag{5.11}$$

Multiplying the nominator and dominator of equation (5.11) by ($1/X_e$),

$$\frac{\partial}{\partial I_x} \left(\frac{I_x}{\varepsilon + \frac{\pi \cdot I_x^2}{N_p}} \right)_{N_P} = 0 \tag{5.12}$$

Applying the quotient derivative rule to equation (5.12) gives:

$$\frac{\varepsilon + \frac{\pi \cdot I_x^2}{N_p} - I_x \left(\frac{d\varepsilon}{dI_x} + \frac{\pi}{N_p} (2 I_x) \right)}{\left(\varepsilon + \frac{\pi \cdot I_x^2}{N_p} \right)^2} = 0 \tag{5.13}$$

Consider **C** as ($\frac{\pi}{N_p}$) then equation (5.13) will be,

$$\varepsilon + C \cdot I_x^2 - I_x \left(\frac{d\varepsilon}{dI_x} + C \cdot (2 I_x) \right) = 0 \tag{5.14a}$$

Or

$$\varepsilon + C \cdot I_x^2 - I_x \frac{d\varepsilon}{dI_x} - 2C \cdot I_x^2 = 0 \tag{5.14b}$$

after some arrangements,

$$\left(\varepsilon - I_x \frac{d\varepsilon}{dI_x}\right) - C \cdot I_x^2 = 0 \tag{5.14c}$$

Let's call $\left(\varepsilon - I_x \frac{d\varepsilon}{dI_x}\right)$ as $f(\varepsilon)$ then,

$$f(\varepsilon) - \frac{\pi}{N_p} \cdot I_x^2 = 0 \tag{5.15}$$

Rearranging equation (5.15) gives::

$$I_{x-opt} = \sqrt{\frac{N_p \cdot f(\varepsilon)}{\pi}} \tag{5.15a}$$

This simple equation can be used to calculate the optimum penetration ratio (**$I_{x\text{-}opt}$**) for any certain proppant number. The optimum penetration (**$I_{x\text{-}opt}$**) value will be the one, which satisfies equation (5.15) or (5.15a). Furthermore, the expression $f(\varepsilon)$ is a pure function of penetration ratio and can be easily calculated using equation (5.8) or (5.9) depending on the assumed boundary conditions. Indeed, equation (5.15) or (5.15a) can be solved using excel spreadsheet application as we will show in the next few paragraphs but first more details about the $f(\varepsilon)$ expression will be given.

$f(\varepsilon)$ Under Steady-State Conditions:

Figure 5.5 shows the variation of $f(\varepsilon_{SS})$ with respect to (ε_{SS}), where the subscript (SS) refers to steady-state conditions. It has been shown in Chapter 3 that (ε_{SS}) decreases as penetration ratio (Ix) increases and that it ranges from a value of 2 at minimum penetration ratio (Ix ≈ zero) to a value of 1.45 at maximum penetration value (Ix = 1). From Figure 5.5, it can be noticed that $f(\varepsilon_{SS})$ increases as (ε_{SS}) decrease or in other words it increases as penetration ratio increase. That is, $f(\varepsilon_{SS})$ ranges from a value of 2 at maximum value of (ε_{SS}) to a value of 4 at the minimum value of (ε_{SS}).

Based on Figure 5.5, $f(\varepsilon_{SS})$ can be represented using the following second order polynomial function with an R-squared value of 1.0:

$$f(\varepsilon_{SS}) = 7.5947\varepsilon_{SS}^2 - 30.406\varepsilon_{SS} + 32.432 \tag{5.16}$$

Combining equation (5.8) with equation (5.16) will give $f(\varepsilon_{SS})$ as a function of I_x,

$$f(\varepsilon_{SS}) = 7.5947\left(2 - \left(\frac{0.112I_x}{1 - 0.796I_x}\right)\right)^2 - 30.406\left(2 - \left(\frac{0.112I_x}{1 - 0.796I_x}\right)\right) + 32.432 \tag{5.17}$$

$f(\varepsilon)$ Under Pseudo-Steady State Conditions:

Figure 5.6 shows the variation of $f(\varepsilon_{PSS})$ with respect to (ε_{PSS}), where the subscript (PSS) refers to Pseudo-Steady state conditions. It has been shown in Chapter 3 that (ε_{PSS}) increases as penetration ratio (I_x) increases and that it ranges from a value of 2 at minimum penetration ratio (Ix ≈ zero) to a value of 3.15 at maximum penetration value (I_x = 1). From Figure 5.6, It can be noticed that $f(\varepsilon_{PSS})$ decreases as (ε_{PSS}) increase or in other words it decreases as penetration ratio increase.

Based on Figure 5.6, $f(\varepsilon_{PSS})$ can be represented using the following second order polynomial function with an R-squared value of 0.98:

$$f(\varepsilon_{PSS}) = -2.02\varepsilon_{PSS}^2 + 8.07\varepsilon_{PSS} - 6.07 \tag{5.18}$$

Combining equation (5.9) with equation (5.18) will give $f(\varepsilon_{PSS})$ as a function of I_x,

$$f(\varepsilon_{PSS}) = -2.02\left(2+\left(\frac{0.355I_x}{1-0.704I_x}\right)\right)^2 + 8.07\left(2+\left(\frac{0.355I_x}{1-0.704I_x}\right)\right) - 6.07 \tag{5.20}$$

Up to this point, a mathematical formula for ($I_{x\text{-}opt}$) estimation was derived for both SS and PSS conditions. In the same manner, a derivation of the appropriate formula to estimate ($J_{D\text{-}max}$) under both SS and PSS conditions will be presented next.

5.2.1 Dimensionless Productivity Index as a Function of Proppant Number

In this section the author will present a formula for estimating the maximum achievable productivity index for a certain proppant number. This formula gives both ($J_{D\text{-}max}$) and ($I_{x\text{-}opt}$) at the same time.

First let's recall the effective wellbore radius formulation equation (5.7):

$$r_w' = \frac{x_f}{\varepsilon + \frac{\pi}{C_{FD}}} \tag{5.7}$$

Combining equation (5.7) with the proppant number equation (5.1) will give the following definition of effective wellbore radius:

$$r_w' = \frac{X_e \cdot I_x}{\varepsilon + \frac{\pi \cdot I_x^2}{N_p}} \tag{5.21}$$

Knowing that $X_e = \left(\frac{\sqrt{\pi}\cdot r_e}{2}\right)$, then we can re-write the above equation as follows:

$$r_w^{'} = \frac{\left(\frac{\sqrt{\pi}\cdot r_e}{2}\right)\cdot I_x}{\varepsilon + \frac{\pi \cdot I_x^2}{N_p}} \tag{5.22}$$

Now, recall the productivity index definition from equation (5.4):

$$J_D = \frac{1}{\ln\left(\frac{r_e}{r_w^{'}}\right) + S\ - c} \tag{5.4}$$

Substituting equation (5.22) into the productivity index definition shown above will give us

$$J_D = \frac{1}{\ln\left(\frac{\left(\varepsilon + \frac{\pi \cdot I_x^2}{N_p}\right) r_e}{\left(\frac{\sqrt{\pi}\cdot r_e}{2}\right)\cdot I_x}\right) + S\ - c} \tag{5.23}$$

The above equation can be re-written as:

$$J_D = \frac{1}{\ln\left(\left(\frac{2}{\sqrt{\pi}}\right)\frac{\left(\varepsilon + \frac{\pi \cdot I_x^2}{N_p}\right)}{I_x}\right) + S\ - c} \tag{5.24}$$

After some re-arrangements,

$$J_D = \frac{1}{\ln\left(\frac{\varepsilon}{I_x} + \frac{\pi \cdot I_x}{N_p}\right) + \ln\left(\frac{2}{\sqrt{\pi}}\right) + S\ - c} \tag{5.25}$$

Here S would represent the summation of damage and shape skin factor. Shape skin factor, which depends only on the shape of the drainage area and the well location, is zero for cylindrical or square drainage area. ***c*** is a constant which is ½ for steady-state systems and ¾ for pseudo-steady systems.

For zero skin case and after summing the two constants in the dominator of equation (5.25), then the final form of (J_D) will be as follow:

$$J_D = \frac{1}{\ln\left(\frac{\varepsilon}{I_x} + \frac{\pi \cdot I_x}{N_p}\right) + \ln\left(\frac{2}{\sqrt{\pi}}\right) - c} = \frac{1}{\ln\left(\frac{\varepsilon}{I_x} + \frac{\pi \cdot I_x}{N_p}\right) - c_1} \tag{5.26}$$

Where, c_1 is a constant, which is (3/8) for steady-state systems and (5/8) for pseudo-steady systems.

As explain earlier, the expression (ε) is a function of penetration ratio and can be calculated using equation (5.8) or (5.9) depending on the assumed boundary conditions.

Up to this point, the new single phase Darcy flow optimization formula can be summarized as follows:

To obtain the optimum penetration ratio **($I_{x\text{-}Opt}$)**, at fixed proppant number, equation (5.27) should be solved,

$$f(\varepsilon) - \frac{\pi}{N_p} \cdot I_x^2 = 0 \tag{5.27}$$

To estimate the maximum achievable dimensionless productivity index ($J_{D\text{-}max}$), at fixed proppant number, equation (5.28) should be solved. This equation will also give optimum penetration ratio **($I_{x\text{-}Opt}$)** at ($J_{D\text{-}max}$).

$$J_D = \frac{1}{\ln\left(\frac{\varepsilon}{I_x} + \frac{\pi \cdot I_x}{N_p}\right) - c_1} \tag{5.28}$$

These equations are applicable for both SS and PSS.

To have a better comparison between these equations and those of, Valko and Economides, their formulations (which are only valid for PSS conditions) are summarized below:

To obtain the optimum penetration ratio **($I_{x\text{-}Opt}$)** for fixed proppant number equation (5.1a) should be used: (Valko and Economides 2002, and Economides *et al.* 2004)

$$I_{x-opt}(N_P) = \begin{cases} \sqrt{\dfrac{N_P}{1.6}} \Rightarrow N_P < 0.1 \\ \sqrt{\dfrac{N_p}{\left(1.6 + \exp\left[\dfrac{-0.583 + 1.48\ln(N_P)}{1 + 0.142\ln(N_P)}\right]\right)}} \Rightarrow 0.1 \le N_P \le 10 \\ 1 \Rightarrow N_P > 10 \end{cases} \tag{5.1a}$$

To estimate the maximum achievable dimensionless productivity index ($J_{D\text{-}max}$) for fixed proppant number equation (5.1b) should be used: (Valko and Economides 2002, and Economides *et al.* 2004)

$$J_{D-\max}(N_P) = \begin{cases} \dfrac{1}{0.99 + 0.5\ln(N_P)} \Rightarrow N_P \le 0.1 \\ \dfrac{6}{\pi} - \exp\left[\dfrac{0.423 - 0.311N_P - 0.089N_P^2}{1 + 0.667N_P + 0.015N_P^2}\right] \Rightarrow N_P > 0.1 \end{cases} \quad (5.1b)$$

The main differences between the proposed formulations and those of (Valko and Economides) are as follow:

1. The proposed formulations are valid for both steady-state and pseudo-steady state conditions, whilst Valkos's correlation is applicable only for pseudo-steady state conditions.
2. Valko's correlation requires two steps of calculation; that is the user need to calculate ($I_{x\text{-}opt}$) first and then use another correlation to calculate ($J_{D\text{-}max}$). While, the formulation presented here (Equation 5.28) requires one step of calculation to find both ($I_{x\text{-}opt}$ and $J_{D\text{-}max}$) as will be shown in the next section.

In the next section an illustration of the proposed formulation will be presented and later a comparison between the results of the proposed formulation and those of Valko's formulation will be given.

5.2.2 Graphical Representation of ($\mathbf{I_{x\text{-}Opt}}$) and ($\mathbf{J_{D\text{-}max}}$)

As mentioned earlier that the new formulations (equations 5.27 and 5.28) are simple and easy to use, due to the fact that these two equations can be solved using simple spread sheet applications.

First, ($\mathbf{J_D}$) versus **($\mathbf{I_x}$)** is plotted using equation (5.28) for the whole range of I_x (i.e. from near zero to 1), then the maximum value of dimensionless productivity index curve will represents ($\mathbf{J_{D\text{-}max}}$) and the correspondent penetration ratio will represents **($\mathbf{I_{x\text{-}Opt}}$)**.

The same procedure can be applied to equation (5.27). That is, if this equation is multiplied by a factor of (1/4) on both sides and re-written, it gives:

$$\text{F}(\mathbf{I_x}) = \frac{N_p}{4\pi} - \frac{I_x^2}{4f(\varepsilon)} = 0 \quad (5.29)$$

Now a plot of F ($\mathbf{I_x}$) versus (I_x) will give a curve, which always ranges from (1 to zero) and the optimum penetration ratio ($\mathbf{I_{x\text{-}opt}}$) value will be the one which correspond to F ($\mathbf{I_x}$) intercepting the x-axis (that is, F($\mathbf{I_x}$) equal to zero).

Using equation (5.28) or equation (5.29) will give the same optimum penetration ratio. However, the author recommends using equation (5.28) as it gives two important parameters in one calculation step (i.e. $\mathbf{I_{x\text{-}Opt}}$ **and** $\mathbf{J_{D\text{-}max}}$). In other words, if equation

(5.29) is used then ($\mathbf{I_{x\text{-}Opt}}$) is calculated separately and afterward equation (5.26) is used to find ($\mathbf{J_{D\text{-}max}}$).

Nonetheless, for sake of completeness we will show the results of both equations (5.28 and 5.29) for all optimization cases presented in this chapter.

5.2.3 Single Phase Flow illustration

In order to show the application of the newly developed method, introduced earlier, and to verify its accuracy, the geometry of some different Hydraulic Fractures (HF) are optimized in this section, and the results will be compared with the results of Valko's correlation.

Figure 5.7 show the optimum penetration ratio for different N_P values ($0.01< N_P<0.08$) under Steady-State conditions. In this figure F (I_x) (equation 5.29) has been drawn versus the whole range of penetration ratio (near zero to one), it can be seen from this figure that the optimum penetration ratio is obtained when F (I_x) intercept the x-axis. Also, it can be concluded that as the proppant number increase the optimum penetration number increases as well. Nonetheless, using the definition of proppant number (equation 5.1) we can conclude that the optimum dimensionless fracture conductivity (for the range of N_P presented here) is always equal to 1.6, For instance, for Np = 0.01 and 0.08, $I_{x\text{-}opt}$ = 0.079 and 0.224, respectively.

Thus, $\text{CFD} = \frac{Np}{(Ix)^2} = \frac{0.08}{(0.224)^2} = \frac{0.01}{(0.079)^2} = 1.6$.

Figure 5.8 show the maximum achievable dimensionless productivity index for different N_P values ($0.01< N_P<0.08$) under Steady-State conditions. In this figure J_D (equation 5.28) has been plotted versus the whole range of penetration ratio (near zero to one), it can be seen from this figure that (the optimum penetration ratio and the maximum achievable productivity index) are achieved when J_D curve reach its maximum with respect to I_x. For example, the $J_{D\text{-}max}$ for the proppant number of 0.04 is equal to 0.352 and the optimum penetration ratio corresponding to this $J_{D\text{-}max}$ is equal to 0.15. Also, it can be concluded (from the trend of this figure) that as the proppant number increase the $J_{D\text{-}max}$ and $I_{x\text{-}opt}$ increase as well.

Figure 5.9 show the optimum penetration ratio for different N_P values ($0.01< N_P<0.08$) under Pseudo-Steady State conditions. In this figure, F (I_x) (equation 5.29) has been drawn versus the whole range of penetration ratio (near zero to one). It can be concluded that similar to the SS results as the proppant number increase the optimum penetration ratio increases for PSS conditions. Furthermore, it can be seen from this figure that the optimum penetration ratio is exactly the same as the one presented earlier for SS (for this specific range of N_P). This is due to the fact that for the range of N_P used

in both figures the optimum penetration ratio was always around (0.2). It should be noted that in chapter 3 section 3.3, it was shown that the geometric fracture skin (S_{gf}) (and the effective wellbore radius) under SS and PSS are equal when the penetration ratio is less than or equal 0.2. However, when the penetration ratio is greater than 0.2 then S_{gf} at PSS is greater than that at SS, and the difference is more significant when I_X approaches one, especially for higher conductive fractures.

Accordingly for low proppant numbers (typically <0.1) the optimum penetration ratio is less than or equal 0.2, therefore the effective wellbore radius for PSS and SS are the same and in turn the optimum penetration ratio and optimum fracture conductivity for SS and PSS are similar.

Figure 5.10 show the maximum achievable dimensionless productivity index for different N_P values ($0.01< N_P<0.08$) under Pseudo-Steady State conditions. In this figure J_D (equation 5.28) has been plotted versus the whole range of penetration ratio (near zero to one). Considering the same example as that presented for the SS case, the PSS-$J_{D\text{-}max}$ of the proppant number equal to 0.04 is equal to 0.383 and the optimum penetration ratio corresponding to $J_{D\text{-}max}$ is equal to 0.15 ($I_{x\text{-}opt} = 0.15$). In summary, for this low proppant number the optimum penetration ratio is the same for both PSS and SS conditions; however the maximum dimensionless productivity index is higher in case of PSS compared to SS. These results are consistent with the understanding that a well under PSS conditions give higher productivity compared to a well under SS provided that all other conditions are the same (i.e. fluid properties, rock properties,..etc).

Figure 5.11 and 12 show the optimum penetration ratio at higher N_P values ($0.1< N_P<1$) under Steady-State and Pseudo-Steady state conditions, respectively. It can be seen from these two figures that as the proppant number increase the difference in optimum penetration ratio increase between PSS and SS cases for the same N_P value. As mentioned previously this is due to the fact that as the proppant number increase the optimum penetration ratio increase, which in turn results in the more significant difference between effective wellbore radius values of PSS and SS cases.

From Figure 5.11 we can see that for $N_P = 1$ the curve of F (I_x) does not intersect the x-axis, which indicates that the optimum penetration ratio is equal to one ($I_x =1$). That is, for steady state conditions the optimum penetration ratio is equal to one when the proppant number is greater than or equal to one. However this is not the case for pseudo-steady state conditions where the optimum penetration ratio reaches one when

the proppant number is greater than or equal to 10. This can be seen in Figure 5.13, which shows the optimum penetration ratio for N_P values ranging from 1 to 10.

Figure 5.14 shows a comparison between the proposed $I_{x\text{-}opt}$ formulation and that of Valko . This figure shows the optimum penetration ratio for different proppant numbers. As explained earlier the authors proposed formulation gives two separate values for the SS and PSS optimum penetration ratio while Valko's formulation gives only one value for PSS. It is clear from this figure that there is a a very good agreement between the two formulations under PSS conditions. These two also agree with SS values when I_x is less than 0.2. However at higher I_x the plots of SS and PSS deviate from each other, highlighting that if at such conditions the use of Valkos' formulation is erroneous.

Figure 5.15 shows a comparison between the optimum dimensionless fracture conductivity ($C_{FD\text{-}opt}$) obtained by these two set of formulations. Again the good agreement between results of author's formulation and the correspondent ones from Valko's correlation both under PSS conditions are observed. Furthermore, it is noticed that as proppant number increases the optimum fracture conductivity under SS conditions decreases compared to that of PSS conditions. This is due to the fact that the shape of variation of (ε) with I_X is different in SS and PSS systems, i.e. with an increase in I_x, (ε_{PSS}) increases while (ε_{SS}) decreases. Therefore, it is expected that the shape of variation of $C_{FD\text{-}opt}$ with NP for SS will be different from what it is for PSS. Moreover, it is expected that $C_{FD\text{-}opt}$ will decrease as NP increase while the opposite is true in case of PSS.

Finally, Figure 5.16 shows a comparison between the estimated maximum achievable dimensionless productivity index ($J_{D\text{-}max}$) by the author's and Valko's PSS formulations. It can be noticed that there is a close agreement between the ($J_{D\text{-}max}$) calculated using these two approaches both under PSS conditions.

In summary, the newly developed formulation integrity has been validated by comparing its results with those of the well-known UFD equation for single phase Darcy flow. In the next section, the extension of this approach to the single phase Non-Darcy flow and two- phase gas condensate flow will be presented.

5.3 Gas Condensate Flow Optimization

To generalize the above formulation, the concept of the effective proppant number is used. That is, a formula for correcting the absolute proppant number (N_P) to account for the combined effect of coupling and inertia in gas condensate systems is proposed. Furthermore, the aim is to make this formula general in a sense that it correctly converts

to that suitable for single-phase Non-Darcy flow when total gas fractional flow (GTR) is unity and to Darcy flow when velocity is low.

5.3.1 Gas Condensate Formulation

In the same manner as that presented in the previous section, the author benefits from the effective wellbore radius formulation developed in the Chapter 3 to derive the required formula for the optimum penetration ratio and maximum achievable dimensionless productivity index.

In Chapter 3 (section 3.5), the following formula for effective wellbore radius under two phase gas condensate flow conditions was proposed:

$$r_w^{'} = \frac{x_f}{\varepsilon + \frac{\pi \cdot (1 + 0.5 R_{ew})}{\left(C_{FD-base} \cdot \left(\frac{k_{rg}}{k_{rgb}} \right)_{well} \right)}} \tag{5.30}$$

Where, R_{ew} is the Reynolds number at wellbore conditions, $\left(\frac{k_{rg}}{k_{rgb}} \right)_{well}$ is the ratio of (the velocity/IFT affected to the base) matrix gas relative permeability curve evaluated at wellbore conditions, ($C_{FD\text{-}base}$) is the base dimensionless fracture conductivity, and (ε) is the reciprocal effective wellbore radius for infinite conductivity fracture. ($C_{FD\text{-}base}$ and ε) are defined as follow:

Base Fracture conductivity: $$C_{FD-base} = \frac{k_f \cdot w_f}{k_m \cdot x_f} \cdot \left(\frac{k_{rgb-f}}{k_{rgb-m}} \right)_{well} \tag{5.31}$$

For SS conditions: $$\varepsilon_{SS} = 2 - \left(\frac{0.112 I_x}{1 - 0.796 I_x} \right) \tag{5.32}$$

For PSS conditions: $$\varepsilon_{PSS} = 2 + \left(\frac{0.355 I_x}{1 - 0.704 I_x} \right) \tag{5.33}$$

It should be noted that $C_{FD\text{-}base}$ is the extension of absolute single phase dimensionless conductivity (C_{FD}) to the two phase gas condensate dimensionless conductivity using the ratio of (fracture to matrix) base gas relative perm-abilities (evaluated at wellbore pressure).

Combining equation (5.30) with the proppant number equation (5.1) will give the following definition of two-phase effective wellbore radius:

$$r_w^{'} = \frac{X_e \cdot I_x}{\varepsilon + \dfrac{\pi \cdot I_x^2 (1 + 0.5 R_{ew})}{\left(N_{P_b} \cdot \left(\dfrac{k_{rg}}{k_{rgb}} \right)_{well} \right)}} \tag{5.34}$$

Where, N_{Pb} is the base Proppant number defined as:

$$N_{P_b} = I_X^2 C_{FD-base} = I_X^2 C_{FD} \cdot \left(\frac{k_{rgb-f}}{k_{rgb-m}} \right)_{well} = N_P \cdot \left(\frac{k_{rgb-f}}{k_{rgb-m}} \right)_{well} \tag{5.35}$$

Now, substituting Equation 5.34 in Equation 5.6 for a fixed proppant number and bottom-hole pressure, will give.

$$\frac{\partial}{\partial x_f} \left(\frac{X_e \cdot I_x}{\varepsilon + \dfrac{\pi \cdot I_x^2 (1 + 0.5 R_{ew})}{\left(N_{p_b} \cdot \left(\dfrac{k_{rg}}{k_{rgb}} \right)_{well} \right)}} \right)_{N_P, P_w} = 0 \tag{5.36}$$

Multiplying the nominator and dominator of equation (5.36) by ($1/X_e$) results in:

$$\frac{\partial}{\partial I_x} \left(\frac{I_x}{\varepsilon + \dfrac{\pi \cdot I_x^2 (1 + 0.5 R_{ew})}{\left(N_{p_b} \cdot \left(\dfrac{k_{rg}}{k_{rgb}} \right)_{well} \right)}} \right)_{N_P, P_w} = 0 \tag{5.37}$$

Knowing that equation (5.37) is solved for a fixed proppant number and a certain bottom-hole pressure, $\dfrac{\pi}{N_{p_b} \cdot \left(\dfrac{k_{rg}}{k_{rgb}} \right)_{well}}$ can be considered as constant C to re-write equation (5.37) as follows:

$$\frac{\partial}{\partial I_x} \left(\frac{I_x}{\varepsilon + C \cdot I_x^2 (1 + 0.5 R_{ew})} \right)_{N_P, P_w} = 0 \tag{5.38}$$

Applying the quotient derivative rule to equation (5.38) gives:

$$\frac{\left(\varepsilon + C \cdot I_x^2 + 0.5 \cdot C \cdot I_x^2 \cdot R_{ew} \right) - I_x \left(\dfrac{d\varepsilon}{dI_x} + 2 \cdot C \cdot I_x + C \cdot I_x \cdot R_{ew} + 0.5 \cdot C \cdot I_x^2 \left(\dfrac{\partial R_e}{\partial I_x} \right) \right)}{\left(\varepsilon + C \cdot I_x^2 + 0.5 \cdot C \cdot I_x^2 \cdot R_{ew} \right)^2} = 0 \tag{5.39}$$

Or

$$\left(\varepsilon + C\cdot I_x^2 + 0.5\cdot C\cdot I_x^2\cdot R_{ew}\right) - I_x\left(\frac{d\varepsilon}{dI_x} + 2\cdot C\cdot I_x + C\cdot I_x\cdot R_{ew} + 0.5\cdot C\cdot I_x^2\left(\frac{\partial R_e}{\partial I_x}\right)\right) = 0 \quad (5.40)$$

R_{ew} is the Reynolds number at wellbore condition, defined as:

$$R_{ew} = \frac{\rho\cdot k_f\cdot\beta_f\cdot q_w}{2w_f h}\left(\frac{k_{rg-b}}{k_{rgtr}}\right)_{well} = \frac{\rho\cdot k_f\cdot\beta_f\cdot q_w\cdot x_f}{2w_f h\cdot x_f}\left(\frac{k_{rg-b}}{k_{rgtr}}\right)_{well} = \frac{\rho\cdot k_f\cdot\beta_f\cdot q_w\cdot x_f}{V_f}\left(\frac{k_{rg-b}}{k_{rgtr}}\right)_{well} \quad (5.41)$$

From the proppant number definition (equation 5.1) we can write V_f as follows:

$$V_f = \frac{2\cdot N_P\cdot X_e^2 k_m}{k_f} = a\cdot X_e \quad (5.42)$$

Where, a = $\frac{2\cdot N_P\cdot X_e\cdot k_m}{k_f}$

Substituting V_f equation into equation 5.41, then R_{ew} can be written as follows:

$$R_{ew} = \frac{\rho\cdot k_f\cdot\beta_f\cdot q_w\cdot x_f}{\left(a\cdot X_e\right)}\left(\frac{k_{rg-b}}{k_{rgtr}}\right)_{well} \quad (5.43)$$

Consider $C' = \frac{\rho\cdot k_f\cdot\beta_f}{a}\cdot\left(\frac{k_{rg-b}}{k_{rgtr}}\right)_{well}$, then the final form of R_{ew} will be:

$$R_{ew} = C'\cdot q_w\cdot I_x \quad (5.44)$$

Therefore,

$$\frac{\partial R_{ew}}{\partial I_x} = C'\frac{\partial\left(q_w\cdot I_x\right)}{\partial I_x} \quad (5.45a)$$

or

$$\frac{\partial R_{ew}}{\partial I_x} = C'\left(q_w + I_x\cdot\frac{\partial q_w}{\partial I_x}\right) \quad (5.45b)$$

Considering that at the optimum point q_w is at the maximum value for a fixed drawdown, then it should be stated that $\frac{\partial q_w}{\partial I_x}$ at optimum point equal to zero. Accordingly, equation (5.45b) can be re-written as:

$$\frac{\partial R_{ew}}{\partial I_x} = C' q_w \quad (5.46)$$

Substituting equation (5.46) into equation (5.40) will give:

$$\left(\varepsilon + C\cdot I_x^2 + 0.5\cdot C\cdot I_x^2\cdot R_{ew}\right) - I_x\left(\frac{d\varepsilon}{dI_x} + 2\cdot C\cdot I_x + C\cdot I_x\cdot R_{ew} + 0.5\cdot C\cdot I_x^2\left(C' q_w\right)\right) = 0 \quad (5.47a)$$

Or

$$\left(\varepsilon + C \cdot I_x^2 + 0.5 \cdot C \cdot I_x^2 \cdot R_{ew}\right) - \left(I_x \frac{d\varepsilon}{dI_x} + 2 \cdot C \cdot I_x^2 + C \cdot I_x^2 \cdot R_{ew} + 0.5 \cdot C \cdot I_x^2 \left(R_{ew}\right) \right) = 0 \quad (5.47b)$$

And after adding the similar terms we will get:

$$\left(\varepsilon - I_x \frac{d\varepsilon}{dI_x} \right) - C \cdot I_x^2 - C \cdot I_x^2 \cdot R_{ew} = 0 \quad (5.48a)$$

Or

$$\left(\varepsilon - I_x \frac{d\varepsilon}{dI_x} \right) - C \cdot I_x^2 \cdot \left(1 + R_{ew}\right) = 0 \quad (5.48b)$$

Let's call $\left(\varepsilon - I_x \frac{d\varepsilon}{dI_x} \right)$ as $f(\varepsilon)$, and knowing that C equal to $\frac{\pi}{N_{p_b} \cdot \left(\frac{k_{rg}}{k_{rgb}} \right)_{well}}$, then the final form of equation (5.48b) is as follow:

$$f(\varepsilon) - \left(\frac{\pi}{N_{P_b} \left(\frac{k_{rg}}{k_{rg-b}} \right)_m} \right) \cdot I_x^2 \cdot \left(1 + R_{ew}\right) = 0 \quad (5.49)$$

This equation can be re-written in terms of effective proppant number as follows:

$$f(\varepsilon) - \left(\frac{\pi}{N_{P_{eff}}} \right) \cdot I_x^2 = 0 \quad (5.50)$$

Where, the effective proppant number (N_{Peff}) is defined as follows:

$$N_{P_{eff}} = \frac{N_{P_b}}{\left(1 + R_{ew}\right)} \cdot \left(\frac{k_{rg}}{k_{rg-b}} \right)_{well} \quad (5.51)$$

It should be noted, that the expression $f(\varepsilon)$ is exactly the one which has been presented in the single phase optimization section. That is, $f(\varepsilon)$ is not a function of phases present.

Based on that, we can conclude that equation (5.50) is the general form of equation (5.27) which has been presented for the single phase optimization.

Furthermore, the proposed effective proppant number equation (5.51) is general in the sense that it is used for two phase gas condensate flow, and if the total gas fractional flow is equal to one (i.e. $\left(\frac{k_{rg}}{k_{rg-b}} \right)_{well}$ =1 and $N_{P_b} = N_P$) then it will correctly convert to that

suitable for single-phase Non-Darcy flow for high velocity systems and to Darcy flow when velocity is low.

Finally, in the next section a formula is presented for estimating the maximum achievable productivity index for a certain proppant number and bottom-hole pressure under two-phase flow. This formula should give us both ($\mathbf{J_{D\text{-}max}}$) and ($\mathbf{I_{x\text{-}opt}}$) at the same time.

First, let's recall the general effective wellbore radius formulation equation (5.30):

$$r_w' = \frac{X_e \cdot I_x}{\varepsilon + \dfrac{\pi \cdot I_x^2 (1 + 0.5 R_{ew})}{\left(N_{p_b} \cdot \left(\dfrac{k_{rg}}{k_{rgb}} \right)_{well} \right)}} \tag{5.52}$$

Writing this equation in term of N_{Peff} will give:

$$r_w' = \frac{X_e \cdot I_x}{\varepsilon + \dfrac{\pi \cdot I_x^2}{N_{p\,eff}}} \tag{5.53}$$

Knowing that $X_e = \left(\dfrac{\sqrt{\pi} \cdot r_e}{2} \right)$, then the above equation can be re-written as follows:

$$r_w' = \frac{\left(\dfrac{\sqrt{\pi} \cdot r_e}{2} \right) \cdot I_x}{\varepsilon + \dfrac{\pi \cdot I_x^2}{N_{p\,eff}}} \tag{5.54}$$

Now, let's recall the productivity index definition from equation (5.4):

$$J_D = \frac{1}{\ln\left(\dfrac{r_e}{r_w'} \right) + S - c} \tag{5.55}$$

Substituting equation (5.54) into the productivity index definition shown above will give:

$$J_D = \frac{1}{\ln\left(\dfrac{\left(\varepsilon + \dfrac{\pi \cdot I_x^2}{N_{p_{eff}}} \right) r_e}{\left(\dfrac{\sqrt{\pi} \cdot r_e}{2} \right) \cdot I_x} \right) + S - c} \tag{5.56}$$

The above equation can be re-written as:

$$J_D = \frac{1}{\ln\left(\frac{\varepsilon}{I_x} + \frac{\pi \cdot I_x}{N_{p_{eff}}}\right) + \ln\left(\frac{2}{\sqrt{\pi}}\right) + S - c} \tag{5.57}$$

Here S would represent the summation of damage and shape skin factor. As mentioned before, shape skin factor is zero for cylindrical or square drainage area. ***c*** is a constant which is ½ for steady-state systems and ¾ for pseudo-steady systems.

For zero damage skin case and after summing the two constants in the dominator of equation (5.57), then the general form of (J_D) will be:

$$J_D = \frac{1}{\ln\left(\frac{\varepsilon}{I_x} + \frac{\pi \cdot I_x}{N_{p_{eff}}}\right) - c_1} \tag{5.58}$$

Where, c_1 is a constant which is (3/8) for steady-state systems and (5/8) for pseudo-steady systems.

The expression (ε) is a function of penetration ratio and can be calculated using equation (5.8 or 5.9) depending on the assumed boundary conditions.

In summary, the proposed formulations for fracture optimization in gas (Darcy and Non-Darcy flow) and gas condensate flow are summarized as follow,

To estimate the maximum achievable dimensionless productivity index ($\mathbf{J_{D\text{-}max}}$), at fixed proppant number and bottom-hole pressure, equation (5.58) should be solved. This equation will also give optimum penetration ratio ($\mathbf{I_{x\text{-}Opt}}$) at ($\mathbf{J_{D\text{-}max}}$).

$$J_D = \frac{1}{\ln\left(\frac{\varepsilon}{I_x} + \frac{\pi \cdot I_x}{N_{peff}}\right) - c_1} \tag{5.58}$$

To obtain the optimum penetration ratio ($\mathbf{I_{x\text{-}Opt}}$), at fixed proppant number and bottom-hole pressure, equation (5.59) should be solved,

$$\text{F}(\mathbf{I_x}) = \frac{N_{peff}}{4\pi} - \frac{I_x^2}{4 f(\varepsilon)} = 0 \tag{5.59}$$

These formulations are applicable for both SS and PSS.

Effective proppant number is defined as,

$$N_{P_{eff}} = \frac{N_{P_b}}{(1 + R_{ew})} \cdot \left(\frac{k_{rg}}{k_{rg-b}}\right)_{well} \tag{5.60}$$

Also, (Valko and Economides 2002) formulation is modified by the author as follow,

To obtain the optimum penetration ratio **($I_{x\text{-}Opt}$)** for fixed proppant number and bottom-hole pressure equation (5.61) should be used,

$$I_{x-opt}(N_{Peff}) = \begin{cases} \sqrt{\dfrac{N_{Peff}}{1.6}} \Rightarrow N_{Peff} < 0.1 \\ \sqrt{\dfrac{N_{peff}}{\left(1.6 + \exp\left[\dfrac{-0.583 + 1.48\ln\left(N_{Peff}\right)}{1 + 0.142\ln\left(N_{Peff}\right)}\right]\right)}} \Rightarrow 0.1 \le N_{Peff} \le 10 \\ 1 \Rightarrow N_{Peff} > 10 \end{cases} \quad (5.61)$$

To estimate the maximum achievable dimensionless productivity index (**$J_{D\text{-}max}$**) for fixed proppant number and bottom-hole pressure equation (5.62) should be used,

$$J_{D-\max}(N_{Peff}) = \begin{cases} \dfrac{1}{0.99 + 0.5\ln\left(N_{Peff}\right)} \Rightarrow N_{Peff} \le 0.1 \\ \dfrac{6}{\pi} - \exp\left[\dfrac{0.423 - 0.311N_{Peff} - 0.089N_{Peff}^2}{1 + 0.667N_{Peff} + 0.015N_{Peff}^2}\right] \Rightarrow N_{Peff} > 0.1 \end{cases} \quad (5.62)$$

The modified (Valko and Economides 2002) formulation is only valid for PSS conditions.

Finally, it should be mentioned that calculating N_{Peff} (Equation 5.60) requires an iterative process since it is a function of velocity. That is, either the flow rate or the bottom-hole pressure needs to be known prior to the optimization process. The iterative procedure is summarized below.

If the bottom-hole pressure is known then,

1- Assume the production rate (q_{well}).

2- Calculate effective proppant number, Equation 5.60

3- Calculate optimum fracture penetration ratio (i.e. fracture dimensions), Equation 5.59.

4- Calculate optimum effective wellbore radius. ($r_w^{'} = \dfrac{x_{f-opt}}{\varepsilon + \dfrac{\pi}{C_{FD-opt}}}$)

5- Calculate the flow rate.

6- Check if the difference between the calculated production rate and the assumed value is less than the acceptable error tolerance value.

YES: Stop and report the optimum design.

NO: Readjust the assumed value for q_{well} and go back to step 2.

The same procedures can be used if the unknown is the bottom-hole pressure instead of flow rate.

5.3.1 Gas Condensate flow illustration

In order to show the application of the newly developed method, and to verify its accuracy, the geometry of different Hydraulic Fractures (HF) is optimized and the results are compared with the results of the In-house numerical simulator.

In this section, a brief description of in house simulators used in the optimization process will be given. Then the results of new formulation are compared with those of the numerical simulator.

5.3.2 Gas condensate optimization In house Simulators

Two types of in house simulators have been used in here. The first one is the 3-D Comsol in-house simulator. The formulation and assumption of this simulator was presented in Chapter 3 for both Steady-State and Pseudo-Steady state conditions. We used this simulator to obtain the productivity index curve for different fracture (width to length) ratio under a fixed proppant number. That is, for a given proppant number different fracture geometries were simulated. The in house simulator is linked to a mesh generator that creates the required mesh files using a Mat-Lab code, which also automatically runs the simulations. Each mesh file corresponds to a one numerical simulation run and gives one J_D value for a fracture width-to-length combination. Then, the J_D values for all combinations are drawn in one curve and the optimum combination is the one, which correspond to maximum J_D value in the curve.

The second simulator is a 1-D open-hole optimization simulator developed using excel sheet VBA, which performs the same task but using the effective wellbore radius formulation developed in Chapter 3 of this thesis. That is, this simulator was also used to find the productivity index curve for different fracture (width to length) ratio under a fixed proppant number. Similar to the previous simulator for a given proppant number different fracture geometries were simulated and the optimum combination of fracture width-to-length ratio was determined using the J_D curve of all possible fracture geometries. The main reason of using this 1-D optimizer is to “propose it” as a quick optimization tool rather than using the 3-D in-house simulator, which requires significant CPU time. It should be noted that if the in-house 1-D and 3-D simulators were not available, a commercial simulator, should have been used. This task would be cumbersome and associated with numerical instability, which makes it practically unattractive especially when the number of fracture width-to-length combination is high and large number of simulation runs is required. This last requirement, albeit to a lesser

extent, also applies to the 3D in-house simulator. However the 1-D in-house simulator, which solves the same governing equation in conjunction with the proposed effective wellbore radius produces the same results as those of the 3D simulators but with much less CPU time.

It should be noted that for all the optimization examples presented (hereafter) the average absolute deviation of error between the 3-D in house simulator and the 1-D open hole optimizer was less than 4%, which verify the accuracy of the 1-D optimizer, and highlight the added value of using it.

Steady State Example – Single Phase:

Figure 5.17 shows the in-house simulator J_D curve versus penetration ratio for a low proppant number of 0.05 (N_P = 0.05) when a single-phase fluid is flowing under steady-state Darcy and Non-Darcy conditions. The details of this HF are described in OPT-1 data set, Table 4.1. Here the well was producing under a constant bottom-hole pressure resulting in a pressure drop of (DP = 200 Psi).

The optimum fracture geometry is the one which corresponds to the maximum productivity value. Accordingly, the maximum dimensionless productivity index for Darcy flow curve has a value of 0.368 ($J_{D\text{-}max}$ = 0.368) and the optimum penetration ratio corresponding to this $J_{D\text{-}max}$ has a value of ($I_{x\text{-}opt}$ = 0.17). However, when Non-Darcy flow was activated the maximum productivity index was reduced significantly to a value of 0.237 ($J_{D\text{-}max}$ = 0.237). This represents a reduction of (35%) in dimensionless productivity index due to Non-Darcy effects. Also, the optimum penetration ratio under this inertial effect was 0.04 ($I_{x\text{-}opt}$ = 0.04). Thus the optimum fracture length has reduced by a factor of (4) compared to that of Darcy flow conditions. Such numbers show how inertia can badly affect the post fracture performance if not taken into account during the fracture design phase.

Figures 5.18 and 5.19 show the optimum penetration ratio and maximum achievable dimensionless productivity curve for the previous example (N_P = 0.05) using the newly developed formulae (equations 5.59 and 5.58).

In Figure 5.18 F (I_x) was drawn versus penetration ratio (near zero< I_x >1) in order to find the optimum penetration ratio which correspond to (F (I_x) = zero). Under Darcy flow conditions, Reynolds number was low and the effective proppant number (equation 5.60) was set equal to the absolute proppant number (i.e. N_{Peff} = N_P = 0.05). This effective proppant number was used to calculate F (I_x). It can be seen from Figure 5.18 that F (I_x) = zero at penetration ratio of (0.17), that is the optimum penetration ratio

corresponding to this proppant number was ($I_{x\text{-}opt}$ = 0.17) which is exactly the same value as that obtained from the in-house numerical simulator.

Under Non-Darcy flow conditions, the optimum Reynolds number was equal to (R_{ew}=17.95) and accordingly the corresponding effective proppant number was equal to (N_{Peff} = 0.0026). This effective proppant number was used to calculate F (I_x). It can be seen from Figure 5.18 that inertia has reduced the optimum penetration ratio to a value of ($I_{x\text{-}opt}$ = 0.04) which is the same as that obtained from the developed in house simulator, confirming the integrity of the new formula for finding optimum penetration ratio.

In Figure 5.19 shows the dimensionless productivity (equation 5.58) was drawn versus penetration ratio. Similar to the procedure used in Figure 5.18, the effective proppant number was used to calculate ($J_{D\text{-}max}$, Equation 5.58) under Darcy and Non-Darcy conditions for ($0.01 < I_x < 1$).

It can be noticed from this figure that the ($J_{D\text{-}max}$) for (N_P = 0.05, i.e. Darcy condition) was equal to ($J_{D\text{-}max}$ = 0.367) which is very close to the value obtained from the in-house simulator (AAD of less than 3%), Also the optimum penetration ratio corresponding to $J_{D\text{-}max}$ was equal to 0.17 ($I_{x\text{-}opt}$ = 0.17) which is the same as the one presented in Figure 5.18. Furthermore, under Non-Darcy flow (N_{Peff} = 0.0026) was used in Equation 5.58 and the ($J_{D\text{-}max}$, $I_{x\text{-}opt}$) values were (0.242 and 0.04, respectively) which is in a very close agreement to the results of the in-house simulator.

In order to further confirm the integrity of the new formulae, the same exercise was repeated with two different absolute proppant values (N_P = 0.5 and 1).

Figures 5.20 and 21, 5.22 and 23 show the results of the in-house simulator and that obtained from equations (5.58) and (5.59) for proppant number of 0.5 and 1 (N_P = 0.5 and 1), respectively. A summary of these results are compared below.

For N_P = 0.5, OPT-2data set in Table 4.1,

In-house simulator results (Figure 5.20): Darcy flow ($I_{x\text{-}opt}$ = 0.57 and $J_{D\text{-}max}$ = 0.645), Non-Darcy flow ($I_{x\text{-}opt}$ = 0.14 and $J_{D\text{-}max}$ = 0.351).

Equations (5.58 and 5.59) results (Figure 5.21): Darcy flow ($I_{x\text{-}opt}$ = 0.57 and $J_{D\text{-}max}$ = 0.645), Non-Darcy flow ($R_{ew\text{-}opt}$ =14, N_{Peff} = 0.033, $I_{x\text{-}opt}$ = 0.14 and $J_{D\text{-}max}$ = 0.341).

For N_P = 1, OPT-3data set in Table 4.1,

In-house simulator results (Figure 5.22): Darcy flow ($I_{x\text{-}opt}$ = 1.0 and $J_{D\text{-}max}$ = 0.867), Non-Darcy flow ($I_{x\text{-}opt}$ = 0.22 and $J_{D\text{-}max}$ = 0.41).

Equations (5.58 and 5.59) results (Figure 5.23): Darcy flow ($I_{x\text{-}opt}$ = 1 and $J_{D\text{-}max}$ = 0.867), Non-Darcy flow ($R_{ew\text{-}opt}$ =12.7, N_{Peff} = 0.073, $I_{x\text{-}opt}$ = 0.22 and $J_{D\text{-}max}$ = 0.395).

The very good agreements between these results further confirm the integrity of the proposed approach and formulation.

Pseudo-Steady State Example – Single Phase:

Figure 5.24 shows the J_D curve versus penetration ratio for a proppant number of 0.5 (N_P = 0.5) under Darcy and Non-Darcy flow for Pseudo-steady state conditions. These results were obtained using the developed PSS in-house simulator.

In this exercise, the well was running under very low constant flow rate of ($q_{well} = 1^{-5}$ m^3/s), which confirms Darcy flow conditions, then this well flow rate was significantly increased to a value of ($q_{well} = 5^{-3}$ m^3/s), in order to activate Inertial effects.

It can be noted from this figure that the optimum penetration ratio for this proppant number is equal to 0.53 ($I_{x\text{-}opt}$ = 0.53) and the maximum achievable productivity index is equal to 0.71 ($J_{D\text{-}max}$ =0.71) when Darcy flow is present. However, activating inertia has significantly reduced these two values to 0.22 in case of optimum penetration ratio ($I_{x\text{-}opt}$ = 0.22) and a value of 0.45 in case of the maximum achievable productivity index is ($J_{D\text{-}max}$ =0.45).

The optimum penetration ratio and maximum achievable productivity index were calculated using (Equations 5.59 and 5.58, respectively).

The Darcy flow optimum penetration ratio is equal to 0.53 as shown in Figure 5.25 (which shows F (I_x) versus I_x); this value of ($I_{x\text{-}opt}$) is the same as that calculated from in-house simulator Figure 5.24. Using this value in Equation 5.59 gives a $J_{D\text{-}max}$ value of 0.71 as that obtained from the in-house simulator.

For Non-Darcy flow, the optimum Reynolds number was equal to ($R_{ew\text{-}opt}$ =5.2) and the effective proppant (N_{Peff} = 0.0806, calculated using Equation 5.60). it can be seen from Figure 5.24 that using the calculated effective proppant number in Equation 5.59 gives an optimum penetration ratio of (0.22) which is exactly the same as that of the in-house simulator. It should be noted that the same effective proppant number has been used in (the modified Valko's formulation, Equation 5.61) and it also gives a value of (0.22).

Also, using the effective proppant number in the proposed $J_{D\text{-}max}$ formula (Equation 5.59) and the modified Valko's $J_{D\text{-}max}$ formula (Equation 5.62) gives a value of 0.44 ($J_{D\text{-}max}$ =0.44) which is in a very close agreement with that of the in-house simulator.

This confirms the integrity of the introduced effective proppant number (N_{Peff}) as it has been verified by the in house simulator. Furthermore, when (N_{Peff}) is used with the modified Valko's formulation it gives the same results as that of the in-house simulator.

Finally, the same exercise has been repeated for a proppant number of (N_P = 1.5) under PSS condition and the results of the in-house simulator and that of the proposed formulation (Equations 5.58 and 5.59) and the modified Valko's formulation (Equations 5.61 and 5.62) are presented below.

For N_P = 1.5 under PSS conditions, OPT-5 data set in Table 4.1,

In-house simulator results (Figure 5.26): Darcy flow ($I_{x\text{-}opt}$ = 0.77 and $J_{D\text{-}max}$ = 1.023), Non-Darcy flow ($I_{x\text{-}opt}$ = 0.43 and $J_{D\text{-}max}$ = 0.645).

The proposed formulation and the modified Valko's formulation results (Figure 5.27): under Darcy flow ($I_{x\text{-}opt}$ = 0.77 and $J_{D\text{-}max}$ = 1.023), under Non-Darcy flow ($R_{ew\text{-}opt}$ =3.6, N_{Peff} = 0.326, $I_{x\text{-}opt}$ = 0.43 and $J_{D\text{-}max}$ = 0.63). That is, the proposed formulae (equations 5.58 and 5.59) and Valko's correlation (equations 5.61 and 62) give the same results as the in-house simulator when using the effective proppant number (N_{Peff}, equation 5.60).

Steady State – Two phase example:

Figure 5.28 shows the dimensionless productivity for a gas condensate case under SS with different GTR values calculated using the in-house simulator. In this figure the fluid was (C1-C4, binary mixture, explained in Table 4.2). Also, the external pressure was kept at 1850Psi (which is near to dew point pressure of 1865Psi) while the bottom-hole pressure changes with GTR. P_{well} was equal to 1650, 1350, 900Psi for GTR_{well} of 0.71, 0.81, 0.91, respectively. Furthermore, the absolute proppant number used in here was (N_P = 0.5), OPT-6, 7, and 8 data set in Table 4.1.

For the base curve it can be seen that the dimensionless productivity index increases for the whole range of I_x, accordingly we can conclude that the optimum penetration happens at (I_x =1). However, when velocity effects are activated we can notice that the optimum penetration ratio has reduced to a value of ($I_{x\text{-}opt}$ =0.45) for GTR_{well} of 0.71. A further reduction in optimum penetration has been observed when the GTR_{well} is reduced to a value of 0.81 (i.e. $I_{x\text{-}opt}$ = 0.35.), this is due to the fact that as GTR is reduced the velocity is increased (this is due to the increase in pressure draw-down and the increase in the contribution of gas fractional flow which increases the total flow and velocity of the gas phase). That is, the velocity inside the fracture will increase which in turn increases the inertial effects inside the fracture and reduce the contribution of coupling from the matrix. GTR of 0.91 has the lowest value of optimum penetration ratio (I_x = 0.27) due to the high velocity and low condensate saturation.

Figure 5.29 shows the optimum penetration ratio for the previous example calculated using effective proppant number Equation 5.60 and the optimum penetration ratio

formula Equation 5.59. For the base curve case, the effective proppant number is equal to the base proppant number ($N_{peff} = N_{Pb} = 0.99$), using base proppant number in Equation 5.59 it can be noticed that F (I_x) curve has not intercepted the x-axis and thus the optimum penetration ratio is one ($I_{x\text{-}opt} = 1$) which is the same as the simulation results.

Furthermore, for $GTR_{well} = 0.71$ the optimum Reynolds number was equal to ($R_{ew} = 2.58$) and the effective proppant number equal to ($N_{Peff} = 0.3124$), using this effective proppant number in equation 5.59 gives ($I_x = 0.45$) which is the same as the in house simulator. For $GTR_{well} = 0.81$ and 0.91 the base and effective proppant numbers, and optimum Reynolds number were (0.96, 0.185, 4.23 for GTR = 0.81 and 0.91, 0.1, 8 for GTR =0.91), using this numbers in equation 5.59 gives ($I_{x\text{-}opt} = 0.35$ for GTR =0.81 and $I_{x\text{-}opt} = 0.27$ for GTR =0.91) these are exactly the same as the ones calculated by the in-house simulator, which further confirm the integrity of the proposed approach for two-phase gas condensate flow.

Figure 5.30 summarize the results presented in Figures 5.28 and 29. It shows the optimum penetration ratio versus the well total gas ratio GTR_{well}. It can be seen from this figure that as GTR increase the optimum compromise happens at shorter fracture length in order to compensate for the more pronounced inertial effects at higher GTR_{well}.

Figure 5.31 shows the dimensionless productivity index for the same example discussed above, but keeping GTR_{well} constant of 0.81 and pressure drop varying.. Accordingly, three different pressure drops were simulated (DP = 100, 200, 400Psi), OPT-9, 10, 11 data sets in Table 4.1.

In this figure it can be noted that for the base curve (No velocity effects) run the dimensionless productivity index is increasing for the whole range of I_x which means that the optimum penetration ratio happens at ($I_{x\text{-}opt} = 1$). However, as the pressure drop increase the optimum penetration happens at lower values due to the increase in velocity and the dimensionless productivity index decrease. The optimum penetration ratio and the maximum dimensionless productivity index for (DP = 100, 200, 400Psi) happen at ($I_{x\text{-}opt} = 0.53, 0.45, 0.39$ and $J_{D\text{-}max} = 0.62, 0.58, 0.535$, respectively). In other words for all DP values inertia is always dominant and the optimum penetration ratio of the base curve is always higher than the optimum penetration ratio of all DP values.

Figure 5.31 shows the optimum penetration ratio using equation 5.59 for ($GTR_{well} = 0.81$ with DP = 100, 200, 400Psi). the results from this figure are listed below.

For DP = 100Psi, $R_{ew\text{-}opt}$ = 1.23, N_{Pb} = 0.978, N_{Peff} = 0.439, all these number were used in equation 5.59 and the optimum penetration ratio was ($I_{x\text{-}opt}$ = 0.53). Also, using ($I_{x\text{-}opt}$) in Equation 5.58 give a dimensionless productivity index of 0.62 ($J_{D\text{-}max}$ = 0.62), these results are in very good agreement with the in-house simulator. For DP = 200Psi, $R_{ew\text{-}opt}$ = 1.97, N_{Pb} = 0.978, N_{Peff} = 0.329, the optimum penetration ratio was (I_x = 0.45). Using ($I_{x\text{-}opt}$) in Equation 5.58 give a dimensionless productivity index of 0.56 ($J_{D\text{-}max}$ = 0.56).
For DP = 400Psi, $R_{ew\text{-}opt}$ = 3.34, N_{Pb} = 0.978, N_{Peff} = 0.225, the optimum penetration ratio was (I_x = 0.39). Using ($I_{x\text{-}opt}$) in Equation 5.58 give a dimensionless productivity index of 0.51 ($J_{D\text{-}max}$ = 0.51).
Figure 5.33 summarize the results of Figure 5.31. It shows the optimum fracture penetration ratio and fracture width for different pressure drops (DP = 100, 200, 400Psi). It is clear from this figure that as the pressure drop increase the optimum compromise happens at shorter fracture length and wider fracture width to compensate for the negative effect of inertia.

Pseudo Steady State – Two phase example:

Figure 5.34 shows the dimensionless productivity for a gas condensate case under PSS with GTR_{well} = 0.81 and different flow rate values calculated using in-house simulator. The flow rates are as follow (q_{well} = 1^{-5}, 1^{-4}, 1^{-3} m^3/s), OPT-12, 13, 14 data sets in Table 4.1.
It is clear from this figure that as the flow rate increases the optimum penetration ratio decrease. For (q_{well} = 1^{-5} m^3/s) the optimum penetration ratio is ($I_{x\text{-}opt}$ = 0.67 and $J_{D\text{-}max}$ = 0.86). For (q_{well} = 1^{-4} and 1^{-3} m^3/s) the optimum penetration ratio were ($I_{x\text{-}opt}$ = 0.55 and 0.31and $J_{D\text{-}max}$ = 0.71 and 0.54, respectively).
The corresponding value using the effective proppant number concept with either Equations 5.58 and 5.59 (the proposed formulation) or Equations 5.61 and 5.62 (Modified Valko's formulation), are shown below.
For q_{well} = 1^{-5} m^3/s, $R_{ew\text{-}opt}$ = 0.01, N_{Pb} = 0.97, N_{Peff} = 0.97, $I_{x\text{-}opt}$ = 0.67, $J_{D\text{-}max}$ = 0.88.
For q_{well} = 1^{-4} m^3/s, $R_{ew\text{-}opt}$ = 0.84, N_{Pb} = 0.97, N_{Peff} = 0.526, $I_{x\text{-}opt}$ = 0.55, $J_{D\text{-}max}$ = 0.72.
For q_{well} = 1^{-3} m^3/s, $R_{ew\text{-}opt}$ = 4.7, N_{Pb} = 0.97, N_{Peff} = 0.169, $I_{x\text{-}opt}$ = 0.31, $J_{D\text{-}max}$ = 0.53.
These results confirm the integrity of the proposed formulations for gas condensate flow under PSS. Furthermore, it shows that the effective proppant concept works very well when used in Valko's formulations, that is using the effective proppant number formulation (Equation 5.60) the author was able to remove the restriction on Valko's formulation and made it valid for gas (Non-Darcy flow) and gas condensate flow.

5.4 Summary and Conclusions

In this study the author benefited from the effective wellbore radius formulation presented in Chapter 3, to develop a new fracture optimization formulations to estimate maximum productivity index ($J_{D\text{-}max}$, Equation 5.58) and optimum penetration ratio ($I_{x\text{-}opt}$, Equation 5.59) for a given proppant number in gas condensate reservoirs including coupling and inertial effects. These formulations are applicable to steady state and pseudo-steady state conditions.

The proposed formulations are general in the sense that if the well total gas fractional flow (GTR_{well}) is unity, then it correctly converts to those of single phase gas systems under Non-Darcy flow conditions and when Reynolds number is small to that under Darcy flow conditions.

The author also proposed an effective proppant number (N_{Peff}) formula (Equation 5.60); which corrects the absolute proppant number (N_P) for the combined effect of coupling and inertia in gas condensate reservoirs.

Using the proposed effective proppant number, the author was able to generalize Valko and Economides 2002, UFD formulations (Equations 5.1a and 5.1b) to account for gas (Non-Darcy flow) and Gas Condensate flow under pseudo-steady state conditions. It should be noted that, the original (Valko and Economides) formulations were only applicable for single phase Darcy flow conditions.

Two in-house simulators were developed to verify the integrity of the proposed formulations. These are a (2-D and EOH 1-D) simulators that for a given proppant number perform many simulations (i.e. different simulations with different fracture geometries for a fixed proppant number) and identify the case with optimum fracture geometry (length-width ratio) giving maximum well productivity. The 2D model solves the original governing continuity and flow equations whilst the equivalent 1-D model incorporates the formulations and procedures proposed by the author in Chapters 3. For all optimization cases studied, the results of both simulators were in close agreement (AAD < 4%). This highlight the added value of using the 1-D simulator as a quick tool of numerical optimization since it requires much less computational time compared to 2-D simulators.

Several illustrations confirmed the applicability of the newly developed optimization formulae for single phase gas and gas condensate systems.

5.5 References

Economides, M., Oligney, R., and Valko, P.: Unified Fracture Design, Orsa Press, Alvin, Texas, USA, 2002.

Giddley J.L.: "A Method for Correcting Dimensionless Fracture Conductivity for Non-Darcy Flow Effects" SPE 20710, SPE Production Engineering Journal, pp.391-394, Nov-1991.

Indriati, Sh., Wang, X., Economides, M., J.: "Adjustment of Hydraulic Fracture Design in Gas Condensate Wells" SPE 73751, presented at International Symposium and Exhibition on Formation Damage Control, Louisania, USA, 2002.

Lopez-Hernandez, H., D., Valko, P. P., Pham, T., T.: "Optimum Fracture Design Minimizes the Impact of Non-Darcy Flow Effects" SPE 90195, presented at SPE Annual Technical Conference and Exhibition, Houston, USA, 2004.

Meyer B.R. and Jakot R.H.: "Pseudo-Steady State Analysis of Finite Conductivity Vertical Fractures", SPE 95941, presented at SPE Annual Technical Conference, Texas, USA, 2005.

Mohan J., Pope G.A. and Sharma M. M.: "Effect of Non-Darcy Flow on Well Productivity of a Hydraulically Fractured Gas/Condensate Well" SPE 103025, presented at SPE Gas Technology Symposium, Texas, USA, 2006.

Prats M.: "Effect of Vertical Fractures on Reservoir Behaviour-Incompressible Fluid Case", SPE Journal, pp. 105-118, June 1961.

Valko Peter P. and Economides, Micheal J.: "Heavy Crude Production from Shallow Formations: Long Horizontal Wells Versus Horizontal Fractures" SPE 50421, Presented at SPE International conference on Horizontal Well Technology, Calgary, Canada, 1998.

Wang X., Indriati S., Valko P.P and Economides, M. J.: "Production Impairment and Purpose Built Design of Hydraulic Fracture in Gas Condensate Reservoirs," SPE 64749, Presented at SPE International Oil and Gas Conference and Exhibition, Beijing, China, 2000.

Economides M.J., Demarchos A.S., Mach J.M., Rueda J., Wolcott D.S., Yukos: "Pushing the Limits of Hydraulic Fracturing in Russia" SPE 90357 presented at SPE Annual Technical Conference and Exhibition, 26-29 September 2004, Houston, Texas.

Valko P., 2006:"HF2D FRAC Design Spreadsheet", April 2001 (Updated May 30, 2006), Texas A&M University, http://www.pe.tamu.edu/valko/public_html/Hydraulic_Fracture_Design/xls/Hf2D

Mahdiyar H., Jamiolahmady M., Sohrabi M.: "Optimization of Hydraulic Fracture Geometry" SPE 123466 presented at Offshore Europe, 8-11 September 2009, Aberdeen, UK.

Cinco-Ley H. and Samaniego F.: "Transient Pressure Analysis: Finite-Conductivity Fracture Case Versus Damaged Fracture Case", Paper SPE 10179 presented at AFTCE, San Antonio, Texas, 1981.

Table 5.1: Optimized Geometries in this study.

	OPT-1	OPT-2	OPT-3
Matrix core	Texas Cream k=9.1mD β=3.927E+9	Texas Cream k=9.1mD β=3.927E+9	Texas Cream k=9.1mD β=3.927E+9
Fluid Type	Single Phase	Single Phase	Single Phase
k_f/D	146	146	146
β_f/m^{-1}	3.511E+5	3.511E+5	3.511E+5
Reservoir length, X_e	200	200	200
Formation Thickness/m	10	10	10
Pressure Drop, DP/psi	200	200	200
GTR_w	1	1	1
Absolute Proppant number, N_P	0.05	0.5	1
$\mathbf{I_{x\text{-}opt}}$, Darcy Flow (In-house Simulator & Equation 3.59)	0.17	0.57	1
$\mathbf{J_{D\text{-}max}}$, Darcy Flow (In-house Simulator & Equation 3.58)	0.368	0.645	0.863
Base Proppant number, N_{Pb}	--	--	--
effective Proppant number, N_{Peff}	0.0026	0.033	0.073
$\mathbf{I_{x\text{-}opt,}}$ Non-Darcy Flow (In-House Simulator)	0.04	0.14	0.22
$\mathbf{J_{D\text{-}max,}}$ Non-Darcy Flow (In-House Simulator)	0.237	0.351	0.41
$\mathbf{I_{x\text{-}opt,}}$ Non-Darcy Flow (Equation 5.59)	0.04	0.14	0.22
$\mathbf{J_{D\text{-}max,}}$ Non-Darcy Flow (Equation 5.58)	0.24	0.341	0.395
$\mathbf{R_{ew\text{-}opt}}$	17.95	14	12.7
Comment	SS	SS	SS

Table 5.1: Optimized Geometries in this study.

	OPT-4	OPT-5
Matrix core	Texas Cream k=9.1mD β=3.927E+9	Texas Cream k=9.1mD β=3.927E+9
Fluid Type	Single Phase	Single Phase
k_f/D	146	146
β_f/m^{-1}	3.511E+5	3.511E+5
Reservoir length, X_e	200	200
Formation Thickness/m	10	10
GTR_w	1	1
Well Flow Rate, ms^{-1} (Darcy)	1^{-5}	1^{-5}
Absolute Proppant number, N_P	0.5	1.5
$\mathbf{I_{x\text{-}opt}}$, Darcy Flow (In-house Simulator & Equation 3.59)	0.53	0.77
$\mathbf{J_{D\text{-}max}}$, Darcy Flow (In-house Simulator & Equation 3.58)	0.71	1.023
Base Proppant number, N_{Pb}	--	--
Well Flow Rate, ms^{-1} (Non-Darcy)	5^{-3}	5^{-3}
effective Proppant number, N_{Peff}	0.0806	0.326
$\mathbf{I_{x\text{-}opt,}}$ Non-Darcy Flow (In-House Simulator)	0.22	0.43
$\mathbf{J_{D\text{-}max,}}$ Non-Darcy Flow (In-House Simulator)	0.45	0.645
$\mathbf{I_{x\text{-}opt,}}$ Non-Darcy Flow (Equation 5.59)	0.22	0.43
$\mathbf{J_{D\text{-}max,}}$ Non-Darcy Flow (Equation 5.58)	0.44	0.63
$\mathbf{R_{ew\text{-}opt}}$	5.2	3.6
Comment	PSS	PSS

Table 5.1: Optimized Geometries in this study.

	OPT-6	OPT-7	OPT-8
Matrix core	Texas Cream k=9.1mD β=3.927E+9	Texas Cream k=9.1mD β=3.927E+9	Texas Cream k=9.1mD β=3.927E+9
Fluid Type	Two Phase	Two Phase	Two Phase
k_f/D	146	146	146
β_f/m^{-1}	3.511E+5	3.511E+5	3.511E+5
Reservoir length, X_e	200	200	200
Formation Thickness/m	10	10	10
Pressure Drop, DP/psi	200	500	950
GTR_w	0.71	0.81	0.91
Absolute Proppant number, N_P	0. 5	0.5	0.5
$\mathbf{I_{x\text{-}opt}}$, Darcy Flow (In-house Simulator & Equation 3.59)	1	1	1
Base Proppant number, N_{Pb}	0.99	0.96	0.91
effective Proppant number, N_{Peff}	0.3124	0.185	0.1
$\mathbf{I_{x\text{-}opt,}}$ Two-Phase Flow (In-House Simulator)	0.45	0.35	0.27
$\mathbf{I_{x\text{-}opt,}}$ Two-Phase Flow (Equation 5.59)	0.45	0.35	0.27
$\mathbf{R_{ew\text{-}opt}}$	2.58	4.23	8
Comment	SS	SS	SS

Table 5.1: Optimized Geometries in this study.

	OPT-9	OPT-10	OPT-11
Matrix core	Texas Cream k=9.1mD β=3.927E+9	Texas Cream k=9.1mD β=3.927E+9	Texas Cream k=9.1mD β=3.927E+9
Fluid Type	Two Phase	Two Phase	Two Phase
k_f/D	146	146	146
β_f/m^{-1}	3.511E+5	3.511E+5	3.511E+5
Reservoir length, X_e	200	200	200
Formation Thickness/m	10	10	10
Pressure Drop, DP/psi	100	200	400
GTR_w	0.81	0.81	0.81
Absolute Proppant number, N_P	0. 5	0.5	0.5
$\mathbf{I_{x\text{-}opt}}$, Darcy Flow (In-house Simulator & Equation 3.59)	1	1	1
$\mathbf{J_{D\text{-}max}}$, Darcy Flow (In-house Simulator & Equation 3.58)	0.87	0.87	0.87
Base Proppant number, N_{Pb}	0.978	0.978	0.978
effective Proppant number, N_{Peff}	0.439	0.329	0.225
$\mathbf{I_{x\text{-}opt,}}$ Two-Phase Flow (In-House Simulator)	0.53	0.45	0.39
$\mathbf{J_{D\text{-}max,}}$ Two-Phase Flow (In-House Simulator)	0.63	0.58	0.535
$\mathbf{I_{x\text{-}opt,}}$ Two-Phase Flow (Equation 5.59)	0.53	0.45	0.39
$\mathbf{J_{D\text{-}max,}}$ Two-Phase Flow (Equation 5.58)	0.62	0.56	0.51
$\mathbf{R_{ew\text{-}opt}}$	1.23	1.97	3.34
Comment	SS	SS	SS

Table 5.1: Optimized Geometries in this study.

	OPT-12	OPT-13	OPT-14
Matrix core	Texas Cream k=9.1mD β=3.927E+9	Texas Cream k=9.1mD β=3.927E+9	Texas Cream k=9.1mD β=3.927E+9
Fluid Type	Two Phase	Two Phase	Two Phase
k_f/D	146	146	146
β_f/m^{-1}	3.511E+5	3.511E+5	3.511E+5
Reservoir length, X_e	200	200	200
Formation Thickness/m	10	10	10
GTR_w	0.81	0.81	0.81
Well Flow Rate, ms^{-1}	1^{-5}	1^{-4}	1^{-3}
Absolute Proppant number, N_P	0.5	0.5	0.5
Base Proppant number, N_{Pb}	0.97	0.97	0.97
effective Proppant number, N_{Peff}	0.97	0.526	0.169
$\mathbf{I_{x\text{-}opt,}}$ Non-Darcy Flow (In-House Simulator)	0.67	0.55	0.31
$\mathbf{J_{D\text{-}max,}}$ Non-Darcy Flow (In-House Simulator)	0.86	0.71	0.54
$\mathbf{I_{x\text{-}opt,}}$ Non-Darcy Flow (Equation 5.59)	0.67	0.55	0.31
$\mathbf{J_{D\text{-}max,}}$ Non-Darcy Flow (Equation 5.58)	0.88	0.72	0.53
$\mathbf{R_{ew\text{-}opt}}$	0.01	0.84	4.7
Comment	PSS	PSS	PSS

Table 5.2: Properties of the mixture C1-C4, %C1: 73.6%, P_{Dew}=1865 psi.

P(psi)	**x1**	**y1**	ρ_c **(kg/m^3)**	ρ_g **(kg/m^3)**	μ_c **cp**	μ_g **cp**	**IFT mN.m**
1865	0.4195	0.4195	223.3	223.3	0.0261	0.0261	0
1850	0.3521	0.5049	307.5	220.5	0.0398	0.0255	0.008
1840	0.343	0.5146	317.4	211.4	0.0405	0.0249	0.036
1800	0.3069	0.5535	341.1	188.7	0.0431	0.0211	0.112
1790	0.3018	0.5583	345.1	184.8	0.0474	0.0206	0.149
1750	0.2814	0.5776	359.5	171.3	0.0462	0.0195	0.2809
1700	0.2609	0.5944	374.7	157.4	0.0491	0.0184	0.4318
1650	0.2444	0.6088	387	146.5	0.052	0.0176	0.5785
1600	0.2279	0.6232	397.8	137.8	0.0549	0.017	0.7329
1565	0.2192	0.6297	404	132.6	0.0601	0.0172	0.852
1500	0.203	0.6418	421.76	118.39	0.0608	0.016	1.1106
1400	0.1821	0.655	438.62	106.44	0.0669	0.0152	1.5938
1250	0.154	0.6664	459.64	91.27	0.0762	0.0144	2.3971
1200	0.1452	0.669	466.06	86.68	0.0793	0.0141	2.6907
1000	0.1136	0.6712	487.63	69.89	0.0908	0.0133	3.9239
800	0.0859	0.664	505.63	54.71	0.1015	0.0126	5.2907
600	0.0604	0.6335	522.29	41.17	0.1121	0.012	6.8104
500	0.0484	0.605	530.06	34.86	0.1173	0.0117	7.6186
400	0.0368	0.5636	537.53	28.78	0.1234	0.0114	8.4582
300	0.0257	0.4985	544.48	22.93	0.1283	0.0111	9.3119
200	0.0152	0.3948	551.22	17.16	0.133	0.0106	10.2085
150	0.01	0.3128	554.66	14.33	0.1356	0.0101	10.6795
100	0.0049	0.1901	557.94	11.55	0.1383	0.0094	11.15
80	0.0029	0.123	559.11	10.45	0.1393	0.009	11.3299

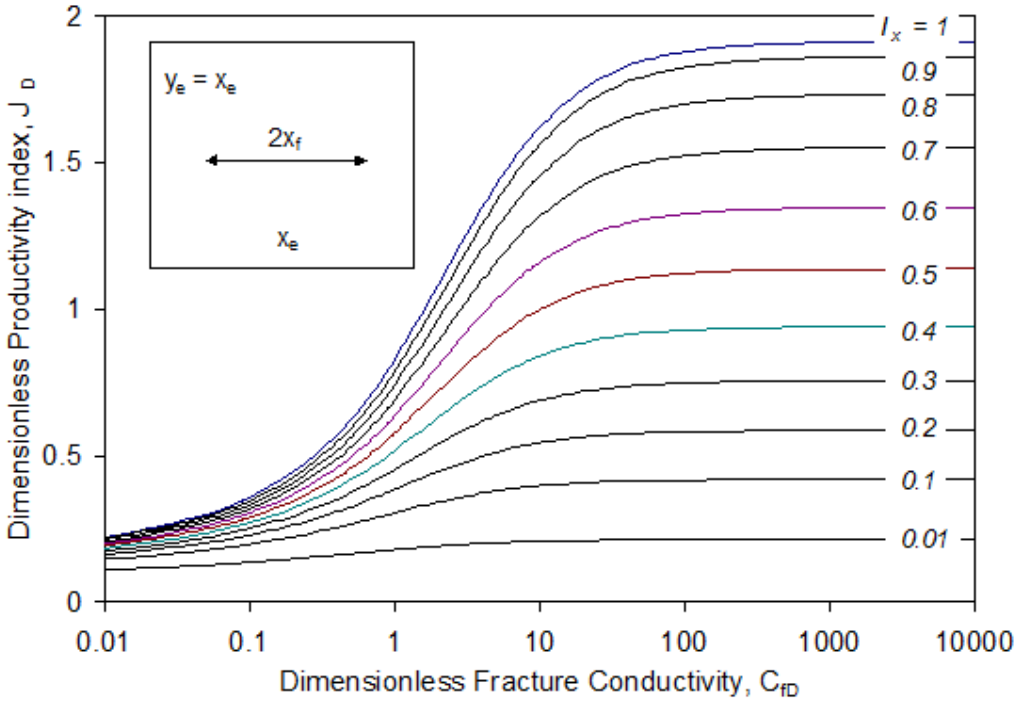

Figure 5.1 Dimensionless productivity index as a function of penetration ratio and fracture conductivity, *(From Valko 2006)*.

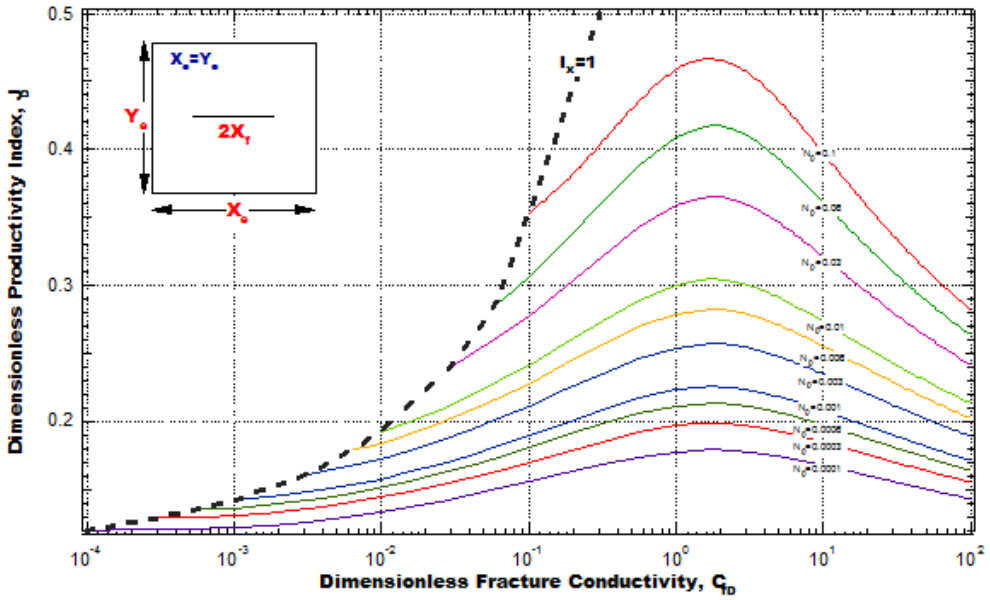

Figure 5.2a Maximum Dimensionless productivity index and optimum fracture conductivity for different prropant numbers N_P<0.1, *(From Valko 2006)*.

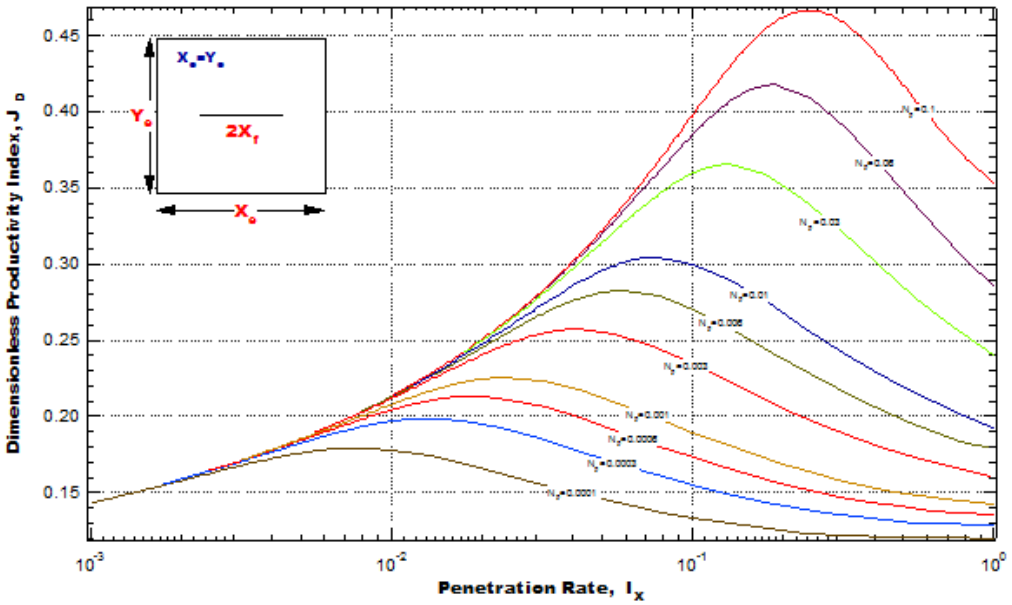

Figure 5.2b Maximum Dimensionless productivity index and optimum penetration ratio for different prropant numbers N_P<0.1, *(From Valko 2006)*.

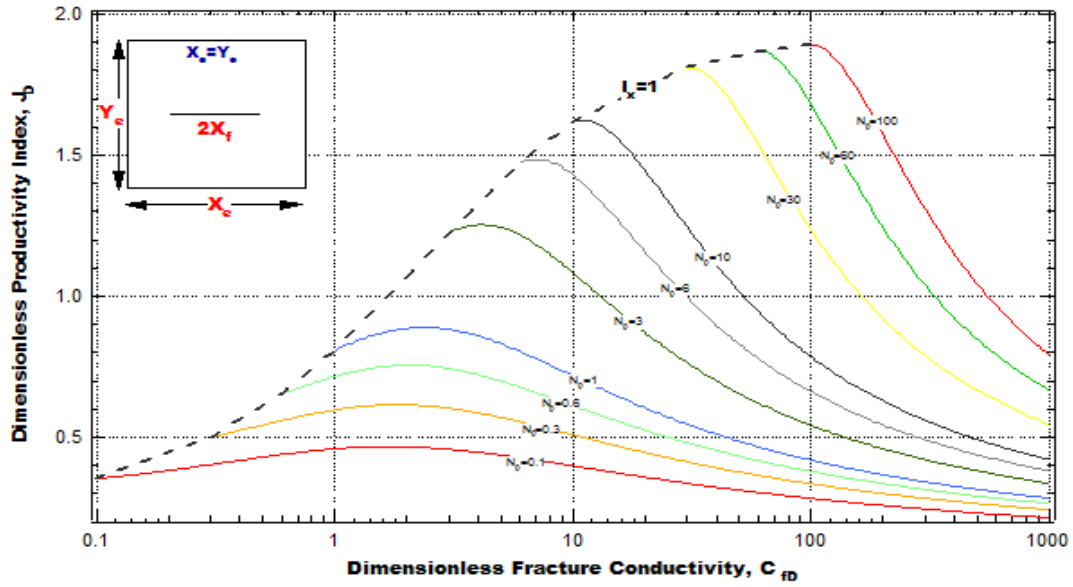

Figure 5.3 Maximum Dimensionless productivity index and optimum fracture conductivity for different prropant numbers N_P>0.1, *(From Valko 2006).*

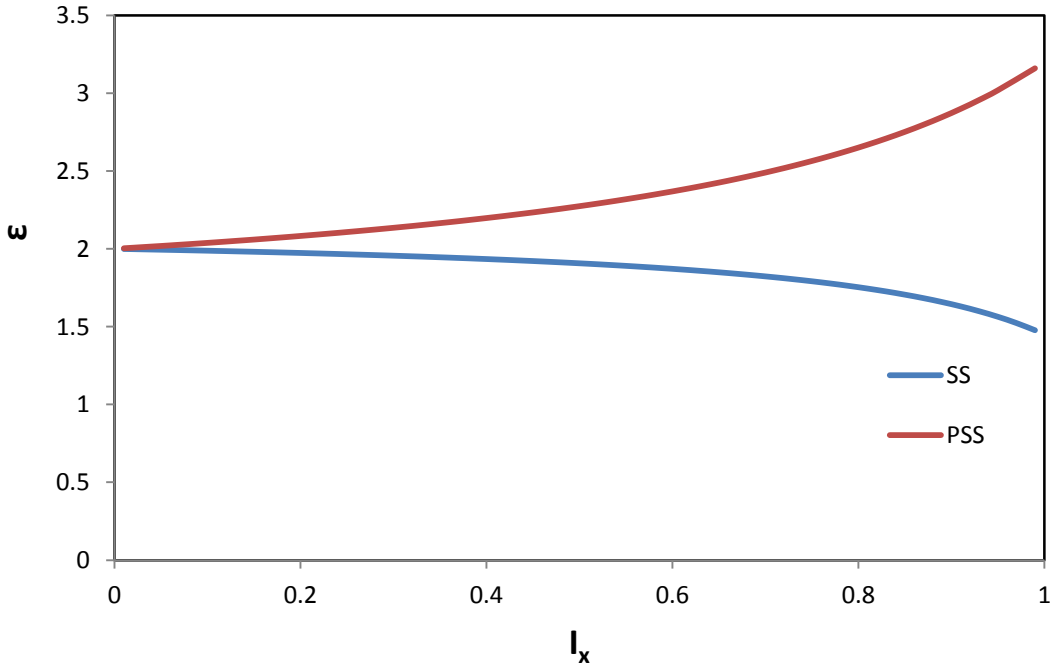

Figure 5.4 Variation of the reciprocal effective wellbore radius (**ε**) with penetration ratio.

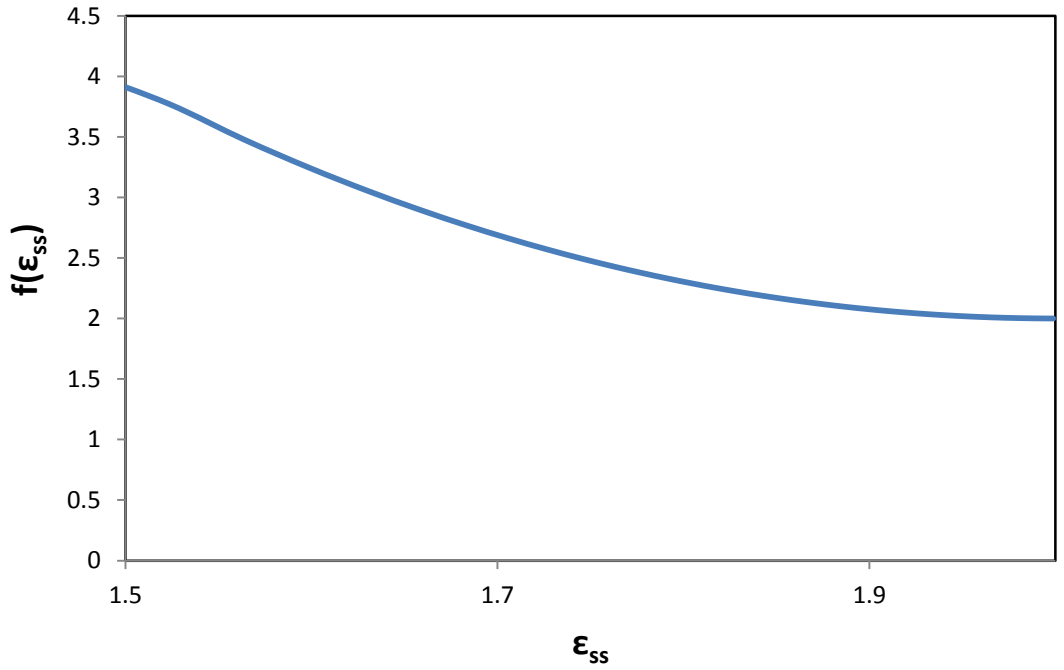

Figure 5.5 Variation of the function f($\boldsymbol{\varepsilon}_{ss}$) with the reciprocal effective wellbore radius ($\boldsymbol{\varepsilon}_{ss}$) under steady state conditions (SS).

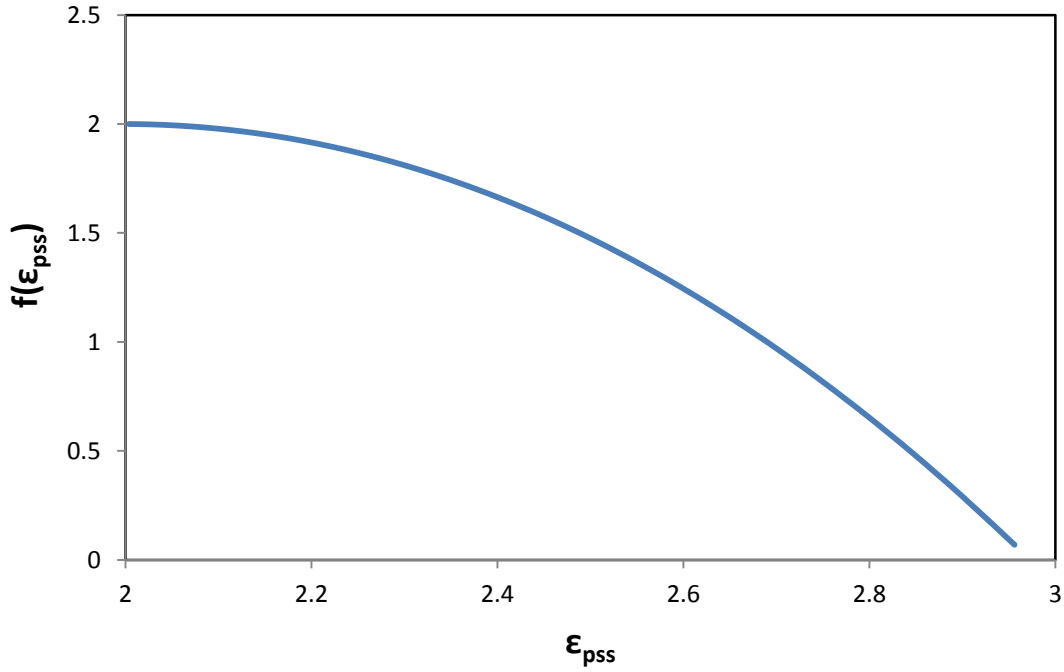

Figure 5.6 Variation of the function f($\boldsymbol{\varepsilon}_{pss}$) with the reciprocal effective wellbore radius ($\boldsymbol{\varepsilon}_{pss}$) under pseudo-steady state conditions (PSS).

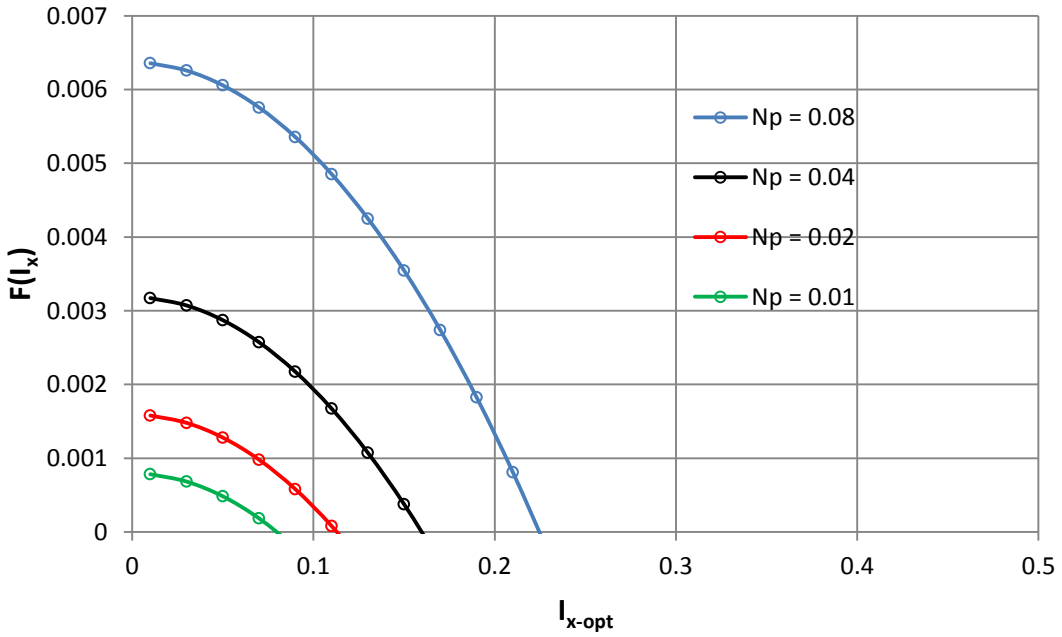

Figure 5.7 Optimum penetration ratio for different proppant numbers 0.01 <N_P> 0.08 under Darcy flow and SS condition using Equations 5.29.

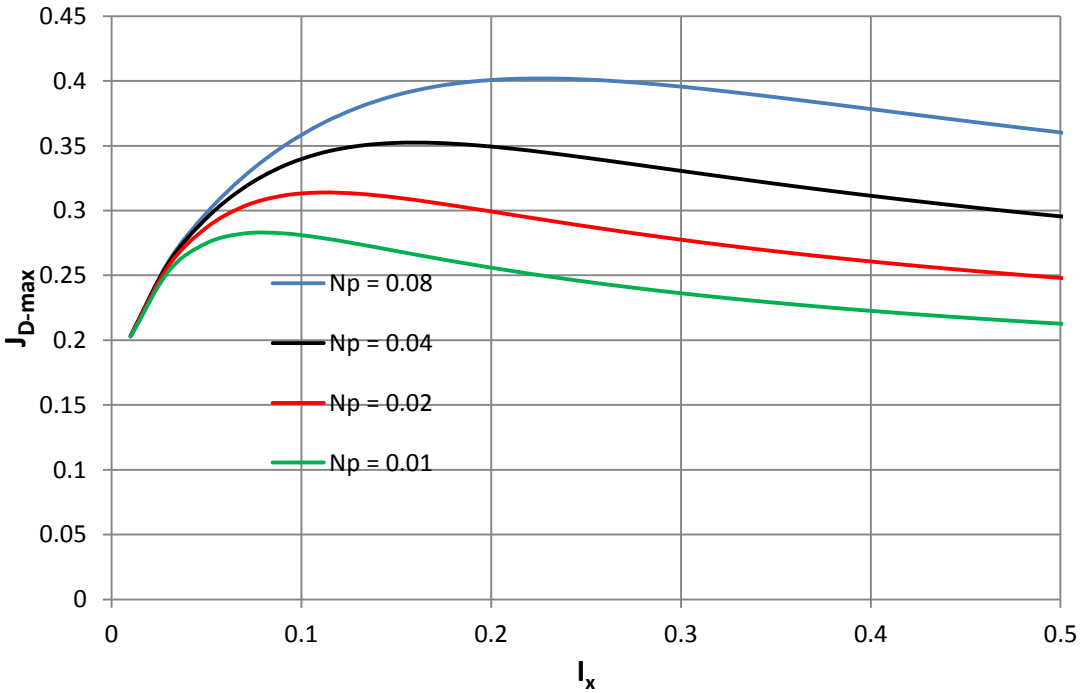

Figure 5.8 Maximum dimensionless productivity index and optimum penetration ratio for different proppant numbers 0.01 <N_P> 0.08 under Darcy flow and SS condition using Equation 5.28.

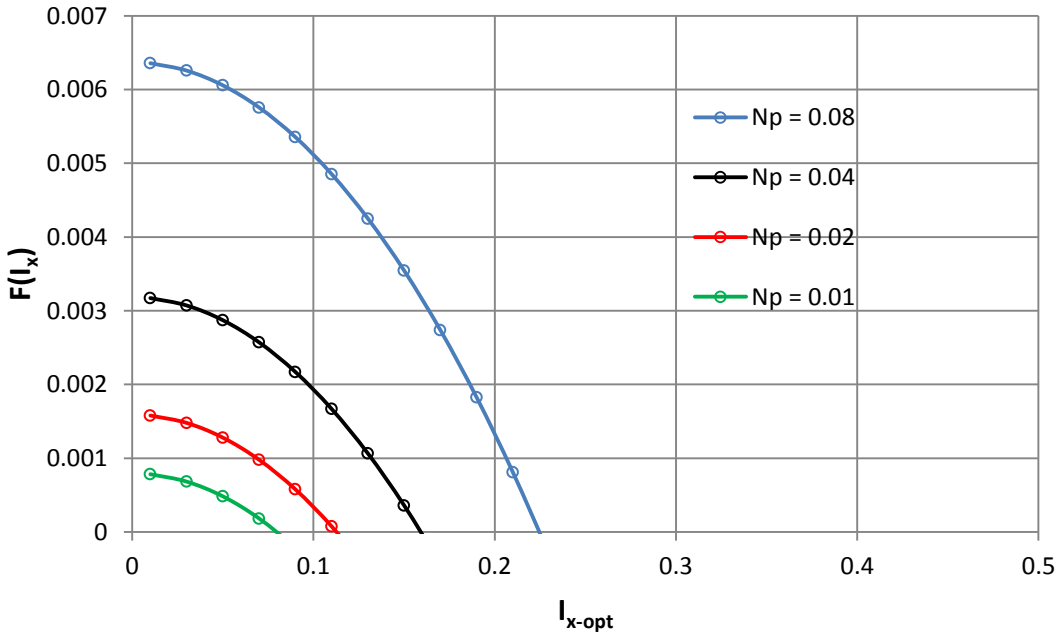

Figure 5.9 Optimum penetration ratio for different proppant numbers 0.01 <N_P> 0.08 under Darcy flow and PSS condition using Equation 5.29.

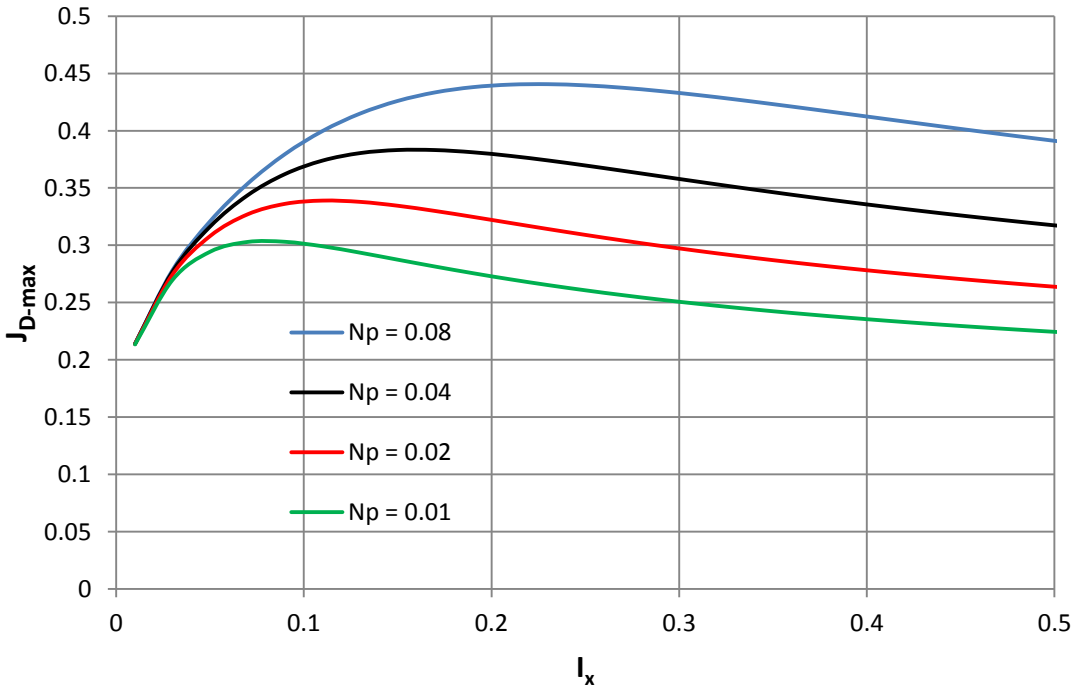

Figure 5.10 Maximum dimensionless productivity index and optimum penetration ratio for different proppant numbers 0.01 <N_P> 0.08 under Darcy flow and PSS condition using Equation 5.28.

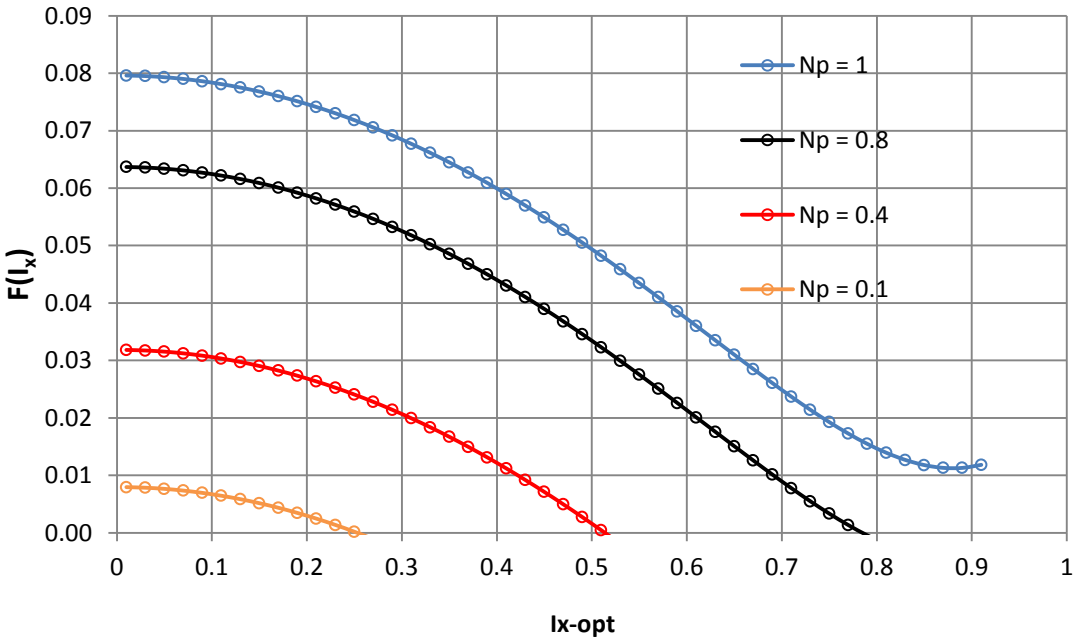

Figure 5.11 Optimum penetration ratio for different proppant numbers 0.1 <N_P> 1 under Darcy flow and SS condition using Equations 5.29.

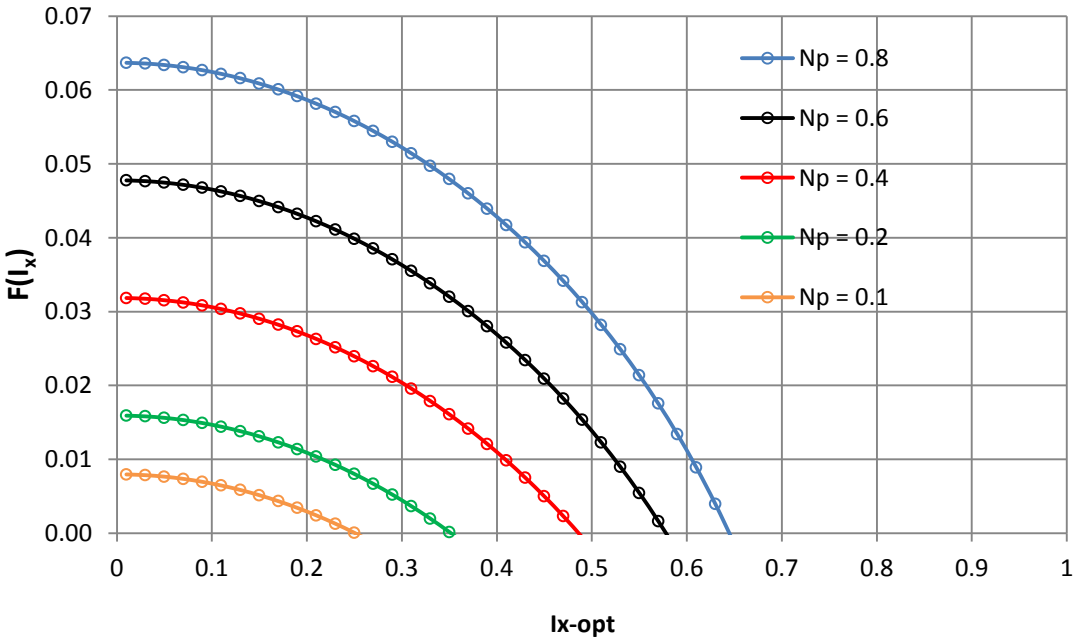

Figure 5.12 Optimum penetration ratio for different proppant numbers 0.1 <N_P> 1 under Darcy flow and PSS condition using Equations 5.29.

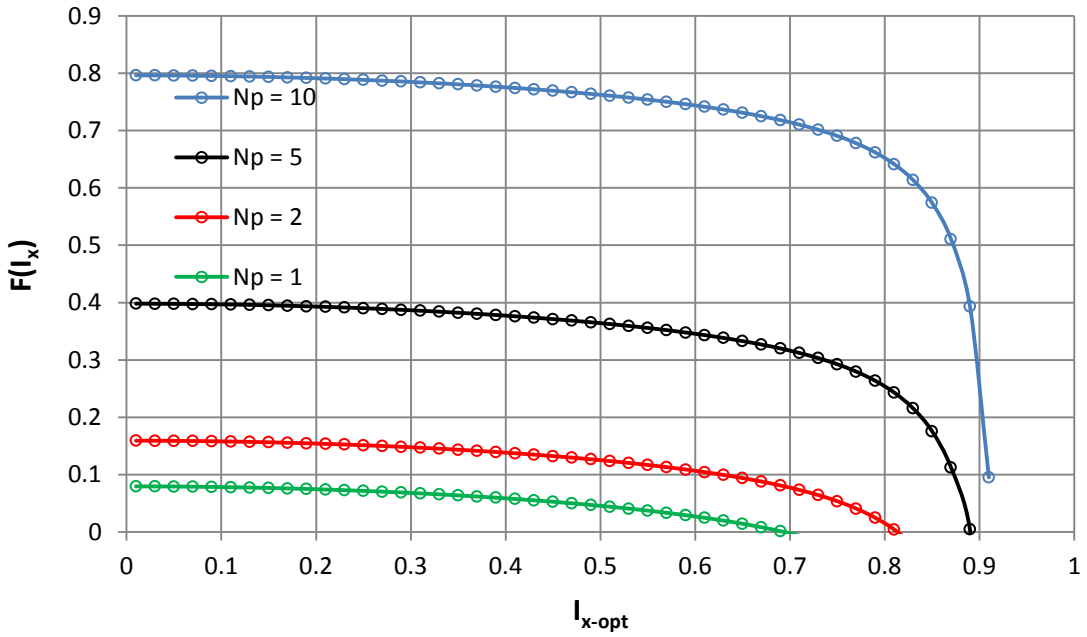

Figure 5.13 Optimum penetration ratio for different proppant numbers 1 <N_P> 10 under Darcy flow and SS condition using Equations 5.29.

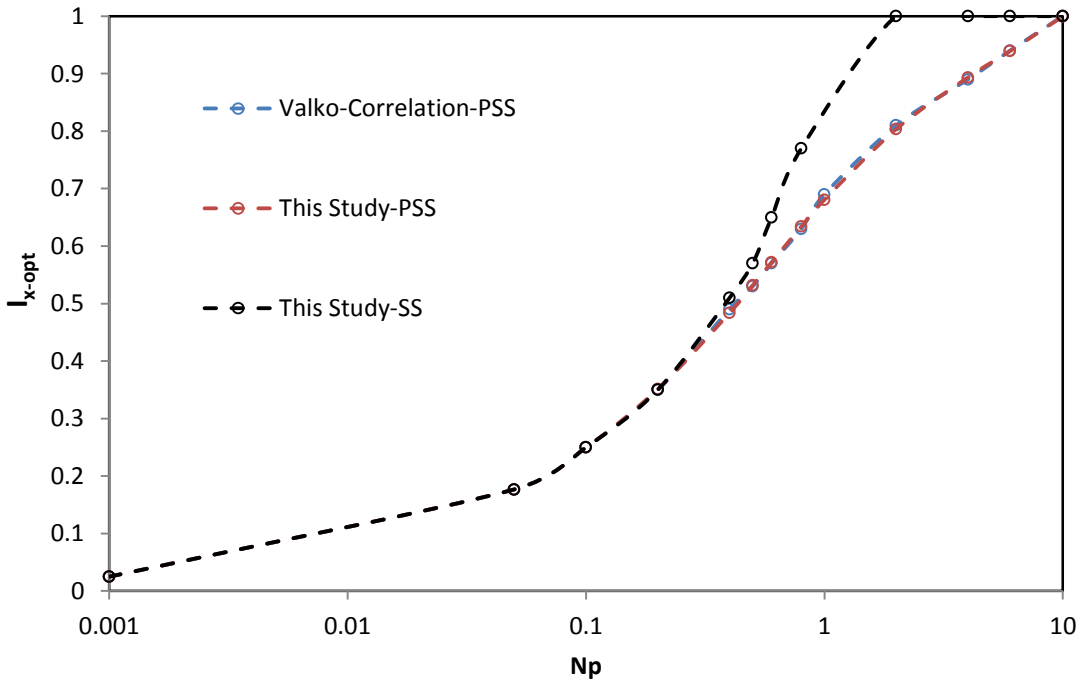

Figure 5.14 Comparison of optimum penetration ratio using this study formulation (Equations 5.29) with Valko and Economides correlation (Equations 5.1a) for PSS conditions.

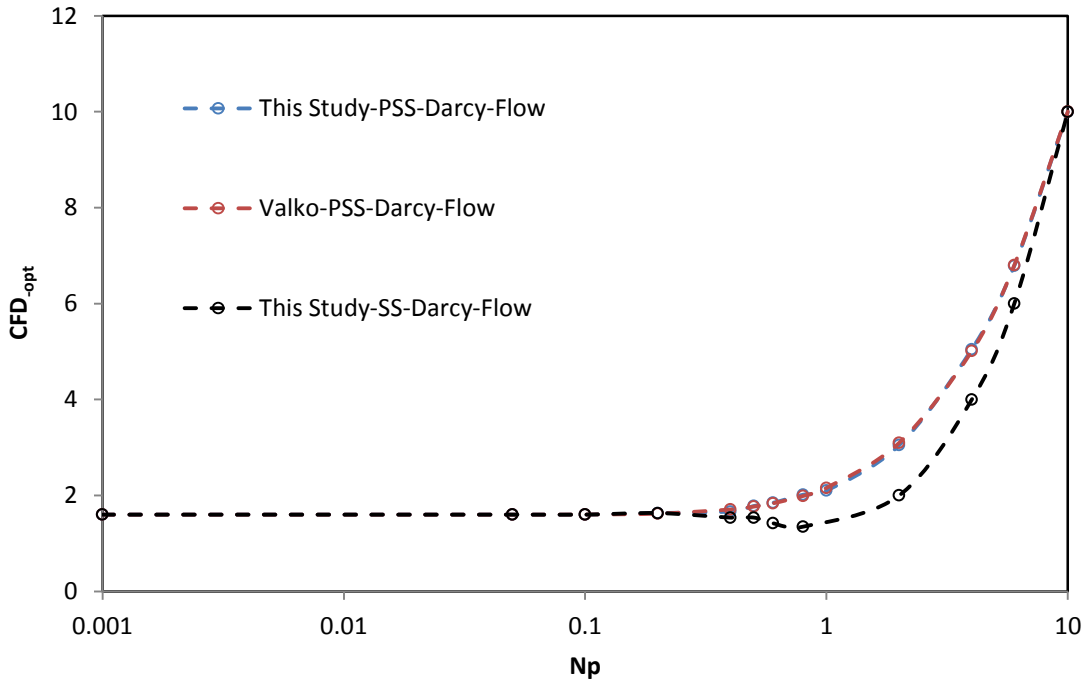

Figure 5.15 Comparison of optimum dimensionless fracture conductivity using this study formulation (Equations 5.29) with Valko and Economides correlation (Equations 5.1a) for PSS conditions.

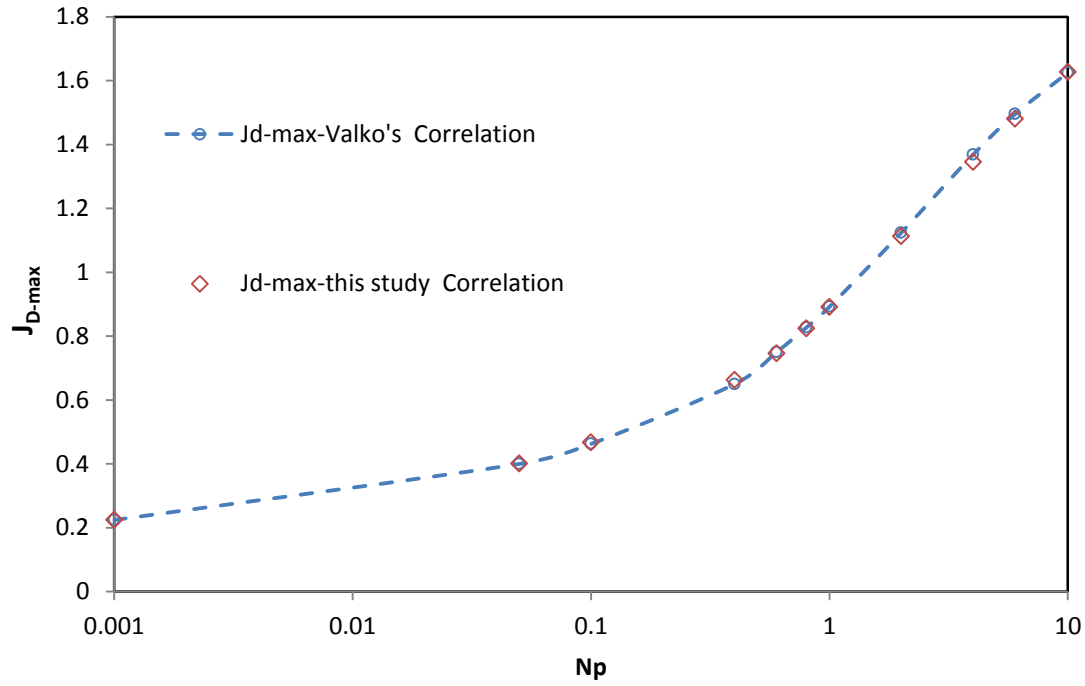

Figure 5.16 Comparison of maximum achievable dimensionless productivity using this study formulation (Equations 5.28) with Valko and Economides correlation (Equations 5.1a) for PSS conditions.

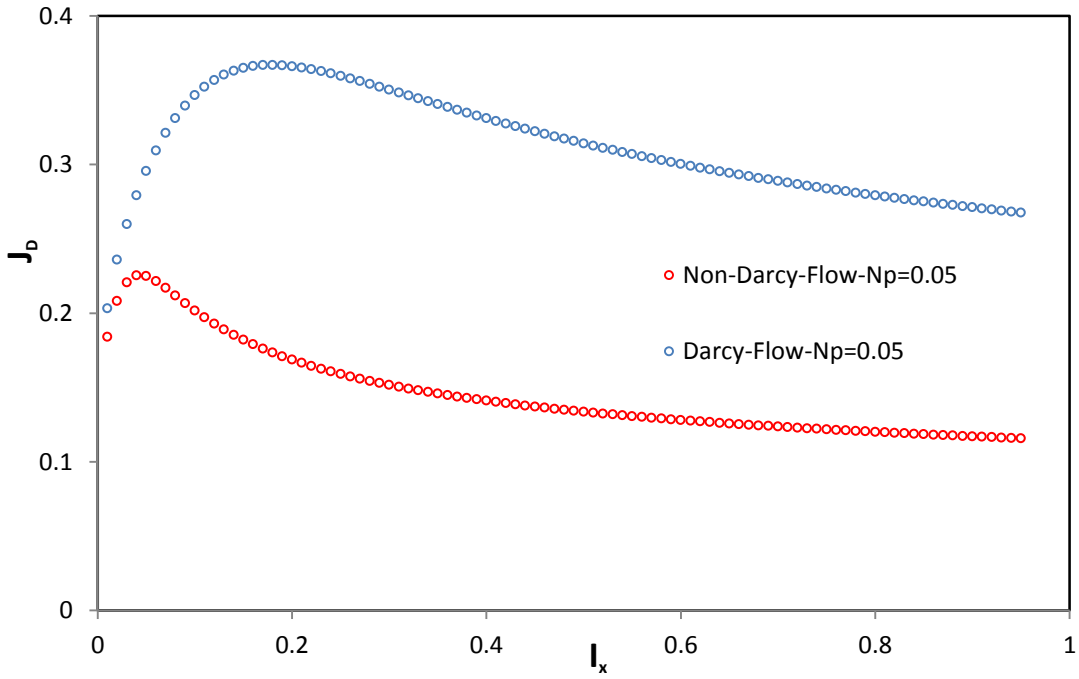

Figure 5.17 Dimensionless productivity index for a proppant number of 0.05 with different fracture geometries using in-house simulator for Darcy and Non-Darcy flow SS conditions, OPT-1 data set Table 5.1.

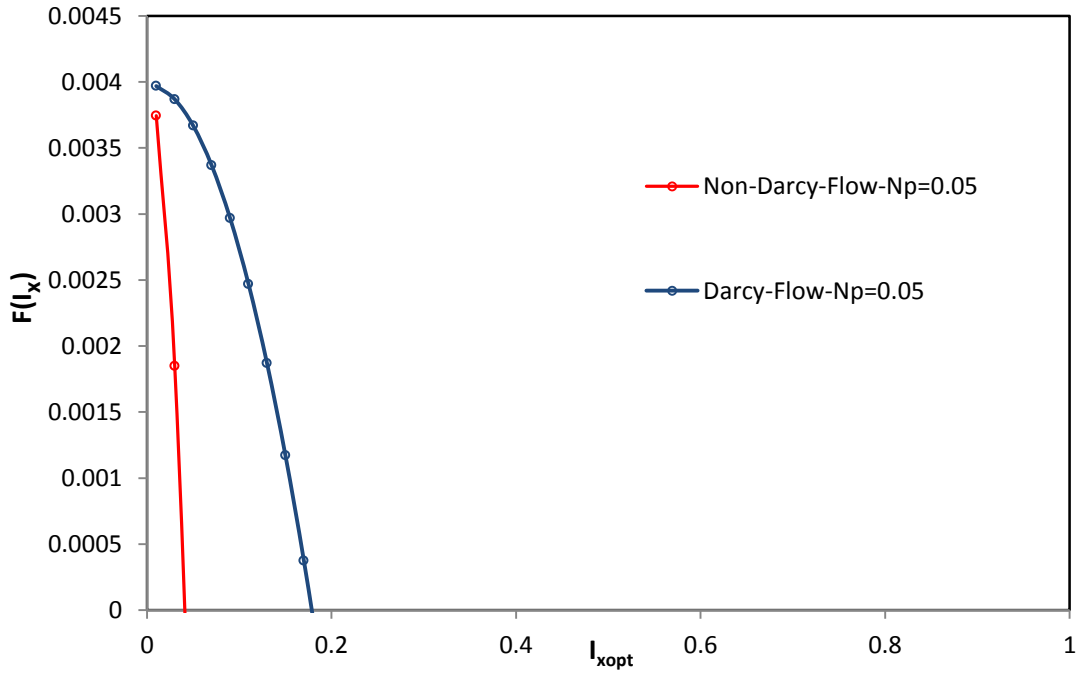

Figure 5.18 Optimum penetration ratio for a proppant number of 0.05 using Equation 5.59 for Darcy and Non-Darcy flow SS conditions, OPT-1 data set Table 5.1.

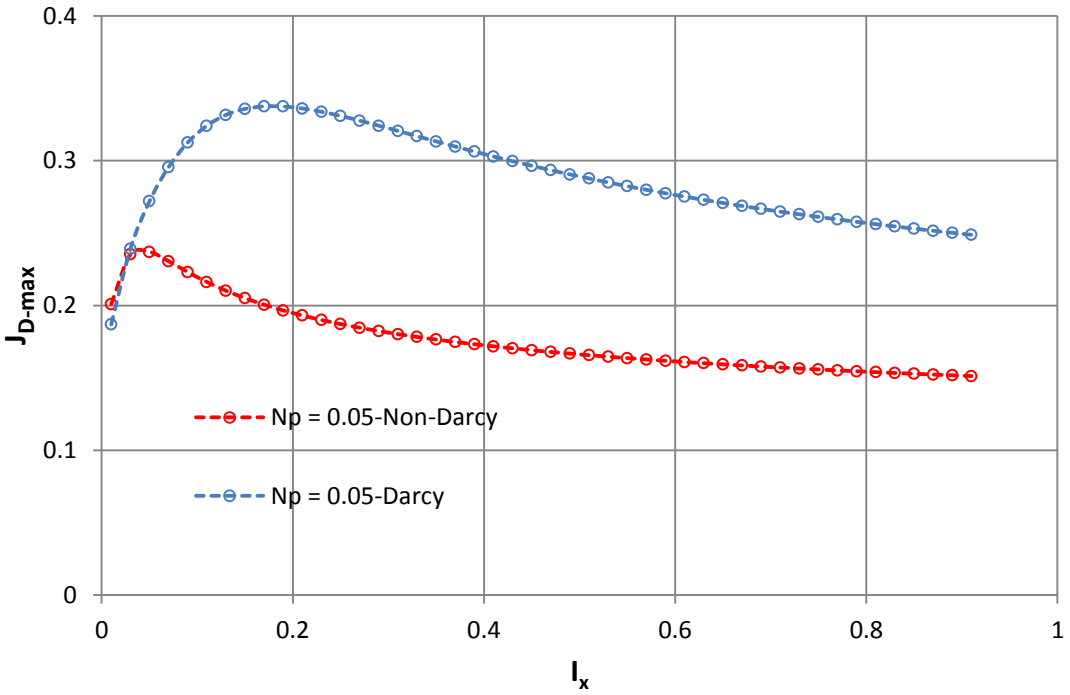

Figure 5.19 Dimensionless productivity index for a proppant number of 0.05 with different fracture geometries using Equation 5.58 for Darcy and Non-Darcy flow SS conditions, OPT-1 data set Table 5.1.

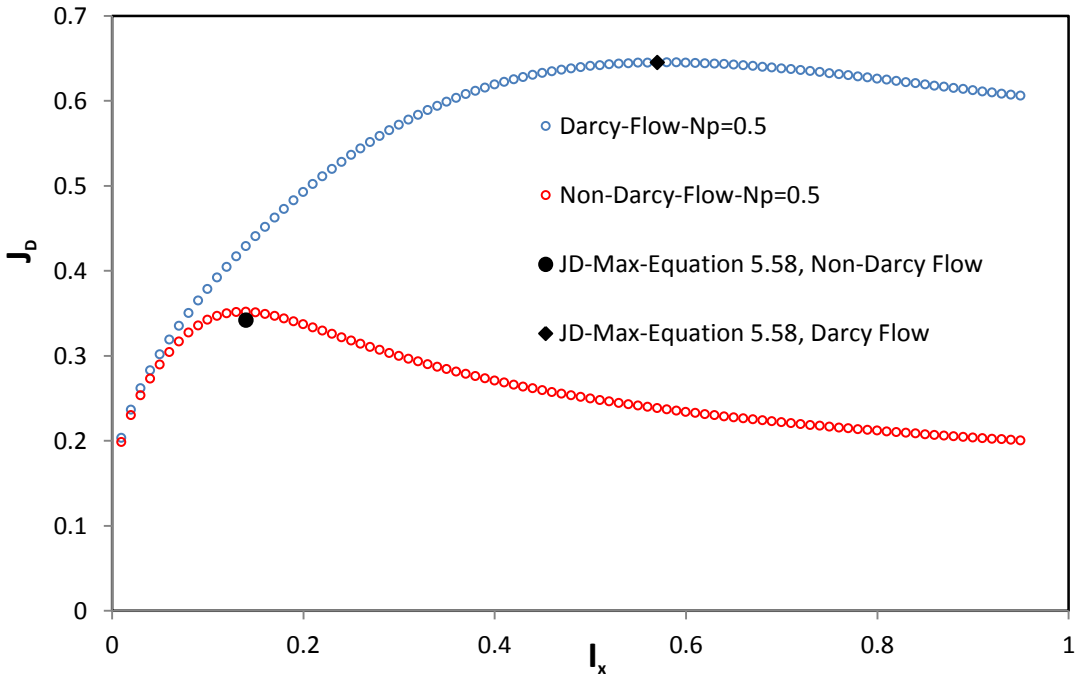

Figure 5.20 Dimensionless productivity index for a proppant number of 0.5 with different fracture geometries using in-house simulator and Equation 5.58 for Darcy and Non-Darcy flow SS conditions, OPT-2 data set Table 5.1.

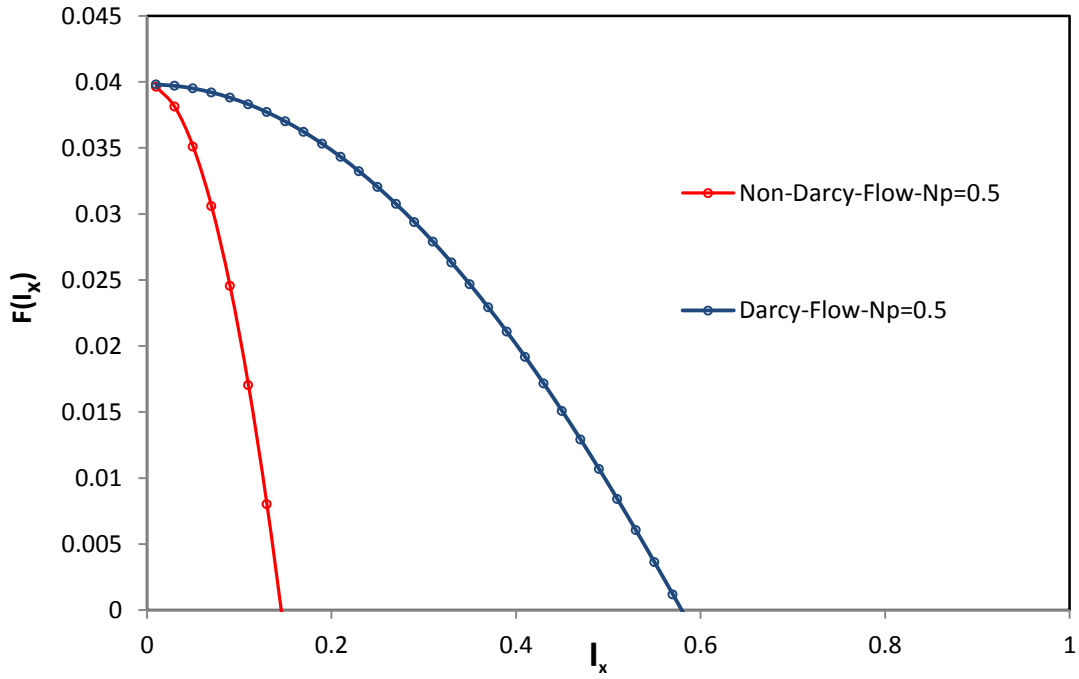

Figure 5.21 Optimum penetration ratio for a proppant number of 0.5 using Equation 5.59 for Darcy and Non-Darcy flow SS conditions, OPT-2 data set Table 5.1.

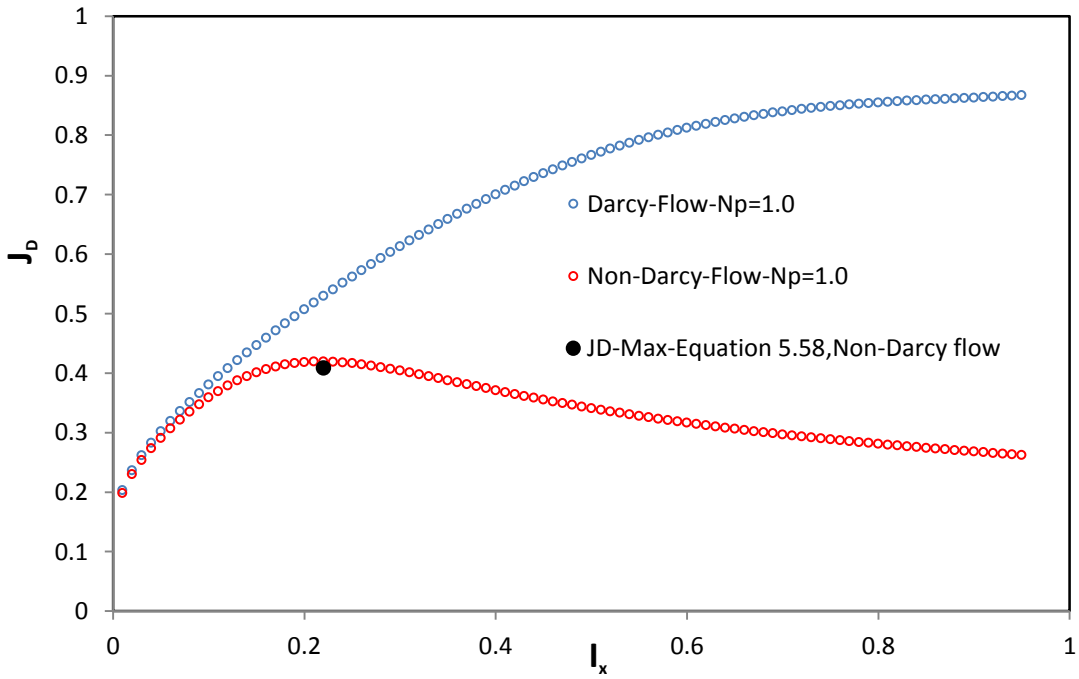

Figure 5.22 Dimensionless productivity index for a proppant number of 1 with different fracture geometries using in-house simulator and Equation 5.58 for Darcy and Non-Darcy flow SS conditions, OPT-3 data set Table 5.1.

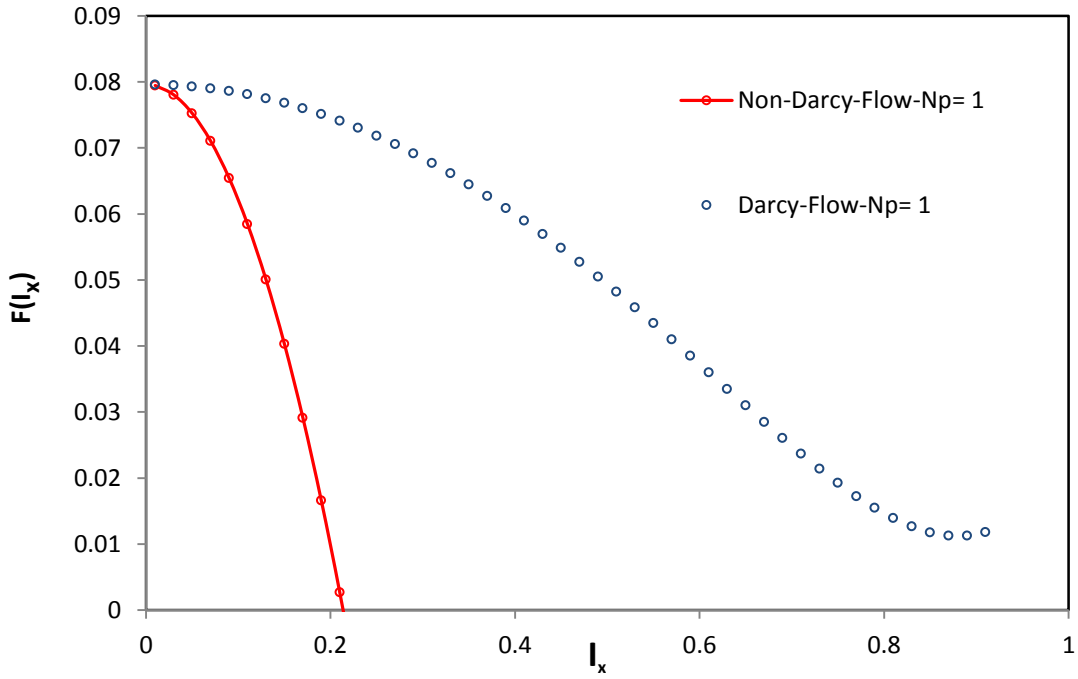

Figure 5.23 Optimum penetration ratio for a proppant number of 1 using Equation 5.59 for Darcy and Non-Darcy flow SS conditions, OPT-3 data set Table 5.1.

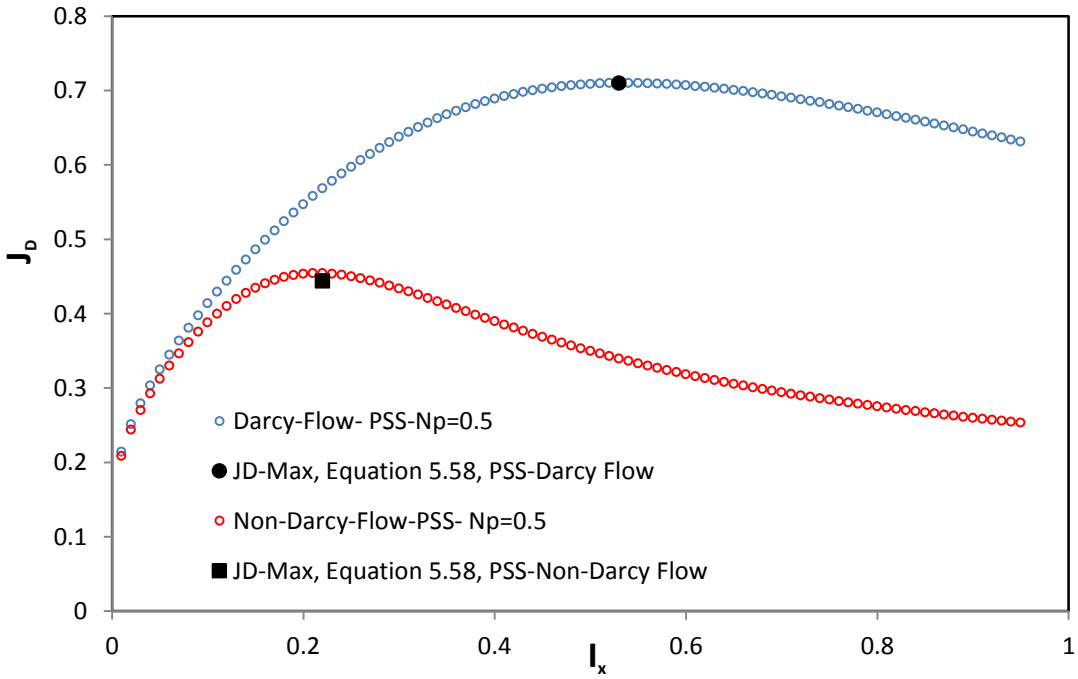

Figure 5.24 Dimensionless productivity index for a proppant number of 0.5 with different fracture geometries using in-house simulator and Equation 5.58 for Darcy and Non-Darcy flow PSS conditions, OPT-4 data set Table 5.1.

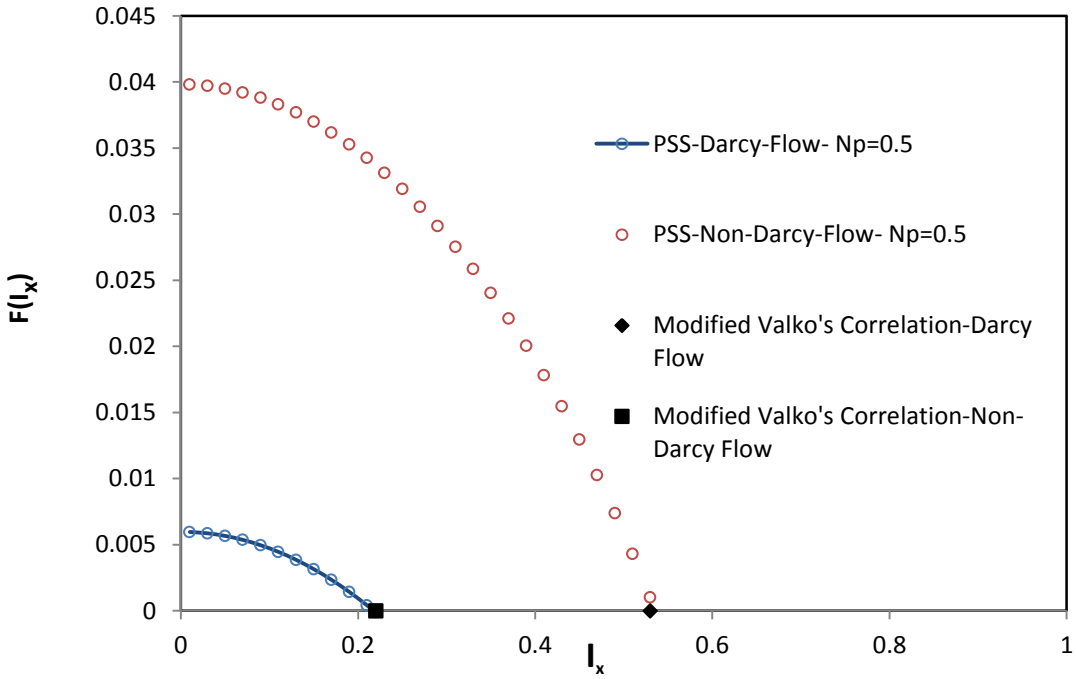

Figure 5.25 Optimum penetration ratio for a proppant number of 0.5 using Equation 5.59 and Modified Valko and Economides formulation Equation 5.61, for Darcy and Non-Darcy flow PSS conditions, OPT-4 data set Table 5.1.

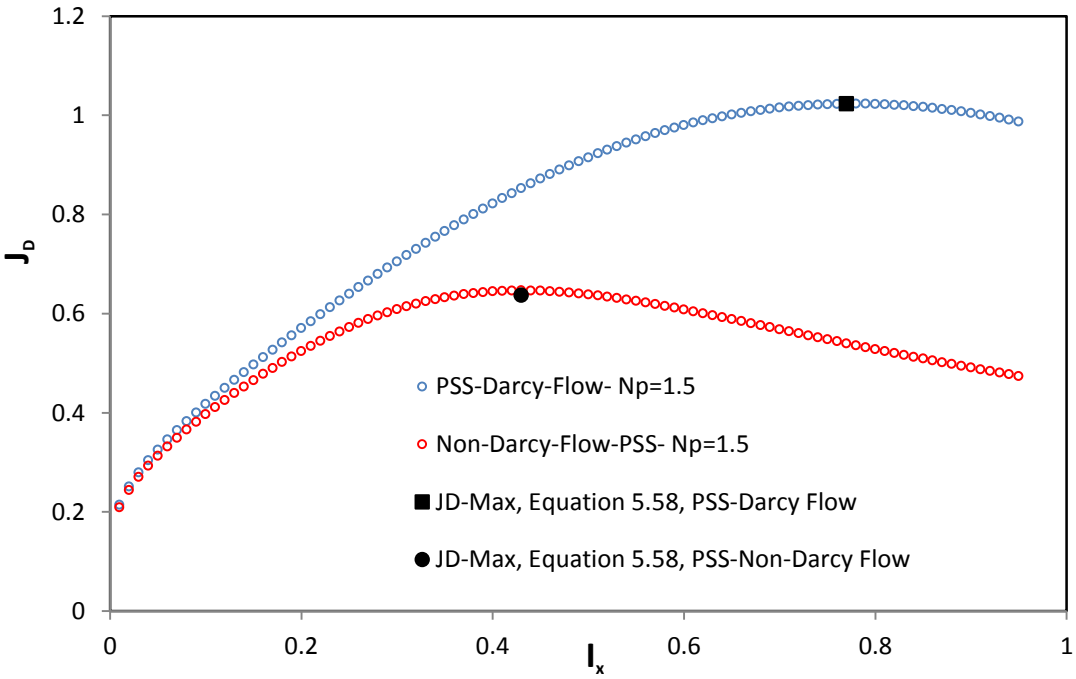

Figure 5.26 Dimensionless productivity index for a proppant number of 1.5 with different fracture geometries using in-house simulator and Equation 5.58 for Darcy and Non-Darcy flow PSS conditions, OPT-5 data set Table 5.1.

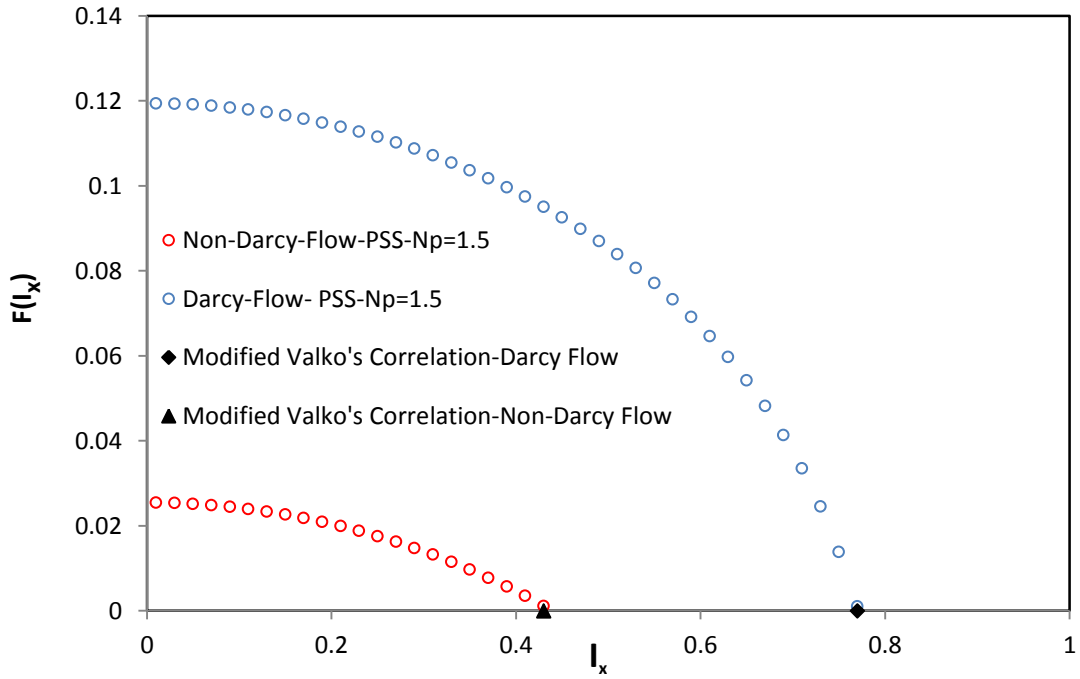

Figure 5.27 Optimum penetration ratio for a proppant number of 1.5 using Equation 5.59 and Modified Valko and Economides formulation Equation 5.61, for Darcy and Non-Darcy flow PSS conditions, OPT-4 data set Table 5.1.

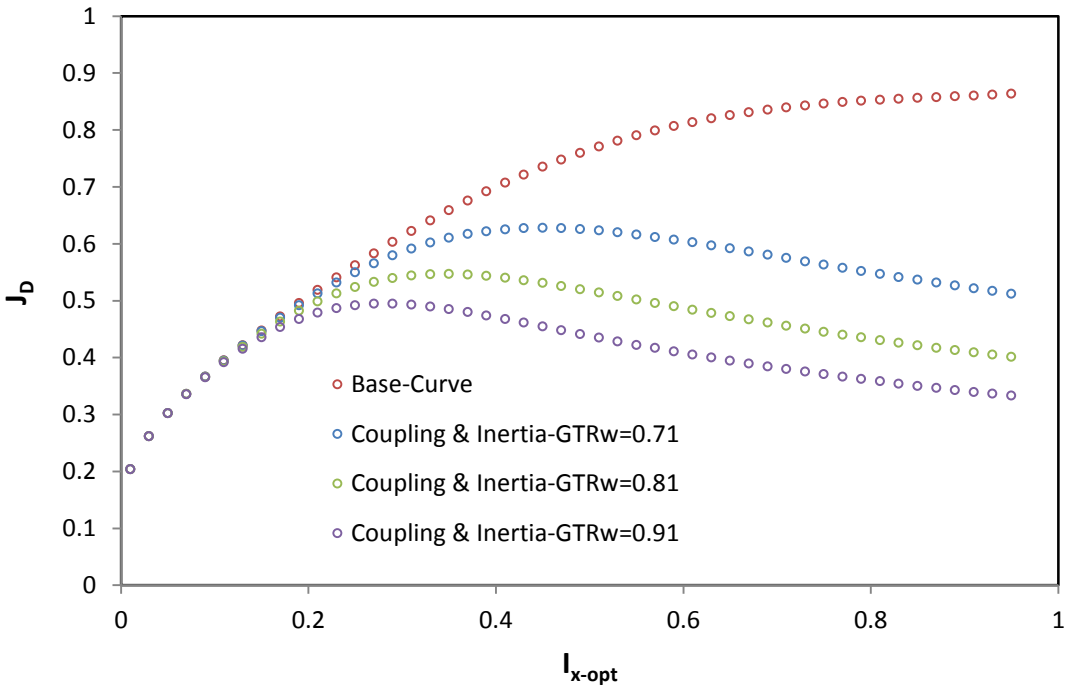

Figure 5.28 Two-phase dimensionless productivity indexes for a proppant number of 0.5 with different fracture geometries using in-house simulator for different GTR_{well} values under SS conditions, OPT-6, 7, and 8 data sets Table 5.1.

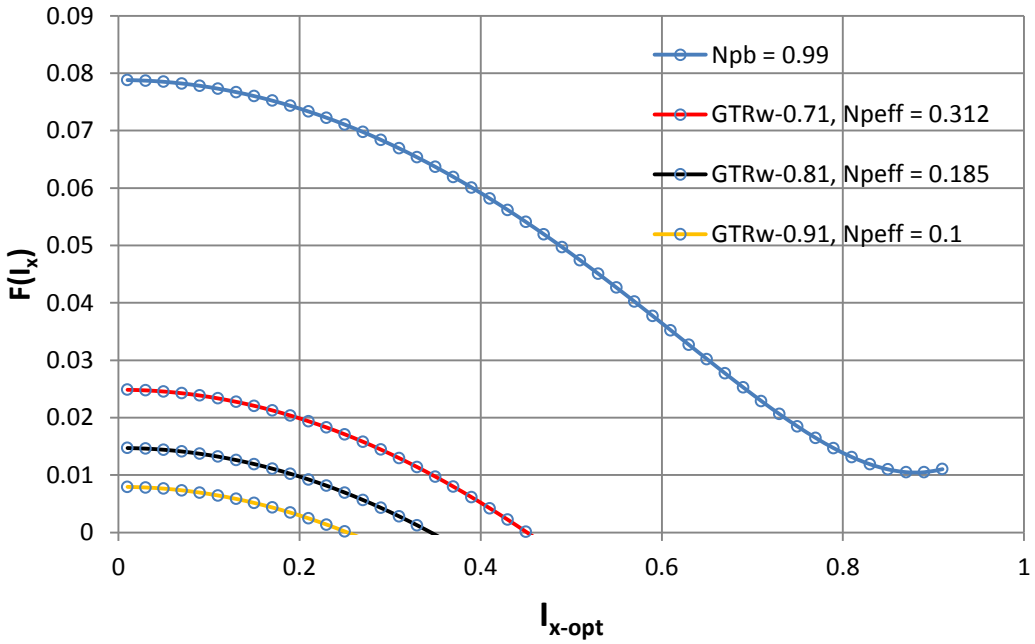

Figure 5.29 Two-phase optimum penetration ratios for a proppant number of 0.5 using equation 5.59 for under SS condition for different GTR_{well} values, OPT-6, 7, and 8 data sets Table 5.1.

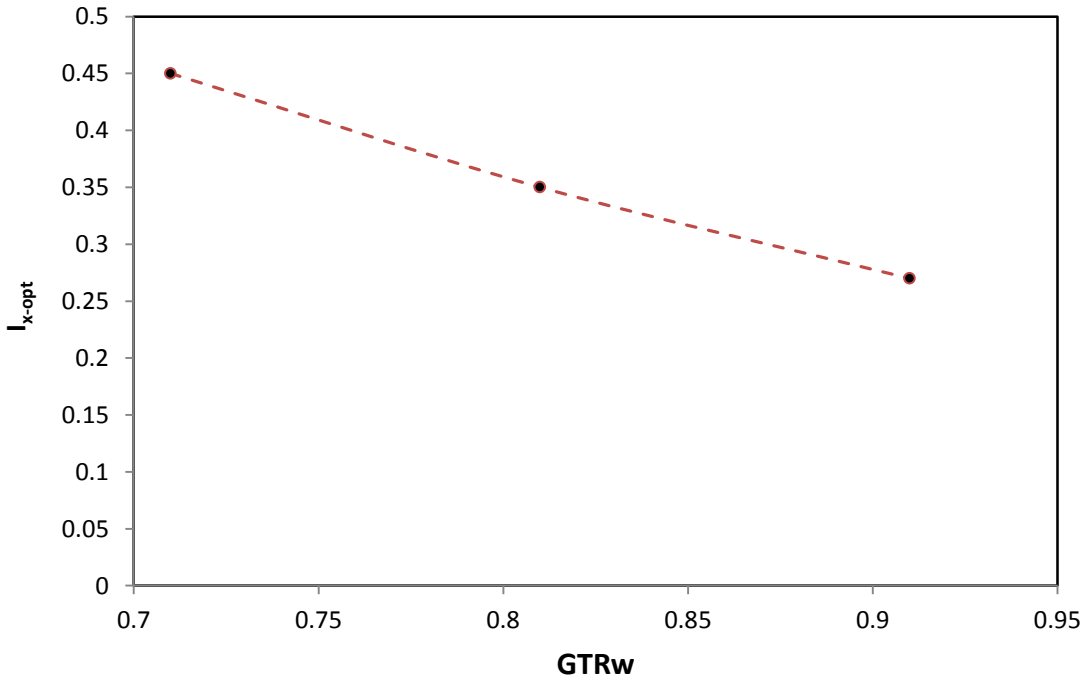

Figure 5.30 variation of optimum penetration ratio with GTR_{well}, for the example shown in Figure 5.28.

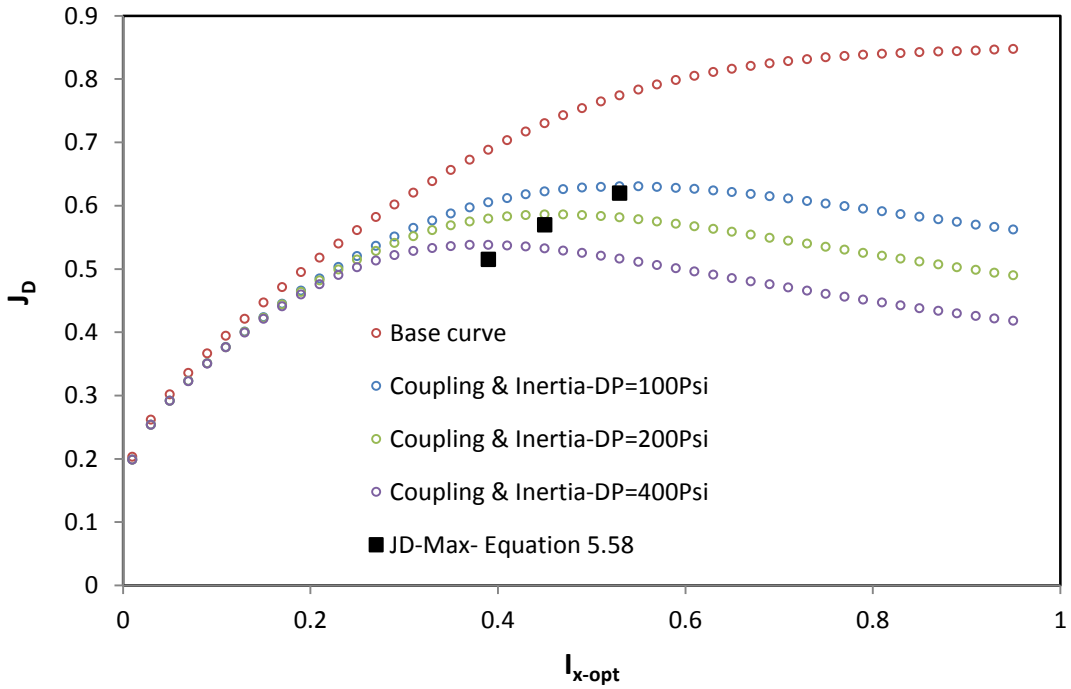

Figure 5.31 Two-phase dimensionless productivity index for a proppant number of 0.5 with different fracture geometries using in-house simulator and Equation 5.58, for SS condition under different pressure drop (DP) values and GTR_{well} = 0.81, OPT-9, 10, and 11 data sets Table 5.1.

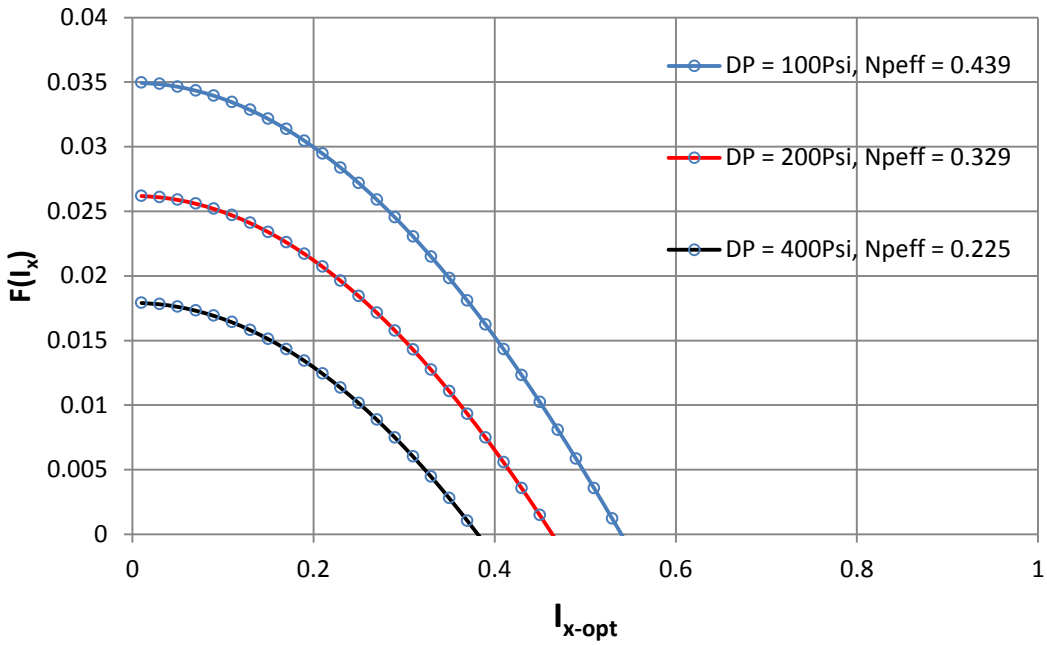

Figure 5.32 Two-phase optimum penetration ratios for a proppant number of 0.5 using Equation 5.59 under SS condition for different DP values and GTR_{well} = 0.8, OPT-9, 10, and 11 data sets Table 5.1.

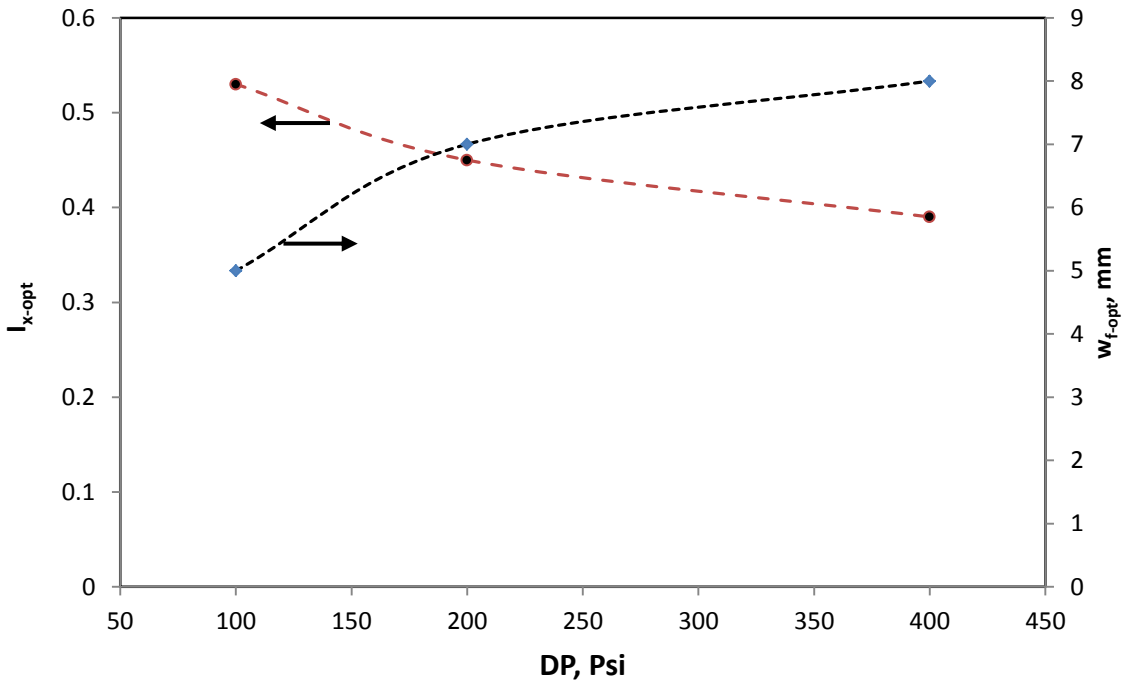

Figure 5.33 variation of optimum penetration ratio and fracture width with GTR for the example shown in Figure 5.31.

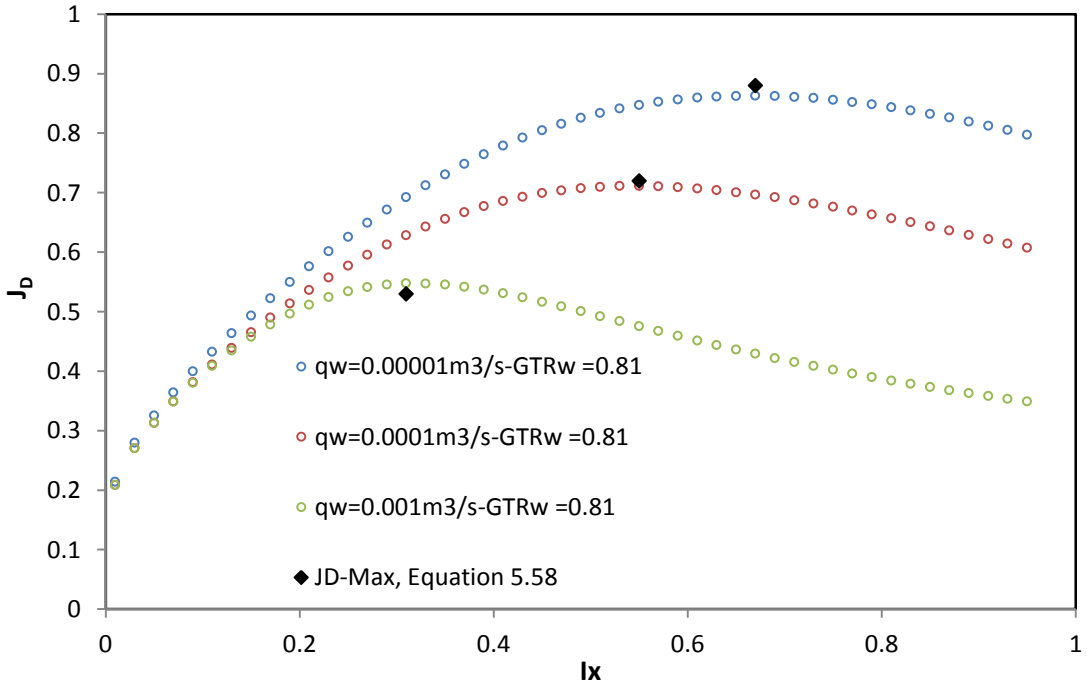

Figure 5.34 Two-phase dimensionless productivity indexes for a proppant number of 0.5 using in-house simulator with different fracture geometries and Equation 5.58 under PSS condition for different well flow rates and a fixed GTR_{well} of 0.81, OPT-12, 13, and 14 data sets Table 5.1.

CHAPTER 6
CLEANUP EFFICIENCY OF HYDRAULICALLY FRACTURED WELLS

6.1 PROBLEM STATEMENT AND OBJECTIVES

Any hydraulic fracture treatment should consist of three main phases, 1) - Pre-treatment design phase, 2) – Execution phase, 3) – Post-treatment evaluation phase. The Pre and Post-treatment phases have been discussed in the previous three chapters of this thesis, (Chapters 3, 4, and 5). That is, the author presented an improvement to numerical modelling of HFWs (i.e. Pre and Post-treatment evaluation phase), and propose a general optimum fracture design method (i.e. Pre-treatment design phase). In this current chapter, the author will present thorough numerical investigations about the effect of fracture clean-up efficiency, which is a key element of fracture execution phase, on HFWs performance.

Fracture execution phase is the most important stage of a hydraulic fracture treatment. In this stage a fracture fluid (FF) is usually injected with high pressure to create the fracture and to transport the proppants which are intended to keep the fracture open. Then, the fracture treatment end with a process called “clean-up”; this is the process where the FF is flowed back to the surface in order to allow reservoir fluids to flow easily through the matrix-fracture face as well as the high conductivity fracture. In fact, ineffective fracture clean-up process is one of the main reasons put forward to explain the failure of any hydraulic fracture treatment job.

Accordingly, fracture fluid clean-up process has gained extensive research in the industry. However, there is a long debate on the impact of pertinent parameters and their relative importance in term of fluid clean-up effectiveness. Thus, some conflicting reports about the effect of fracture fluid clean up efficiency on the performance of HFW, are found in the literature (e.g., Holditch, 1979, compared to Bennion et al., 2000). The numerical simulation of the process is believed to be the reason behind such conflict (as will be explained later in this chapter). Furthermore, all these reports are in the form of “single parameter sensitivity” numerical simulations. That is, none of these studies have investigated the variation of all pertinent parameters simultaneously over a wide practical range of their variation, which may help in better understanding of the

clean-up process and may provide practical guidelines to successful hydraulic fracturing jobs.

With these in mind, the author adopted a statistical approach and developed a methodology to embark on a much needed extensive investigation of variation of all pertinent parameters simultaneously. A new method to simulate a more realistic FF invasion into the matrix and fracture (developed by GCR-HW group) was also adopted.

6.1.1 Introduction

The poor flow-back process of fracturing fluid has been considered as one of the main reasons of hydraulic fracture under-performance. Therefore, the effect of clean-up efficiency on HFW performance has gained the interest of many researchers. Cooke (1973 and 1975) experimental study was among the first to investigate the relationship between fracture fluid and fracture conductivity. That is, he introduced some guidelines on how to correct the fracture conductivity for the combined effect of the closure pressure and reservoir temperature during clean-up process. He also developed a theoretical model to predict fracture permeability and porosity (k_f, φ_f) reduction due to the degraded volume of fracturing fluid residue during the flow-back period.

Holditch (1979) numerical study was one of the first studies to investigate the impact of the fracture fluid invasion into the matrix and the clean-up efficiency process on HFWs performance. In this study, he developed a set of numerical models to predict the gas production loss due to fracture fluid invasion into the matrix, near fracture face, (i.e. fracture face damage). He mainly studied the impact of permeability reduction and relative permeability damage of the invaded matrix zone, as well as the effect of matrix capillary pressure on fracture fluid clean-up rate. The main conclusion in this numerical study is that a serious gas production loss due to fracture fluid invasion (fracture face damage) will not take place unless the permeability of the matrix invaded zone is reduced by 99.9%, or the pressure drawdown does not overcome the capillary pressure in the invaded zone. Later, many numerical studies in the literature followed Holditch (1979) approach of modelling the clean-up efficiency process. A complete literature review on this subject is available elsewhere (Gas Condensate Recovery Final Report 2008-2011, and Ghahri *et. al.* 2010).

Recently, GCR-HW group (Gas Condensate Recovery Final Report 2008-2011, and Ghahri *et. al.* 2010) presented a numerical clean-up efficiency study. In this study, the aim was to first improve the numerical modelling of clean-up efficiency process by developing a more realistic fracture fluid invasion method. Then, to conduct a

comprehensive single parameter sensitivity exercise which evaluate the impact of some factors on HFWs clean-up efficiency. These factors are the fracturing fluid (FF) viscosity variation during clean-up, matrix capillary pressure, matrix and fracture permeability reduction due to FF invasion and reservoir environment (i.e. closure pressure and reservoir temperature), the increase in capillary pressure of the matrix invaded zone, initial water saturation, FF relative permeability hysteresis, and pressure drawdown.

Here, the author has extended the previous work of GCR-HW group to embark on a much needed extensive study, which evaluates the impact of pertinent parameters on the clean-up efficiency of HFWs, over a wide range of their variations using statistical tools.

Here the author first identified the key pertinent parameters. Then, a two-level full factorial statistical experimental design method was used to sample a reasonably wide range of variation of pertinent parameters, covering many practical cases. The variation of a total of 12 parameters describing the matrix and fracture relative permeability of gas and fracture fluid, and matrix capillary pressure curve were studied for two separate fracture fluid volume values.

More than (36,000) simulations were required for this purpose. Therefore, a computer code was developed using MATLAB mathematical package, to simplify the numerical process and automatically link different stages of the simulations conducted using (ECLIPSE, E100). The structure of the computer code will be explained later in this chapter.

In these simulations, the gas production loss (GPL %), defined as a measure of un-clean fracture productivity deviation from the productivity of a fully (100%) clean fracture job, was also calculated automatically as an output data for each run, at different production periods. Then, two linear response surface methods, with and without interaction terms, were used to map the GPL variations with pertinent parameters.

Presenting the results of over 36,000 simulations, using Tornado Charts for the main linear terms, indicated that the clean-up efficiency is mainly affected by a limited number of parameters. Also, Histogram Figures and FF Saturation Maps were used to support the presented discussions and verify the drawn conclusions.

The results highlighted the scenarios where GPL can be significant or minimal at different production time intervals. Such results help in better understanding of the

clean-up process and provide practical guidelines to successful hydraulic fracturing jobs.

6.2 NUMERCIAL SIMULATION METHOD

One of the main challenges in simulating fracture clean-up efficiency process is "how to numerically produce a realistic fracture fluid invasion around the fracture". Actually, the common practice, in most of available clean-up efficiency literature studies, is to assume a constant depth of invasion around the fracture at the beginning of simulation process. That is, all matrix cells perpendicular to the fracture face, within the invaded area will have a fixed fracture fluid saturation (e.g. S_{ff} = 70%) at the beginning of the simulation, therefore the simulation process starts directly with production period (i.e. there is no injection period). Although, this oversimplifying assumption is justified in term of saving CPU time, however the same is not true in term of physics of the process. That is, fracture fluid distribution around the fracture is a complex function of different combination of rock/fracture properties as well as fracture fluid properties (i.e. permeability, relative permeability, viscosity, capillary pressure), and fracture fluid volume (as will be shown later in the results section of this chapter).

Therefore, it is believed that one of the main reasons for the conflicting reports (e.g. Holditch 1979 compared to Bennion *et al.* 2000) on the impact that pertinent parameters have on clean-up efficiency, is the method used to simulate the fracture fluid (FF) invasion.

For instance, Holditch (1979) claimed that the reduction of matrix permeability does not result in loss of gas production unless 99.9 % of the original matrix invaded zone permeability has been damaged by FF prescence. However Bennion (2002) showed that for low permeability gas reservoir, fracture fluid invasion to the matrix zone (i.e. fracture face damage) could significantly reduce the gas production.

Accordingly, in this study the author adopted a new method of simulating fracture clean-up efficiency which consists of two periods, the first is the injection period where fracture fluid is injected and fracture fluid distribution around the fracture is numerically determined, the second simulation period is the production period.

This new method was first introduced by GCR-HW group (Gas Condensate Recovery Final Report 2008-2011, and Ghahri *et. al.* 2010) to model a more realistic invasion of FF into both fracture and matrix. A more description of this method is given below.

In this new method, "A constant volume of FF is injected which invades all the fracture cells instantly, i.e. they are fully saturated with FF at the start of the injection simulation period and the additional injected FF volume is distributed across all the cells adjacent to the fracture cells. In this procedure, the FF saturation distribution within the matrix, which contributes to the performance of clean-up to much greater extent than that within fracture, is obtained by the simulator but that within the fracture is assumed to happen instantly, which is somewhat consistent with what happens in reality and is reported in the literature" (Gas Condensate Recovery Final Report 2008-2011, and Ghahri *et. al.* 2010).

Indeed, this approach simplifies the numerical process, saves CPU time, and most important is more realistic compared to the oversimplified FF invasion method (i.e. assuming constant and uniform FF invasion around the fracture face) which is often followed in some literature studies.

In this current study, the author adopted the GCR-HW method for two fracture fluid volume ratio (FVR) values of 2 and 4, in order to observe the impact of pertinent parameters on clean-up efficiency. It should be noted that, FVR is defined as the ratio of total injection volume (V_{inj}) to fracture volume (V_F) (FVR = $\frac{V_{inj}}{V_F}$).

6.3 FRACTURED WELL MODEL

For this study, a pre-fractured single well model was constructed using ECLIPSE E-100 with dimensions of 2000 by 2000 by 40 m in X, Y and Z-directions and an initial reservoir pressure of 7500 psi. The Cartesian grid was optimised to minimise the numerical error. Table 6.1 shows fracture properties and reservoir dimensions for the reference model used here. The fluid properties of the single-phase gas flowing through the model are listed in Table 6.2. The fracture fluid (FF) was defined as water with viscosity of 0.5 cp and compressibility of 5e-6 (1/psi). Fracture fluid volume of two times fracture volume was considered for the injection periods (FVR = 2), for the reference case. For the reference model the injection volume was 128 m^3. In the second period of simulation, gas and fracture fluid phases are produced under controlled bottom-hole pressure.

The author has tested different fracture models (total of nine, each model requires 4096 simulations) and compared them with the reference model. These models have the same reservoir dimensions as that of the reference model but differ in the fracture dimension (length), fracture properties (permeability distribution), fracture fluid volume

ratio (FVR), or in number of grids in vertical dimension (multi-Layers). The models considered are listed below.

a. Fracture Length: here we modify the reference model by reducing the fracture length to 100 m instead of 400 m presented in the reference model. There are three fracture models under this exercise, listed below.
    1. Short Fracture case-a: this is a 100 m fracture with a fracture fluid volume per fracture length ($V_{FR} = V_{inj} / L_f$, m^3/m) equal to that of the reference model. However, the fracture conductivity (defined as the ratio of conductivity of the fracture for flow into the wellbore to that of the formation into the fracture $C_{FD}=(k_f w_f)/(k_m x_f)$) in this case is higher than that of reference model, as will be explained later in the results section.
    2. Short Fracture case-b: this is a 100 m fracture with a fracture fluid volume per fracture length ($V_{FR} = V_{inj} / L_f$, m^3/m) and fracture conductivity equal to that of the reference model.
    3. Short Fracture case-c: in this case the fracture fluid volume per fracture volume (FVR) is four times that of the short fracture case-a model.

b. Effective fracture Length: here it was assumed that the propped fracture length created during injection period is not equal to the effective length, which contributes to flow during the production period. In other words, it was assumed that during the injection period a 400 m fracture was propped; however when production was resumed only 100 m of this length contributes to flow while the rest of fracture length was damaged and its permeability was equal to that of the formation.

c. Non-uniform permeability distribution: here the reference model was modified by allowing fracture permeability to vary with fracture length. There are two fracture models under this exercise, listed below:
    1. Fracture permeability increases monotonically with fracture length (i.e. the fracture permeability near wellbore is much less than that at the fracture tip). This case is called (Non-uniform permeability case-a).
    2. Fracture permeability decreases monotonically with fracture length (i.e. the fracture permeability near wellbore is much higher than that

at the fracture tip). This case is called (Non-uniform permeability case-b).

d. Multi-Layer: in this case we divide the reference model into two layers to examine the effect of layering in the clean-up process. There are two fracture models under this exercise, listed below:
    1. Multi-Layer (case-a) the matrix permabilities in both layers are equal. Here, there are two sets of simulations with and without cross flow, i.e. kv/kh=1 or kv/kh=0

6.4 RANGE AND NUMBER OF INVESTIGATED VARIABLES

Table 6.3 show the ranges of variation of pertinent parameters that have so far been considered in our numerical simulations. There are 17 parameters for the production period in this Table. These variables was selected based on an extensive previous single parameter study conducted by (GCR-HW, Gas Condensate Recovery Final Report2008-2011, and Ghahri *et. al.* 2010), authors understanding of the process, and literature data.
To conduct these simulations, the author looked at a number of experiment designs and used 2-level full factorial design. To obtain a response surface for a system with "***n***" parameters using the full factorial design of the second order, the number of required experiments is $2^{\mathbf{n}}$ (i.e. number numerical simulations = $2^{\mathbf{n}}$).
To cover the range of variation of all 34 parameters (17 for injection period and 17 for production period, Table 6.3), based on full factorial design, 1.7E10 simulations are required, for which, assuming it takes only one second to complete each simulation, it would take 544 years to complete these simulations. In our model each simulation will take around 120 second, which gives an unrealistic simulation time of 65000 years.
Therefore, in order to reduce the otherwise unacceptable CPU time required, it was assumed that the FF fill in the fracture instantly during the injection period eliminating the need to consider the impact of the 17 parameters on this flow period. As described earlier, the FF saturation distribution within the matrix, which contributes to the performance of cleanup to a much greater extent, is obtained by the simulator but that within the fracture is assumed to happen instantly, which is somewhat consistent with what happens in reality and reported in the literature. Equations 6.1-6.2 describe the capillary pressure and relative permeability curves (GCR-HW, Gas Condensate Recovery Final Report 2008-2011, and Ghahri *et. al.* 2010).

$$\frac{Pd}{IFT} = 0.0075 \times K^{-0.5} \tag{6.1}$$

- Threshold pressure Pd (bar)
- Interfacial tension IFT (dyne/cm)
- Matrix permeability (k_m mD)

$$\left(\frac{Pd}{Pc}\right)^{\lambda} = \frac{Sw - Swr}{1 - Swr} \tag{6.2}$$

$$k_{rw} = K_{\max w} \times \left(\frac{Sw - Swr}{1 - Swr - Sgr}\right)^{nw} \tag{6.3}$$

$$k_{rg} = K_{\max g} \times \left(\frac{Sg - Sgr}{1 - Swr - Sgr}\right)^{ng} \tag{6.4}$$

It should be noted that covering the variation of all (17) parameters of production period (Table 6.3) still require a significant CPU time (i.e. 2^{17}= (131,000) simulation runs × 120 seconds per simulation run = 182 day per one model × 9 models in this study = 4.5 years). Thus, there is a need to reduce the number of pertinent parameter in the production period (Table 6.3).

Accordingly, in the previous equations a constant value of (0.1) for fracture fluid residual saturations inside the fracture ($S_{\mathbf{wrf}}$) and inside the matrix ($S_{\mathbf{wrm}}$), and both residual gas saturation in the matrix (S_{grm}) and fracture (S_{grf}) was assumed to be equal to 0.1. Also, the formation porosity (φ) was assumed to be constant at a value of 0.15.

Therefore, the total number of variables was reduced from 17 to 12 for both pre- and post-treatment simulations. Based on this number of parameters, each fracture well model (presented in section 6.3) required (4096 simulation runs) bringing the total number of simulation runs for the nine models considered in this study to 36,864 simulation runs.

The parameters have been scaled between 0 and 1 with zero corresponding to the lower limit of variation of a selected parameter and 1 corresponding to the maximum limit.

Computer Code

Due to the large number of simulation runs required, a computer code was developed using Mat-Lab to simplify the numerical process, i.e. automatically link different stages of the simulation process.

"In this computer code, initially, the experimental design matrix is read, and then for each case, $\boldsymbol{k_r}$ and $\boldsymbol{P_c}$ curves are generated as include-files. The program also creates another three include-files for porosity, permeability (matrix and fracture) and bottom hole-pressure. It should be noted that these include-files are used for simulation of both injection and production periods. The initial conditions for the production period (pressure and saturation distribution) are those read using the restart files at the last time step of the injection period. To evaluate the FF cleanup efficiency for these cases a 100% cleanup efficiency case is also required to be simulated. This is performed by running a case with the injected FF volume set to zero. After running these cases using Eclipse, total gas and total FF production from summary files are read for three production times, 10, 30 and 365 days" (Code description from GCR-HW, GCR Final Report 2008-2011).

6.5 METHODOLOGY

Analyzing a huge number of numerical simulation runs is a real challenge and hence, should be presented in a very systematic and easy-to-follow way or it will lose its benefit. The aim of this section is to give an introduction to the way of analysis that the author has adopted in this study, and to define terminologies that will be used in order to make it easier for the reader to follow the results and conclusions presented later in this study.

6.5.1 Main Response

The main response in this study is Gas Production Loss (GPL, %), defined as a measure of un-clean fracture productivity deviation from the productivity of a fully (100%) clean fracture.

$$GPL,\% = \left[\frac{q_{clean} - q_{un-clean}}{q_{clean}}\right] \times 100 \tag{6.5}$$

In reality, it is difficult (if not technically infeasible) to get a fully clean fracture job; however if one understands the impact of pertinent parameters on the clean-up process then he/she can provide practical guidelines to get closer to a 100% clean fracture job. One main advantage of GPL is that it is a normalized quantity, which allows the author to compare different scenarios more simply and draw conclusions more properly. In this study the impact of pertinent parameters on GPL are shown. Also, a parameter is

considered to have a positive impact if increasing the value of the parameter reduces GPL while a negative impact parameter is the one, which increases GPL as its value increased.

6.5.2 Linear Response Surface Method

The response surface method is a combination of statistical and mathematical ways to find an appropriate relationship between a main response (e.g. ***y***) and any number of independent variables (e.g. $x_1, x_2, x_3 \ldots x_n$). In other words, it is a technique to fit a polynomial function (***f(x)***, referred to as response surface model) to the main response (***y***). Indeed, the response surface model is a very useful tool to thoroughly analyse the impact that pertinent parameters have on a certain output or response.

In this study the response surface model used is a linear (with or without interaction terms), as shown in Equation 6.5.

$$y = a_0 + \sum_{k=1}^{n} a_k x_n + \sum_{i=1}^{n}\sum_{j=i}^{n} a_i a_j x_i x_j \quad \text{(Linear response model)} \qquad (6.5)$$

The coefficient of the above function is determined by the least square method.

In this research work, the linear response model with and without interaction terms was used to describe the dependency of gas production loss (GPL) to parameters affecting the cleanup efficiency of a HFW. However the author concentrate on the without interaction term scenario as it represent the main impact of individual parameters.

6.5.3 Pertinent Parameters

As mentioned previously, we have used 12 pertinent parameters in this study. Here we will give a brief description of the physical impact that each of the 12 pertinent parameters has on fluid flow.

The exponent of Corey type (gas or fracture fluid) relative permeability curve (n_{gi} and n_{wi}, where *i* refer to inside fracture or inside matrix): Physically, increasing Corey exponent increases the curvature of relative permeability curve and thus reduces the relative permeability of fluid, as shown in Figure 6.1.

The end point of (gas or fracture fluid) relative permeability (K_{maxgi} and K_{maxwi}, where *i* refer to inside fracture or inside matrix): Increasing the end point of fluid relative permeability will increase the relative permeability value, as shown in Figure 6.1.

Capillary pressure: In this study there are three parameters, which affect capillary pressure as demonstrated by Equations 6.1 and 6.2. These parameters are matrix permeability (K_m, mD), interfacial tension (IFT, mN/m), and pore size distribution index (λ).

Interfacial tension (IFT): an increase in interfacial tension will increase capillary pressure, as shown in Figure 6.2.

Pore size distribution index (λ): an increase in Pore size distribution index will decrease capillary pressure, as shown in Figure 6.3.

Matrix permeability (Km): an increase in matrix permeability will decrease capillary pressure, as shown in Figure 6.4.

6.5.4 Figures Used in Analysis:

There are two types of figures used in this study.

First type of figures is the Histogram Figure, which have been used to show the cumulative frequency of a certain range of the main response (GPL) for any numerical model (i.e. reference model, short fracture case-a model ...etc). In this study gas production loss of 20% (called hereafter GPL_{20}) has been used as the reference line for comparison between different models. That is, knowing the frequency of cases, which have GPL_{20}, facilitates the comparison of the severity of gas production loss between different fracture models. For instance, refer to Figure 6.5, which shows a cumulative frequency of GPL for two different models (model A and B). It can be noticed from this figure that model A has a GPL_{20} of 25% while model B has GPL_{20} of 60%, in other words, this means that 75% of the simulated cases in model A has a gas production loss of more than 20%, while the corresponding value in model B is 40%. Also, this suggests that the severity of gas production loss is more in model A compared to that in model B.

Second type of figures is the Tornado chart figure, which is used to show the impact of pertinent parameter on the main response (GPL). It shows parameter's direction of impact (negative or positive) and the relative importance, which each parameter has on the behaviour of the main response. Figure 6.6 shows a tornado chart of two dimensionless pertinent parameters (A and B) effect on gas production loss. It should be mentioned that in Figure 6.6 the parameters values range from 0 to 1, this is due to the fact that all parameters coefficients values have been scaled to the parameter with highest value of coefficient. There are two sets of bars in this figure corresponding to the response with and without interaction parameters.

From a first look to such tornado chart (Figure 6.6), we can draw a general qualitative conclusion about the impact of all pertinent parameters at certain time of production. That is, parameters with a positive scaled value of coefficient have a negative impact on the main response (i.e. gas production loss, GPL); thus as the parameter scaled value increases in the positive direction gas production loss increases. In the same manner, parameters with negative scaled value of coefficient have a positive impact on gas production loss; hence as the parameter absolute scaled value increases in the negative direction gas production loss decreases. Also, from this figure we can observe the relative importance of each parameter; that is the parameter with the highest absolute value has the highest impact on the main response. Based on this, we can conclude that parameter (A) has a negative impact on GPL (i.e. it has a scaled value of (0.5) in the positive direction, which means that as its value increase GPL will increase). In the opposite direction, parameter (B) has a positive impact on GPL with a scaled value of (-0.7). Also, parameter (B) is more important than parameter (A), as it has a higher absolute scaled value compared to that of parameter (A).

Furthermore, from such tornado chart we can determine the worst and best case scenario for a combination of pertinent parameters. That is, the best case scenario with the lowest GPL is the one for which all parameters (with a positive scaled coefficient value) are set to their minimum limit of range while all other parameters (with a negative scaled coefficient value) are set to their maximum limit of range. Conversely, the worst case scenario with the highest GPL is the one for which all parameters (with a positive scaled coefficient value) are set to their maximum limit of range while all other parameters (with a negative scaled coefficient value) are set to their minimum limit of range. For simplicity, refer to Figure 6.6 and let's assume that parameter (A) ranges from (10 at minimum to 100 at maximum) and parameter (B) ranges from (5 at minimum to 50 at maximum). From the tornado chart analysis we find that parameter (A) has a negative impact on (GPL) whilst parameter (B) has a positive impact on (GPL), then the best case scenario is the one for which the parameter (A) is set to its minimum (i.e. a value of 10) and parameter (B) is set to its maximum (i.e. a value of 50). Conversely, the worst case scenario is the one for which the parameter (A) is set to its maximum (i.e. a value of 100) and parameter (B) is set to its minimum (i.e. a value of 5). Nevertheless, any other combination of parameter (A and B) values will be within the best and worst case scenario.

It should be mentioned that the results of the Tornado charts are analysed after 10, 30 and 365 days of productions.

Fracture Fluid Saturation Maps

Fracture fluid was also visualized around the fracture for the worst and best case scenarios of each model studied in this chapter. Such saturation maps will help in supporting the presented arguments and verify any drawn conclusion.

It should be mentioned that due to the very small size of matrix cells around the fracture it was very difficult to properly visualize fracture fluid distribution using *FlowViz* option of Eclipse E-100. Therefore, the saturations of all cells around the fracture were recorded after the well shut-in period (i.e. two days after injection) for all models presented. Then, these saturations were properly visualized using Mat-Lab software.

6.6 RESULTS

6.6.1 Reference Model

As mentioned earlier the first part is aimed at building a reference model to serve as a foundation for all other cases studied here.

Figure 6.7 shows a tornado chart of primary coefficients of all pertinent parameters on gas production loss (with and without interaction) for 400 m fracture length at a production time of 10 days.

It is noted that almost similar trends are observed for both with and without interaction parameters. Here we concentrate on those without interaction parameters. It is noted that all the absolute values of the scaled primary coefficients at this early time of production are less than (0.5). This indicates that the impact of primary coefficients is more or less similar because a large volume of fracturing fluid is produced during this period.

It is clear from this Figure that at early production stage fracture permeability (k_f) has the highest absolute scaled value of coefficient of (0.49). Thus, fracture permeability is the parameter which has the most contribution in reducing gas production loss, GPL. It should be noted that as fracture permeability increases gas production loss decreases. In other words, clean-up of hydraulically fractured wells with higher fracture conductivity is more effective.

The exponent of Corey type relative permeability curve for fracture fluid inside the fracture (n_{wf}) and the permeability end point of Corey type fracture fluid relative permeability inside the fracture (K_{maxwf}) are the next two important parameters both having the same absolute scaled value of primary coefficient of (0.3). However, it should be noted that as the exponent of Corey type relative permeability curves for fracture fluid inside the fracture (n_{wf}) increases GPL increases whilst an increase in

fracture fluid relative permeability endpoint inside the fracture (K_{maxwf}) will reduce GPL. It should be noted that as (n_{wf}) increases the curvature of the relative permeability curve increases and (k_{rwf}) value decreases.

Other important parameters, which have lower absolute values of primary coefficients (compared to K_f, n_{wf}, K_{maxwf}) but still influence gas production loss (GPL), are the Corey exponent for gas relative permeability inside the fracture (n_{gf}) with a coefficient value of (0.22) and that for gas inside the matrix (n_{gm}) with a coefficient value of (0.21), Interfacial tension (IFT) with a coefficient value of (-0.18), and matrix permeability (K_m) with a coefficient value of (-0.19). This means that almost in the same manner as that observed for (n_{wf}), the Corey exponent for gas relative permeability inside the fracture (n_{gf}) and matrix (n_{gm}) has a negative impact on gas GPL. That is, the reduction in gas mobility inside the fracture and matrix increases GPL. Whilst, matrix permeability (k_m) and interfacial tension (IFT) tend to decrease GPL as their values increase. The decrease in GPL by an increase in IFT contradicts the purpose of industry practice in using interfacial tension reducing agents in order to produce most of the fracturing fluid during the back flow period (after fracturing job). This trend will be later supported by the corresponding saturation maps.

In this study we consider a parameter to have a negligible impact on the main response (GPL) if the parameter's primary coefficient has an absolute cut-off value of (0.15). Accordingly, other parameters, which have negligible impact on GPL after 10 days of production are the end point of gas relative permeability inside the fracture (K_{maxgf}), the end point of gas and fracture fluid relative permeability inside the matrix (K_{maxgm} and K_{maxwm}), the exponent of Corey type relative permeability curves for water inside the matrix (n_{wm}), and the index of pore size distribution (λ).

Figure 6.8 shows a tornado chart of primary coefficients of all pertinent parameters on gas production loss, GPL, (with and without interaction) for 400 m fracture length at a production time of 30 days.

This figure clearly shows that the absolute scaled value of all primary coefficients have increased after 30 days of production compared to 10 Days of production. However, the absolute coefficient scaled values of the end point of gas relative permeability inside the fracture (K_{maxgf}), the end point of gas and fracture fluid relative permeability inside the matrix (K_{maxgm} and K_{maxwm}), the exponent of Corey exponent for water relative permeability inside the matrix (n_{wm}), and the index of pore size distribution (λ) are still below the cut-off value of (0.15) and therefore their impact on GPL remains minimal after 30 Days of production.

Similar to the trend observed after 10 Days of production, fracture permeability K_f still has the highest absolute scaled value of coefficient (0.6, which is higher than 0.49, observed after 10 Days of production). Thus, as production time increases the impact of fracture permeability on gas production loss (GPL) increases. This means that the higher the fracture permeability the more pronounced the reduction in GPL at later production time. The absolute scaled values of primary coefficients of the Corey exponent of fracture fluid relative permeability inside the fracture (n_{wf}) and the end point of fracture fluid relative permeability inside the fracture (K_{maxwf}) have also increased (from 0.3 after 10 Days of production to 0.45 and 0.38 after 30 Days of production, respectively). That is, as production time increases the negative impact of (n_{wf}) on GPL increases whilst the positive impact of (K_{maxwf}) increases with time. The scaled values of the Corey exponents of gas relative permeability inside the fracture (n_{gf}), and that inside the matrix (n_{gm}) have slightly increased (from around 0.22 after 10 Days of production to around 0.3 after 30 days of production). Thus, as production time increase the negative impact of (n_{gf} and n_{gm}) on gas production loss increase. Furthermore, the change in the interfacial tension (IFT) and matrix permeability (K_m) scaled coefficients values were minimal (from around -0.19 after 10 Days of production to around -0.21 after 30 Days of production). However, their general direction of impact stays the same (i.e. matrix permeability (k_m) and interfacial tension (IFT) tend to decrease GPL as their values increase).

Figure 6.9 shows a tornado chart of primary coefficients of all pertinent parameters on gas production loss (with and without interaction) for 400 m fracture length at a production time of 365 days.

Comparing these data with those of the previous two Figures a number of main conclusions can be made. First, the impact of the end point of gas and fracture fluid relative permeability inside the matrix (K_{maxgm} and K_{maxwm}), and the Corey exponent of fracture fluid relative permeability inside the matrix (n_{wm}) on gas production loss (GPL) is very minimal at all production stages (10, 30, and 365 Days), this is due to the fact that the matrix permeability range used in this study is very small (0.001-0.1mD) and water viscosity is high compared to that of gas, so any increase in water mobility inside the matrix (either by decreasing n_{wm} or increasing K_{maxwm}) will not be enough to allow more water to flow to the fracture nor it will be enough to hinder gas flow from the matrix; and in both cases it will not affect GPL to a great extent. Second, the absolute scaled values of most of the parameters after 365 days of production have increased significantly compared to the early production stages (10 and 30 Days). This is due to

the fact that at early time of production (10 and 30 Days) a large volume of fracture fluid is produced and thus GPL is significantly high while at late time of production (365 Days) most of fracture fluid has been produced and fracture fluid saturation inside the fracture is quite low so any variation of the parameter value will exaggerate its impact on GPL.

It is also noted from Figure 6.9 that after 365 Days of production the Corey exponent of fracture fluid relative permeability inside the fracture (n_{wf}) has the highest impact on gas production loss with a scaled value of coefficient of (0.95) compared to (0.3 and 0.45, after 10 and 30 Days of production). Similar to the negative impact observed at early production stages (n_{wf}) tends to decrease GPL as its value increases after 365 days. Fracture permeability still has a significant positive impact on GPL with a scaled value of (-0.85) compared to (-0.6 and -0.49, after 10 and 30 Days of production). The third parameter, which has high impact on GPL is the end point of fracture fluid relative permeability inside the fracture (K_{maxwf}) with a scaled value of (-0.7) compared to (-0.22 and -0.38, after 10 and 30 Days of production). In summary, it can be concluded that the impact of (n_{wf}, K_f, K_{maxwf}) is the highest compared to other parameters after 365 Days, also their impact increase as time of production increase (i.e. the magnitude of their scaled value of coefficient increases as production time increases).

Other important parameters, which have lower absolute values of primary coefficients (compared to K_f, n_{wf}, K_{maxwf}) but still influence gas production loss (GPL) are the Corey exponents curves for gas relative permeability inside the fracture (n_{gf}) with a coefficient value of (0.49), and that inside the matrix (n_{gm}) with a coefficient value of (0.3), interfacial tension (IFT), and the end point of gas relative permeability inside the fracture (K_{maxgf}) with a coefficient value of around (-0.3). That is, as production time increase the negative impact of (n_{gf}, n_{gm}) on GPL increase whilst the positive impact of (IFT and K_{maxgf}) on GPL decrease.

The impact of pore size distribution index (λ), which was negligible at early time stages, has slightly increased after 365 Days with a coefficient value of (0.21). Interestingly, the impact of matrix permeability impact on GPL has significantly been reduced after 365 days of production compared to early production stages (10 and 30 Days). That is, the value of its coefficient has reduced to (0.09) after 365 Days compared to around (0.2) after (10 and 30 Days). This means that at early production stages an increase in matrix permeability will decrease GPL whilst at late production stages an increase in k_m will not affect GPL. The matrix permeability impact on GPL depends on two parameters one is operational (i.e. Pressure Drop) and the other is

capillary pressure (i.e. fluid and rock related properties). In this study as explained earlier we have fixed the pressure drop at a value of 1000Psi while capillary pressure is changing with (K_m, IFT, λ). It should be noted that (P_c) decrease as IFT decreases and (K_m and λ) increase. Accordingly, as matrix permeability increase then more fracture fluid will penetrate the matrix during injection period and later (i.e. during production period) more fracture fluid will be produced from the matrix. Thus, in early time of production significant amount of fracture fluid is produced from the fracture so the effect of fracture fluid coming from the matrix on gas production loss will be minimal, however as production time increase most fracture fluid inside the fracture has been produced and the impact of fracture fluid coming from the matrix on gas effective permeability inside the fracture will be exaggerated. In other words, These two (imbibed and produced) fracture fluid volumes have opposite effect on GPL (i.e. the former reduces GPL by keeping the fracture as the main flow path for gas whilst the latter increases GPL by allowing more fracture fluid presence in the fracture). Hence, depending on their relative magnitude the impact of k_m varies. In fact it will be shown later that for a shorter fracture length the direction (as well as the magnitude) of impact of k_m on GPL changes with time due to the significant change in this competition.

Figure 6.10a and b show the saturation map of fracture fluid around the fracture for reference model, after two days of shut-in period, worst case scenario and best case scenario respectively.

As mentioned earlier, visualizing the cells adjacent to the fracture face was not clear using Eclipse, so the author used Mat-Lab to visualize the saturation distribution around the fracture, accordingly the grid blocks in X and Y-directions have been enlarged, i.e. they are not in real scale, to show the FF distribution more clearly.

It can be seen from Figure 6.10a and b that when all parameters were set to their limits of increasing gas production loss (i.e. worst case scenario), high saturation was present inside the fracture and in the first raw of matrix cells adjacent to the fracture face, by the end of the shut-in period, i.e. fluid imbibition was limited compared to the best case, Figure 6.10b.

However, for the best case scenario it is clear from Figure 6.10b that the fracture is almost free from fracture fluid and the same is true for most of the cells adjacent to the fracture face, that is most of fracture fluid was imbibed deep inside the matrix leaving the fracture almost clean. It should be noted that for the best case scenario “interfacial tension” was set to it is maximum value (50 mN/m) which believed to increase the

imbibition rate for this case and contributes in leaving the fracture clean with very low fracture fluid saturation.

Up to now, a detailed statistical explanation of the trend of each pertinent parameter on gas production loss (GPL) at each production time separately has been given. In the next Figure we will show the trend of all parameters at all production times and draw practical conclusions of the impact of pertinent parameters on clean-up efficiency process. In other words, we will answer the question of "how we can use the previous discussion in field applications?"

Figure 6.11 shows a tornado chart of primary coefficients of all pertinent parameters on gas production loss (Linear Response Surface Model, without interaction) for 400 m fracture length at three different production times (10, 30, 365 days).

Based on the trends of pertinent parameters presented in this figure the following practical conclusions can be made:

- Clean-up efficiency of hydraulically fractured wells with high fracture conductivity is more effective; however the effectiveness of clean-up process is more dependent on fracture conductivity at long post-treatment times. This is due to the fact that at early production stages fracture fluid saturation inside the fracture is very high and the fracture is mainly producing fracture fluid, however as production time increase fracture fluid saturation inside the fracture decrease and more gas is permitted to flow alongside water (i.e. gas effective permeability increased). Thus, the higher the fracture permeability is, the higher the gas effective permeability and the lower the gas production loss are.
- Clean-up efficiency of hydraulically fractured wells with high fracture fluid mobility (k_r/μ) inside the fracture is more effective. This can be done by either (decreasing n_{wf} and/or increasing K_{maxwf}) or (decreasing fracture fluid viscosity, which has not been discussed in this study). That is, an effective fracture fluid is the one, which ensures maximum k_r value as well as the lowest possible viscosity that ensure proppant transportability.
- Clean-up efficiency of hydraulically fractured wells with high fracture fluid interfacial tension is more effective. As we mentioned earlier that increasing IFT will increase matrix capillary pressure, which in turn retains the fracture fluid inside the matrix and allow more gas to flow freely inside the fracture. This contradicts the purpose of industry practice in using interfacial tension

reducing agents in order to produce most of the fracturing fluid during the back flow period (after fracturing job).

- Clean-up efficiency of hydraulically fractured wells with high gas mobility inside the fracture and matrix is more effective, mainly at late stages of production. As noticed in Figure 6.9 decreasing (n_{gf} and n_{gm}) decreases GPL (mostly after 365 Days). This can be done by performing a chemical treatment to improve either matrix or fracture wettability toward increasing kr of gas. However, this treatment can be more effective if done at late stage of production when most of fracture fluid is produced from the fracture (i.e. the timing of performing such treatment is very important).

Up to now, the impact of pertinent parameters on the clean-up process for a long fracture (Reference Model) was investigated and accordingly some practical conclusions were made. In the coming sections we will discuss the results of different scenarios and compare them to our reference model, and most importantly we will find out if the conclusions drawn previously are general or will change as we add complexity to our reference model.

6.6.2 Short Fracture Model

Case-a

Figures 6.12 and 6.13 show the percentage of the cumulative frequency of the cases with both fracture lengths of 100 m (short fracture case-a) and 400 m (reference model) versus gas production loss (GPL) at three different production times (10, 30 and 365 days, respectively). The results indicate that as production of gas and fracture fluid continues the number of the cases with severe GPL decreases. For example, for the reference model, 82% of the simulated cases have GPL of more than 20% after 10 days of production (Figure 6.12), while this value is reduced to 70% and 25% of the simulated cases after 30 and 365 days of production (Figure 6.13), respectively. The corresponding values for the short fracture well model are 50%, 30% and 10%, after 10, 30 and 365 days, respectively. These data also clearly show that, severity of fracture fluid damage for the shorter fracture is much less than the longer fracture. Decreasing the fracture length increases the dimensionless fracture conductivity (Dimensionless fracture conductivity is the ratio of ability of fracture to pass on the fluid to the wellbore to that of the matrix to pass on the fluid to the fracture $C_{fD}=k_f w_f/(k_m L_f)$), which in turn reduces the percentage of the cases with severe damage, because it means that under the same reservoir conditions, the fracture, compared to the matrix, has a better ability to

flow the fluid. This is consistent with the earlier presented results demonstrating that impact of the parameters, which affect fracture fluid mobility inside the fracture, on GPL are more important.

Figure 6.14 shows the tornado chart of primary coefficients (corresponding to the Linear Response Surface Model, without interaction parameters) of all pertinent parameters on GPL for 100 m fracture length (Short fracture case-a) at three different production times (10, 30, 365 days).

From Figure 6.14 it can be noticed that similar to data corresponding to the reference model shown in Figure 6.11, the parameters, which have prominent impact on gas production loss (GPL) at all times are the parameters, which affect fracture fluid mobility inside the fracture. These are fracture permeability (K_f), the Corey exponent curves for fracture fluid relative permeability inside the fracture (n_{wf}), and the end point of fracture fluid relative permeability inside the fracture (K_{maxwf}). It is noted that at early production stages (10 and 30 Days) fracture permeability is the parameter with the highest scaled coefficient; however at late stages (365Days) n_{wf} impact increases significantly and its scaled coefficient is the highest. This is due to the fact that at early production time fracture fluid saturation inside the fracture is high whilst at later stages it reduces and as a result the impact of relative permeability becomes more pronounced. It should be noted that mathematically speaking, these two parameters have different directions of impact on GPL. That is, GPL increases as n_{wf} increases and its impact is much more pronounced at late production time (after 365 days) compared to early production stages (10 and 30 days). While, increased fracture permeability results in decreased GPL and its impact is important at all production times. Almost in the same manner as that observed with n_{wf}, the end point of fracture fluid relative permeability inside the fracture (K_{maxwf}) has a positive impact on GPL especially at late stages of production with a coefficient value of (-0.75). In other words, the results of these parameters show that the improvement of fracture fluid mobility inside the fracture decreases GPL.

In the opposite direction, the parameters, which have minimal impact on gas production loss (GPL), are the end point of gas and fracture fluid relative permeability inside the matrix (K_{maxgm} and K_{maxwm}), and the Corey exponent of fracture fluid relative permeability inside the matrix (n_{wm}).

Furthermore, the parameters, which affect matrix capillary pressure (K_m, IFT, λ), and the parameters, which affect gas mobility inside the matrix and the fracture (n_{gm}, n_{gf},

and K_{maxgf}), have a scaled value of less than (0.5) at all times, yet they still play an important rule on GPL.

The general trend of most parameters in Figure 6.14 suggests that the impact of parameters increases as production times increases (i.e. the magnitude of parameters coefficient increases as production time increases). However, this trend was not observed in the case of (IFT, λ, and n_{gm}), especially at late production stages. That is, the scaled values of these parameters increases from 10 to 30 days then decrease as production time is increased to 365 days. This indicates that at early production stages, an increase in IFT and λ has significant impact on gas production loss (GPL) improvement due to the fact that significantly more amount of fracture fluid is imbibed into the matrix at higher capillary pressure values, which helps the fracture to clean faster. However at later production stages when the fracture fluid saturation inside the fracture is low; their impact is not significant. It should be noted that the back flow of imbibed water also affect this process in the opposite direction, which is why the maximum impact is after 30 days of production. Similar statement can be made for the trend of n_{gm}. In the case of, matrix permeability (K_m) the direction of the impact as well as its value changes as production time increases. That is, as it can be noticed from Figure 6.14 after 10 days of production the scaled value of K_m was (-0.35) then its absolute decreases to (0.3) after 30 days and then its scaled value increases to (0.35) after 365 days. As mentioned earlier the competition between the fracture fluid volumes that imbibes into the fracture and its back flow volume both strongly affected by km dictates the relative magnitude of its coefficient. That is, at early stage of production, an increase in km decreases GPL because the imbibition of fracture fluid into the matrix is facilitated at early production stage whilst at late production period of 365 days, an increase in km increases GPL because the backflow of fracture fluid is facilitated at late production stage.

Now we look more closely at the differences between the results for two fracture lengths values.

Figure 6.15 shows the tornado chart of primary coefficients of all pertinent parameters on gas production loss (GPL) after 10 days of production for the 100 meter fracture (short fracture case-a) and 400 meter fracture (Reference model) cases. It seems that the general direction of impact for each parameter is the same in both models. However, the magnitude of all coefficients are not the same (i.e. the magnitude of their impact is different). That is, the scaled values of all parameters coefficients are higher in the case of short fracture case-a compared to the reference model. For instance, the

direction of fracture permeability impact on GPL is the same for both models (GPL decrease as fracture permeability increases). However, the magnitude of impact is higher in the case of short fracture case-a compared to that of the reference model. This difference in scaled values between the two models is more pronounced for the parameters, which affect fracture fluid mobility inside the fracture (i.e. K_f, n_{wf}, K_{maxwf}). As described earlier, this is due to a better cleanup of fracture fluid (refer to Figure 6.12 and 6.13), i.e. the short fracture case-a model has larger dimensionless fracture conductivity, i.e. better flow in the fracture.

With regard to the role of capillary pressure, it can be noticed that after 10 days of production (in both models) increasing capillary pressure by increasing interfacial tension and/or decreasing index of pore size distribution decreases gas production loss due to more imbibition of fracture fluid into the matrix and out of the fracture. Increasing matrix permeability will also decreases gas production loss for both models due the improved imbibition rate of the fracture fluid into the matrix.

Figure 6.16 shows the tornado chart of all pertinent parameters on gas production loss after 30 days of production for both the short fracture case-a and reference models. This Figure shows almost the same trend as seen in Figure 6.15.

Figure 6.17 shows the tornado chart of primary coefficients of all pertinent parameters on gas production loss after 365 days of production for the short fracture case-a and reference models. It can be noticed that (apart from K_m, IFT and λ) the direction of impact and magnitude is almost the same in both models.

One of the main differences between short and long fracture models is the interfacial tension and matrix permeability responses. That is, in the reference model interfacial tension and matrix coefficient scaled value increases with time; which means that increasing λ , IFT, n_{gm} and/or km decrease gas production loss at all production stages (10, 30, 365 days). While, in the case of short fracture case-a, this trend is not monotonic for the reasons mentioned above. Accordingly, it can be concluded that the clean-up efficiency of hydraulically fractured wells depends on the fracture conductivity (i.e. the corresponding conclusions, that were presented earlier in the discussion part of the reference model depends on the fracture conductivity value used).

To complement the previous discussion a fracture fluid saturation map (after two days shut-in time) for the worst case scenario of the short fracture model (case a) is presented in Figure 6.18.

It can be noticed that the fracture fluid distribution around the fracture is more uniform compared to that presented for the reference model (Figure 6.10a). that is

increasing fracture conductivity has allowed the fracture fluid to distribute uniformly in the short fracture model, while in the case of lower fracture conductivity (i.e. reference model) the fluid distribution was mainly concentrated in the area near to the wellbore, this consistent with the results presented in Chapter 3 of this thesis where it was stated that as fracture conductivity decrease the flow from the farthest portion of the fracture decrease and most of the flow happens in the near wellbore area.

In the next section the impact of fracture length when fracture conductivity are equal in both models are investigated.

Case-b

In the short fracture (case-b) model, we have changed the fracture permeability in order to make dimensionless fracture conductivity equal to that of the reference model.

Figures 6.19 to 6.21 show the percentage of the cumulative frequency of the cases for (short fracture case-a, short fracture case-b, and reference models) versus GPL at three different production times of 10, 30, and 365 days, respectively. The results indicate that compared to case-a with higher fracture conductivity, the number of cases with severe GPL has increased for the case-b but it is still lower than the long fracture, which has the same value of fracture conductivity as case-b. For instance, for the reference model, 82% of the simulated cases have GPL more than GPL_{20} after 10 days of production, while this value is reduced to 70% (for the short fracture case-b model) and 50% (for the short fracture case-a model). The same trend is also observed after 30 and 365 days of production.

These results confirm the fact that for the same fracture length increasing fracture conductivity reduces the number of cases with severe gas production loss, GPL, (comparing the short fracture case-a model against short fracture case-b model). Furthermore, the results indicate that for (the same fracture conductivity) increasing fracture length increase the number of cases with severe GPL (comparing the reference model with short fracture case-b model). This is due to the fact that increasing fracture length will increase the exposure of matrix area to fracture fluid invasion.

Figure 6.22 shows the saturation map of fracture fluid around the fracture for short fracture case b, after two days of shut-in period.

It can be clearly seen that the fluid distribution around the fracture for short fracture case b model is almost similar to that observed with the reference model (Figure 6.10). This is due to the fact that both models have the same fracture conductivity and the same (injection volume per fracture length ratio). However, comparing the saturation

map of short fracture case a model (Figure 6.18) with this figure shows that for the same fracture length increasing fracture conductivity results in a more uniform fracture fluid distribution around the fracture while as fracture conductivity decrease most of the fracture fluid is concentrated at the near wellbore area.

Figure 6.23 shows the tornado chart of primary coefficients of all pertinent parameters on gas production loss (GPL) after 10 days of production for (reference model, short fracture case-a, short fracture case-b).

In this Figure it can be noticed that the short fracture (case-b) case has the same trend as that observed in (the reference and short fracture case-a models). However, the magnitude of scaled values of the short fracture (case-b) model are lower than those observed for the short fracture (case-a) model, due to better clean-up for the case-a model. At the same time, the magnitude of scaled values of the short fracture (case-b) model are higher than those observed for the reference model, due to the fact that fracture fluid has more area of exposure in the reference model and thus requires more time to clean-up.

Furthermore, it can be noticed that the difference between the three models in terms of the magnitude of scaled coefficient for the parameters, which controls fracture fluid mobility inside the fracture (i.e. K_f, n_{wf}, and K_{maxwf}) is high compared to all other parameters. Thus, at early time (10 days) the main difference between three models is how much impact fracture fluid mobility has on clean-up process. Also, it is clear that after 10 days fracture permeability is the most prominent factor with the highest scaled value of coefficient.

Figure 6.24 shows the tornado chart of primary coefficients of all pertinent parameters on gas production loss (GPL) after 30 days of production for the reference, short fracture case-a, short fracture case-b models. This figure shows almost the same trend as that seen in Figure 6.23 at 10 days of production. However the magnitudes of scaled values are somewhat higher than those observed after 10 days of production.

Figure 6.25 shows the tornado chart of primary coefficients of all pertinent parameters on GPL after 365 days of production for the reference, short fracture case-a, short fracture case-b models. It can be seen from this Figure that (apart from IFT and K_m) all parameters in the three models have almost the same direction and magnitude of impact. Actually, the main difference between the three models (after 365 days) is the impact that (λ , IFT, n_{gm} and K_m) have on GPL. Indeed, the behaviour they show confirms the conclusion mentioned in the previous section. That is, the absolute value of the λ , IFT, n_{gm} coefficients for these three cases, which has been the highest for the

short fracture (case-a) model at 10 and 30 days of production is the lowest after 365 days. Similarly it can be noticed that after 10 days the absolute value of the k_m coefficient is highest for the short fracture (case-a) model. However after 30 days all models have almost the same value of k_m scaled coefficient value (-0.35). This value was then changed to (-0.08) for the reference, (0.05) for short fracture (case-b) and (0.25) for short fracture (case-a) models. This indicates that the increase in K_m at late production stages will increase GPL in the short-fracture cases only. It can also be stated that a decrease in fracture conductivity will decrease the adverse effect of K_m increase on GPL, i.e., a decrease in the fracture conductivity reduces the scaled value of K_m from (0.25) in the short fracture (case-a) to (0.05) in short fracture (case-b) model.

Case-c

In this section, the fracture fluid injection volume of short fracture (case-a) was increased from two to four times fracture volume to study the impact of fracture fluid injection volume.

Figures 6.26 to 6.28 show the percentage of the cumulative frequency of the cases (for the short fracture case-a, and short fracture case-c models) versus GPL at three different production times of 10, 30, and 365 days, respectively. It can be noticed that increasing the fracture fluid injection volume, more amount of fluid present in the system, has increased the number of cases with severe GPL. For instance, GPL_{20} has increased from 50% (for the short fracture case-a model) to 80% (for the short fracture case-c model), after 10 days of production. Also, GPL_{20} has increased from 30 to 65% and 10 to 20%, after 30 and 365 days, respectively.

Figure 6.29 shows the tornado chart of primary coefficients of all pertinent parameters on gas production loss (GPL) after 10 days of production for the short fracture case-a, and short fracture case-c models).

It can be noticed from this figure that all parameters have the same direction of impact in both models but there is a significant difference in most parameters scaled values, especially for the parameters, which control fracture fluid mobility inside the fracture. Thus, the scaled values of the short fracture case-a model is always higher than those of the short fracture case-c model; this due to the fact that most cases of the latter case have severe GPL compared to those of the former case .

Figure 6.30 shows the tornado chart of primary coefficients of all pertinent parameters on GPL after 30 days of production (for the short fracture case-a and short fracture case-c models). The general trend is almost the same as that observed after 10

days. The differences in scaled values of n_{wf}, K_{maxwf} parameters, which in addition to K_f, control fracture fluid mobility between the two models become more pronounced after 30 days.

Figure 6.31 shows the tornado chart of primary coefficients of all pertinent parameters effect on gas production loss after 365 days of production (for the short fracture case-a and short fracture case-b models). It can be noticed that when the injected volume increased to 4 times the fracture volume, K_f, become the most important parameter compared to n_{wf}, which was the parameter with highest scaled value (after 365 days) for the short (case-a) model. It can be noticed that n_{gm} has increased from (0.35) after 30 days to (0.5) after 365 days for the short fracture (case-c) model while it has decreased from (0.35) after 30 days to (0.27) after 365 days for the short fracture (case-a) model. That is, the importance of gas mobility inside the matrix increases as fracture fluid injection volume increases, i.e. the two-phase flow region is more expended into the reservoir.

It is noted that the impact of IFT is different in both models. That is, IFT absolute scaled value has decreased from (0.25) after 30 days to (0.2) after 365 days for the short fracture (case-a) model whilst it has increased from (0.1) to (0.2) for the short fracture (case-c) model. Finally, the direction of k_m impact on GPL only reverses for the short fracture (case-a) model when moving from 30 days to 365 days of production.

Figure 6.32 shows the saturation map of fracture fluid around the fracture for short fracture (case c) after two days of shut-in period.

It can be observed from this figure that increasing the injection volume in short fracture case c to four times the fracture volume has increased the depth of invasion compared to short fracture case a (Figure 6.18). Also, it can be seen that the fracture fluid distribution around the fracture is more uniform compared to that observed for short fracture case a model. This further confirm our previous discussion about fluid distribution around the fracture, that is fracture fluid distribution is a function of different combination of rock and fluid properties as well as injection volume, and therefore considering a constant thickness of invasion is not representative of the physics of the process.

6.6.3 Effective Fracture Length

Effective fracture length is considered in the literature due to the fact that in most hydraulic fractures the resultant fracture length is less than the designed propped fracture length. In other words, during fracture job a high propped length is achieved but

during flow back and production period the effective length of fracture, which contributes to the production is reduced.

In this section, we have run the reference model but considering that only the first 100 meters of the fracture is contributing to production rather than the full 400 meters. That is, during injection period the fracture fluid filled the whole length of the fracture (i.e. 400 meters) but after production begun only the first 100 meters was contributing to the flow.

Figure 6.33 shows the percentage of the cumulative frequency of the cases (for the reference and effective length models) versus gas production loss (GPL) after 10 days of production.

It can be noticed from this figure that the frequencies of cases with a given GPL is the same in both (reference and effective length) models. The same trend was observed after 30 and 365 days of production.

Figure 6.34 and 35 shows the tornado chart of primary coefficients of all pertinent parameters on gas production loss (GPL) after 10 and 30 days of production for (the reference and effective facture length models).

Form Figure 6.34, which corresponds to data after 10 days of production, it can be noticed that all parameters have the same direction of impact in both models. The most important parameters are those, which control fracture fluid mobility inside the fracture (K_f, n_{wf}, K_{maxwf}) as well as (n_{gm} and n_{gf}). However, K_f and n_{gm} are more important in the case of the effective fracture model compared to the reference model. The same trend is also observed in Figure 3.35 and after 30 days of production but with an increase in the scaled values of parameters coefficient in both models.

Figure 6.36 shows the tornado chart of primary coefficients of all pertinent parameters on gas production loss after 365 days of production (for the reference and effective facture length models).

It can be seen from this figure that in both models the parameters, which controls fracture fluid mobility inside the fracture (n_{wf}, K_{maxwf}, and K_{maxgf}) are the ones with highest scaled value of coefficients. However, the scaled values of n_{wf} and K_{maxwf} in the reference model are higher than their corresponding ones in the effective fracture length model whilst the scaled value of K_f in effective fracture length is higher than that of the reference model. The scaled value of n_{gm} in the effective fracture length model is significantly higher than that of the reference model. That is, an increase in n_{gm} significantly increases GPL of the effective fracture length model compared to that of the reference model at late stages of production.

Furthermore, the scaled value of IFT is higher in case of the reference model compared to the effective fracture length model at all production times. Thus, increasing capillary pressure by increasing IFT decreases GPL (mostly at late stage of production) and its impact is more pronounced if the effective fractured length is equal to the propped length (i.e. the reference model).

Finally, it can be noticed from this figure that the parameters, which control fluid mobility inside the fracture are more important for the reference model compared to the effective length model. Whilst, the parameters, which control fluid mobility inside the matrix are more important for the effective length model compare to the reference model. That is, n_{wf}, K_{maxwf}, and K_{maxgf} have higher scaled values in the case of the reference model compared to the effective length model while (K_{maxwm}, K_{maxgm}, n_{wm}, and n_{gm}) have higher scaled values compared to those of the reference model. This suggests that if the effective fracture length is less than the propped fracture length then the parameters, which control matrix fluid mobility, become slightly more important.

6.6.4 Non-Uniform Fracture Permeability Distribution

Case a

In this exercise the effect of fracture permeability distribution (Non-uniform fracture conductivity) on clean-up process was examined. Here we presents two models (Non-uniform permeability case-a and Non-uniform permeability case-b). Apart from fracture permeability, all other parameters in this model are the same as the reference model. In the Non-uniform permeability (case-a) model the fracture permeability was decreasing toward the wellbore (i.e. Chocked Fracture). The opposite trend was considered for the Non-uniform permeability (case-b) model. In both models the fracture was divided into four equal zones where each zone has different permeability; the difference in fracture permeability between each zone was 50%. That is, the fracture permeability is decreasing by a factor of (50%) between each two successive zones.

Figures 6.37 to 3.39 show the percentage of the cumulative frequency of the cases for Chocked fracture (case-a) model and reference model) versus GPL% at three different production times of 10, 30, and 365 days, respectively. After 10 days, GPL_{20} of the chocked fracture (case-a) model was almost 95% while it was around 82% for the reference model. After 30 and 365 days, the corresponding values for the chocked fracture (case-a) model were 84 and 55% compared to 65 and 30% for the reference model. That is, the number of cases with high GPL is more for the chocked fracture (case-a) model even at late stages of production (i.e. after 365 days of production).

Figure 6.40 shows the tornado chart of all pertinent parameters effect on gas production loss (GPL) after 10, 30, and 365 days of production for (Chocked Fracture model).

It can be noticed that the impact of all parameters increases as production time increases (i.e. their scaled value of coefficients increase with time). The increase in parameters scaled values is significant after 365 days compared to that at early production stages (10 and 30 days). For instance, the absolute scaled value of all parameters (apart from fracture permeability) was less than (0.2) after 10 and 30 days. This is due to the fact that at early production stages huge amount of fracture fluid is being produced and thus GPL is severe, which minimize the impact of parameters. It can be noticed that the impact of the parameters, which control fracture fluid mobility inside the fracture (i.e. K_f, n_{wf}, and K_{maxwf}) is prominent at all production times. Fracture permeability was the parameter with the highest impact at all production stages, hence its impact increased significantly after 365 days to reach (-0.7) compared to (-0.45) and (-0.3) after 30 and 10 days, respectively. The same trend has been observed for the fracture fluid Corey exponent (n_{wf}) and end point of fracture fluid inside the fracture (K_{maxwf}). It is noticed that, (n_{wf} and K_{maxwf}) scaled values have increased to (-0.65 and -0.5, respectively) after 365 days compared to less than (-0.2) for both parameters after 10 and 30 days. Other important parameters are Corey exponent of gas inside the matrix and fracture (n_{gf} and n_{gm}), and interfacial tension (IFT). (n_{gf} and n_{gm}) have the same magnitude and direction of impact at all production stages.

Figure 6.41 shows the tornado chart of all pertinent parameters effect on gas production loss after 10 days of production (for the reference and Non-uniform case-a models).

It can be noticed from this figure that all parameters have the same direction of impact in both models. It can be seen that almost all parameters have lower scaled values of coefficient in the chocked fracture model compared to that of the reference model, especially for the parameters, which control fracture fluid mobility inside the fracture (K_f, n_{wf}, and K_{maxwf}). As mentioned earlier, this indicates that GPL severity is higher in the case of the chocked fracture model compared to that of the reference model.

Figure 6.42 shows the tornado chart of all pertinent parameters effect on GPL after 30 days of production (for the reference and Non-uniform case-a models).

This figure shows almost the same trend as seen after 10 days. However the magnitude of scaled value is higher than those observed after 10 days production (i.e. as

production time increase gas production loss severity decrease and the relative importance of parameters magnified).

Figure 6.43 shows the tornado chart of all pertinent parameters effect on gas production loss after 365 days of production (for the reference and Non-uniform case-a models).

It can be noticed that the parameters, which control fluid mobility inside the fracture are the ones, which have different scaled values in both models, while all other parameters have (more or less) the same magnitude and direction of impact on gas production loss in both models.

It can be seen from this figure that in both models the parameters, which controls fracture fluid mobility inside the fracture (n_{wf}, K_{maxwf}, and K_{maxgf}) are the ones with the highest scaled value of coefficients. However, in both models the difference in (n_{wf} and K_{maxwf}) is more significant compared to that of (K_f). That is, the scaled value of n_{wf} and K_{maxwf} have increased from (0.53 and 0.5, respectively) for the chocked fracture (case-a) model to (0.95 and 0.7) for the reference model, whilst (K_f) has increased from (0.7) for the chocked fracture (case-a) model to (0.85) for the reference model. This suggests that a chocked fracture needs more time to be cleaned compared to a homogenous and constant conductivity fracture. In other words, fracture chocking does not change the direction of impact of parameters compared to that of a homogenous case, however it delays the clean-up process and require more time to clean the fracture.

Case b

Now we compare the behaviour of the Non-uniform fracture permeability model in the case where fracture permeability is increasing toward the wellbore (i.e. Non-uniform case-b model).

Figure 6.44 to 3.46 show the tornado chart of all pertinent parameters effect on gas production loss after 10, 30, 365 days of production (for the reference and Non-uniform case-b models).

Interestingly, it can be seen from this figure that for all production times the magnitude and direction of impact is almost the same in both models. That is, the difference in scaled values between reference and Non-uniform case-b models is very minimal. It should be noted that although the average fracture permeability of Non-uniform case (a and b) are equal, however the relative importance of pertinent parameter impact is different in both models (compare Figures 6.41 to 6.43 with Figures 6.44 to 6.46). That is, the fracture clean-up process is facilitated and the gas production loss is

reduced if fracture permeability is increasing toward the wellbore. This confirms our previous conclusion that fracture permeability is one of the most important parameters that controls fracture clean-up process and furthermore fracture permeability distribution is as important as fracture permeability magnitude.

6.6.5 Multi-layer System

Here a two layer model was considered to represent the effect of layering, where the matrix permabilities in both layers are equal. However, there are two sets of simulations with and without cross flow, i.e. $k_v/k_h=1$ or $k_v/k_h=0$.

It should be noted that for these simulations, a 3-diemnsional (3D), rather than a 2D constructed for the previous cases, system should be setup. Such simulations require large CPU time and often unstable, even with two layers. Therefore significant amount of time and effort was devoted to optimise the simulation parameter and have stable numerical simulations.

In this part of the study, the author used the total gas production loss GPL_T and the individual layers gas production loss GPL_i in order to better analyse the results. The main aim here is to examine if the previous discussion and arguments presented for the reference model should change if the number of numerical grids in the vertical direction is higher than one (i.e. layering effect).

Figure 6.47 to 6.49 shows the show the tornado chart of all pertinent parameters effect on total gas production loss (GPL_T) after 10, 30, 365 days of production (for the reference and (with and without cross flow) models).

It can be clearly seen from Figures 6.47 and 6.48 that the impact of pertinent parameters is the same for all models in these early stages of production. Also, it should be noticed that the trend and direction of impact of all pertinent parameters is the same in reference model (one layer) and in the multi-layer models.

After one year of production Figure 6.49, it can be seen that the impact and trend of all pertinent parameters, apart from those which control fracture fluid mobility inside the fracture (i.e. k_f and n_{wf}), is the same in the reference and the multi-layer model. However, this is not the case for k_f and n_{wf}, where the magnitude of k_f and n_{wf} absolute coefficients is lower than those for the reference and no cross flow models. This means that the importance of fracture permeability and fracture fluid Corey exponent inside the fracture has decreased for the case of cross flow. The behaviour of these two pertinent parameters can be explained if we look at the individual layers gas production loss GPL_i.

Figures 6.50 and 6.51 show the tornado chart of all pertinent parameters effect on bottom layer gas production loss ($GPL_{Bottom\text{-}Layer}$) after 10 and 365 days of production (for both models with and without cross flow).

It can be seen from Figure 6.50 that after 10 days of production the magnitude of fracture permeability coefficient is higher in case of no cross flow, also after one year of production (Figure 6.51) this difference become very significant (i.e. (0.85) for cross flow compared to (0.25) for case of with cross flow). This indicates that fracture permeability has an adverse effect on the bottom layer; that is if cross flow is active then as fracture permeability increase, more fracture fluid will come from top layer to bottom layer and therefore higher fracture permeability will cause more gas production loss to the bottom layer. While in the case of no cross flow, the bottom layer will be isolated from the top layer and any increase in fracture permeability will facilitate fluid clean-up and reduce gas production loss. In other words, it can be said that if cross flow exist then fracture permeability will facilitate fracture fluid flow to bottom layer and thus increase gas production loss to the bottom layer. However, this also means that the top layer will have the chance to clean faster and to contribute to more gas production, actually for some of the simulated cases we found that $GPL_{Top\text{-}Layer}$ have negative values which indicate that the top layer has cleaned and gas start flowing from the bottom layer to the top layer due to cross flow, i.e. the impact of layering on Total gas production loss is minimal for the simulated cases.

In conclusion, it can be said that when the reference model was divided to two layers, the general trend of impact and relative importance of pertinent parameters have not changed (i.e. the effect of layering in this case is minimal). However, the absolute magnitudes of the parameters which control fracture fluid mobility inside the fracture (i.e. k_f and n_{wf}) have changed only at late stages of productions.

6.7 SUMMARY AND CONCLUSIONS

This study is aimed at evaluating of the impact of pertinent parameters on the clean-up efficiency of a hydraulically fractured (gas) well.

First, the author identified some of the key pertinent parameters. a two-level full factorial statistical experimental design method was used to sample a reasonably wide range of variation of pertinent parameters, covering many practical cases. The variation of a total of 12 parameters describing the impact of fracture permeability, matrix permeability, pore size distribution index, threshold pressure, interfacial tension, the exponents and end points of Corey type relative permeability curve for gas and FF in the matrix and fracture have been studied for two separate fracture fluid (FF) volumes.

Since over 36,000 simulation runs were required, to cover the range of variation of all parameters, the simulation process has been simplified using a computer code, which was developed to automatically link different stages of these simulations.

In these simulations, the gas production loss (GPL), compared to the 100% clean fracture case, was also calculated automatically as an output data for each run, at different production periods.

The analysis of the simulation runs using two response surface models (with and without interaction of parameters) demonstrates the relative importance of the pertinent parameters after different production time periods. Also, Histogram Figures and FF Saturation Maps around the fracture were used to support the presented discussions and verify conclusions.

Based on the results of the numerical analysis, first the conclusions of the study are presented followed by some important practical considerations:

1. Fracture fluid distribution around hydraulic fractures is a function of different combination of (rock and fluid) parameters, and does not always yield a uniform distribution as it is often assumed in the literature.
2. As fracture fluid and gas production continues, the number of the cases with severs gas production loss decreases but the relative importance of the pertinent parameters increases.
3. GPL is significantly affected by the parameters which control fracture fluid mobility inside the fracture (K_f, n_{wf}, K_{maxwf}) for all models studied here.
4. Interfacial tension reduces gas production loss (GPL) (especially at late stages). However, its impact reduces significantly as fracture conductivity increases.

5. For the same fracture conductivity, increasing fracture length increases the number of cases with severe GPL.
6. For the same fracture length, increasing fracture conductivity decreases GPL severity.
7. An increase in the fracture fluid injection volume increases the number of cases with severe GPL and delays the fracture clean up.
8. Increasing fracture fluid injection volume increases the importance of gas mobility inside the matrix.
9. GPL is significantly affected by the direction of fracture permeability variation along the fracture length. That is, decreasing fracture permeability toward the wellbore increases GPL severity, i.e. it increases the number of cases with high GPL. There was hardly any difference between the results of the uniform fracture permeability and the case with deceasing permeability away from the wellbore. The results highlight the importance of fracture permeability near the wellbore.

Practical Considerations

10. Clean-up efficiency of hydraulically fractured wells with high fracture conductivity is more effective; however the effectiveness of clean-up process is more dependent on fracture conductivity at later post-treatment times. This is due to the fact that at early production stages fracture fluid saturation inside the fracture is very high and the fracture is mainly producing fracture fluid, however as production time increases fracture fluid saturation inside the fracture decrease and more gas is permitted to flow alongside fracture fluid (i.e. gas effective permeability increased). Thus, the higher the fracture permeability, the higher the gas effective permeability and the lower the gas production loss.
11. Clean-up efficiency of hydraulically fractured wells with high fracture fluid mobility (k_r/μ) inside the fracture is more effective. This can be done by either (decreasing n_{wf} and/or increasing K_{maxwf}) or (decreasing fracture fluid viscosity, which has not been discussed in this study). That is, an effective fracture fluid is the one, which ensures maximum k_r value as well as the lowest possible viscosity that ensure good proppant transportability.
12. Clean-up efficiency of hydraulically fractured wells with high fracture fluid interfacial tension is more effective, for the range of dimensionless fracture conductivity (C_{FD}) used in this study ($1 < C_{FD} > 5$). That is, increasing IFT

increases matrix capillary pressure, which in turn retains the fracture fluid deep inside the matrix and allows more gas to flow freely along fracture face and inside the fracture. This contradicts the purpose of industry practice in using interfacial tension reducing agents in order to produce most of the fracturing fluid during the back flow period (after fracturing job).

13. Clean-up efficiency of hydraulically fractured wells with high gas mobility inside the fracture and matrix is more effective, mainly at late stages of production. This can be achieved by performing a chemical treatment to improve either matrix wet-ability toward increasing k_r of gas provided that the treatment process do not add additional flow barrier. However, this treatment can be more effective if it is done at late stage of production when most of fracture fluid is produced from the fracture (i.e. the timing of performing such treatment is very important).

Finally, the author would like to highlight the fact that, the approach and methodology of analysis used in this chapter can be applied to other numerical studies of similar nature. That is, if a reservoir modeller has a numerical problem with different number of pertinent parameters, then it is recommended to follow the belowmentioned procedures in order to evaluate the impact that these pertinent parameters have on a particular output or response.

1. Define the key pertinent parameters.
2. Define a main response, preferably a "normalized" factor, in order to better compare different results and generalize the conclusions.
3. Use experimental design and statistical tools to cover the ranges of variation of all pertinent parameters.
4. Simplify simulation process, i.e. use computer codes to automatically handle huge number of simulations.
5. Define simple way of analysis, e.g. combining Tornado charts with Cumulative frequency figures and saturation maps as presented in this study.

6.8 REFERENCES

Cooke, C.E., October 1975: Effect of fracturing fluids on fracture conductivity, JPT, pp. 1273-83, Trans., AIME, 259.

Cooke, C.E., Sep 1973: Conductivity of Fracture Proppants in Multiple Layers, SPE 4117, JPT.

Holditch S. A., Dec 1979: Factors Affecting Water Blocking and Gas Flow from Hydraulically Fractured Gas Wells, JPT 1515-1524.

Bennion D. B., Thomas F. B. and Ma T., 12-15 March 2001: Recent Advances in Laboratory Test Protocols to Evaluate Optimum Drilling, Completion and Stimulation Practices for Low Permeability Gas Reservoirs, SPE 60324.

Ghahri P., Jamiolahmady M. and Sohrabi M. , 27–29 May 2009: Investigation of Cleanup Efficiency of Hydraulically Fractured Wells in Gas Condensate Reservoirs, SPE 121916, SPE European Formation Damage Conference held in Scheveningen The Netherlands.

Panteha Ghahri: "Modelling of Gas-Condensate Flow around Horizontal and Deviated wells and Cleanup Efficiency of Hydraulically Fractured Wells", PhD 2010, Heriot-Watt University.

Gas Condensate Recovery Project (2008-2011) Final Report, 2011, IPE, Heriot Watt University, UK.

Table 6.1: The basic input data for the single-well pre-fractured well model used in this study.

X_f(m)	w_f(m)	Xres(m)	Yres(m)	Zres(m)
400	0.004	2000	2000	40

Table 6.2: Fluid properties of gas used here.

P (psi)	Bg	$\mu(cp)$
14.65	260.21	0.0147
400	9.4295	0.0149
600	6.2505	0.015
800	4.6658	0.0152
1000	3.7189	0.0154
1500	2.4673	0.016
2000	1.8527	0.0168
2500	1.492	0.0177
3000	1.2574	0.0187
3500	1.0942	0.0198
4000	0.9749	0.021
5000	0.8137	0.0235
6000	0.7109	0.026
7000	0.6401	0.0283
7500	0.6124	0.0295
8000	0.5886	0.0306
8500	0.5677	0.0317

Table 6.3: The range of variation of uncertain parameters after fracturing.

	Parameter	Min	Max
Fracture Conductivity	K_f (D)	1	30
Matrix Permeability	K_m	1 μD	0.1 mD
Matrix capillary pressure curve (P_c)	Pore size index λ	2	4
Matrix capillary pressure curve (P_c)	Interfacial Tension (mNm/m)	2	50
Porosity	ϕ	0.15	0.15
Matrix krg curve	S_{gr}	0.1	0.1
Matrix krw curve	S_{wr}	0.1	0.1
Matrix krg curve	n_g	1.5	5
Matrix krw curve	n_w	1.2	4
Matrix krg curve	K_{maxg}(end point)	0.5	1.0
Matrix krw curve	K_{maxw}(end point)	0.05	0.6
Fracture krg curve	S_{gr}	0.1	0.1
Fracture krw curve	S_{wr}	0.1	0.1
Fracture krg curve	n_g	1.5	5
Fracture krw curve	n_w	1.2	4
Fracture krg curve	K_{maxg}(end point)	0.5	1.0
Fracture krw curve	K_{maxw}(end point)	0.1	0.75

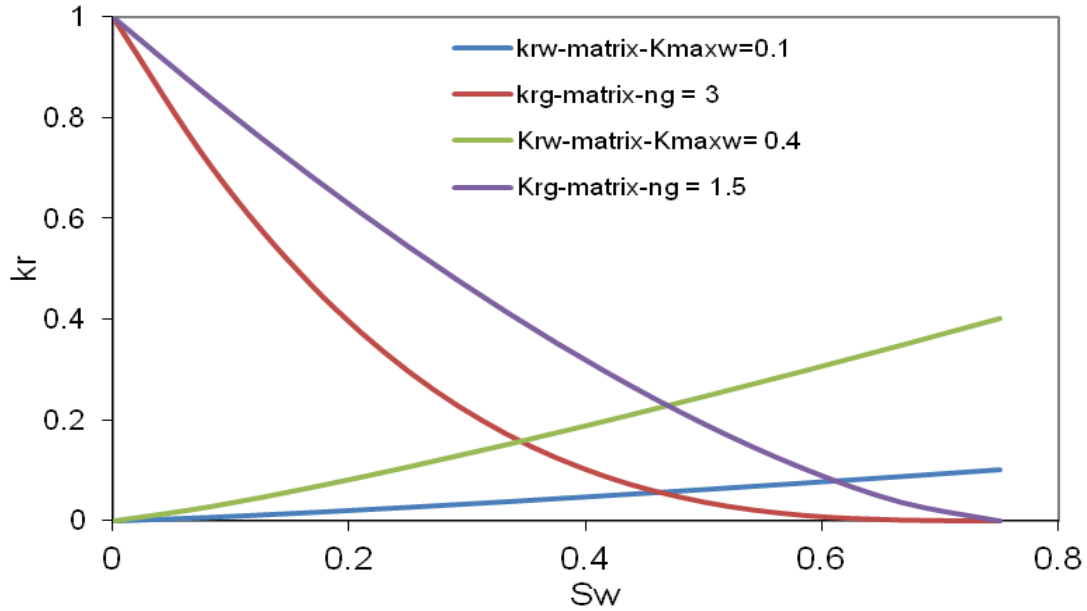

Figure 6.1: The variation of krg and krw vs Sw by changing the Corey endpoints and exponents.

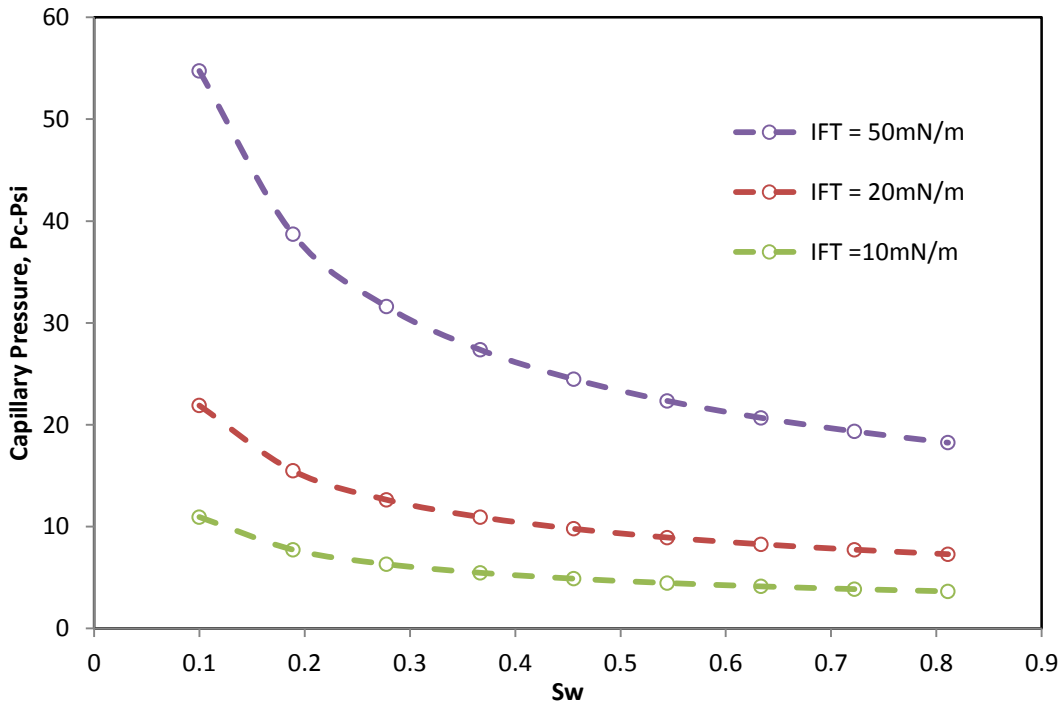

Figure 6.2: The variation of Pc by changing IFT.

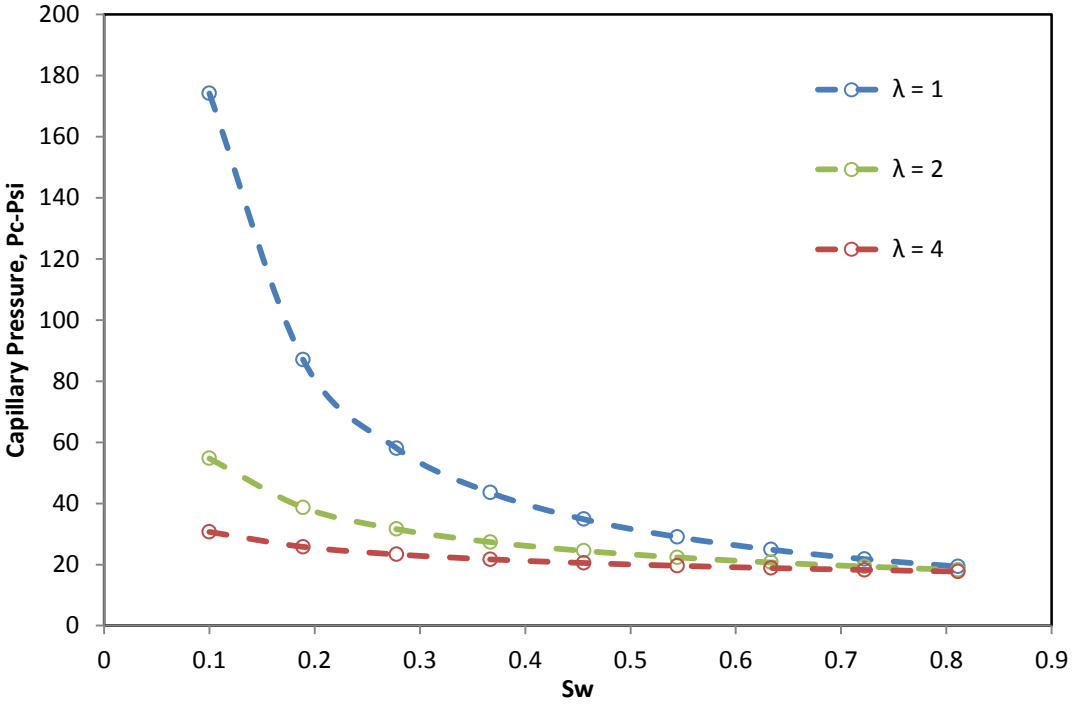

Figure 6.3: The variation of Pc by changing λ.

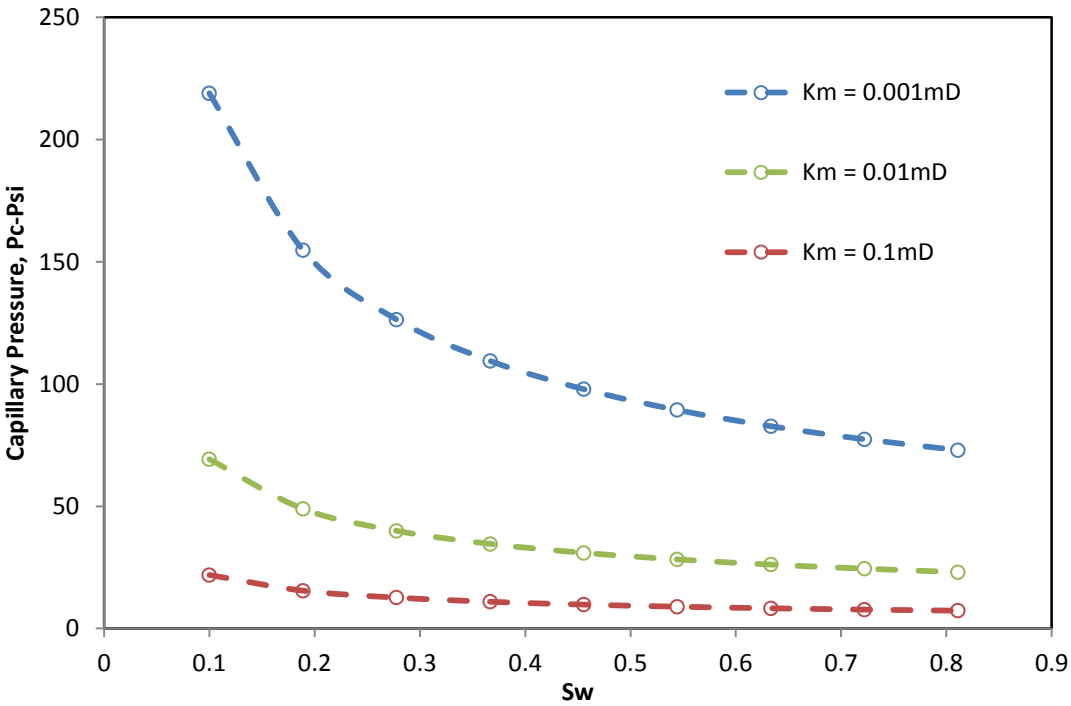

Figure 6.4: The variation of Pc by changing K_m.

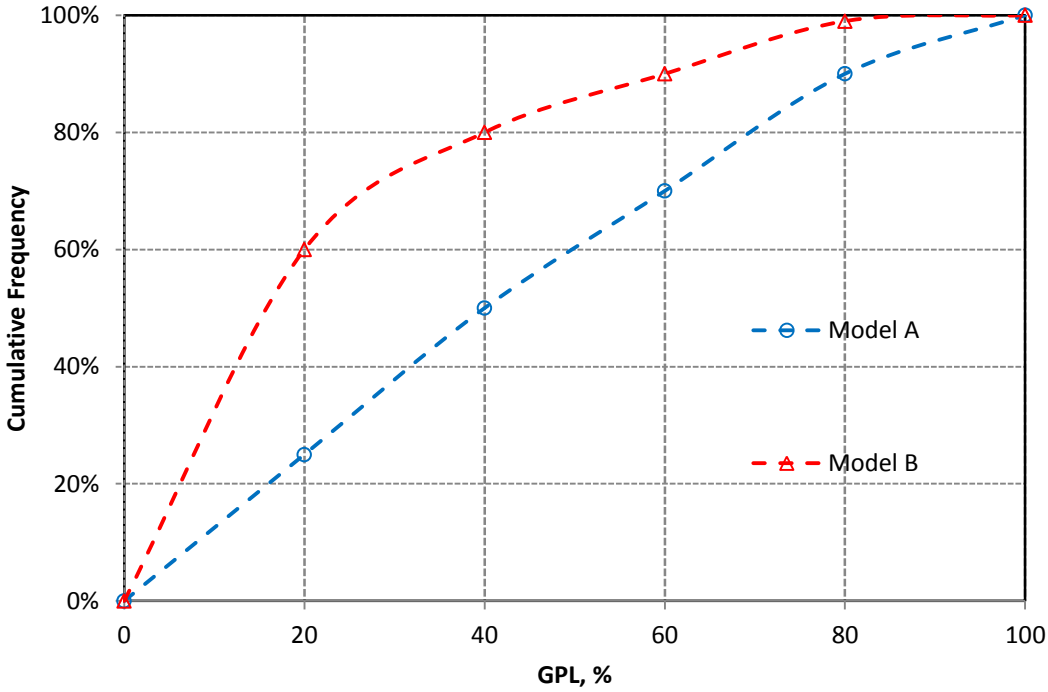

Figure 6.5: The percentage of the cumulative frequency of the cases for (model A and B) versus GPL%. (For demonstration purposes).

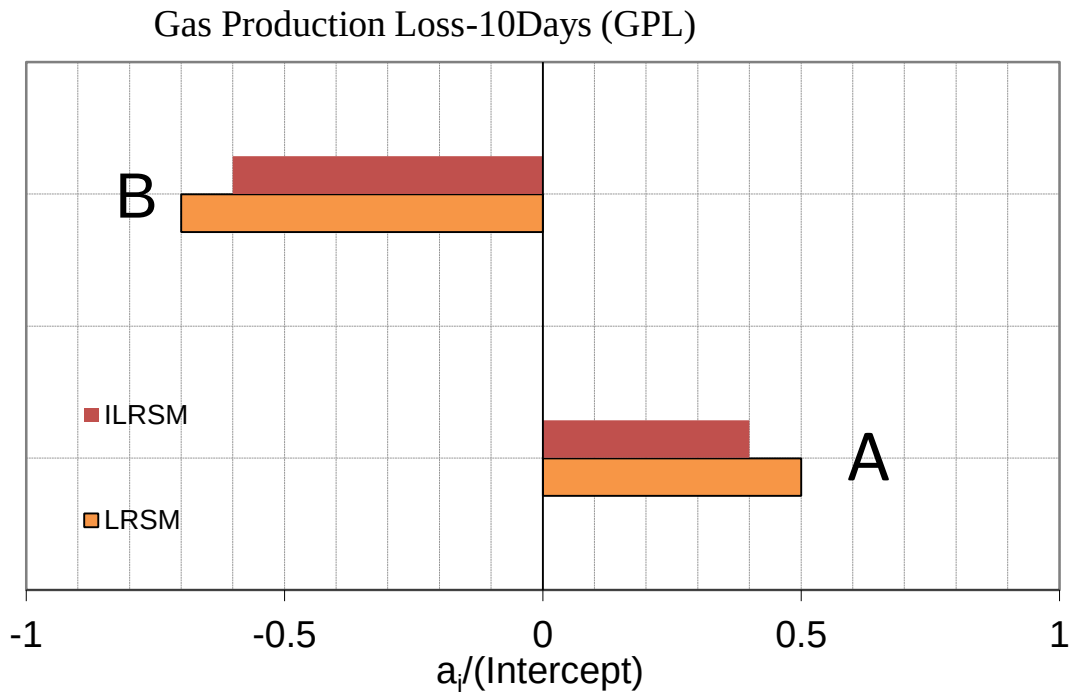

Figure 6.6: Tornado chart of primary coefficients of all pertinent parameters on gas production loss (Linear Response Surface Model, without interaction) for (Model A and B). (For demonstration purposes)

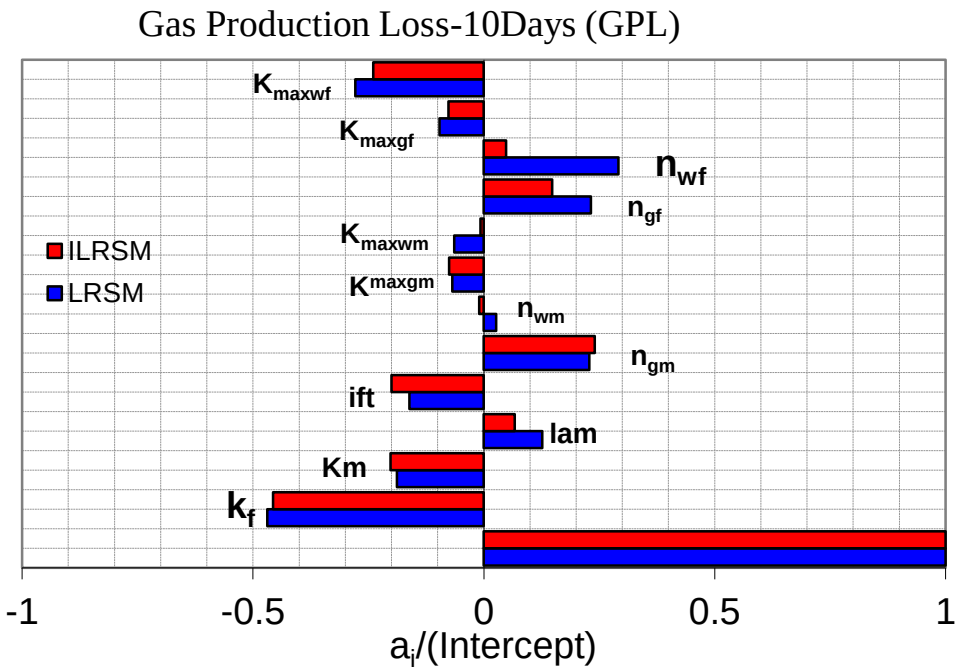

Figure 6.7: Tornado chart of primary coefficients of all pertinent parameters on gas production loss (Linear Response Surface Model, without interaction) for Reference Model after 10 days of production.

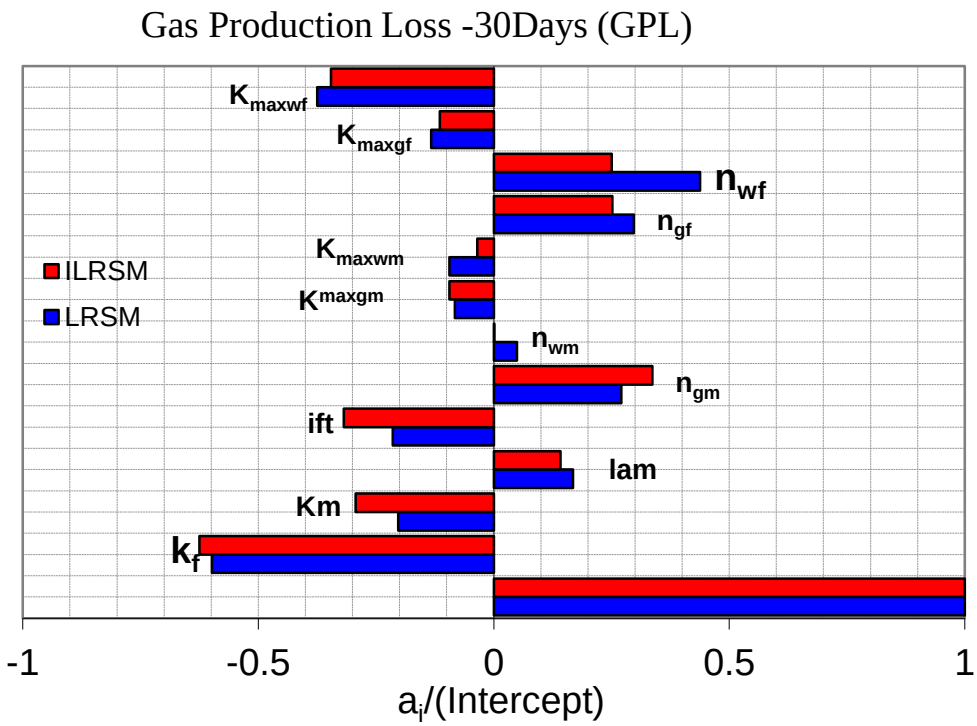

Figure 6.8: Tornado chart of primary coefficients of all pertinent parameters on gas production loss (Linear Response Surface Model, without interaction) for Reference Model after 30 days of production.

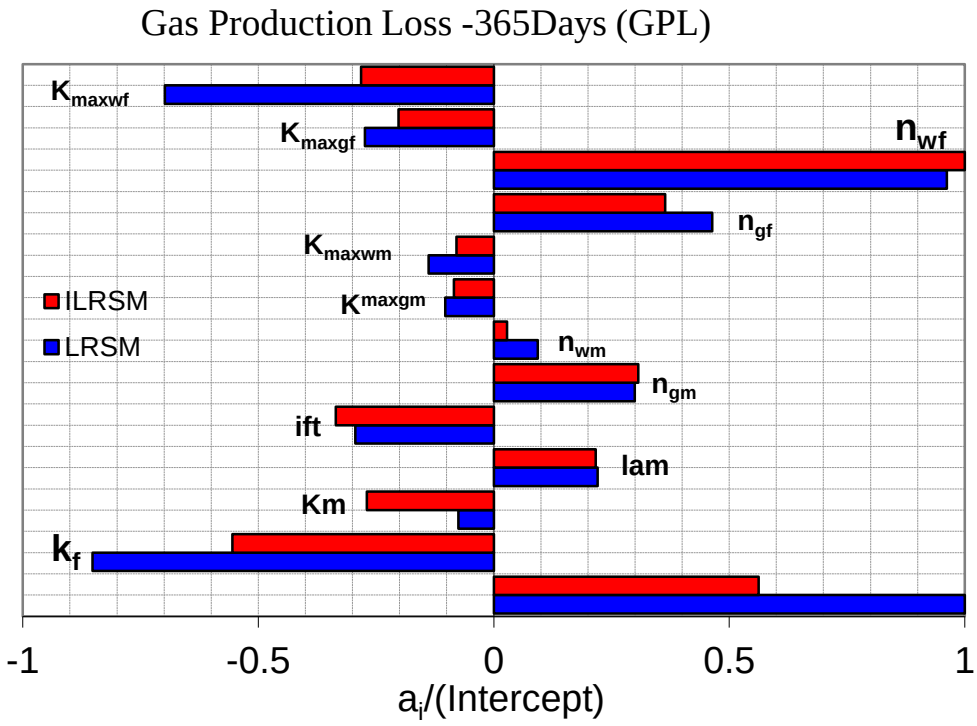

Figure 6.9: Tornado chart of primary coefficients of all pertinent parameters on gas production loss (Linear Response Surface Model, without interaction) for Reference Model after 365 days of production.

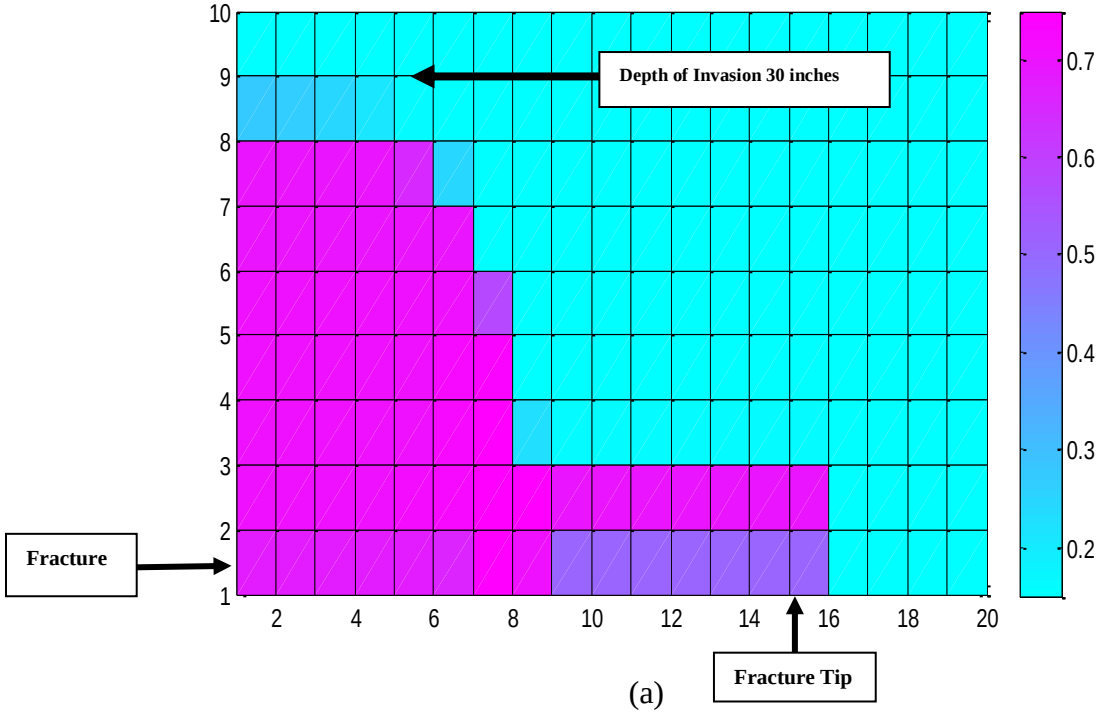

(a)

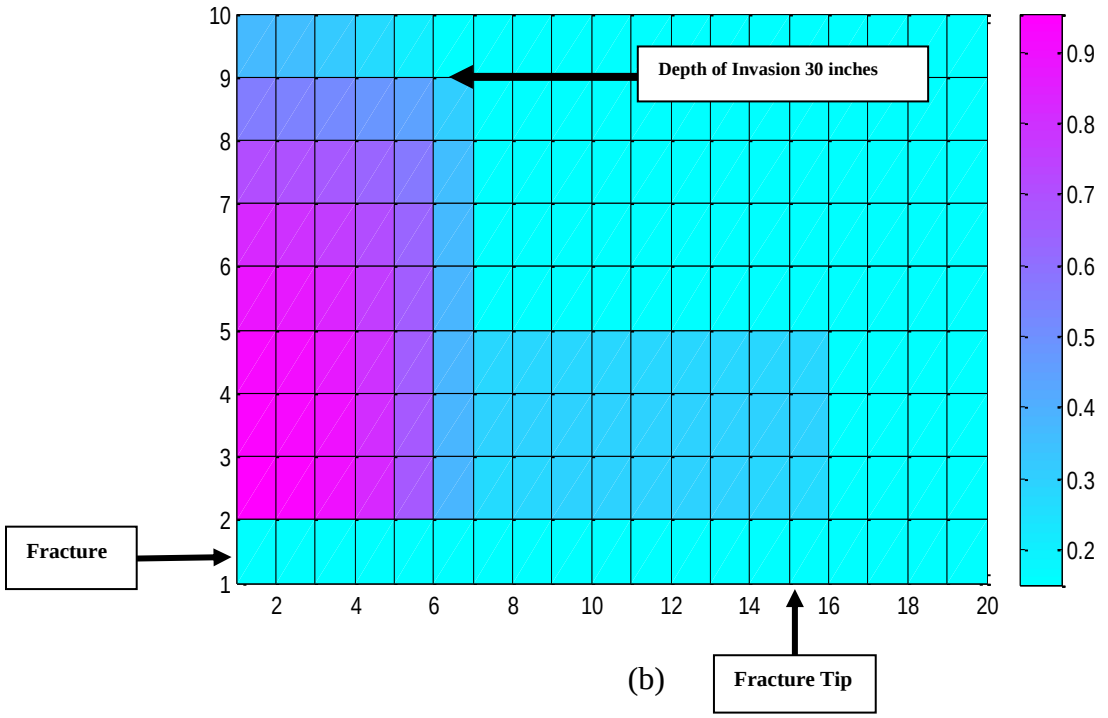

(b)

Figure 6.10: Fracture fluid distribution around the fracture for short fracture (case a) model after two days of shut-in time. a) - Worst Case Scenario, b) Best Case Scenario.

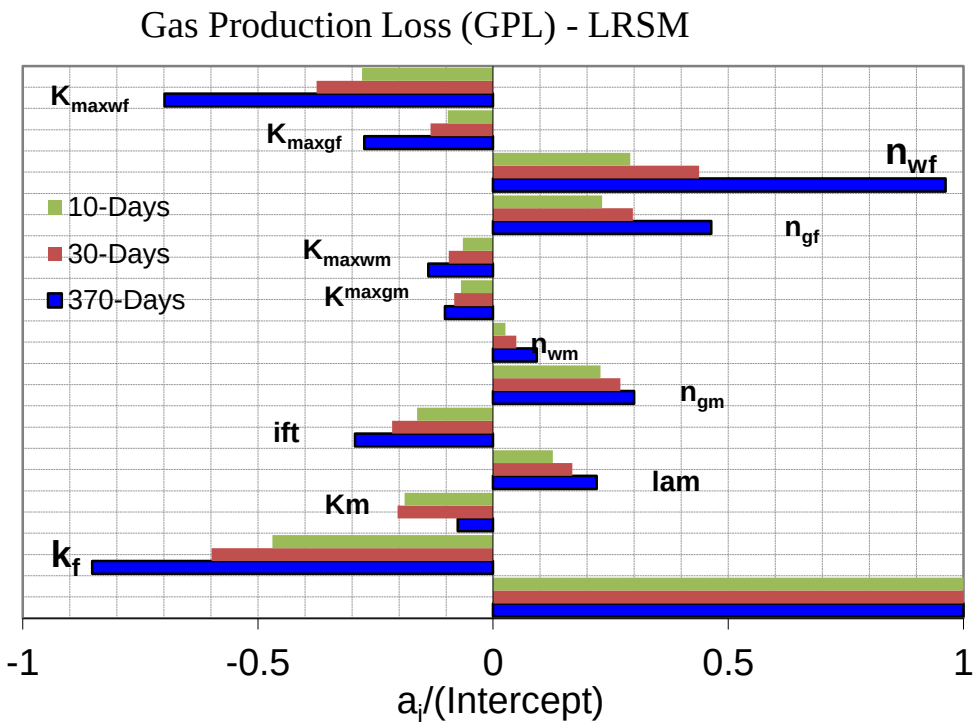

Figure 6.11: Tornado chart of primary coefficients of all pertinent parameters on gas production loss (Linear Response Surface Model, without interaction) for Reference Model after 10,30, and 365 days of production.

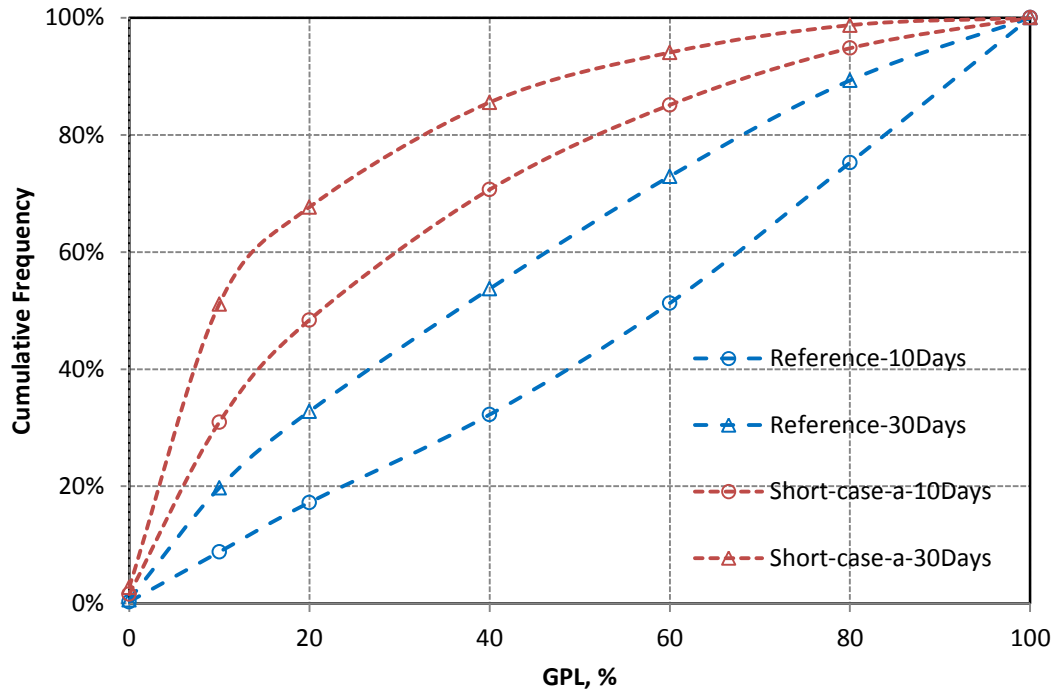

Figure 6.12: The percentage of the cumulative frequency of the cases with both fracture lengths of 100 m (short fracture case-a) and 400 m (reference model) versus GPL% after 10 and 30 days

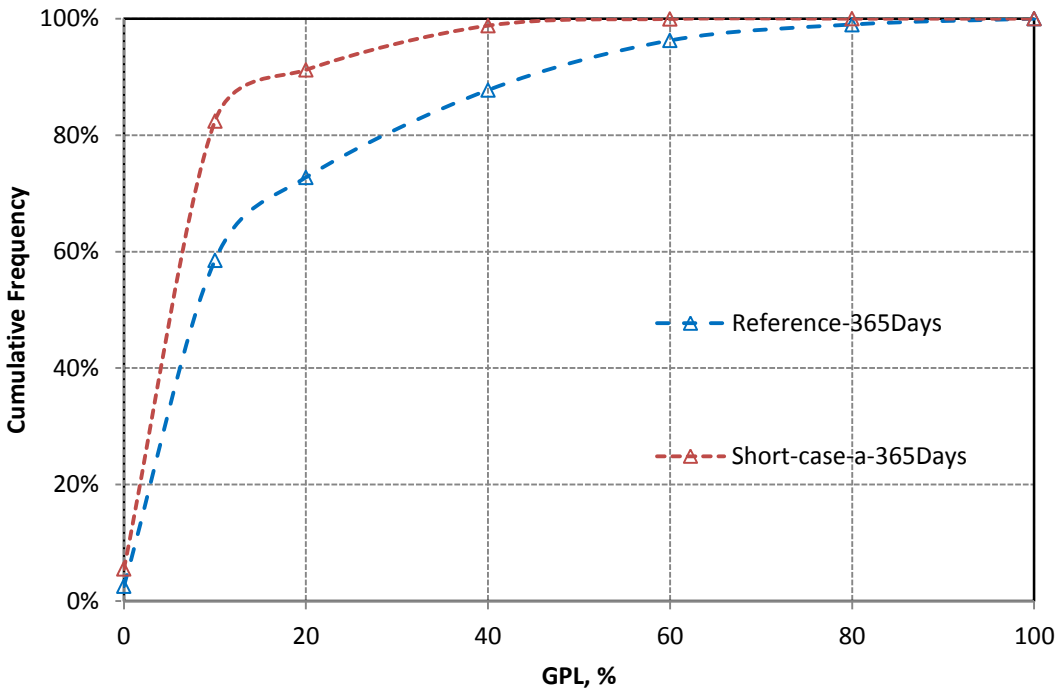

Figure 6.13: The percentage of the cumulative frequency of the cases with both fracture lengths of 100 m (short fracture case-a) and 400 m (reference model) versus GPL% after 365 days

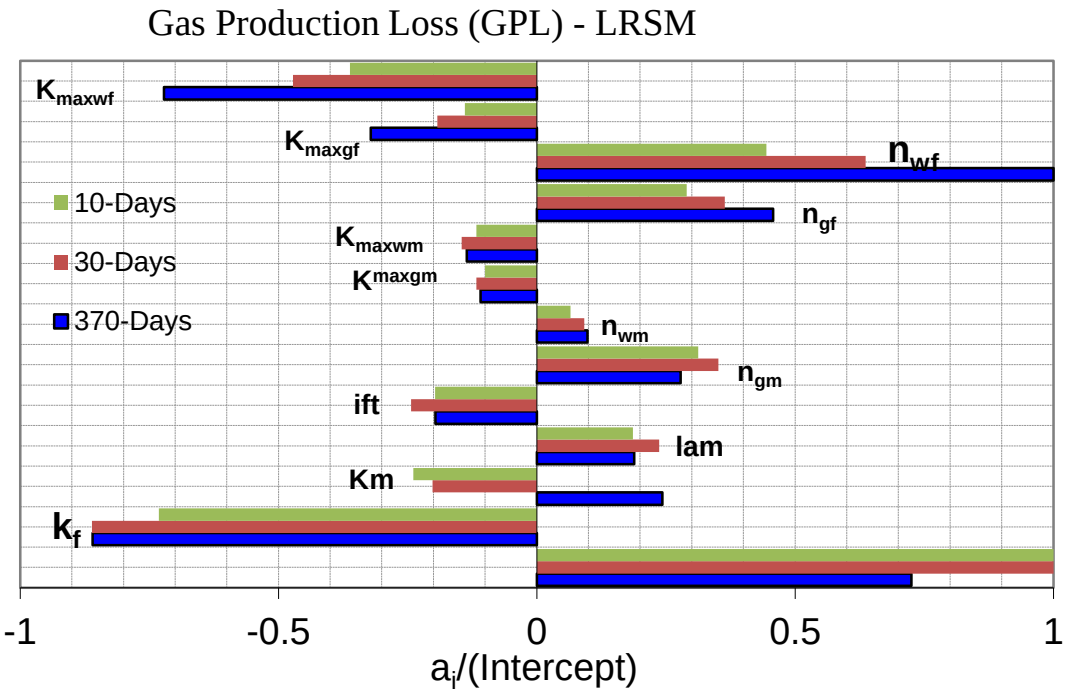

Figure 6.14: Tornado chart of primary coefficients of all pertinent parameters on gas production loss (Linear Response Surface Model, without interaction) for Short fracture case-a Model after 10,30, and 365 days of production.

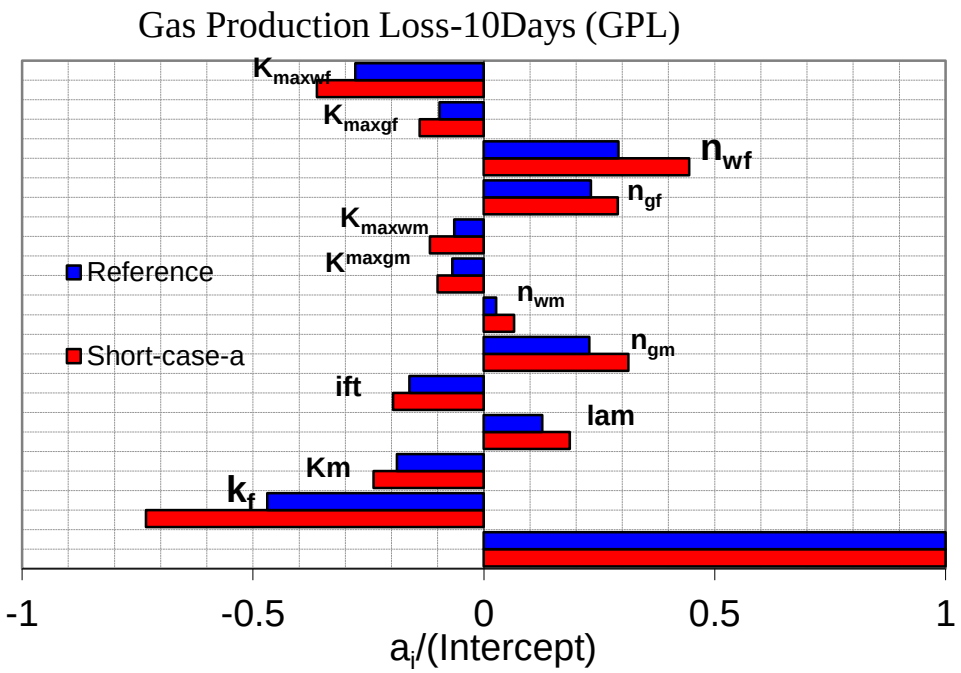

Figure 6.15: Tornado chart of primary coefficients of all pertinent parameters on gas production loss (Linear Response Surface Model, without interaction) for Reference and short fracture case-a Model after 10days of production.

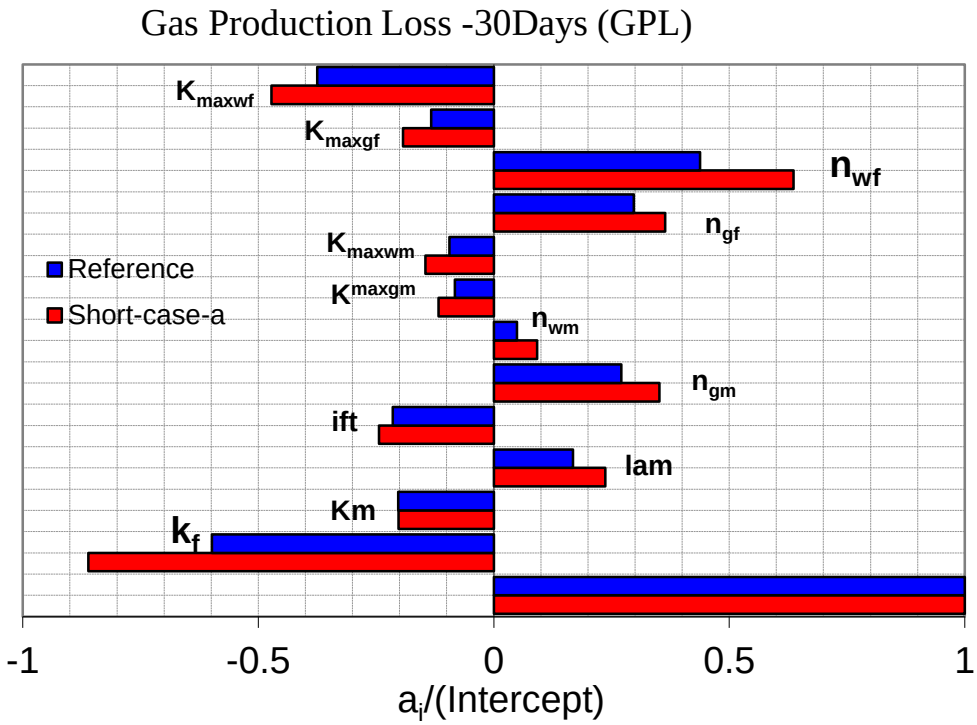

Figure 6.16: Tornado chart of primary coefficients of all pertinent parameters on gas production loss (Linear Response Surface Model, without interaction) for Reference and short fracture case-a Model after 30 days of production.

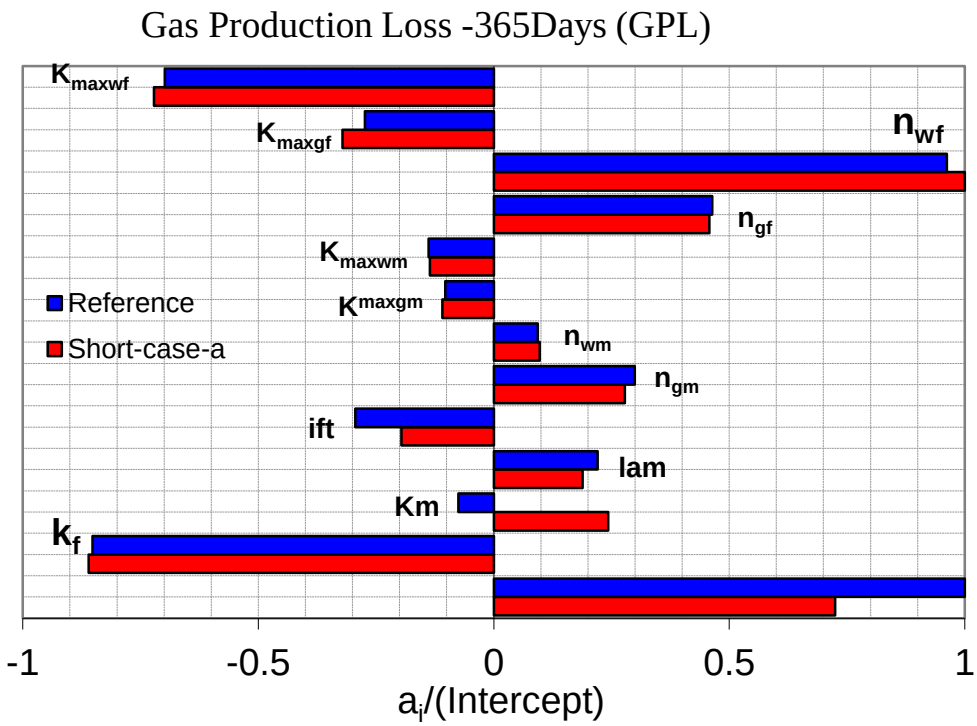

Figure 6.17: Tornado chart of primary coefficients of all pertinent parameters on gas production loss (Linear Response Surface Model, without interaction) for Reference and short fracture case-a Model after 365 days of production.

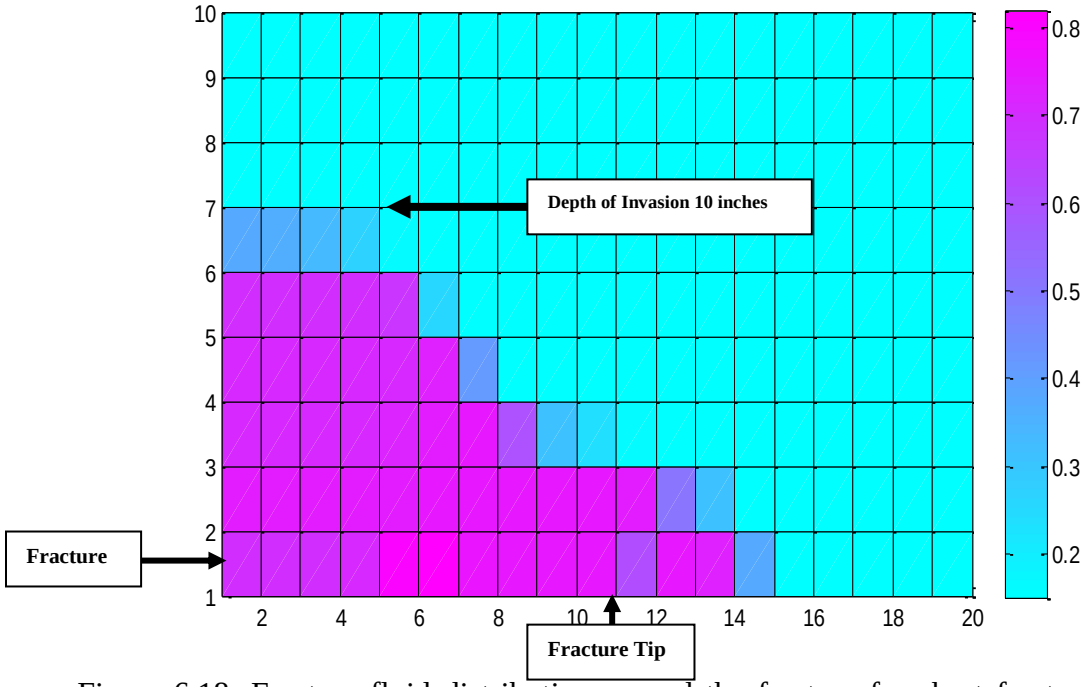

Figure 6.18: Fracture fluid distribution around the fracture for short fracture (case a) model after two days shut-in time. Worst Case Scenario

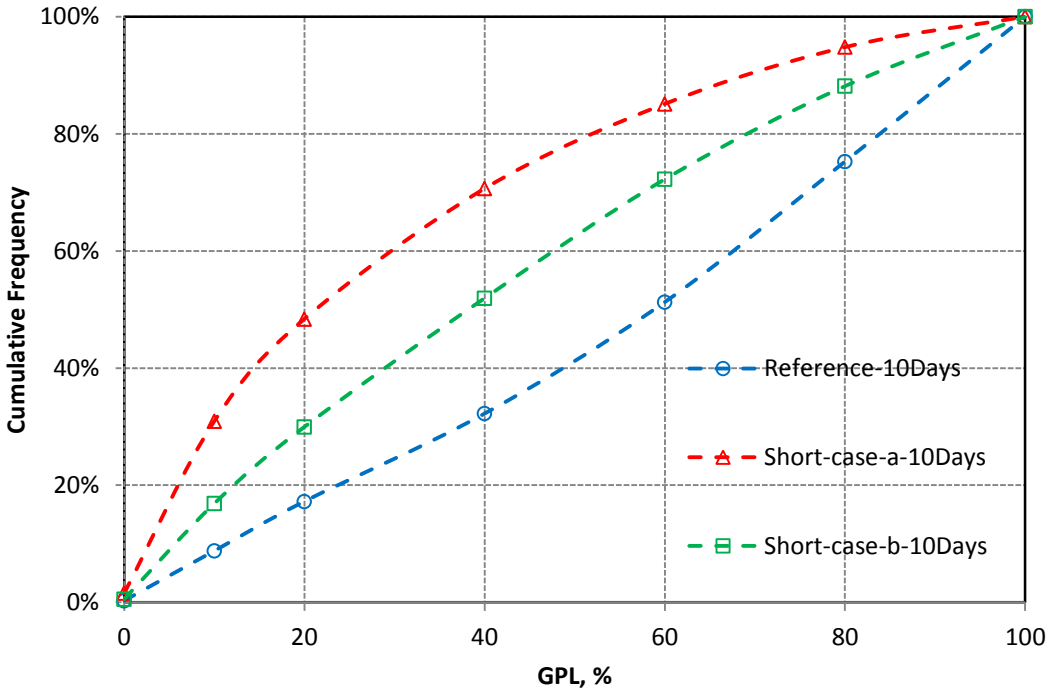

Figure 6.19: The percentage of the cumulative frequency of the cases with both fracture lengths of 100 m (short fracture case-a and case-b) and 400 m (reference model) versus GPL% after 10 days

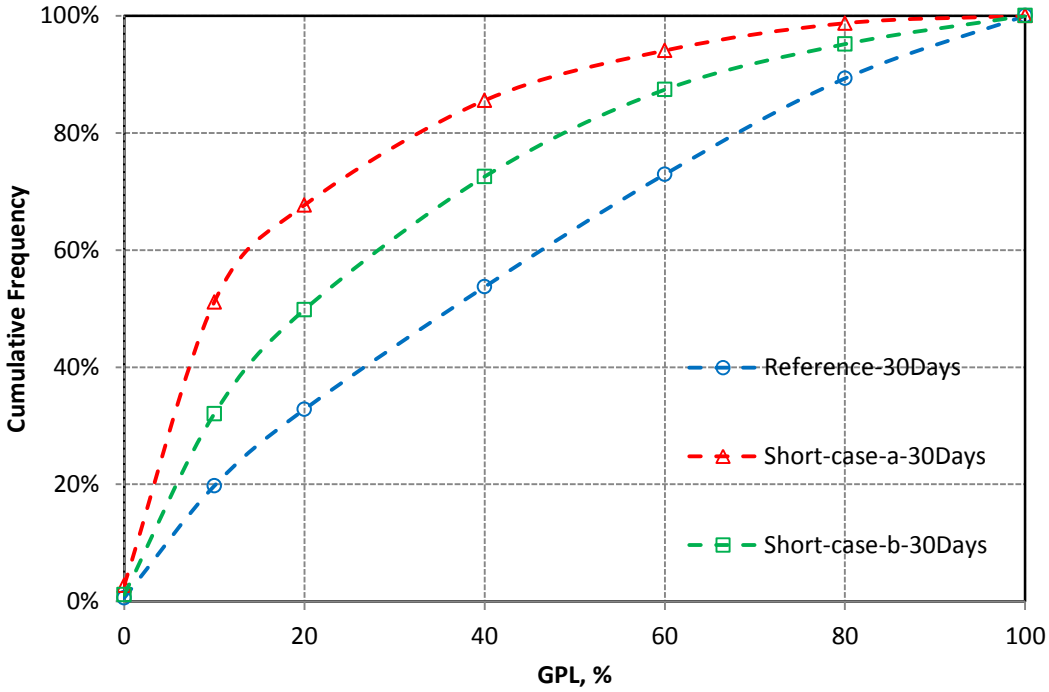

Figure 6.20: The percentage of the cumulative frequency of the cases with both fracture lengths of 100 m (short fracture case-a and case-b) and 400 m (reference model) versus GPL% after 30 days

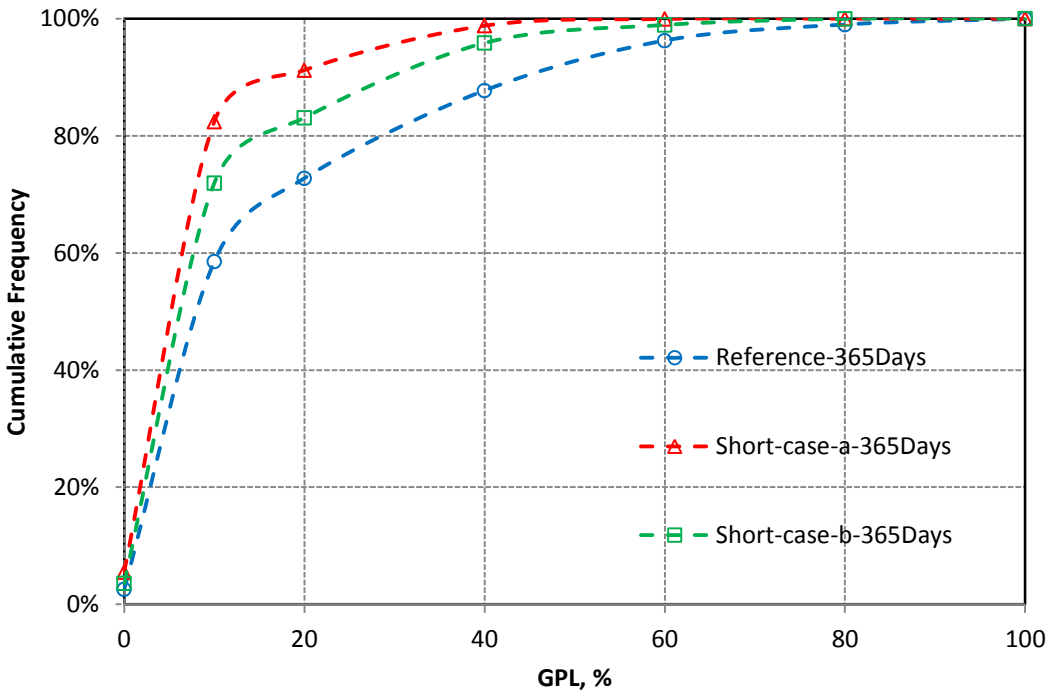

Figure 6.21: The percentage of the cumulative frequency of the cases with both fracture lengths of 100 m (short fracture case-a and case-b) and 400 m (reference model) versus GPL% after 365 days

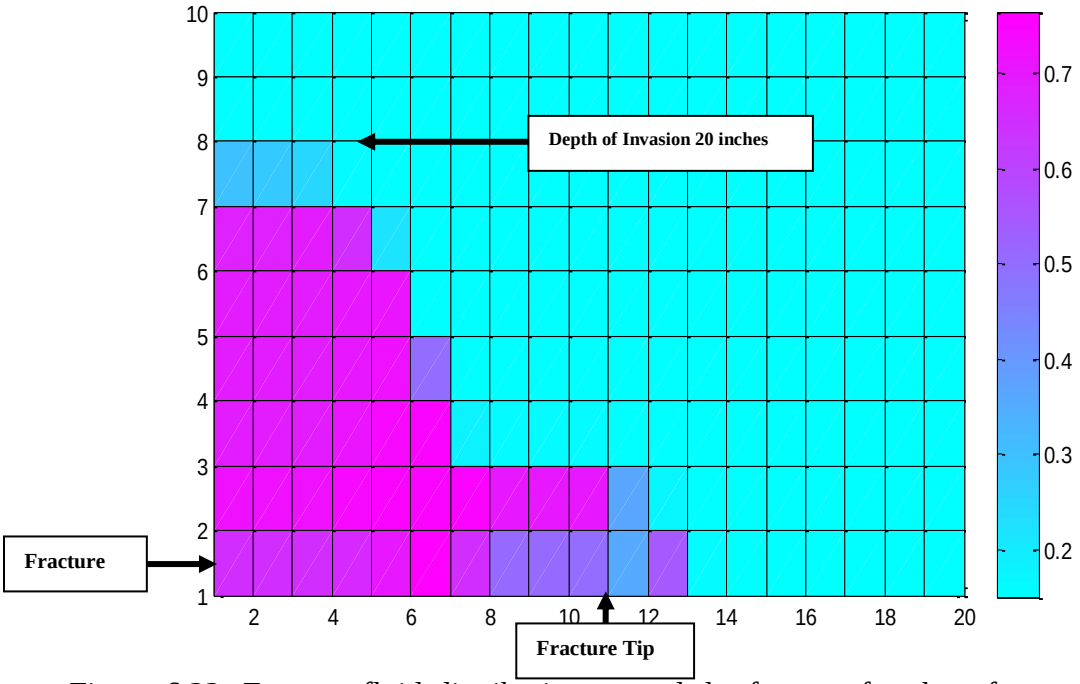

Figure 6.22: Fracture fluid distribution around the fracture for short fracture (case b) model after two days shut-in time. Worst Case Scenario

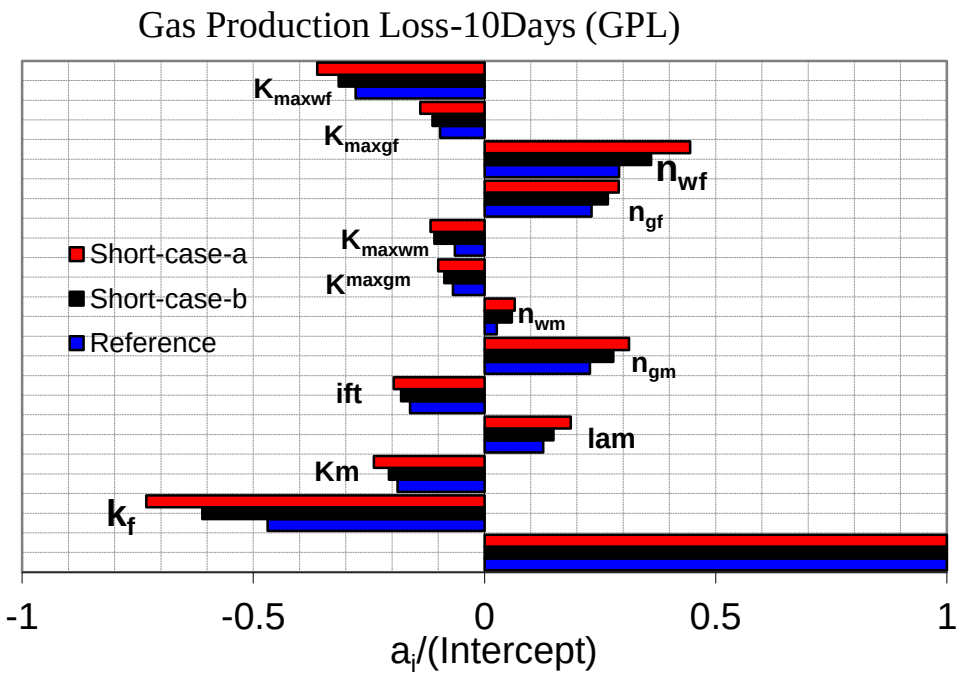

Figure 6.23: Tornado chart of primary coefficients of all pertinent parameters on gas production loss (Linear Response Surface Model, without interaction) for Reference, short fracture case-a, and case-b Models after 10 days of production.

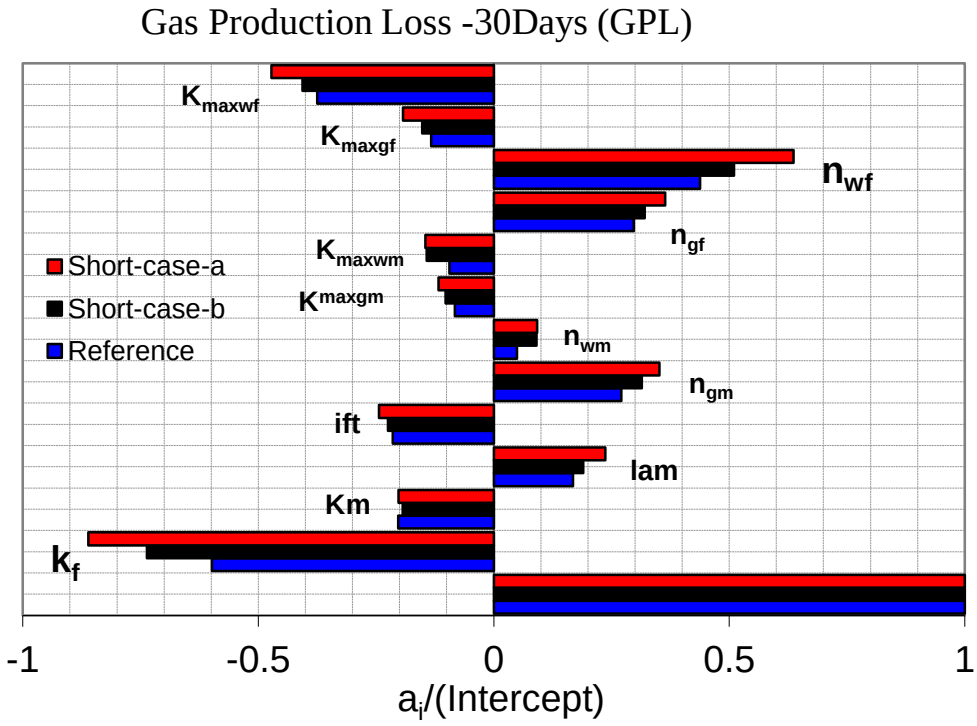

Figure 6.24: Tornado chart of primary coefficients of all pertinent parameters on gas production loss (Linear Response Surface Model, without interaction) for Reference, short fracture case-a, and case-b Models after 30 days of production.

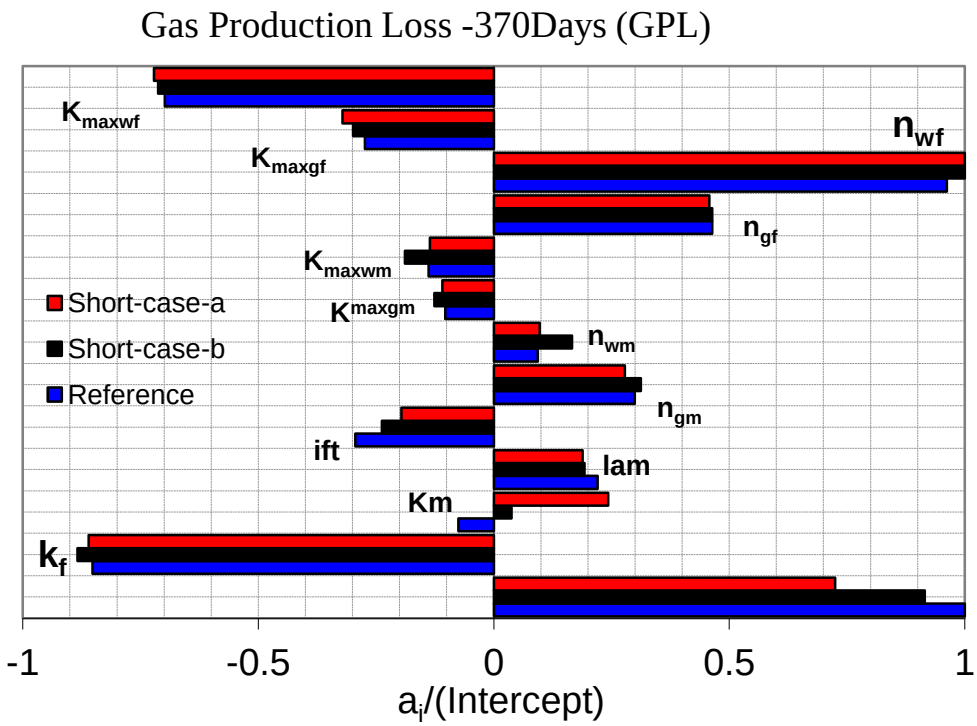

Figure 6.25: Tornado chart of primary coefficients of all pertinent parameters on gas production loss (Linear Response Surface Model, without interaction) for Reference, short fracture case-a, and case-b Models after 365 days of production.

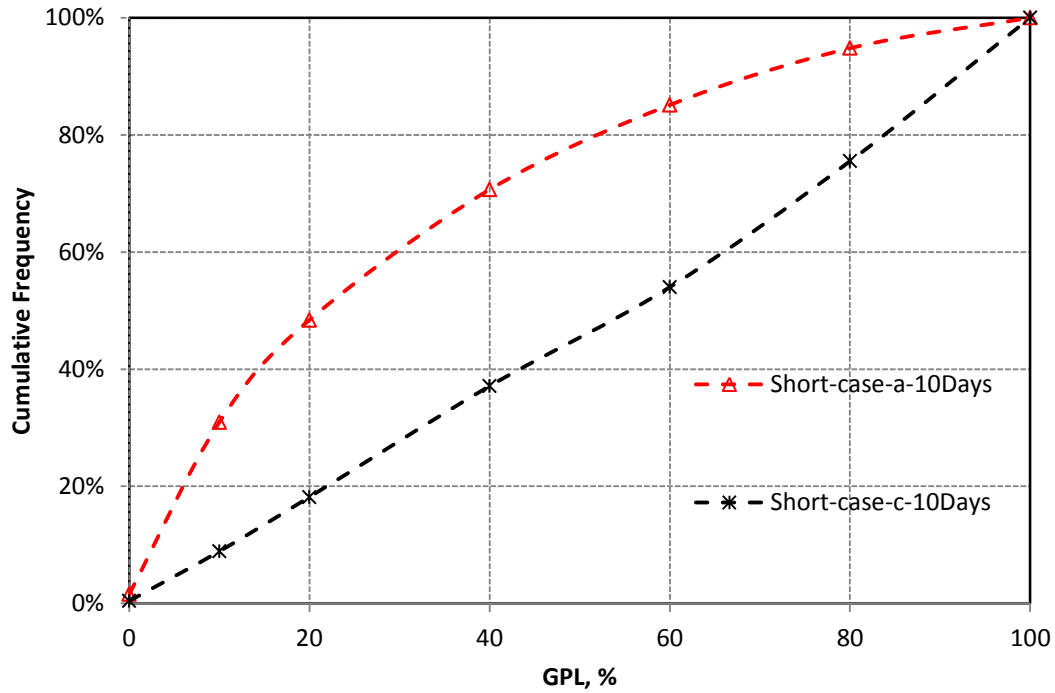

Figure 6.26: The percentage of the cumulative frequency of the cases with both fracture lengths of 100 m (short fracture case-a and case-b) versus GPL% after 10 days

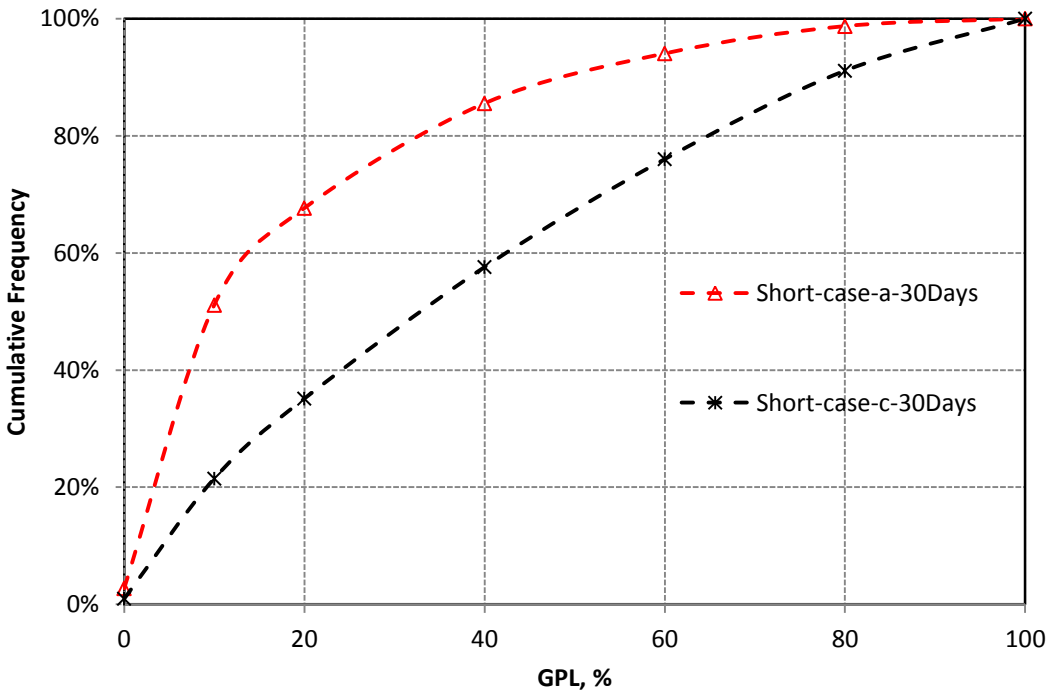

Figure 6.27: The percentage of the cumulative frequency of the cases with both fracture lengths of 100 m (short fracture case-a and case-b) versus GPL% after 30 days.

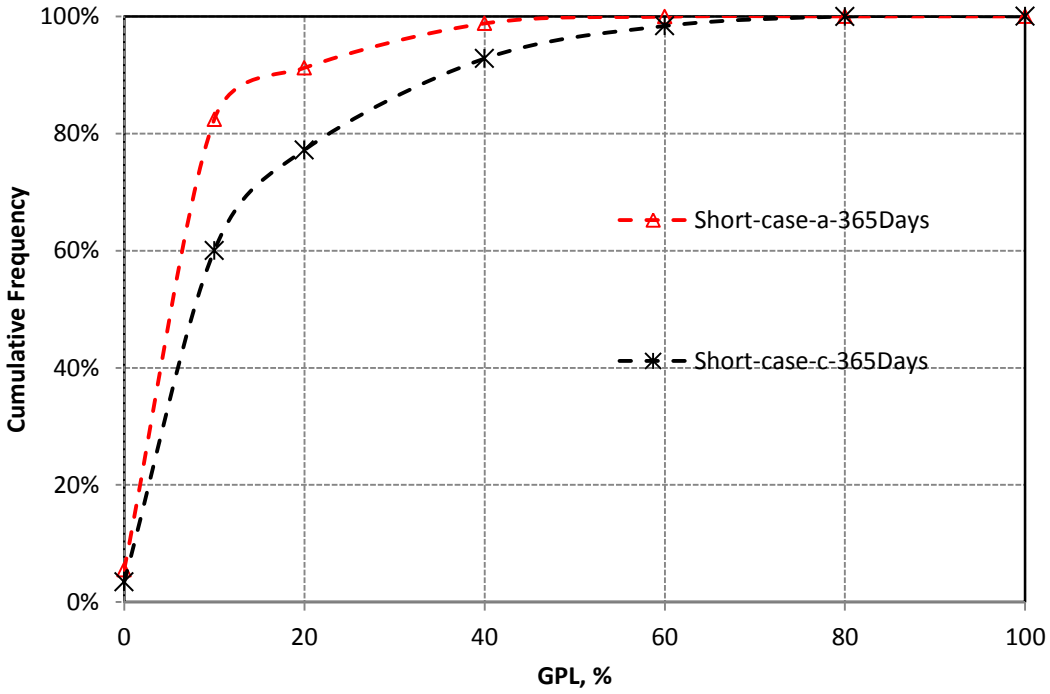

Figure 6.28: the percentage of the cumulative frequency of the cases with both fracture lengths of 100 m (short fracture case-a and case-b) versus GPL% after 365 days

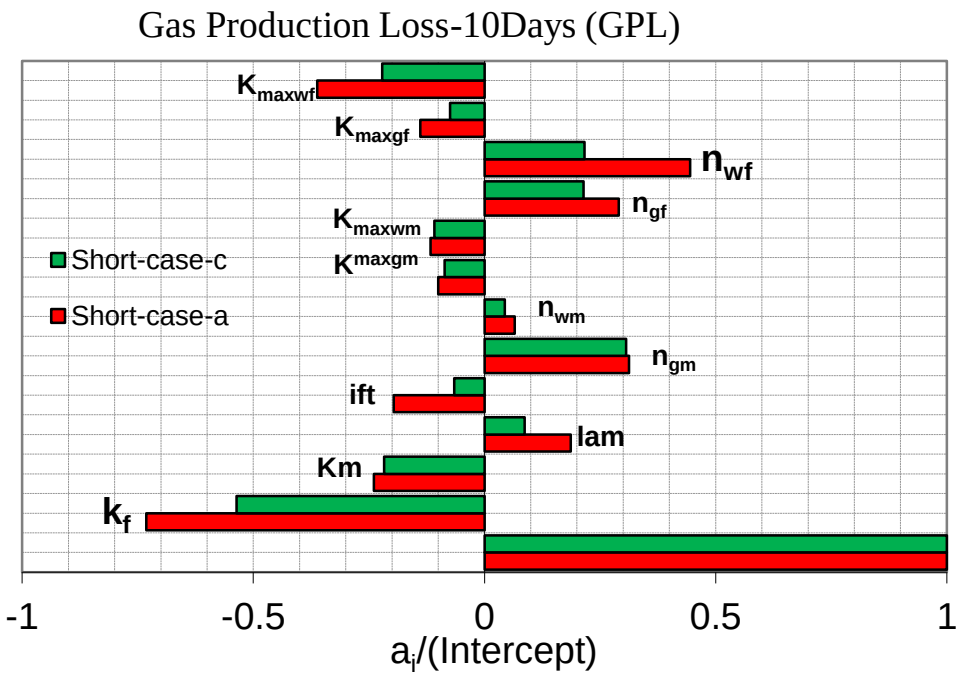

Figure 6.29: Tornado chart of primary coefficients of all pertinent parameters on gas production loss (Linear Response Surface Model, without interaction) for short fracture case-a, and case-c Models after 10 days of production.

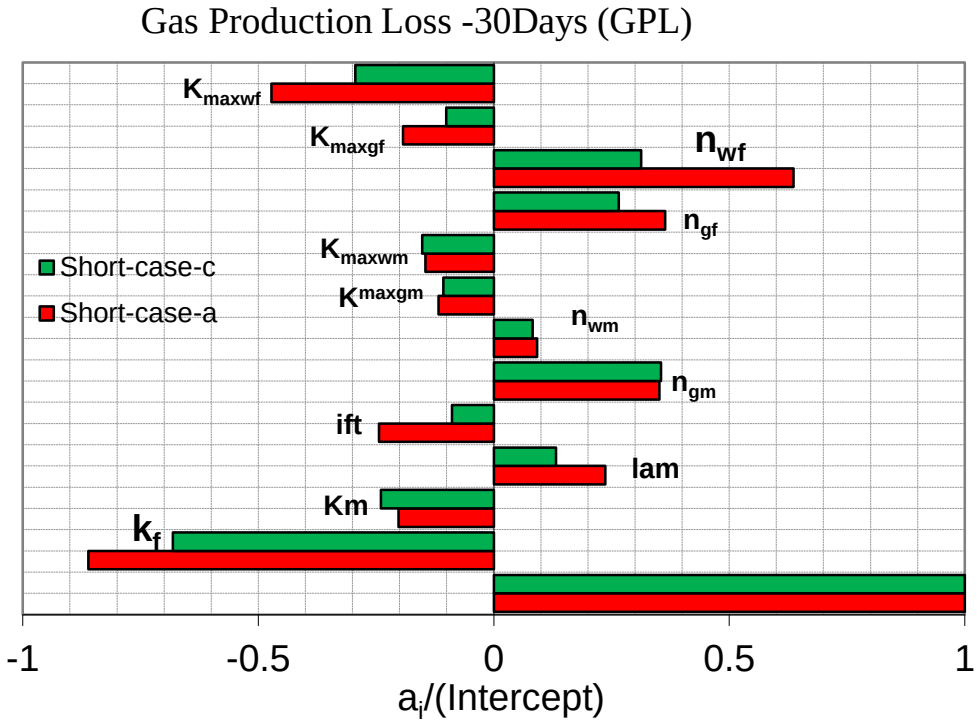

Figure 6.30: Tornado chart of primary coefficients of all pertinent parameters on gas production loss (Linear Response Surface Model, without interaction) for short fracture case-a, and case-c Models after 30 days of production.

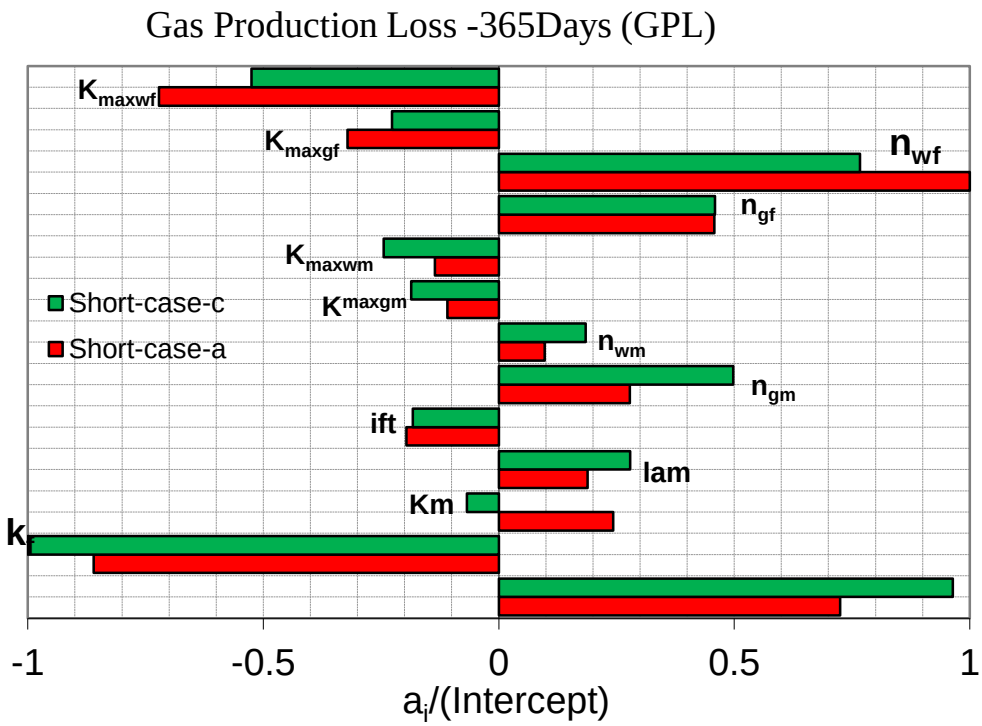

Figure 6.31: Tornado chart of primary coefficients of all pertinent parameters on gas production loss (Linear Response Surface Model, without interaction) for short fracture case-a, and case-c Models after 365 days of production.

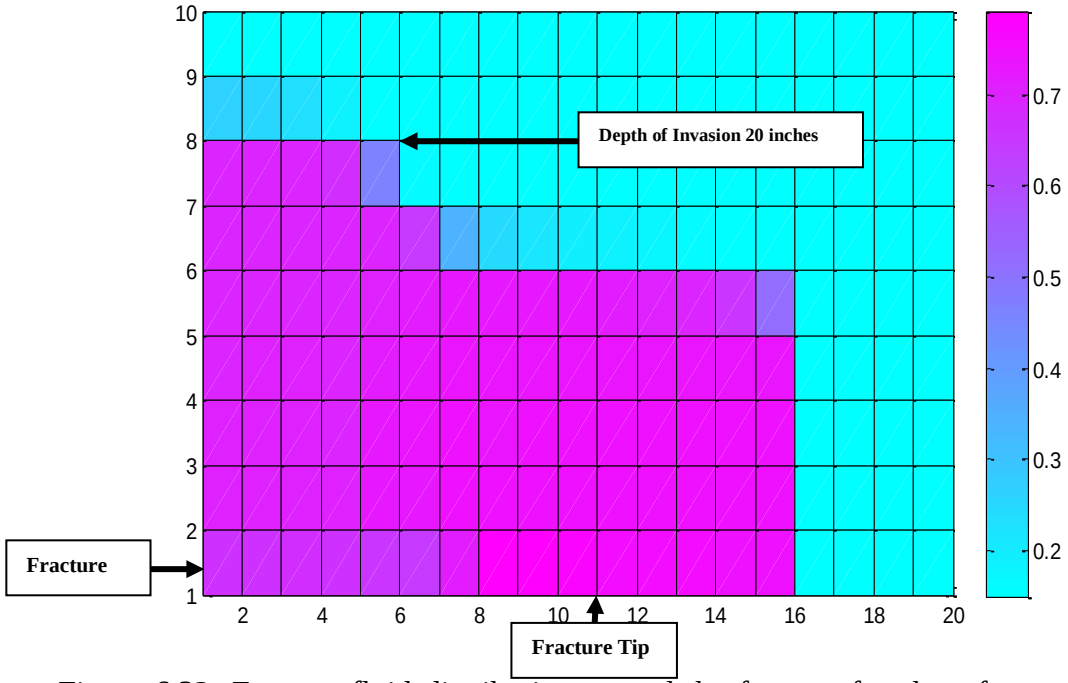

Figure 6.32: Fracture fluid distribution around the fracture for short fracture (case c) model after two days shut-in time. Worst Case Scenario

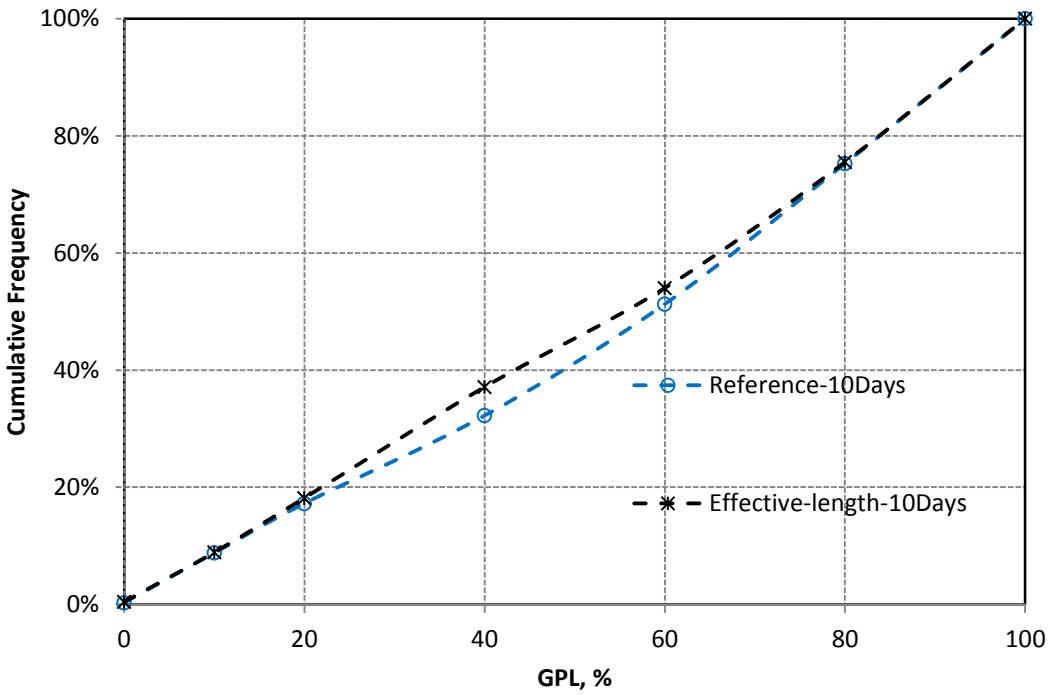

Figure 6.33: The percentage of the cumulative frequency of the cases with both fracture lengths of 100 m (reference and effective length models) versus GPL% after 10 days.

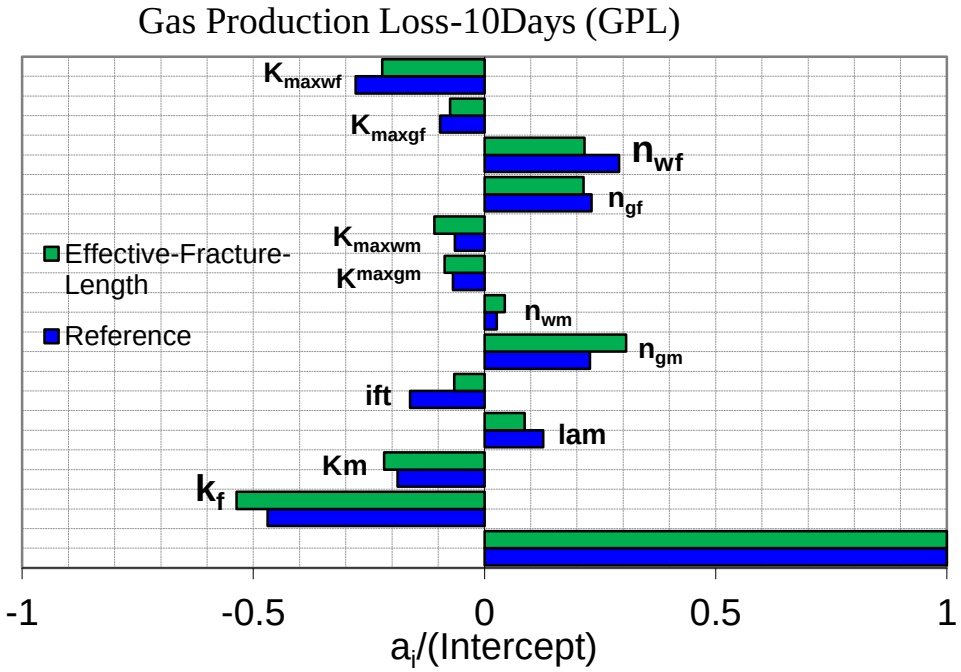

Figure 6.34: Tornado chart of primary coefficients of all pertinent parameters on gas production loss (Linear Response Surface Model, without interaction) for reference and effective length Models after 10 days of production.

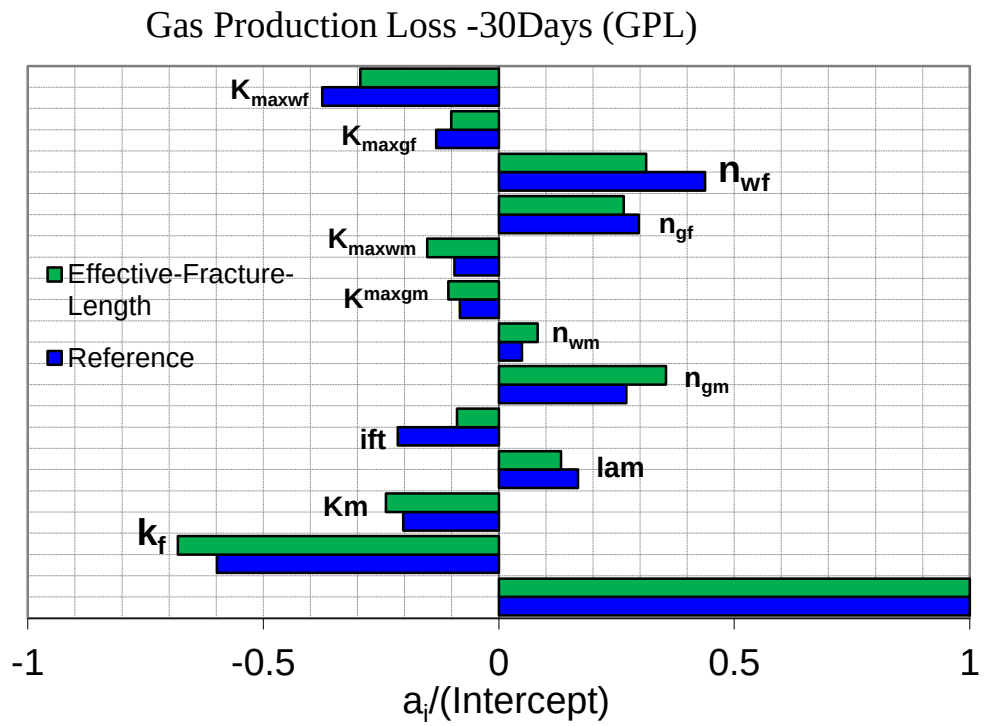

Figure 6.35: Tornado chart of primary coefficients of all pertinent parameters on gas production loss (Linear Response Surface Model, without interaction) for reference and effective length Models after 30 days of production.

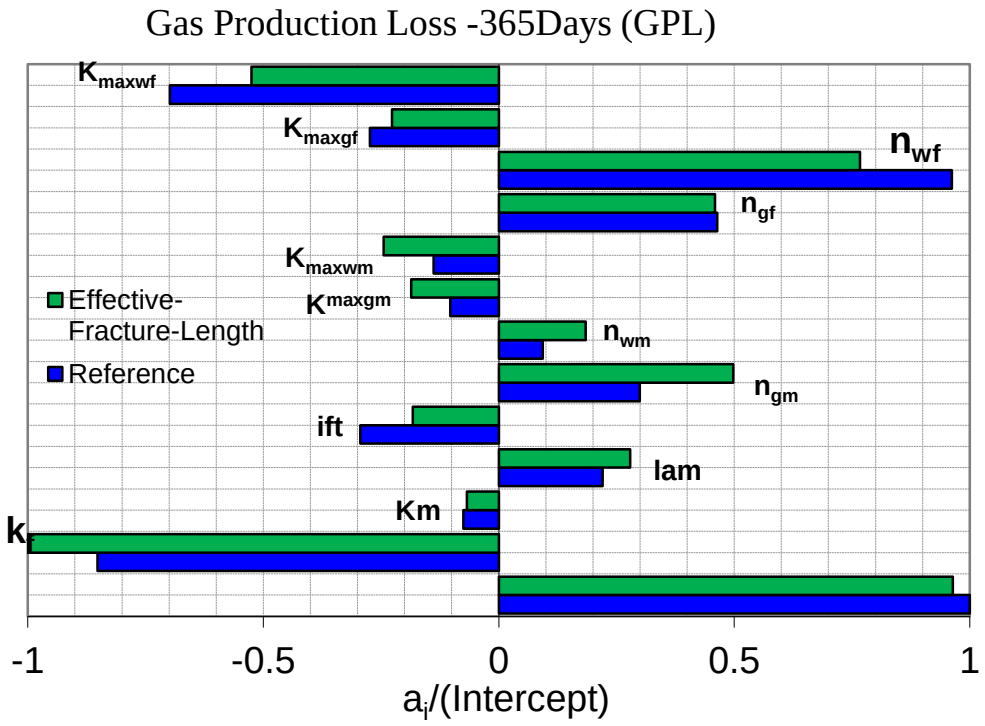

Figure 6.36: Tornado chart of primary coefficients of all pertinent parameters on gas production loss (Linear Response Surface Model, without interaction) for reference and effective length Models after 365 days of production.

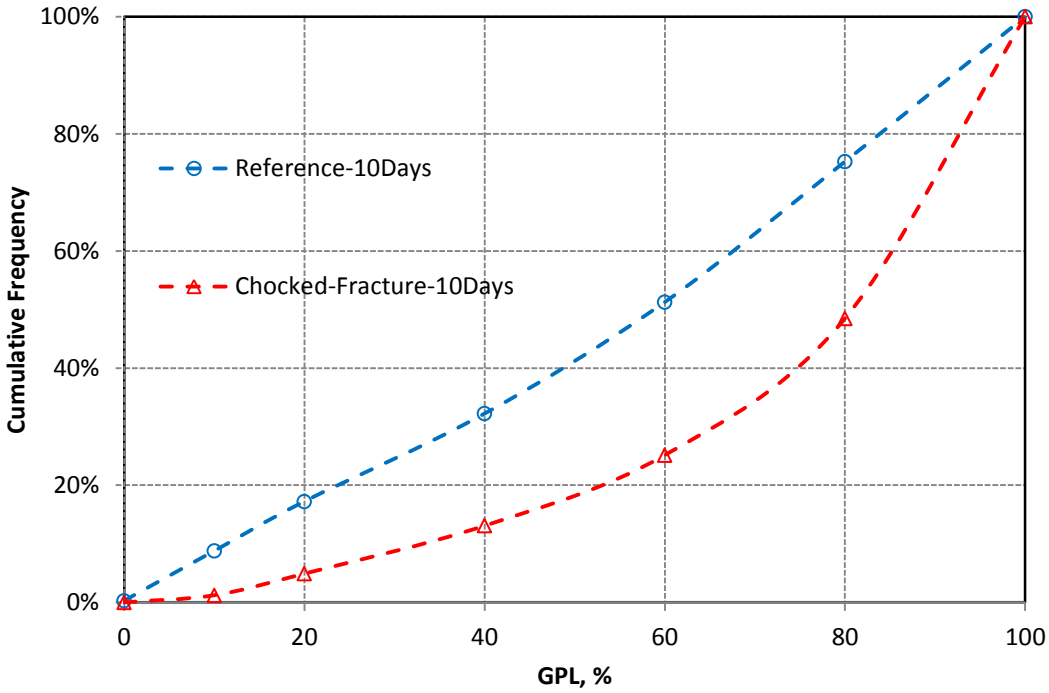

Figure 6.37: the percentage of the cumulative frequency of the cases with both fracture lengths of 100 m (Non-uniform permeability case-a and reference model) versus GPL% after 10 days

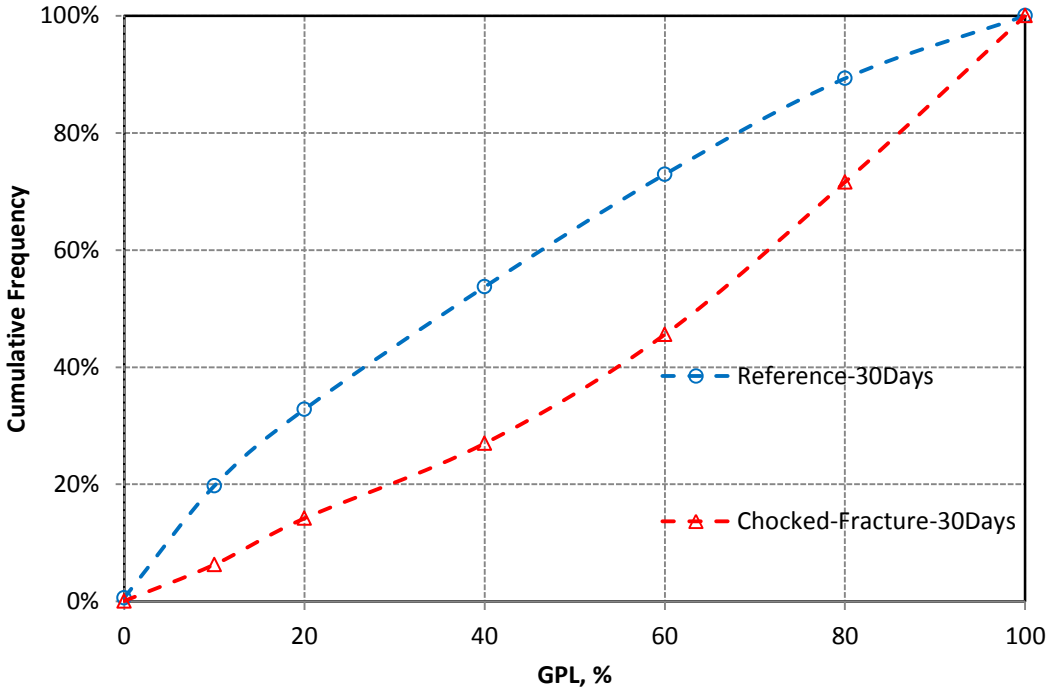

Figure 6.38: the percentage of the cumulative frequency of the cases with both fracture lengths of 100 m (Non-uniform permeability case-a and reference model) versus GPL% after 30 days

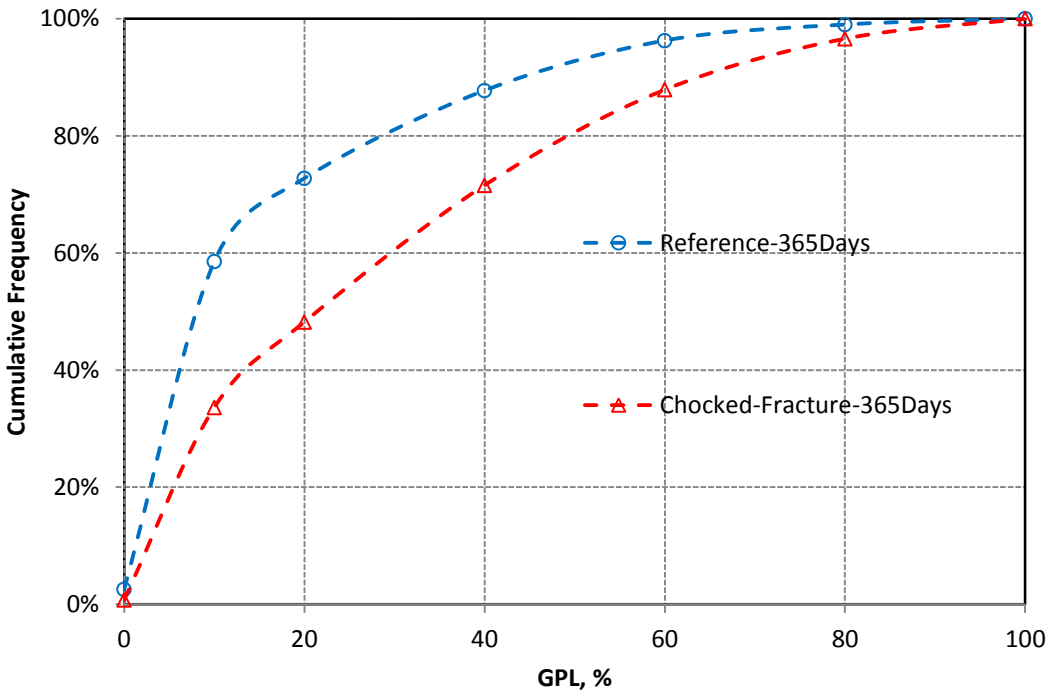

Figure 6.39: the percentage of the cumulative frequency of the cases with both fracture lengths of 100 m (Non-uniform permeability case-a and reference model) versus GPL% after 365 days

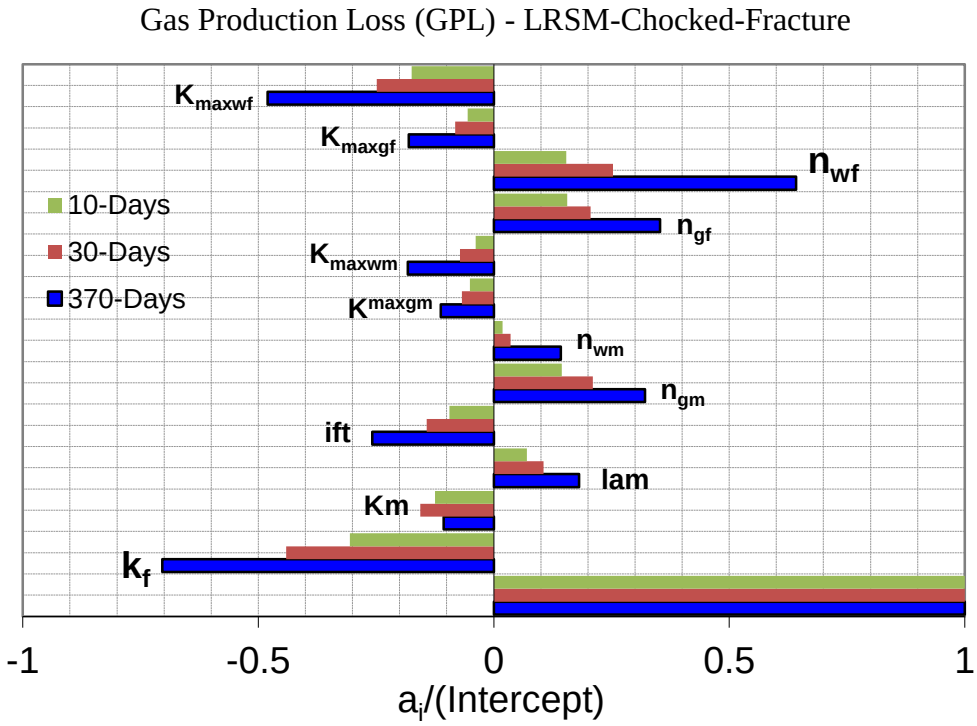

Figure 6.40: Tornado chart of primary coefficients of all pertinent parameters on gas production loss (Linear Response Surface Model, without interaction) for Non-uniform permeability case-a after 10,30,365 days of production.

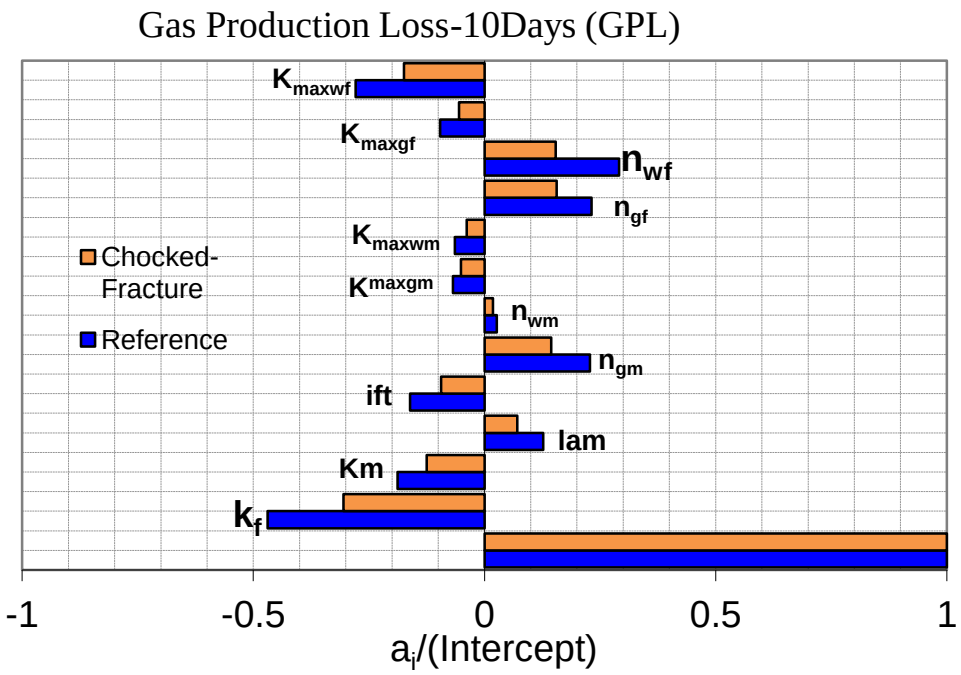

Figure 6.41: Tornado chart of primary coefficients of all pertinent parameters on gas production loss (Linear Response Surface Model, without interaction) for reference and Non-uniform permeability case-a Models after 10 days of production.

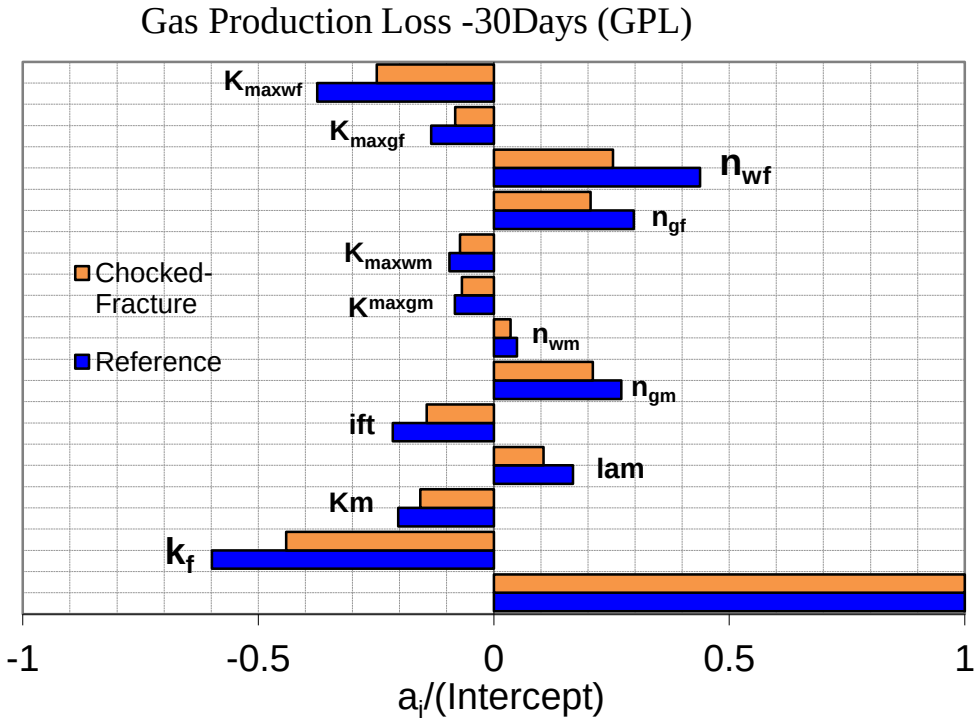

Figure 6.42: Tornado chart of primary coefficients of all pertinent parameters on gas production loss (Linear Response Surface Model, without interaction) for reference and Non-uniform permeability case-a Models after 30 days of production.

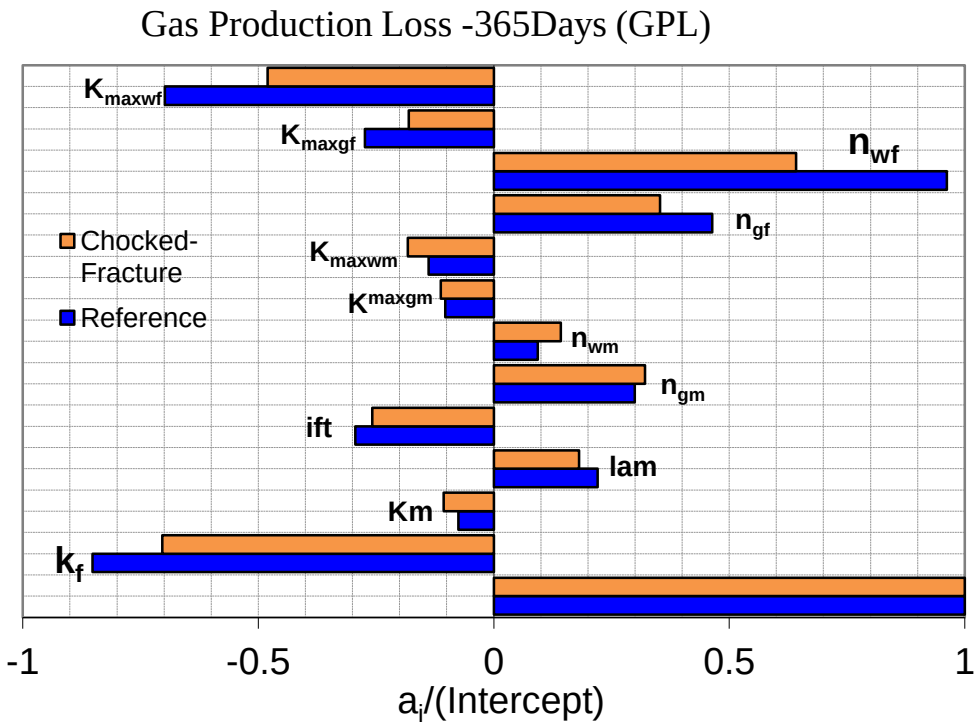

Figure 6.43: Tornado chart of primary coefficients of all pertinent parameters on gas production loss (Linear Response Surface Model, without interaction) for reference and Non-uniform permeability case-a Models after 365 days of production.

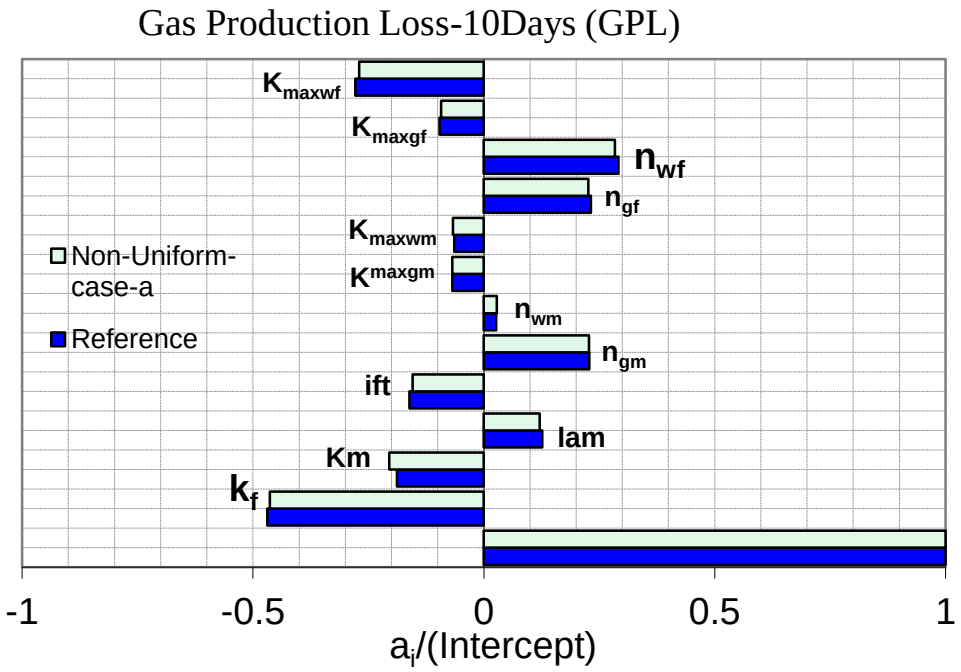

Figure 6.44: Tornado chart of primary coefficients of all pertinent parameters on gas production loss (Linear Response Surface Model, without interaction) for reference and Non-uniform permeability case-b Models after 10 days of production.

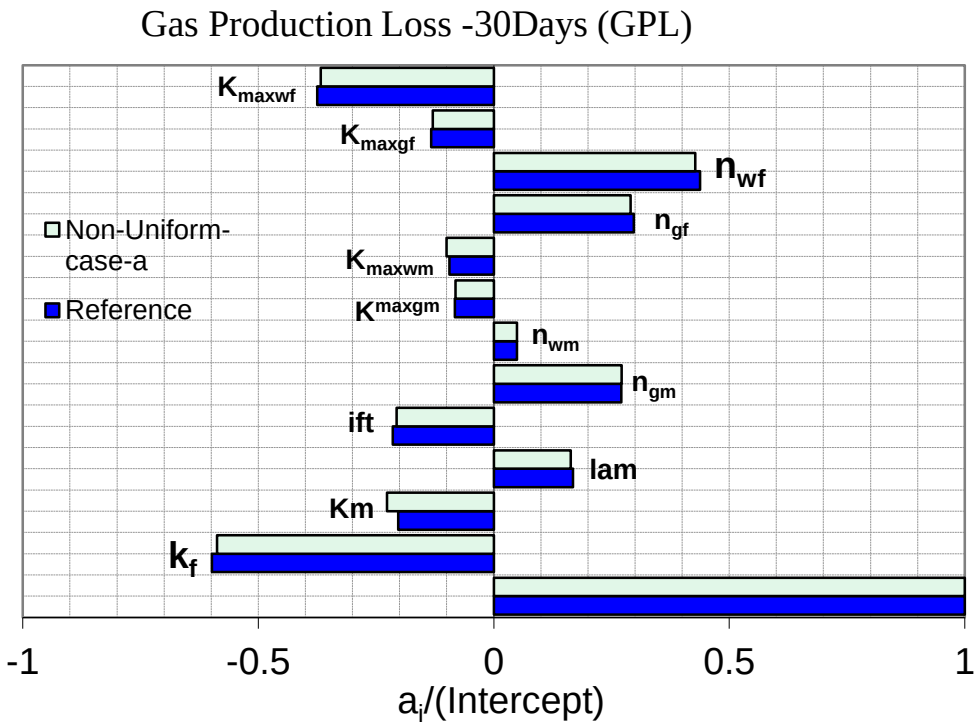

Figure 6.45: Tornado chart of primary coefficients of all pertinent parameters on gas production loss (Linear Response Surface Model, without interaction) for reference and Non-uniform permeability case-b Models after 30 days of production.

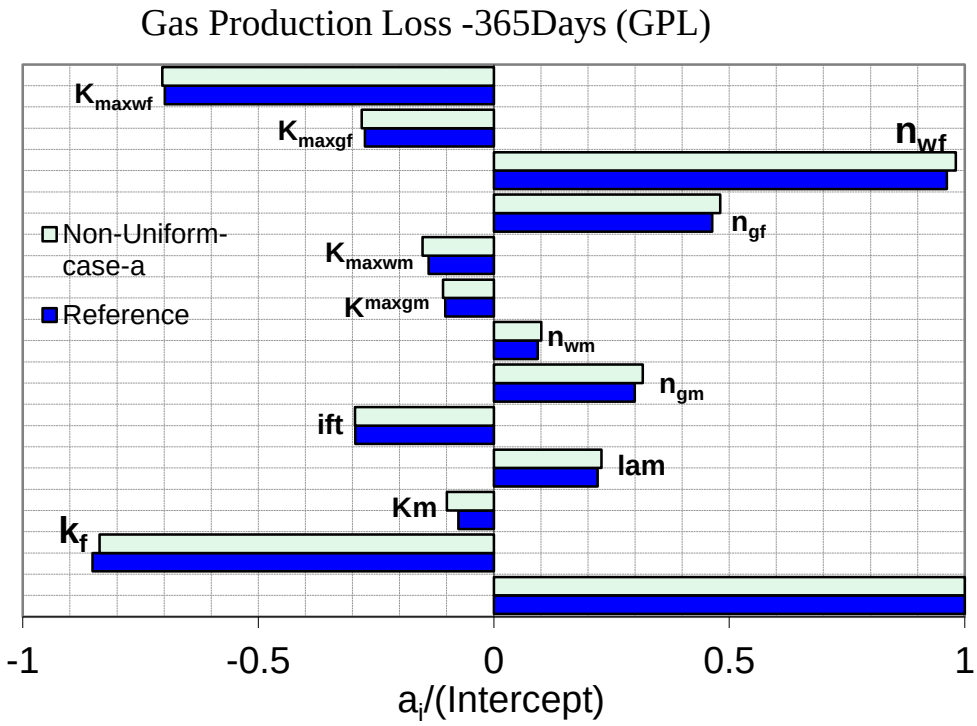

Figure 6.46: Tornado chart of primary coefficients of all pertinent parameters on gas production loss (Linear Response Surface Model, without interaction) for reference and Non-uniform permeability case-a Models after 365 days of production.

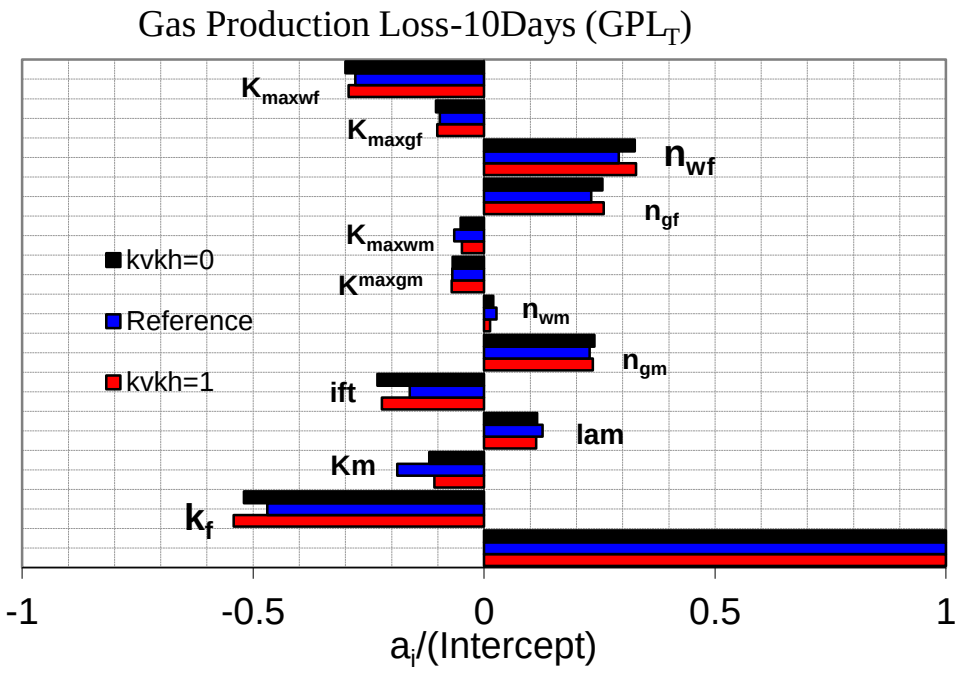

Figure 6.47: Tornado chart of primary coefficients of all pertinent parameters on gas production loss (Linear Response Surface Model, without interaction) for reference and multi-layer (with and without cross flow) Models after 10 days of production.

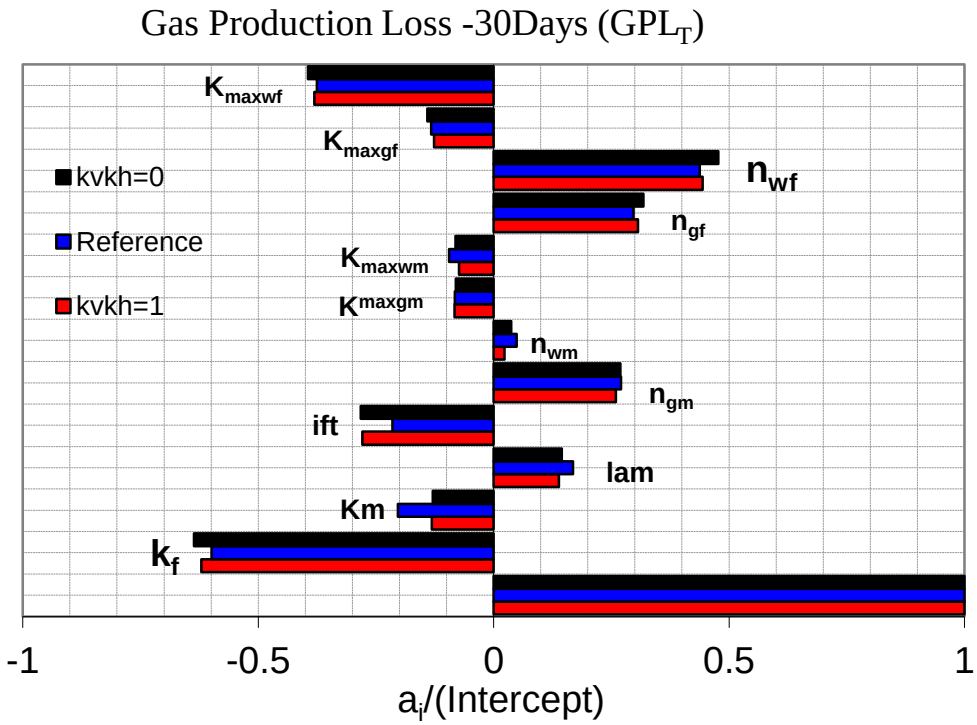

Figure 6.48: Tornado chart of primary coefficients of all pertinent parameters on gas production loss (Linear Response Surface Model, without interaction) for reference and multi-layer (with and without cross flow) Models after 30 days of production.

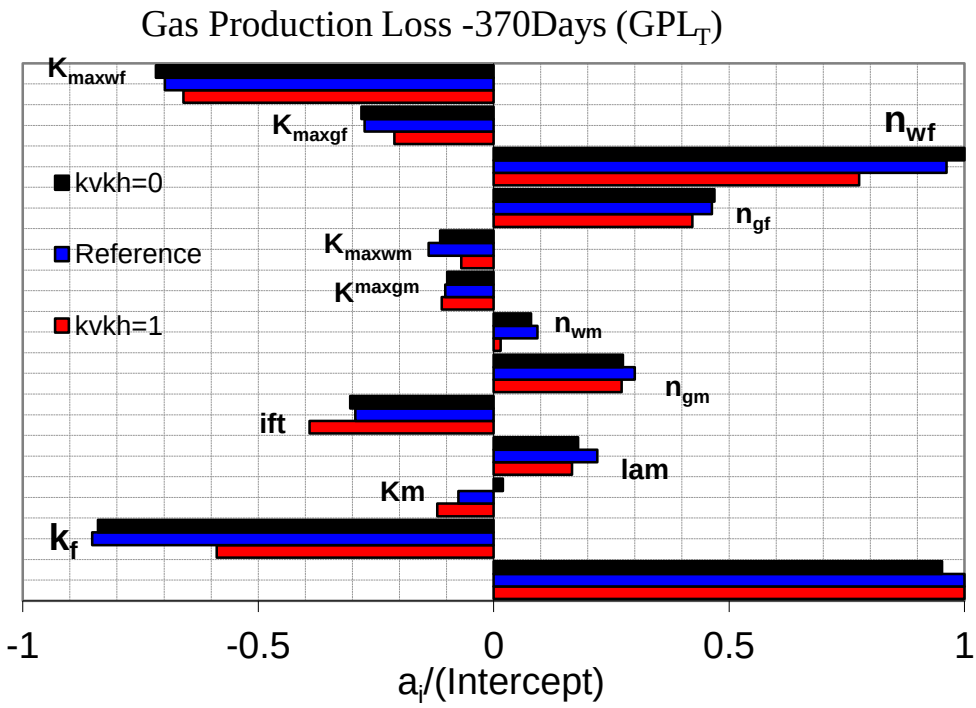

Figure 6.49: Tornado chart of primary coefficients of all pertinent parameters on gas production loss (Linear Response Surface Model, without interaction) for reference and multi-layer (with and without cross flow) Models after 365 days of production.

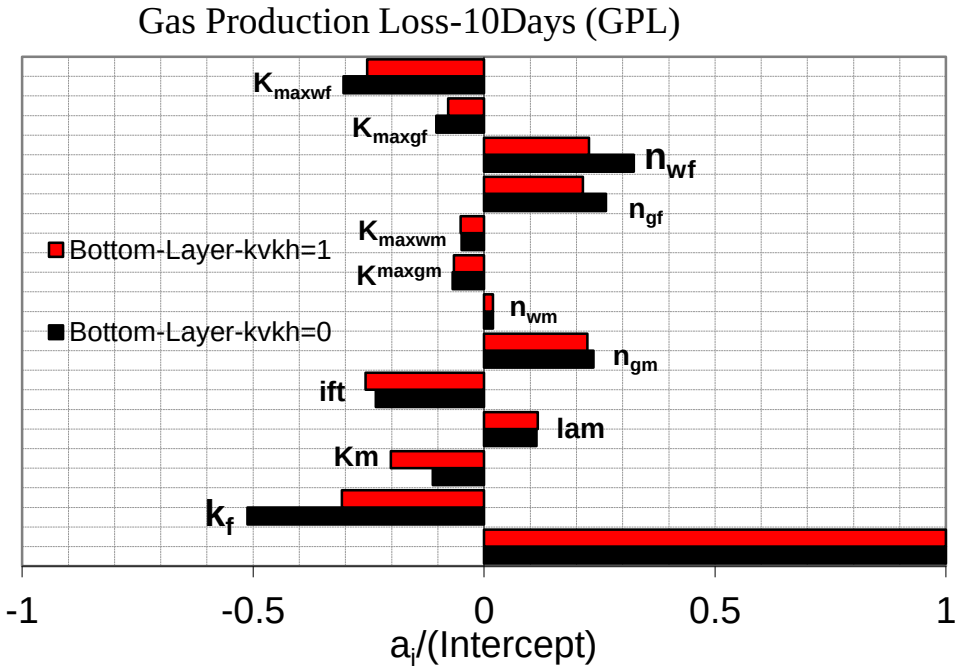

Figure 6.50: Tornado chart of primary coefficients of all pertinent parameters on Bottom layer gas production loss (Linear Response Surface Model, without interaction) for multi-layer (with and without cross flow) Model after 10 days of production.

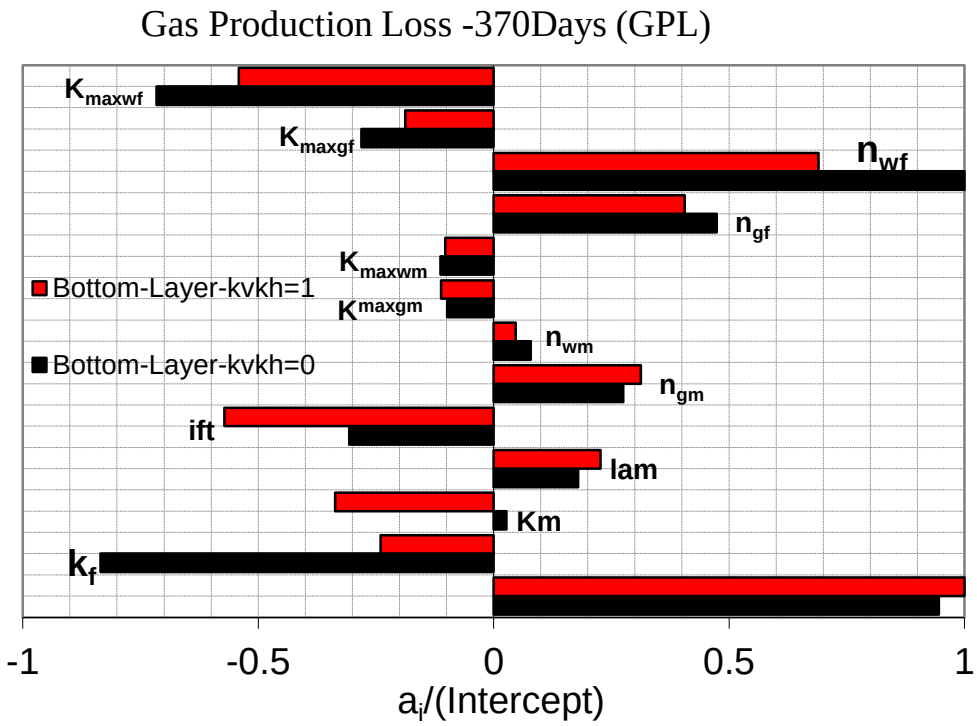

Figure 6.51: Tornado chart of primary coefficients of all pertinent parameters on Bottom layer gas production loss (Linear Response Surface Model, without interaction) for multi-layer (with and without cross flow) Model after 365 days of production

CONCLUSIONS AND RECOMMENDATIONS

7.1 CONCLUSIONS

Gas Condensate Flow around Single Layer Hydraulically Wells:

A number of in-house simulators were developed to study the well performance of single layer hydraulically fractured wells (HFWs) in gas and gas condensate reservoirs. The simulator initially simulated both steady-state or pseudo-steady state flow around one planar HF but then for the first time, extended to two fractures intersecting the well at 90 degree angle. The models correctly account for the coupling (increase in *kr* by a decrease in IFT or increase in velocity) and inertia (decrease in *kr* by an increase in velocity) that affect the flow performance of gas condensate reservoirs. The integrity of the results of the in-house simulators were confirmed by comparing some of their results with those obtained using ECLIPSE with fine grid for the same prevailing flow conditions. Based on the assumption and results presented in chapter 3, the following conclusions can be drawn

1. Based on the pressure distribution maps around HFWs, it was shown that flow around high conductivity fractures is elliptical; however it converges to radial flow with decreasing fracture conductivity. These observations are consistent with literature studies (e.g. Prats 1961).
2. Based on the dimensionless velocity profile inside the fracture, it was shown that flow velocity across the fracture is uniform and directly proportional to dimensionless distance for high conductivity fractures ($24< C_{FD} >240$), while as fracture conductivity decreases ($0.24< C_{FD} >2.4$) the flow velocity decrease significantly in the farthest part of the fracture, however, it increases steeply in the area near to the wellbore.
3. It was shown that for small fracture conductivity ($C_{FD} \rightarrow$ zero) or small penetration ratio ($I_x < 0.2$) the geometric skin of HFW at steady-state conditions is the same as that at pseudo-steady state conditions, however, as fracture conductivity increase and the fracture penetration ratio is greater than 0.2 ($I_x > 0.2$), geometric skin of SS and PSS are different. These observations are in line with similar studies in the literature (e.g. Raghavan 1978).

4. New formulae (Equations 3.53 and 3.54) were developed for estimation of geometric skin of HFW intercepted by two perpendicular fractures at SS and PSS.
5. For Single phase Non-Darcy flow, it was explained that the inertia is dominant inside the fracture; while velocity effects inside the matrix are not significant. These observations are consistent with literature studies (e.g. Guppy 1982).
6. Also, it was shown that Non-Darcy effects can manifest itself as a reduction in absolute fracture dimensionless conductivity $C_{FD.}$
7. A new more efficient formulation to estimate single phase effective dimensionless fracture conductivity ($C_{FD\text{-}eff}$) was proposed (Equation 3.67) based on the results of more than 1400 (Non-Darcy flow simulations) covering a wide range of pertinent geometrical and flow parameters. This approach was initially followed for a single-fracture model but then, for the first time, extended to multiple (two-perpendicular) fracture systems, which simplifies to single planner fracture system when the number of fracture is set to one.
8. A new and efficient formula (Equation 3.76) for single phase total skin of HFW was proposed benefiting from the newly developed ($C_{FD\text{-}eff}$) formula (Equation 3.67).
9. This total skin (Equation 3.76) was used to estimate effective wellbore radius (Equation 3.78) for an equivalent open-hole (EOH) system replicating flow around HFWs.
10. Because of dependency of effective wellbore radius formulation to flow rate (Equation 3.78) an iterative procedure for using the developed formula for estimation of effective wellbore radius was proposed.
11. It was shown that for most practical cases of two phase flow, inertia is dominant inside the fracture, while coupling is more dominant inside the matrix. This is in line with similar observations made by Carvajal (2005) and Mahdiyar (2008) who worked in the HW-GCR research team.
12. Accordingly a new and efficient formula (Equation 3.110) was proposed to estimate two phase effective dimensionless fracture conductivity ($C_{FD\text{-}eff}$).
13. A new formula (Equation 3.113) for two phase total skin of HFW was proposed based on the newly developed two phase dimensionless fracture conductivity formula (Equation 3.110).
14. The proposed formulations are general, as it correctly extends to the single fracture case if the number of fracture is set to one. If gas fractional flow

(GTR_{well}) is set to unity, it also correctly converts to the single phase gas systems under Non-Darcy flow, and if Reynolds number is small to that under Darcy flow.

15. The author developed a 1-D equivalent open-hole (EOH) simulator that incorporates the proposed effective wellbore radius formulation and associated iterative procedure to model gas condensate flow around HFW.
16. It was shown that the 1-D simulator can saves CPU time and reduces troubleshooting process associated with modelling such complex flow geometries using commercial compositional simulators.
17. The integrity of the 1-D simulator was verified by comparing its results with those of (fine grid) 2-D in-house simulator for more than (1600 simulations) covering a wide range of geometrical and flow parameters including single and two phase flow conditions for both single and two fracture systems considered here. It was also shown that the convergence rate for the incorporated iterative process acceptable (around 2-3 iterations for most studied cases), all making the proposed approach very attractive.
18. The close agreement between both simulators, highlight the added value of using 1-D simulator as a quick tool for long term performance prediction and reservoir sensitivity analysis.
19. The proposed formulations and procedures mentioned above are applicable to both steady state and pseudo-steady state conditions.

Gas Condensate Flow around Multi-Layer Hydraulically Wells:

A number of in-house simulators were developed, for the first time, to study the well performance of Multi-Layer hydraulically fractured wells (HFWs) in gas and gas condensate reservoirs under both steady-state and pseudo-steady state conditions. The models correctly account for the coupling and inertial effects. The integrity of the results of the in-house simulators were confirmed by comparing some of their results with those obtained using ECLIPSE with fine grid for the same prevailing flow conditions. Based on the assumption and results presented in chapter 4, the following conclusions can be drawn.

1. The developed single layer geometric skin factor (presented in Chapter 3) can be extended to multi-layer HFW using an equivalent single layer with

equivalent dimensionless fracture conductivity (C_{FD-eq}) and equivalent fracture length (x_{f-eq}).

2. The needed formulation for equivalent dimensionless fracture conductivity (C_{FD-eq}) (Equation 4.8) and equivalent fracture length (x_{f-eq}) (Equation 4.10) has been proposed and verified for a wide range of pertinent geometrical parameters.
3. For Non-Darcy flow, multi-layer systems can be modelled using an equivalent single layer concept, provided that an appropriate expression of effective or equivalent single phase inertial factor (β_{eff}) is available.
4. In this study an approximation for effective or equivalent single phase inertial factor (β_{eff}) (Equation 4.24) has been proposed and verified for Multi-layer fractured and Non-Fractured wells over a wide range of geometrical and flow parameters.
5. For the case of two-phase gas condensate flow, an equivalent single layer (base curve) relative permeability (Equation 4.33) has been presented and its applicability for the calculation of coupling and inertia effects has been verified over a wide range of geometrical and flow parameters.
6. The proposed formulations are general, as it correctly extends to a single layer system if the number of layers is set to one. If gas fractional flow (GTR_{well}) is set to unity, it also correctly converts to the single phase gas systems under Non-Darcy flow, and if Reynolds number is small to that under Darcy flow.
7. A 1-D in-house simulator was developed by the author to study gas condensate flow in multi-layer systems (fractured and Non-fractured wells). The integrity of this simulator has been verified by comparing its results with those obtained using the fine grid 3-D in-house mathematical simulator.
8. The added value of using the 1-D in-house simulator was confirmed by demonstrating the close agreement between its results and those obtained from the fine grid 3-D in-house simulator. That is, the 1-D simulator produces the same results as those of the 3-D simulator with less computational time and minimal troubleshooting process.
9. The proposed formulations and procedures mentioned above are applicable to both steady state and pseudo-steady state conditions.

Fracture Optimization in Gas Condensate Reservoirs:

In this study the author benefited from the effective wellbore radius formulation presented in Chapter 3, to develop a new fracture optimization formulations to estimate maximum productivity index ($J_{D\text{-}max}$, Equation 5.58) and optimum penetration ratio ($I_{x\text{-}opt}$, Equation 5.59) for a given proppant number in gas condensate reservoirs including coupling and inertial effects. These formulations are applicable to steady state and pseudo-steady state conditions.

The proposed formulations are general in the sense that if the well total gas fractional flow (GTR_{well}) is unity, then it correctly converts to those of single phase gas systems under Non-Darcy flow conditions and when Reynolds number is small to that under Darcy flow conditions.

The author also proposed an effective proppant number (N_{Peff}) formula (Equation 5.60); which corrects the absolute proppant number (N_P) for the combined effect of coupling and inertia in gas condensate reservoirs.

Using the proposed effective proppant number, the author was able to generalize Valko and Economides 2002, UFD formulations (Equations 5.1a and 5.1b) to account for gas (Non-Darcy flow) and Gas Condensate flow under pseudo-steady state conditions. It should be noted that, the original (Valko and Economides) formulations were only applicable for single phase Darcy flow conditions.

Two in-house simulators were developed to verify the integrity of the proposed formulations. These are a (2-D and EOH 1-D) simulators that for a given proppant number perform many simulations and identify the case with optimum fracture length-width ratio giving maximum well productivity. The 2D model solves the original governing continuity and flow equations whilst the equivalent 1-D model incorporates the formulations and procedures proposed by the author in Chapters 3. For all optimization cases studied, the results of both simulators were in close agreement (AAD < 4%). This highlight the added value of using the 1-D simulator as a quick tool of numerical optimization since it requires much less computational time compared to 2-D simulators.

Several illustrations confirmed the applicability of the newly developed optimization formulae for single phase gas and gas condensate systems.

Clean-Up Efficiency of Hydraulically Fractured Wells:

This study is aimed at evaluation of the impact of pertinent parameters on the clean-up efficiency of a hydraulically fractured (gas) well.

This study is aimed at evaluating of the impact of pertinent parameters on the clean-up efficiency of a hydraulically fractured (gas) well.

First, the author identified some of the key pertinent parameters. a two-level full factorial statistical experimental design method was used to sample a reasonably wide range of variation of pertinent parameters, covering many practical cases. The variation of a total of 12 parameters describing the impact of fracture permeability, matrix permeability, pore size distribution index, threshold pressure, interfacial tension, the exponents and end points of Corey type relative permeability curve for gas and FF in the matrix and fracture have been studied for two separate fracture fluid (FF) volumes.

Since over 36,000 simulation runs were required, to cover the range of variation of all parameters, the simulation process has been simplified using a computer code, which was developed to automatically link different stages of these simulations.

In these simulations, the gas production loss (GPL), compared to the 100% clean fracture case, was also calculated automatically as an output data for each run, at different production periods.

The analysis of the simulation runs using two response surface models (with and without interaction of parameters) demonstrates the relative importance of the pertinent parameters after different production time periods. Also, Histogram Figures and FF Saturation Maps around the fracture were used to support the presented discussions and verify conclusions.

Based on the results of the numerical analysis, first the conclusions of the study are presented followed by some important practical considerations:

1. Fracture fluid distribution around hydraulic fractures is a function of different combination of (rock and fluid) parameters, and does not always yield a uniform distribution as it is often assumed in the literature.
2. As fracture fluid and gas production continues, the number of the cases with severs gas production loss decreases but the relative importance of the pertinent parameters increases.
3. GPL is significantly affected by the parameters which control fracture fluid mobility inside the fracture (K_f, n_{wf}, K_{maxwf}) for all models studied here.

4. Interfacial tension reduces gas production loss (GPL) (especially at late stages). However, its impact reduces significantly as fracture conductivity increases.
5. For the same fracture conductivity, increasing fracture length increases the number of cases with severe GPL.
6. For the same fracture length, increasing fracture conductivity decreases GPL severity.
7. An increase in the fracture fluid injection volume increases the number of cases with severe GPL and delays the fracture clean up.
8. Increasing fracture fluid injection volume increases the importance of gas mobility inside the matrix.
9. GPL is significantly affected by the direction of fracture permeability variation along the fracture length. That is, decreasing fracture permeability toward the wellbore increases GPL severity, i.e. it increases the number of cases with high GPL. There was hardly any difference between the results of the uniform fracture permeability and the case with deceasing permeability away from the wellbore. The results highlight the importance of fracture permeability near the wellbore.

Practical Considerations

10. Clean-up efficiency of hydraulically fractured wells with high fracture conductivity is more effective; however the effectiveness of clean-up process is more dependent on fracture conductivity at later post-treatment times. This is due to the fact that at early production stages fracture fluid saturation inside the fracture is very high and the fracture is mainly producing fracture fluid, however as production time increases fracture fluid saturation inside the fracture decrease and more gas is permitted to flow alongside fracture fluid (i.e. gas effective permeability increased). Thus, the higher the fracture permeability, the higher the gas effective permeability and the lower the gas production loss.
11. Clean-up efficiency of hydraulically fractured wells with high fracture fluid mobility (k_r/μ) inside the fracture is more effective. This can be done by either (decreasing n_{wf} and/or increasing K_{maxwf}) or (decreasing fracture fluid viscosity, which has not been discussed in this study). That is, an effective fracture fluid is the one, which ensures maximum k_r value as well as the lowest possible viscosity that ensure good proppant transportability.

12. Clean-up efficiency of hydraulically fractured wells with high fracture fluid interfacial tension is more effective, for the range of dimensionless fracture conductivity (C_{FD}) used in this study ($1 < C_{FD} > 5$). That is, increasing IFT increases matrix capillary pressure, which in turn retains the fracture fluid deep inside the matrix and allows more gas to flow freely along fracture face and inside the fracture. This contradicts the purpose of industry practice in using interfacial tension reducing agents in order to produce most of the fracturing fluid during the back flow period (after fracturing job).
13. Clean-up efficiency of hydraulically fractured wells with high gas mobility inside the fracture and matrix is more effective, mainly at late stages of production. This can be achieved by performing a chemical treatment to improve either matrix wet-ability toward increasing k_r of gas provided that the treatment process do not add additional flow barrier. However, this treatment can be more effective if it is done at late stage of production when most of fracture fluid is produced from the fracture (i.e. the timing of performing such treatment is very important).

7.2 RECOMMENDATION

The following recommendation are suggested to extend the research presented in this thesis,

For Hydraulically Fractured Wells:

1. The impact of the formation damage due to the effect of fracture fluid was not considered here. The distribution of damage around the HFWs influences their well performance. It is recommended to extend the study to evaluate the impact of this damage on the HFWs performance. It is suggested to define this effect as another skin, which can be simply employed in the effective wellbore radius calculation.
2. The application of the proposed effective wellbore radius approach can be investigated for fractured horizontal wells.

3. The Multi-Layer HFW study (presented in Chapter 4) was for isotropic case with cross flow, it is recommended to extend this study for anisotropic case and to also consider the effect of hydraulic fracture partial height penetration.

For Fracture Optimization:

1. It is recommended to examine the general UFD formulation for the case of rectangular reservoirs with different aspect ratios.
2. Consideration of the economic element of the optimum fracture design is highly recommended.

For Cleanup Efficiency:

1. As noted Chapter 6, the statistical tool linear LRSM (with and without interaction terms) has been used for analysis of data. Performing the same exercise using quadratic RSM is recommended.
2. The statistical approach followed in Chapter 6, to evaluate the impact of parameters on the GPL for a fractured well can be extended to gas condensate reservoirs.
3. The UFD method presented in chapter 5 was for ideal case with no fracture fluid damage, i.e. the method is based on an ideal fracture with no contribution of cleanup efficiency. It is highly recommended to benefit from the results presented in the clean-up efficiency study in order to improve the optimum fracture design formulations (presented in Chapter 5).